Molecular Simulations of Acid Gas Absorption into Aqueous Solvents

Polat, H.M.

Important note
To cite this publication, please use the final published version (if applicable).
Please check the document version above.

Molecular Simulations of Acid Gas Absorption into Aqueous Solvents

Molecular Simulations of Acid Gas Absorption into Aqueous Solvents

Proefschrift

ter verkrijging van de graad van doctor
aan de Technische Universiteit Delft,
op gezag van de Rector Magnificus prof. dr. ir. T.H.J.J. van der Hagen,
voorzitter van het College voor Promoties,
in het openbaar te verdedigen op
vrijdag 20 september 2024 om 12:30 uur

door

Hüsamettin Mert Polat

Master of Science in Materials Science and Engineering,
Koç University, Türkiye,
geboren te Turhal, Türkiye.

Dit proefschrift is goedgekeurd door de

promotor: prof. dr. ir. T. J. H Vlugt
promotor: dr. O. A. Moultos

Samenstelling promotiecommissie:

Rector Magnificus,	voorzitter
Prof. dr. ir. T. J. H. Vlugt,	Technische Universiteit Delft
Dr. O. A. Moultos,	Technische Universiteit Delft
Onafhankelijke leden:	
Prof. dr. H. Hajibeygi,	Technische Universiteit Delft
Prof. dr. G. Kontogeorgis,	Danmarks Technische Universiteit, Denmark
Prof. dr. K. Hooman,	Technische Universiteit Delft
Dr. S. Lasala,	Université de Lorraine, France
Dr. F. de Meyer,	Total Energies S.E., France
Dr. H. B. Eral,	Technische Universiteit Delft

Keywords:	Acid Gas, Monte Carlo, Molecular Dynamics, Absorption, Reaction Equilibrium, CO_2 Capture, H_2S Capture

Contents

1

Introduction

CO$_2$, a major greenhouse gas, plays a pivotal role in intensifying the greenhouse effect and driving climate change [1]. As shown in Fig. 1.1, an alarming increase in the concentration of CO$_2$ in the atmosphere has been witnessed, surging from 310 ppm in 1960 to 420 ppm in 2023 [2], a trend primarily attributed to fossil fuel combustion [3]. The projections indicate that even if CO$_2$ emissions are kept constant, the concentration of CO$_2$ in the atmosphere is expected to reach 500 ppm by 2050 [1]. This rise in CO$_2$ concentration has already led to a significant increase in the global surface temperature compared to pre-industrial times, with an observed increase of more than 1 °C [2]. In this context, natural gas as a strategic transition fuel until the large scale usage of renewable energy sources becomes feasible gains importance, offering a tangible pathway to mitigate CO$_2$ emissions and transition towards a sustainable global energy landscape. Compared to other fossil fuels, natural gas combustion produces much lower particulate matter emissions and has the highest energy output per mole of emitted CO$_2$ [4–6].

40% of the known natural gas sources have high concentrations of acid gases, specifically, more than 2 mol % of CO$_2$ and 100 ppm of H$_2$S [7]. While some of the reservoirs with the lowest concentrations of CO$_2$ and H$_2$S are located in Russia, central Asia, and the Middle East, typically, the reservoirs in southeast Asia and northwest Australia have the highest concentrations of CO$_2$ and H$_2$S, reaching CO$_2$ and H$_2$S concentrations up to 80 mol % [8] and 26 mol % [9], respectively.

1

Figure 1.1: CO_2 concentration in the atmosphere and global surface temperature anamolies for years from 1960 to 2023 [2]. Surface temperature anamolies are calculated by subtracting the average global surface (land and ocean) temperature (13.9 °C) of the 20th century (1901–2000) from the average surface temperature of a specific year. The dashed line represents the baseline of zero surface temperature anamoly.

Hydrocarbon, CO_2, and H_2S concentrations in different natural gas reservoirs are listed in Table 1.1. CO_2 and H_2S can cause corrosion of the pipelines [10, 11], and therefore, these components must be removed from the natural gas streams. Also, for safety reasons, H_2S must be removed since it is a toxic gas [12]. For transportation in pipelines, CO_2 and H_2S concentrations should be lower than 2 mol % and 4 ppm [13], respectively. In liquefied natural gas (LNG), CO_2 concentrations should be lower than 50 ppm [8] to eliminate the blockages caused by solid CO_2 in the liquefaction process.

1.1. Acid Gas Removal Technologies

Several different processes can be used to remove acid gases from natural gas streams such as membrane-based separation [16, 17], cryogenic distillation [18, 19], direct conversion of H_2S to elemental sulfur [20, 21], adsorption-based separation [22–24], and absorption-based separation [7]. Membrane-based separation uses selective membranes to separate acid gases (CO_2 and H_2S) from industrial gas streams based on molecular size and affinity towards membrane material [25, 26]. Membrane-based separation processes offer reduced capital and maintenance cost (as there are no moving parts), operational simplicity, and space efficiency [27]. However, with most commercial membranes, there is a trade-off between selectivity and permeability, i.e., multistage units and high surface areas are needed for an efficient separation with high permeability [25, 26, 28]. Membrane-based

Table 1.1: Hydrocarbons, N_2, CO_2, H_2S composition of the natural gas in different reservoirs. All concentrations are reported in mol%. C_2+ denotes the hydrocarbons heavier than methane.

Location	CH_4	C_2+	N_2	CO_2	H_2S	Source
Groningen, The Netherlands	81.28	3.51	14.27	0.94	Unknown	[14]
Pars, Iran	89.24	3.44	1.70	3.28	0.66	[14]
Waterton, Canada	65.49	14.03	0.97	3.48	16.03	[14]
Velebit, Serbia	88.50	3.85	3.72	3.88	Unknown	[15]
Novi Kneževac, Serbia	83.00	7.55	5.00	4.14	Unknown	[15]
Libo Southeast, Indonesia	62.48	15.52	Unknown	22.00	0.00	[9]
Tanjung Miring Timur, Indonesia	63.82	9.29	Unknown	0.50	26.40	[9]
Bojongraong, Indonesia	4.58	3.18	Unknown	92.24	0.00	[9]
Walio, Indonesia	73.60	20.76	Unknown	4.31	1.33	[9]

separation may also suffer from fouling of the membranes [29]. In cryogenic distillation, CO_2 and H_2S are separated from natural gas streams using the difference in boiling points of the components. This technology offers high separation efficiency, however, it is a very energy intensive process as the required temperatures are very low (<200 K) [28, 30]. The direct conversion of H_2S to elemental sulfur involves a chemical reaction using a catalyst that transforms H_2S into solid sulfur [31]. This technology is known for its simplicity and high efficiency of H_2S removal from natural gas, however, other stages of CO_2 removal are required. This process is also energy intensive as the required temperatures are high (>493 K) [31–33]. Adsorption-based separation, using solid materials such as activated carbons, zeolites, or metal-organic frameworks for selective chemical and/or physical adsorption, stands out for its versatility and low energy consumption [26]. However, most available adsorbents offer low selectivity of acid gases and low adsorption capacities [28, 34, 35].

Absorption-based separation is commonly preferred for acid gas removal from natural gas streams as it is a mature and reliable process which also results in very low amounts of absorbed (lost) methane [36–38]. This process uses liquid solvents to remove CO_2 and H_2S from natural gas streams [7, 37, 39, 40]. The liquid solvents are typically aqueous solutions of alkanolamines, such as monoethanolamine (MEA), diethanolamine (DEA), and N-methyldiethanolamine (MDEA), which can absorb acid gases by physical and/or chemical absorption [7, 36]. In absorption-based separation of acid gases, the natural gas stream flows through a high pressure column (usually at pressures of 20–100 bar [41]) at temperatures in the range of 313–353 K [42]. The acid gases come in contact with the solvent and are absorbed by the liquid phase. Another advantage of the absorption-based separation process is that the liquid solvents can be regenerated at high temperature (typically at 363–383 K) and reused. A schematic of absorption-based acid gas removal process is shown in Fig. 1.2. To optimize this process, process simulation software is typically used [43–46]. The process simulation software requires parameters such as the vapor-liquid equilibrium (VLE) curve of acid gases at very low pressures

(the partial pressure of CO_2 and H_2S can be lower than $1\,\text{kPa}$ in the absorption column), diffusion coefficients of the acid gases, and the viscosity and the density of the solvent [47]. Therefore, accurate knowledge of these properties is crucial for the process design of both the absorption and regeneration stages. Stirred cell setups are used to measure the VLE of acid gases in aqueous alkanolamine solutions [48–54]. Stirred cell setups are designed to investigate the equilibrium and mass transfer kinetics in an absorption process, typically containing a vessel equipped with stirring mechanisms to facilitate gas-liquid contact and a pressure gauge to measure the pressure of the gas phase [53]. Due to the limitations of this setup, it is very challenging to measure VLE of CO_2 and H_2S in liquid solvents at very low pressures. In the stirred cell method, the partial pressure of acid gases at equilibrium are measured as the difference between the total pressure measured in the cell and the vapor pressure of the solvent measured before the absorption takes place ($P_{\text{acid gas}} = P_{\text{total}} - P_{\text{vapor}}$). At very low partial pressures of CO_2 and H_2S, the values P_{total} and P_{vapor} are very close to each other which introduces a significant uncertainty in the measured partial pressures of acid gases. To circumvent this issue, Derks [53] suggested the use of a second stirred cell, which measures P_{vapor} continuously during the experiment, decreasing the uncertainty in the measured values of P_{vapor}. Derks [53] was able to measure partial pressures of CO_2 as low as $0.148\,\text{kPa}$ with an uncertainty of $0.01\,\text{kPa}$. For more details of this experimental setup, the reader is referred to Ref. [53]. In addition to these challenges, experiments with H_2S pose significant safety risks due to toxicity, especially at high-pressure and high-temperature conditions [12]. Since CO_2 and H_2S react with the solvent, it is challenging to experimentally measure their diffusivities in aqueous alkanolamine solvents. For this reason, estimates of the diffusion coefficients of acid gases are obtained by performing experiments with surrogate non-reacting molecules such as N_2O instead of CO_2 [55–57]. For example, Sada et al. [58] estimated the diffusion coefficient of CO_2 in aqueous solutions of different alkanolamines by measuring the diffusion coefficient of N_2O in these solutions. For more examples of the CO_2/N_2O analogy, the reader is referred to refs. [55, 59, 60].

1.2. Simulations of Absorption-Based Acid Gas Removal

1.2.1. Simulation Methods

To address experimental challenges in measuring very low partial pressures and diffusivities of acid gases, computational methods play a crucial role [61]. In this section, simulation methods, including quantum chemistry calculations and force field-based molecular simulations, are explained. These simulation methods offer valuable insights into the reaction equilibria and transport phenomena in absorption-based acid gas removal processes.

Quantum chemistry calculations solve an approximation of the Schrödinger equation (as the Schrödinger equation is not solvable for systems of physical interest, i.e., molecules with many atoms), providing insight into the electronic structure of molecules [62–65]. Quantum chemistry calculations are used to study the struc-
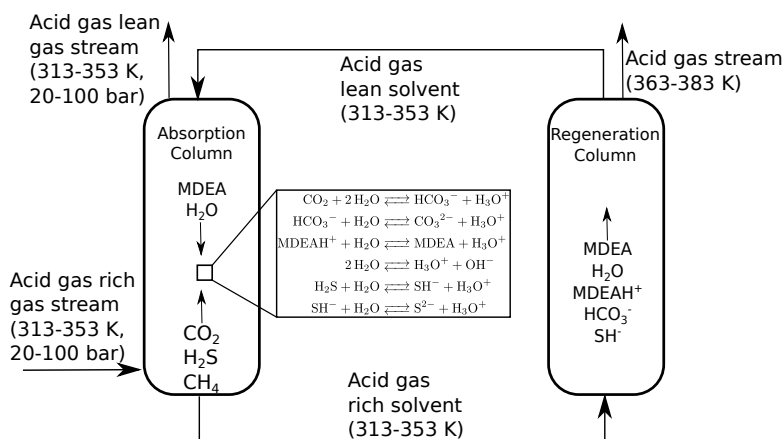
Figure 1.2: Schematic representation of a absorption-based acid gas removal process using aqueous alkanolamine solvent as absorbent. Acid gas rich natural gas stream enters the absorption column and comes in contact with the absorbent solvent (usually at temperatures in the range of 313–353 K [42] and pressures in the range of 20–100 bar [41]). Acid gases are absorbed into the solvent where CO_2 and H_2S reacts and forms reaction products such as HCO_3^- and SH^-. Acid gas rich solvent is transferred to the regeneration column where it releases CO_2 and H_2S at high temperatures, usually in the range of 363–383 K. In this schematic, an aqueous MDEA solution as absorbent is shown as an example.

ture and behavior of molecules at the electron scale. These calculations are often performed at a steady state and a temperature of $0\,\mathrm{K}$ [66, 67]. Quantum chemistry calculations involve choosing appropriate (1) levels of theory, and (2) basis sets. A level of theory is a method to approximate the complex interactions between electrons in a molecule [68]. Common levels of theory in quantum chemistry calculations are Hartree-Fock (HF) [69], second order Møller-Plesset perturbation (MP2) [70], and density functional theory (DFT) [64, 71–73]. In selecting levels of theory for quantum chemistry calculations, there is typically a trade-off between computational cost and calculation accuracy [74]. For example, in the HF level of theory [69], the electron-electron interactions in a molecule are computed using a mean-field approximation, i.e., each electron interacts with an average field of all other electrons, while the MP2 level of theory [70] accounts for the interactions between pairs of electrons. The HF and MP2 levels of theory scale approximately with $\mathcal{O}(N^4)$ and $\mathcal{O}(N^5)$, respectively, where N is the number of atoms [75]. Basis sets are the mathematical functions used to approximate the wavefunctions (probability distributions) of electrons in molecules [76]. The trade-off between computational cost and accuracy is also apparent in basis sets choice. Minimal basis sets such as STO-3G are less costly and less accurate, while more elaborate ones such as 6-311+G are more accurate but come with higher computational costs [76]. These calculations yield valuable information about the molecular electronic energies and geometries which can be essential for understanding chemical processes. Another important thermodynamic property that can be computed using quantum chemistry calculations is the partition function of an isolated molecule. Partition function of an isolated molecule is a sum over all possible states of the specific molecule [77].

The partition function bridges the gap between quantum chemistry and thermodynamics at larger scales by allowing for the calculation of various thermodynamic quantities such as heat capacities and standard ideal gas chemical potentials (μ_i^0) [77–79]. To perform quantum chemistry calculations, software packages such as Gaussian [78], ORCA [80], and NWChem [81] can be used.

In many molecule systems, a system state refers to a specific configuration of molecules of the simulated system. At constant temperature or pressure, not all system states have the same statistical weight (probability) [82, 83]. Given the enormous number of potential system states, individually analyzing each one is computationally not possible. The probability of a system state occurring is governed by the principles of statistical mechanics, which take into account factors such as energy, entropy, and volume [82]. To compute the energy of a system state, quantum chemistry [78, 84] or classical force field-based [85, 86] approaches can be used. Due to the high computational cost of quantum chemistry approach, classical force fields are more practical to use for systems with many (>100) molecules [82]. Classical force field-based methods, i.e., molecular simulations, simplify molecular interactions by using empirically- or quantum chemically-derived potentials, enabling efficient exploration of different system states [87–92]. Therefore, molecular simulations provide valuable insights into system behavior while mitigating the computational demands associated with quantum mechanical calculations. Classical force fields used in molecular simulations typically include non-bonded and bonded potentials. Non-bonded potentials often consist of two components: the Lennard Jones (LJ) potential, which characterizes the van der Waals interactions, and electrostatic potentials, which describe the interactions between atoms due to their charges [82, 83]. Bonded potentials are used to describe the bonds, angles, and torsions (dihedral angles) within molecules to accurately capture the molecular structure [88, 89, 93]. There are molecule-specific force fields tailored for individual molecules, such as the TIP4P/2005 force field [94] for water, as well as generic force fields, such as the Optimized Potentials for Liquid Simulations-All Atom (OPLS-AA) [88, 89] force field and General Amber Force Field (GAFF) [95], which can be applied to a broader range of chemical compounds in molecular simulations.

There are two main methods to the molecular simulations: (1) the Monte Carlo (MC) approach where the system states are sampled according to their statistical weight, and (2) Molecular Dynamics (MD) approach where the dynamical evolution of a system as a function of time is followed. These two methods are considered equivalent, as proposed by the ergodicity hypothesis [82]. In MC simulations, favorable system states, corresponding to lower potential energies, are sampled with higher probabilities, while unfavorable system states are rejected or accepted with a lower probability (as these have lower statistical weight) [82]. MC simulations sample relevant system states using trial moves, which are actions that change the configuration of molecules in the system [82, 85, 96]. These trial moves include translation of molecules, rotation of molecules, and volume changes of the system [85, 86, 96]. For example, a translation trial move involves randomly selecting a molecule and displacing it by a certain distance in a random direction within the simulation box. Typically, thousands to millions MC cycles are performed in an MC

simulation where each MC cycle consists of N number of trial moves [97]. MC simulations can be used to compute equilibrium properties such as densities [90, 93], fugacity coefficients [98, 99], heat capacities [100–102], and excess chemical potentials of species (μ_i^{ex}) [103–108]. However, challenges exist in MC simulations, particularly when computing μ_i^{ex} of a species in a dense solution, as the lack of available space hinders the insertion/deletion of a molecule. To overcome this problem, advanced methods such as the Configurational-Bias MC (CBMC) [109–113] and Continuous Fractional Component MC (CFCMC) [97, 114–119] methods have been developed. For example, the CFCMC method uses gradual insertions/deletions of particles to/from the simulation box, allowing surrounding molecules to configure accordingly with the insertion/deletion. MC simulations can be performed using software packages such as RASPA [85, 113, 120, 121], GOMC [86], Cassandra [122], and Brick-CFCMC [96, 97, 123].

In MD simulations, the dynamical evolution of a system in time is followed by solving Newton's equations of motion for each atom in the simulation [82, 83]. MD simulations are constrained by computational resources, and can be applied to systems with millions of atoms [124, 125] and up to timescales of milliseconds [126, 127]. This limitation impacts the ability of the simulation to provide insight into rare events (such as unfolding of a protein), long-timescale phenomena (such as clustering of molecules over several seconds), or macroscopic behaviors (such as the flow of fluids through pores) [82]. MD simulations are particularly effective in capturing dynamic properties of materials and molecules, making them valuable for predicting transport properties such as thermal conductivities, viscosities, and diffusion coefficients [82, 83]. Popular MD simulation software packages include GROMACS [128, 129], LAMMPS [130], AMBER [131, 132], and NAMD [133].

1.2.2. Predicting Reaction Equilibria and VLE using Free Energy and Quantum Chemistry Calculations

The equilibrium condition for a chemical reaction can be computed using the chemical potentials of the species involved in the reaction [134]:

$$\sum_{i=1}^{N_{\text{species}}} \nu_{i,j} \mu_i = 0 \tag{1.1}$$

where N_{species} is the number of species involved in reaction j (including the solvent and the solutes), $\nu_{i,j}$ is the stoichiometric coefficient of species i in reaction j, and μ_i is the chemical potential of species i. The chemical potential of species i is calculated using an ideal gas reference state [96]:

$$\mu_i = \mu_i^0 + \mu_i^{\text{ex}} + RT \ln\left[\frac{\rho_i}{\rho_0}\right] \tag{1.2}$$

where T is the absolute temperature, ρ_i is the number density of solute i in the solvent, and ρ_0 is the reference number density of 1 molecule Å^{-3} [96]. The value of μ_i^0 of a molecule depends on the internal degrees of freedom in the molecule and

can be computed using quantum chemistry calculations or thermodynamic tables, such as JANAF tables [135, 136].

Noroozi et al. [104] computed the values of μ_i^0 for 7 different alkanolamines using quantum chemistry calculations. Rahbari et al. [137] used JANAF tables to compute the values of μ_i^0 for CO, H_2O, CO_2, H_2, HCOOH, and CH_4 to predict reaction equilibria in combined steam reforming of methane and formic acid. The value of μ_i^{ex} of a molecule is determined by the interactions between the molecule and surrounding molecules [134]. This value can be computed using free energy calculations in MC or MD simulations. In dense solutions such as the aqueous alkanolamine solutions relevant to absorption-based acid gas removal processes, the CFCMC method offers accuracy as the molecules are inserted/deleted gradually to/from the simulation box using an interaction scaling parameter λ in an expanded ensemble [96, 123]. The interactions of a molecule (or a molecule group) are scaled from no interactions with the surrounding ($\lambda = 0$) to full interactions with the surrounding ($\lambda = 1$). In the CFCMC method, the values of μ_i^{ex} can be computed as [96, 106]:

$$\mu_i^{ex} = -RT \ln \left[\frac{p(\lambda_i = 1)}{p(\lambda_i = 0)} \right] \tag{1.3}$$

where $p(\lambda_i = 1)$ and $p(\lambda_i = 0)$ are the probabilities of λ of species i being 1 and 0, respectively. Using Eq. (1.3), Hens et al. [96] computed the values of μ_i^{ex} for methanol, acetic acid, methyl acetate, and water to predict the reaction equilibrium constant of the esterification of methanol with acetic acid. In another study, Poursaeidesfahani et al. [117] computed the values of μ_i^{ex} of H_2, N_2, and NH_3 using the CFCMC method. Despite the application of the CFCMC method to many species in different solutions [97, 108, 138–140], its use for ionic species such as HCO_3^-, CO_3^{2-}, and SH^-, which are relevant to absorption-based acid gas removal processes, is not documented in literature. Also, the accuracy of computing μ_i^0 and μ_i^{ex} using quantum chemistry and free energy calculations, respectively, and the accuracy of reaction equilibria computed using predicted values of μ_i^0 and μ_i^{ex} has not been tested in literature.

Reaction equilibria can be used to determine the loading of acid gases in a reactive liquid solvent. By using the concentrations of dissolved free gases (free CO_2 or H_2S) in the liquid phase (obtained from reaction equilibria calculations), the partial pressure of acid gases in the gas phase can be computed [5]. The VLE of acid gases in a reactive liquid solvent is characterized by the loading of the acid gas in the liquid phase and the partial pressure of the acid gas in the gas phase.

1.2.3. Predicting Transport Properties using Molecular Dynamics Simulations

Viscosities and diffusivities of acid gas loaded and unloaded aqueous alkanolamine solutions are crucial for the optimization of the absorption-based acid gas removal processes [47, 141, 142]. MD simulations offer a powerful tool for predicting transport properties in different solutions [143–149]. However, accurate determination of viscosities and diffusion coefficients requires MD simulations to span sufficiently

long time scales to capture diffusive processes. Typically, MD simulations must extend over nanosecond to microsecond time scales to accurately capture transport properties such as viscosities and diffusivities [82, 83, 144, 145]. As a rule of thumb, longer MD simulations need to be performed for more viscous solutions, in which the movement of molecules is slower compared to a less viscous solution. Despite the importance of transport properties in the optimization of absorption-based acid gas removal processes, the available studies in literature are scarce. Chen et al. [56] computed the diffusion coefficients of CO_2 and H_2S in aqueous MEA solutions at 303 K to validate the CO_2/N_2O analogy, a method to predict the diffusivity of CO_2 from the measured diffusivity of N_2O (as CO_2 reacts with the solution and N_2O does not [55, 60]). Melnikov et al. [150] computed the diffusion coefficients of CO_2 in aqueous MEA solutions for different loadings of CO_2 at 313 K, revealing that the diffusion coefficients of all the species in CO_2 loaded aqueous MEA solution decrease significantly with increasing CO_2 loading. Yiannourakou et al. [7] computed the diffusion coefficients of MDEA and CO_2 in 30 wt.% MDEA/water solutions for a temperature range of 300–400 K. However, there is a notable gap in the literature regarding the temperature and alkanolamine concentration dependence of diffusion coefficients of acid gases in commonly used aqueous alkanolamine solutions such as MEA and MDEA. Additionally, the viscosities and diffusion coefficients of reaction products from CO_2 and H_2S absorption in aqueous alkanolamine solutions remain unexplored.

1.3. Outline of This Thesis

This thesis introduces numerical methods, mainly molecular simulation-based techniques, as a complementary approach to address experimental challenges encountered in measuring VLE and diffusivities of acid gases in aqueous alkanolamine solutions, paving the way for more efficient absorption-based acid gas removal processes. The thesis is organized as follows:

Chapter 2 presents several new major features added to Brick-CFCMC (https://gitlab.com/ETh_TU_Delft/Brick-CFCMC). Brick-CFCMC is an advanced open-source MC code to calculate phase- and reaction equilibria using classical force fields in different ensembles with the CFCMC method. In Brick-CFCMC, excess chemical potentials of species, μ^{ex}, can be computed using the "probability" route (Eq. (1.3)), however this method requires sampling of the entire λ-space in a single simulation. As this is very challenging for ionic and/or polar species, the first newly implemented feature is thermodynamic integration for the computation of μ^{ex} because this method eliminates the need for sampling the full λ-space in a single MC simulation and enables the computation of μ^{ex} for ionic and/or polar molecules (as relevant to acid gas removal using aqueous alkanolamine solutions). For this purpose, the computation of the ensemble average of the derivative of the potential energy with respect to the scaling factor for intermolecular interactions ($\langle \partial U/\partial \lambda \rangle$) was implemented for LJ and electrostatic interaction potentials. Efficient bookkeeping is implemented so that the value of the term $\partial U/\partial \lambda$ is updated after every MC trial move with negligible computational cost. The accuracy and reliability of the calculation of μ^{ex} is demonstrated by computing the free energy of hydration

of sodium chloride in water. Also, hybrid MC/MD translation and rotation trial moves to increase the efficiency of sampling of the configuration space are implemented. In these trial moves, short MD trajectories are performed to collectively displace or rotate all molecules in the system. These trajectories are accepted or rejected based on the drift of the total energy. The efficiency of these trial moves can be tuned by changing the timestep and the trajectory length. The new trial moves increase the efficiency of MC simulations, as shown using a case study of a viscous fluid.

In Chapter 3, an open-source chemical reaction equilibrium solver in Python (CASpy, https://github.com/omoultosEthTuDelft/CASpy) is developed to compute the concentration of species in any reactive liquid-phase absorption system. An expression for a mole fraction-based equilibrium constant as a function of μ_i^{ex} (that can be computed using Brick-CFCMC), μ_i^0 (that can be computed using quantum chemistry calculations), temperature, and volume is derived. As a case study, the CO_2 absorption isotherm and speciation in a 23 wt.% MDEA/water so-lution at 313.15 K are computed, and the results are compared with available data from literature. The results show that the computed CO_2 isotherms and speciations are in excellent agreement with experimental data, demonstrating the accuracy and the precision of CASpy. The binary absorption of CO_2 and H_2S in 50 wt.% MDEA/water solutions at 323.15 K are computed and compared with available data from literature. The computed CO_2 isotherms showed good agreement with other modeling studies from literature, while the computed H_2S isotherms did not agree well with experimental data. This is because the experimental equilibrium constants used as an input were fitted to reproduce H_2S solubility in pure water and need to be adjusted for H_2S/CO_2/MDEA/water systems. Using free energy calculations with two different force fields for MDEA and MDEAH$^+$ (GAFF and OPLS-AA) and quantum chemistry calculations, the equilibrium constant (K) of the MDEAH$^+$ dissociation reaction are computed. Despite the good agreement of the OPLS-AA force field $(\ln[K] = -24.91)$ with the experiments $(\ln[K] = -23.04)$, the partial pressures of CO_2 computed using the experimental equilibrium constant are ca. 6 times higher than the ones computed using the equilibrium constants from the OPLS-AA force field at low CO_2 loadings. The limitations of computing CO_2 absorption isotherms using free energy and quantum chemistry calculations are systematically investi-gated. Results show that the computed values of μ_i^{ex} are very sensitive to the point charges used in the simulations which limits the predictive power of this method.

Chapter 4 investigates the effect of temperature and MEA concentration on the self-diffusivity of acid gases, CO_2 (D_{CO_2}), and H_2S (D_{H_2S}) in aqueous MEA solutions. For this purpose, densities of pure MEA and 30 wt.% MEA/water solutions are computed while scaling the LJ energy parameters $(\varepsilon$, from OPLS-AA force field) and point charges (obtained using quantum chemistry calculations) of all atoms in MEA. Results show that with a scaling factor of 0.80 applied to the point charges of MEA, computed densities agree well with the experimental ones from literature. This was tested by computing viscosities and the self-diffusivity of pure MEA and 30 wt.% MEA/water solutions and comparing these with experiments. Results show that the scaling factor of 0.80 also works well for predicting transport properties

of MEA/water solutions. Finally, self-diffusivities of infinitely diluted CO_2 and H_2S for temperatures ranging from 293–353 K and MEA concentrations of 10–50 wt.% are computed. The self-diffusivity of both acid gases depends significantly on the temperature and MEA concentration in the solution.

In Chapter 5, the effects of temperature and MDEA concentration on D_{CO_2} and D_{H_2S} in unloaded and acid gas loaded aqueous MDEA solutions are investigated. The densities and viscosities of aqueous MDEA solutions for an MDEA concentration range of 10–50 wt.% and a temperature range of 288–333 K are computed, showing an excellent agreement with experimental data from literature. The self-diffusivities of MDEA (D_{MDEA}) in aqueous MDEA solutions are computed and the results show that the computed values of D_{MDEA} are in excellent agreement with experimental and simulation results from literature. The self-diffusivities D_{CO_2} and D_{H_2S} in aqueous MDEA solutions are computed for a wide range of temperatures and MDEA concentrations, and the results show that both D_{CO_2} and D_{H_2S} depend significantly on temperature and MDEA concentration. Comparing results with Chapter 4, it is shown that both CO_2 and H_2S diffuse slower in aqueous MDEA solutions than in aqueous MEA solutions. The slower diffusion of acid gases in aqueous MDEA solutions can be attributed to the branched structure of MDEA which presents a larger hindrance compared to the linear and smaller MEA molecules. By comparing the radial distribution functions of CO_2, H_2S, water, and MDEA, it is revealed that H_2S has stronger interactions with the surrounding molecules than CO_2, which makes H_2S diffuse slower in aqueous MDEA solutions. The densities and viscosities of the acid gas loaded aqueous MDEA solutions and self-diffusivities of the reaction products of CO_2 and H_2S with aqueous MDEA solutions are also investigated. The self-diffusivities of CO_2-loaded solutions significantly decrease with increasing CO_2 loading, while the self-diffusivities of H_2S-loaded solutions do not change with changing H_2S loading. This phenomenon can be attributed to the distinct shapes of the reaction products formed during CO_2 and H_2S absorption in aqueous MDEA solutions. The linear shape of the reaction product from H_2S absorption (SH^-) contrasts with the spherical shape of the reaction product from CO_2 absorption (HCO_3^-), potentially explaining the observed differences in self-diffusivities as a function of acid gas loading. The results of this thesis will be helpful in the design and optimization of acid gas removal units.

2

Thermodynamic Integration and Hybrid MC/MD Trial Moves in Brick-CFCMC
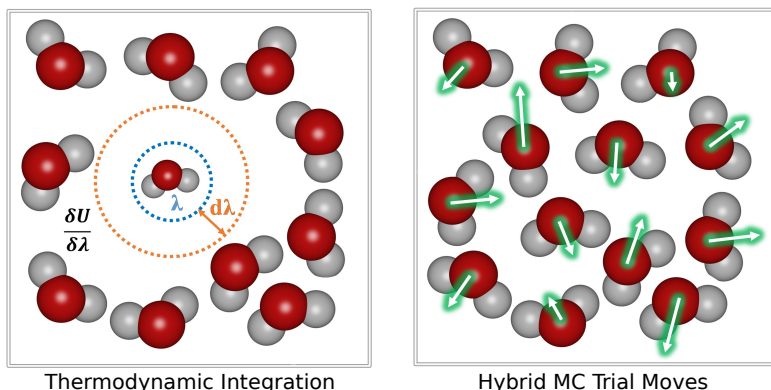
Thermodynamic Integration   Hybrid MC Trial Moves

Thermodynamic integration for the computation of excess chemical potentials μ^{ex} and hybrid MC/MD trial moves were implemented in Brick-CFCMC. Thermodynamic integration eliminates the need to sample the entire λ-space in a single simulation and increases the precision in the computed μ^{ex}, while hybrid MC/MD trial moves increases the efficiency of MC simulations.

2.1. Introduction

Recently, we presented Brick-CFCMC [96], an open source molecular simulation code for the calculation of phase and reaction equilibria using the state-of-the-art force field-based MC simulations in different ensembles, such as the *NVT*, the *NPT*, the grand-canonical ensemble, the reaction ensemble [151–153], and the Gibbs ensemble [154–156]. Brick-CFCMC uses the CFCMC method [114–116, 123, 157] for molecule exchanges. This method involves a fractional molecule whose interactions with the surrounding molecules are scaled using a continuous scaling factor, λ, from zero interactions with the surroundings ($\lambda = 0$) to full interactions with the surroundings ($\lambda = 1$) [114]. MC trial moves that modify the value of λ are used to sample λ-space and these trial moves can be included in expanded ensembles such as the *NVT* ensemble, the *NPT* ensemble, and the Gibbs ensemble [123]. The CFCMC method considerably improves the insertion or deletion of molecules while allowing for a direct computation of chemical potentials and partial molar properties [106, 116–118, 138]. Brick-CFCMC has been used in many studies, especially for the computation of gas solubilities in solvents [107, 108, 116, 123, 148, 158–163]. For example, Dawass et al. [160] computed the solubility of CO_2, oxalic acid, and formic acid in the mixtures of deep eutectic solvents, methanol, and propylene carbonate. Another example is the study by Kobayashi and Firoozabadi [161] where the authors computed the solubility of *n*-decane, *n*-hexadecane, and *n*-eicosane (and corresponding structural isomers) in the CO_2-rich and hydrocarbon-rich phases using the CFCMC method in the Gibbs ensemble.

We present the implementation of two new features, (1) the computation of excess chemical potentials (μ^{ex}) using thermodynamic integration [82, 164]:

$$\mu^{\text{ex}} = \int_0^1 \left\langle \frac{\partial U}{\partial \lambda} \right\rangle_{NPT} \mathrm{d}\lambda \qquad (2.1)$$

and (2) hybrid MC/MD trial moves. Thermodynamic integration allows for the calculation of μ^{ex} by integrating the average derivative of potential energy with respect to the interaction scaling factor ($\langle \partial U/\partial \lambda \rangle$). Using μ^{ex}, activity and fugacity coefficients of species can be computed [165, 166]. Brick-CFCMC can already calculate μ^{ex} using the probability distribution of the scaling factor $p(\lambda)$ of fractional molecules (Eq. (1.3)) [96, 106]. This method requires the probabilities $p(\lambda = 0)$ and $p(\lambda = 1)$. A weight function ($W(\lambda)$) is required to ensure a flat probability distribution of λ [114, 167]. Although this method works efficiently for small molecules, we found that it is difficult for large and/or strongly polar molecules because (1) the probability distribution of λ can be sensitive to the changes in the biasing function, and (2) the biasing function can be very large for ionic systems (e.g., of the order of $100k_{\text{B}}T$). Therefore, a flat distribution of the observed probability of λ is challenging to achieve in a single simulation, resulting in a large uncertainty for the computed μ^{ex}. It is more convenient to calculate μ^{ex} of large and/or strongly polar molecules using thermodynamic integration because it eliminates the need for sampling the full λ-space with equal probabilities in a single simulation. With thermodynamic integration, $\langle \partial U/\partial \lambda \rangle$ can be computed from several independent simulations at dif-

ferent fixed values of λ (or a limited range of λ-values) or by sampling the whole λ-space in a single simulation. We implemented an efficient bookkeeping, so the instantaneous value of $\partial U/\partial \lambda$ is updated after every MC trial move. Therefore, the ensemble average $\langle \partial U/\partial \lambda \rangle$ is computed with negligible computational costs. Alternatively, the weighted histogram analysis (WHAM) method [168, 169], the Bennett acceptance ratio (BAR) method [170], and the multistate Bennett acceptance ratio (MBAR) method [171] may also be used for the computation of μ^{ex} using post-processing of simulation data [172].

In the CFCMC method, trial moves are attempted to reinsert the fractional molecule at a random position in the simulation box. Additionally, trial moves are attempted to transform the fractional molecule into a whole molecule, while a randomly selected whole molecule is transformed into a fractional molecule (at the same value of λ) [123]. These trial moves help sampling the λ-space more efficiently, as well as thermalizing the system. However, for viscous liquids with strong intermolecular interactions, such as ionic liquids and deep eutectic solvents (DES) [158], the sampling of configuration space is not efficiently performed by single-molecule trial moves, even if the aforementioned trial moves are carried out [83, 108, 173]. It is well-known that single-molecule trial moves are not efficient in inducing collective motion in a dense fluid [83, 173]. A variety of advanced techniques have been developed and reported in literature for improving the sampling of configuration space in MC simulations. Well-known examples of such techniques are the smart MC algorithm by Rossky et al. [173], force bias MC by Pangali et al. [174], multiparticle MC moves by Moučka et al. [175], and hybrid MC by Duane et al. [176]. We have implemented hybrid MC/MD trial moves for translation and rotation of molecules (conceptually similar to Duane et al. [176]) in Brick-CFCMC. We chose to have separate hybrid translation and rotation moves because combining these two trial moves were found to be less efficient [86]. In these trial moves, short Molecular Dynamics (MD) simulations are performed in the *NVE* ensemble, where Newton's equations of motion are integrated according to the computed resultant force or torque on each molecule. A schematic representation of the hybrid translation trial move is shown in Fig. 2.1. The hybrid trial moves are performed collectively, meaning all molecules are translated or rotated at every MD timestep, using a time-reversible (and area-preserving) integrator. During the hybrid trial moves, all molecules are kept rigid (intramolecular degrees of freedom are sampled differently in Brick-CFCMC [96]). Therefore, translations are applied to the centers of mass of the molecules, and rigid-body rotations are performed around the centers of mass. The short MD trajectories generated by the hybrid trial moves are accepted or rejected with a probability proportional to the Boltzmann factor of the total energy of the system [82]:

$$\mathrm{acc(o \to n)} = \min\left(1, \exp[-\beta(\Delta U + \Delta K)]\right) \qquad (2.2)$$

where o and n denote the old and new (initial and final) configurations of the MD trajectory, and ΔU and ΔK are the differences in potential energy and kinetic energy (translational or rotational), respectively, between the old and new configurations. β is defined as $1/(k_{\mathrm{B}}T)$, where k_{B} is the Boltzmann constant, and T is absolute
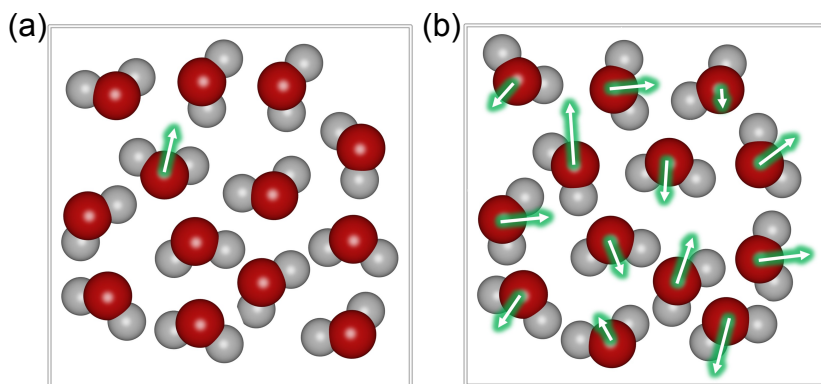
Figure 2.1: Schematic representation of (a) a conventional translation trial move and (b) a hybrid translation trial move. The conventional translation move attempts to displace a single randomly selected molecule in the simulation box in a random direction, while the hybrid translation trial move displaces all the molecules simultaneously, according to the magnitude and direction of the resultant forces acting on the molecules, using a short MD trajectory in the *NVE* ensemble. The length of the short MD trajectory as well as the timestep Δt can be adjusted to have a required acceptance probability. These trial moves increase the efficiency of the simulations significantly in the equilibration of the system and the sampling of configuration space [83, 173]. The red and gray atoms represent oxygen and hydrogen atoms, respectively. This figure was created with iRASPA [177].

temperature.

2.2. Implementation

In the CFCMC method, intermolecular LJ and electrostatic interactions are scaled differently as a function of λ. The scaling of LJ and electrostatic interactions are denoted by λ_{LJ} and λ_{el} respectively, and both are functions of λ. It is important to note that λ_{LJ} and λ_{el} should be continuous functions of λ, and that electrostatics are fully switched off ($\lambda_{\mathrm{el}} = 0$) before scaling down the LJ interactions [178]. The scaling scheme that we used for thermodynamic integration in Brick-CFCMC is shown in Fig. 2.2 and the details of this scaling are provided in Appendix A1. In Brick-CFCMC, the value of $\langle \partial U / \partial \lambda \rangle$ can only be computed for one charge-neutral group of fractional molecules, however, this group can contain several different molecules or ions. For example, a fractional group can consist of both a sodium ion (Na^+) and a chloride ion (Cl^-), so that thermodynamic integration directly results in the excess chemical potential of sodium chloride $\mu_{\mathrm{NaCl}}^{\mathrm{ex}}$. Analytic expressions for $\partial U / \partial \lambda$ were derived for intermolecular LJ and electrostatic potentials. For the LJ potential, terms were derived for truncated, truncated and shifted potentials, and for tail corrections. Analytic expressions for derivatives of electrostatic potentials may seem trivial at first sight because for linear charge scaling $\partial U / \partial \lambda$ is proportional to λ [86]. It is important to note that such a scaling may lead to overlaps between atoms for low values of λ_{el}. For this reason, we have used an offset for interatomic distances which makes the computation of $\partial U / \partial \lambda$ numerically stable (but leading to more complex expressions). For electrostatic interactions, we derived analytic
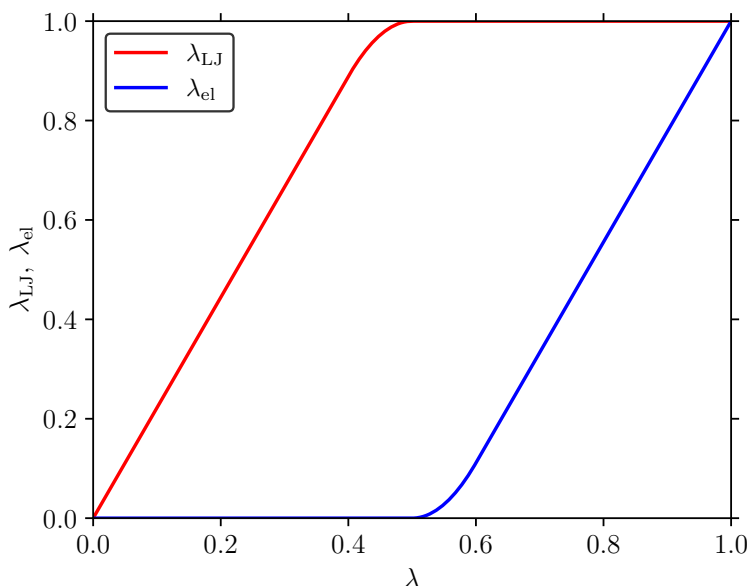
Figure 2.2: Scaling of LJ (λ_{LJ}) and electrostatic (λ_{el}) interactions as a function of λ for the computation of $\langle \partial U/\partial \lambda \rangle$ which is used for thermodynamic integration in Brick-CFCMC. Both λ_{LJ} and λ_{el}, and the derivatives of these functions with respect to λ are continuous. Red and blue lines are the plots of the scaling of LJ (Eq. (A1.3)) and electrostatic (Eq. (A1.4)) interactions, respectively.

expressions for the Wolf method [179], for the damped and shifted version of the Wolf method [119, 180, 181], and for the Ewald summation [182]. These analytic expressions can be found in Appendix A1. The computation of $\langle \partial U/\partial \lambda \rangle$ can be switched on with the respective keyword in the input files as described in the manual of Brick-CFCMC. The value of $\partial U/\partial \lambda$ is computed in Brick-CFCMC for every MC trial move. The software prints the values of $\langle \partial U/\partial \lambda \rangle$ for each λ to a file. We implemented the thermodynamic integration with efficient bookkeeping so that the computation of $\langle \partial U/\partial \lambda \rangle$ has negligible additional computational cost as the number of fractional molecules in the simulation box is low compared to the total number of molecules. Thermodynamic integration can be performed by post-processing computed values of $\langle \partial U/\partial \lambda \rangle$ using a tool provided with Brick-CFCMC. Brick-CFCMC also provides values for $\partial U/\partial \lambda$ that can be read directly into alchemlyb [183], and we have verified that identical excess chemical potentials are obtained.

The velocity Verlet algorithm [184, 185] is used to integrate the equations of motion in hybrid translation trial moves. In hybrid rotation trial moves, the quaternions of molecules need to be integrated simultaneously with the angular velocities. The NOSQUISH algorithm of Miller et al. [186] is used for the integration of equations of motion. The algorithms used for both the hybrid translation and hybrid rotation trial moves are symplectic (area-preserving) and time-reversible [82, 186]. Details of these algorithms as implemented in Brick-CFCMC can be found in Appendix A2.

2

For the hybrid trial moves, for efficiency reasons, the electrostatic forces/torques needed to create the short MD trajectories are always computed using the damped, shifted Wolf potential [180], for which the damping parameter and cutoff radius (independent of the cutoff for electrostatic energies) can be provided in the simulation input. The fact that the actual interaction potential (e.g. electrostatics with the Ewald summation) is different than it is accounted for in the acceptance rules [187].

2.3. Simulation Details

2.3.1. Thermodynamic Integration

All simulations were performed using Brick-CFCMC [96]. For the computation of $\mu_{\text{NaCl}}^{\text{ex}}$, the SPC/E [188] and Joung-Cheatham [189] force fields were used for water and NaCl, respectively. The force field parameters used in the simulations are listed in Appendix C (Appendices C.1.1 and C.2). 102 independent MC simulations with different and fixed values of λ were performed at 298 K and 1 bar, in the *NPT* ensemble. Initial configurations for these simulations were generated with a simulation box length of 20.8 Å, using 300 water molecules and a fractional group consisting of one sodium ion and one chloride ion. Atomic overlaps, caused by the random generation of initial configurations were removed by 10^3 initialization MC cycles, where only translation and rotation trial moves were used. Equilibration and production stages of the simulations were carried out, each for 10^6 MC cycles. In Brick-CFCMC, a single MC cycle consists of N MC trial moves where N is the number of molecules in the simulation box. During the equilibration and production cycles, different trial moves were performed with fixed probabilities: translations (49.49%), hybrid translations (0.01%), rotations (49.5%), and volume changes (1%). LJ interactions were truncated at 10 Å. Analytic tail corrections [83] were applied, and the Lorentz-Berthelot mixing rules [83] were used to compute interaction parameters for different atom types. For electrostatic interactions, the damped and shifted version of the Wolf method was used [180]. The Wolf method parameters were set to 8.25 Å and 0.22 Å^{-1} for the cutoff radius and damping parameter, respectively. For the simulations using Ewald summation for electrostatic interactions, a relative precision of 10^{-6} was used. In post-processing, $\langle \partial U / \partial \lambda \rangle$ was integrated using a tool provided with Brick-CFCMC. This tool fits a spline to $\langle \partial U / \partial \lambda \rangle$, and subsequently integrates the spline from $\lambda = 0$ to $\lambda = 1$ using the trapezoidal rule.

2.3.2. Hybrid Translation Trial Moves

The optimal time step size (Δt) for the hybrid translation trial move was obtained for a system of a choline chloride/urea (ChClU) deep eutectic solvent (DES) at 338.15 K and 1 bar, in the *NPT* ensemble. The Generalized AMBER force field (GAFF) [95] parameters were used for the DES, and the charges of cation and anion were scaled by 0.8 [190]. All force field parameters are tabulated in the Supporting Information of Ref. [158]. 100 urea molecules and 50 choline chloride ion pairs were used in the simulations. A well-equilibrated configuration of ChClU was used as initial configuration. Independent runs were performed with different values of the time step,

and the average acceptance probabilities and displacements were computed. All runs consisted of 500 production MC cycles (no equilibration), during which only the hybrid translation trial move was carried out with a trajectory length of 5 timesteps. The Ewald summation method [182], with $k = 8$ and a damping parameter of $\alpha = 0.3\,\text{Å}^{-1}$ was used to compute long-range electrostatic energies. For the computation of electrostatic forces in the short MD trajectories, the damped, shifted Wolf method [180] was used, which is computationally less expensive than the Ewald summation. The damping parameter of the damped, shifted Wolf method was set to $0.2\,\text{Å}^{-1}$. The cutoff radius was set to $10\,\text{Å}$ for all short-range energies and forces. Analytic tail corrections [83] were used for the long-range LJ interactions, and the Lorentz-Berthelot mixing rules [83] were applied to compute the LJ interactions between non-identical atom types.

2.4. Case Studies

To validate the implementation of thermodynamic integration and hybrid MC/MD trial moves, we present two case studies. Using the new thermodynamic integration feature in Brick-CFCMC, we computed the excess chemical potential of infinitely diluted sodium chloride in water at 298 K and 1 bar in the *NPT* ensemble. It is important to note that with the CFCMC technique we could not achieve a flat probability distribution of λ in a single simulation and multiple simulations were needed in which the λ-space is confined. The weight function and the probability distribution of λ of this simulation are shown in Fig. 2.3. Using the thermodynamic integration, we performed 102 different MC simulations of NaCl/water solutions at different and fixed values of λ. In Fig. 2.4(a), $\langle \partial U / \partial \lambda \rangle$ of NaCl in water as a function of λ is shown. Using the thermodynamic integration, $\mu_{\text{NaCl}}^{\text{ex}}$ was calculated as $-741.7\,\text{kJ}\,\text{mol}^{-1}$. This value is consistent with literature as it is within the chemical accuracy ($1\,\text{kcal}\,\text{mol}^{-1} = 4.18\,\text{kJ}\,\text{mol}^{-1}$) [191] of previous simulations ($-742\,\text{kJ}\,\text{mol}^{-1}$) [192]. Note that $-741.7\,\text{kJ}\,\text{mol}^{-1}$ corresponds to ca. $-300\,k_{\text{B}}T$, so it is expected that a single CFCMC simulation sampling the full λ-space will not be sufficient to overcome this free energy difference. The results show that the calculation of μ^{ex} using our implementation of thermodynamic integration is an accurate and reliable method for strongly polar molecules. $\mu_{\text{NaCl}}^{\text{ex}}$ computed using thermodynamic integration is also consistent with the experiments ($-743\,\text{kJ}\,\text{mol}^{-1}$) [193] in the literature. We also simulated the same system using the Ewald summation for electrostatics instead of the damped and shifted version of the Wolf method. In this case, $\mu_{\text{NaCl}}^{\text{ex}}$ was computed as $-739.2\,\text{kJ}\,\text{mol}^{-1}$, showing that thermodynamic integration with the Ewald summation yields results nearly identical to those obtained by the damped and shifted version of the Wolf method (see Fig. 2.4(b)). We also tested the number of data points in λ-space that are needed for an accurate calculation of $\mu_{\text{NaCl}}^{\text{ex}}$. Table 2.1 shows the computed values of $\mu_{\text{NaCl}}^{\text{ex}}$ for different numbers of data points in λ-space. These results show that the number of data points can be decreased from 102 to 19 without any loss in accuracy.

2
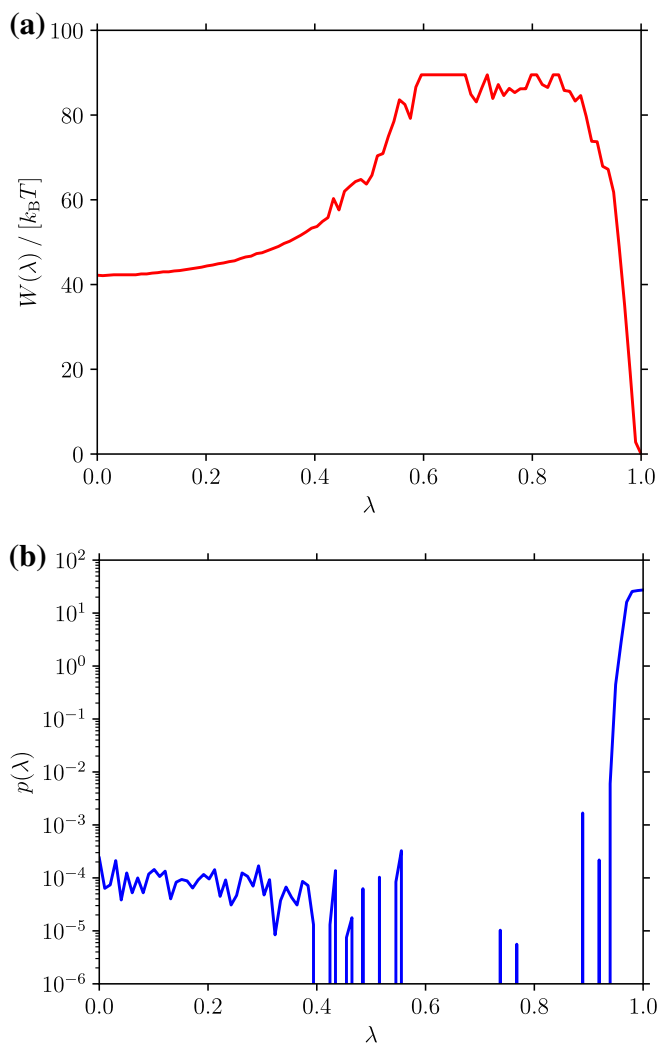
Figure 2.3: (a) Weight function and (b) probability distribution of the NaCl fractional group as a function of λ when making an attempt to compute the excess chemical potential of NaCl at infinite dilution in water from a single simulation. From subfigure (a), it can be seen that the biasing function reaches up to ca. $90\,k_{\mathrm{B}}T$. As a result, same interval with very large biasing function is not sampled at all. From subfigure (b), it can also be seen that only very high λ values are sampled. To obtain a flat probability distribution of λ, multiple simulations with a confined λ-space is required.

(a)

(b)
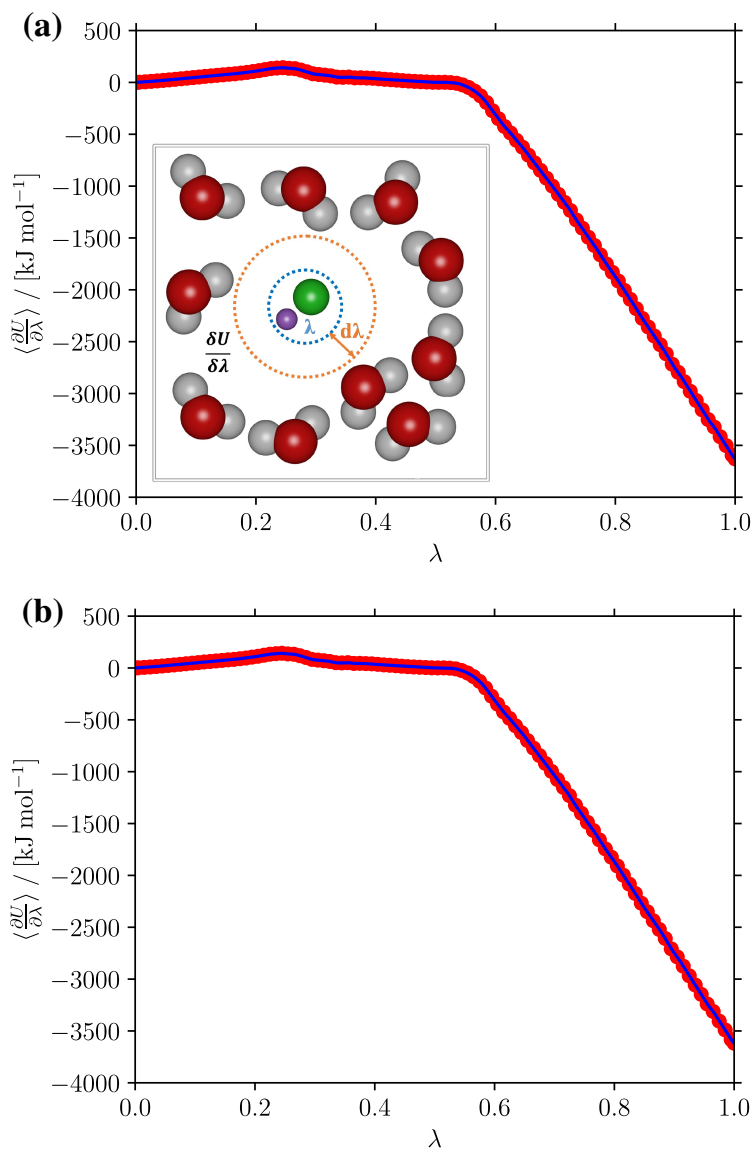
Figure 2.4: Values of $\langle \partial U / \partial \lambda \rangle$ as a function of λ computed using (a) the damped and shifted version of the Wolf method and (b) the Ewald summation (with a relative precision of 10^{-6}) for infinitely diluted NaCl in water at 298 K and 1 bar. The quantities of $\langle \partial U / \partial \lambda \rangle$ were collected from 102 independent simulations at different and fixed values of λ. The red circles and the blue lines represent the values of $\langle \partial U / \partial \lambda \rangle$ and the fitted splines, respectively. The values of $\mu_{\mathrm{NaCl}}^{\mathrm{ex}}$ were computed as $-741.7\,\mathrm{kJ\,mol^{-1}}$ and $-739.2\,\mathrm{kJ\,mol^{-1}}$ using the damped and shifted version of the Wolf method and the Ewald summation, respectively, from the integration of the fitted splines. The inset in subfigure (a) schematically shows a NaCl fractional group in water. Modifying the scaling factor λ by $\mathrm{d}\lambda$ changes the strength of the interactions between the fractional group and the surrounding molecules, allowing for the computation of $\langle \partial U / \partial \lambda \rangle$. In the inset, the red and gray atoms represent the oxygen and hydrogen of water, while the green and purple atoms represent chloride and sodium ions, respectively.

Table 2.1: Computed values of $\mu_{\text{NaCl}}^{\text{ex}}$ in water at infinite dilution, 298 K, and 1 bar using thermodynamic integration for different numbers of (equidistant) λ points. The values of $\mu_{\text{NaCl}}^{\text{ex}}$ from simulations and experiments from literature are -742 kJ mol^{-1} [191] and -743 kJ mol^{-1} [193], respectively. 300 water molecules and a fractional group consisting of one sodium ion and one chloride ion are used in these simulations. Spline fitting was used for the numerical integration. The subscripts in the second column show uncertainties computed as one standard deviation.

Number of λ points	$\mu_{\text{NaCl}}^{\text{ex}}$ / [kJ mol^{-1}]
102	$-741.7_{0.3}$
52	$-741.9_{0.3}$
36	$-741.9_{0.3}$
27	$-742.0_{0.5}$
22	$-742.1_{0.8}$
19	$-742.6_{0.8}$
9	$-751.3_{2.8}$

To increase the efficiency of the hybrid trial moves, it is recommended that the size of the MD timestep Δt is specified according to the maximum average displacement of molecules and an acceptance probability of ca. 50%. Therefore, for each system, short test simulations should be performed to obtain the optimal timestep size. In Fig. 2.5, the acceptance probability and the average displacement are presented for the hybrid translation trial move as a function of timestep size, for a system of choline chloride/urea deep eutectic solvent at 323 K and 1 bar. It can be observed that based on the acceptance probability of 50% and the maximum average displacement, the optimal timestep size is obtained as 0.0075 ps and 0.0095 ps, respectively. Therefore, a value within this range is deemed efficient for the hybrid translation trial move of this system. It is important to note that a timestep of 0.001 ps is typically used for reasonable energy conservation in classical MD simulations of this system [190, 194], which is significantly smaller than the optimal timestep for hybrid translation moves. The timestep size and the trajectory length can be specified independently for the hybrid translation and hybrid rotation trial moves. A similar procedure to the one for hybrid translation trial move can be followed for hybrid rotation trial moves. It is important to note that the optimal timestep size depends on the length of the MD trajectory (specified as 5 timesteps in the simulations of Fig. 2.5). In principle, longer MD trajectories result in smaller values for the optimal timestep size (and vice versa). Short test simulations can be conducted to determine the optimal values of the timestep and the number of timesteps. For a detailed study on how to choose the optimal number of timesteps and the integration timestep size, the reader is referred to Ref. [96].To show the effect of hybrid MD trial moves, we have conducted simulations of choline chloride/urea DES for various fractions of hybrid trial moves in a cubic simulation box at 323 K, starting from random initial configurations. In Fig. 2.6, the running potential energy is shown as a function of the number of MC steps. Clearly, the use of hybrid MD trial moves significantly facilitates equilibration of the system.

2
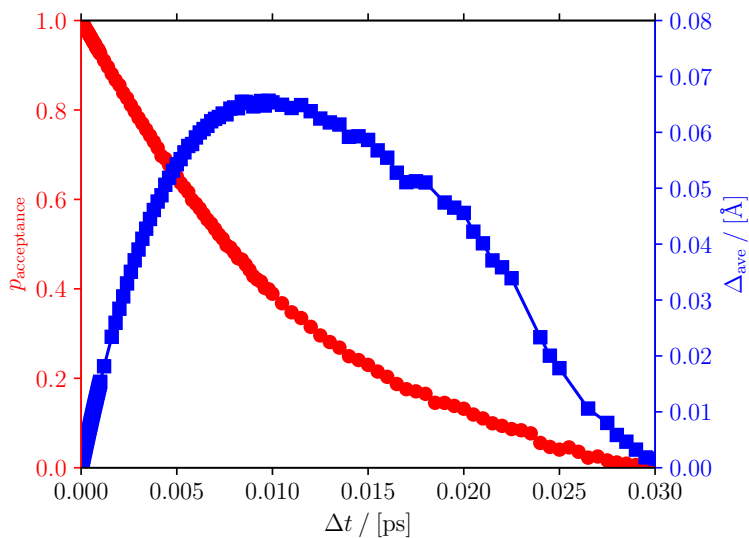
Figure 2.5: Average acceptance probabilities (red) and molecule displacements (blue) for the hybrid translation trial move as a function of timestep size, for a choline chloride/urea deep eutectic solvent at 338.15 K and 1 bar. 5 timesteps are used as trajectory length for all simulations. The lines are drawn to guide the eye.

2
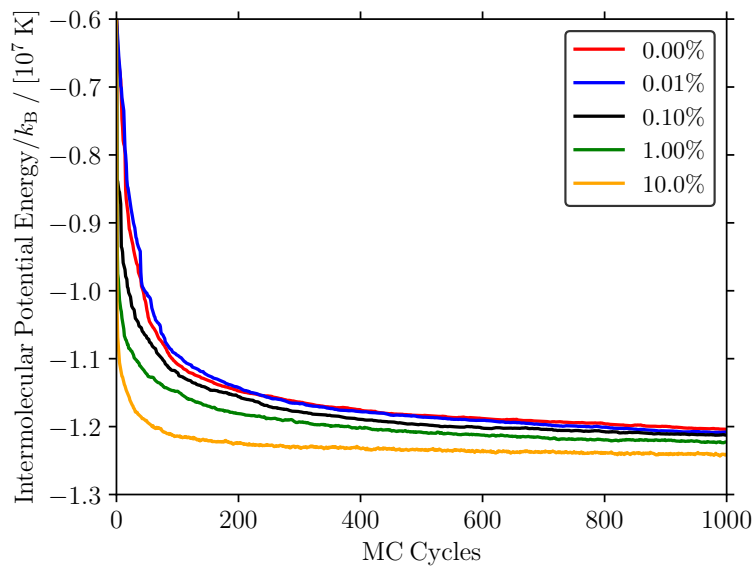
Figure 2.6: Intermolecular potential energy as a function of the number of MC cycles for different fractions of hybrid MD/MC trial moves. The other trial moves are single-molecule displacement and rotations. The numbers of attempted rotations and translation are equal, both for hydrid MD/MC trial moves and single-molecule trial moves. The simulations were performed for choline chloride/urea DES at 323 K in *NVT* ensemble. For both hybrid MD/MC translation and hybrid MD/MC rotation moves, a timestep of 1 fs and a trajectory length of $N_{\text{step}} = 10$ were used. The results show that the use of hybrid MD/MC moves significantly facilitates the equilibration of the simulation box.

2.5. Conclusions

We present new features implemented in the Brick-CFCMC MC simulation code for phase and reaction equilibria. We implemented thermodynamic integration for the calculation of μ^{ex}. With efficient bookkeeping, we compute $\langle \partial U / \partial \lambda \rangle$ which can then be integrated to obtain μ^{ex}. We show the accuracy and reliability of this method by computing the excess chemical potential of NaCl ($\mu^{\text{ex}}_{\text{NaCl}}$) in water at infinite dilution. Analytic derivatives of all interaction potentials with respect to the scaling factor for intermolecular interactions are provided. Our results showed that the computed value of the excess chemical potential $\mu^{\text{ex}}_{\text{NaCl}}$ is in agreement with simulations and experiments from literature. We also implemented hybrid translation and rotation trial moves to increase the efficiency of the equilibration and configuration space sampling of the system. These trial moves collectively translate/rotate all molecules in the simulation box by performing short MD simulations in the microcanonical ensemble, according to the computed forces/torques on every molecule. These short MD simulations are accepted or rejected based on the Boltzmann factor of the total energy difference. We showed how the optimum timestep size of the MD trajectory can be obtained using the simulation of a deep eutectic solvent system as an example.

2

3

Solving Chemical Absorption Equilibria Using Free Energy and Quantum Chemistry Calculations

Absorption

Chemical Reactions

$$CO_{2(gas)} \rightleftharpoons CO_{2(liquid)}$$

$$H_2S_{(gas)} \rightleftharpoons H_2S_{(liquid)}$$

$$CO_{2(aq.)} + 2\,H_2O \rightleftharpoons HCO_3^- + H_3O^+$$

$$HCO_3^- + H_2O \rightleftharpoons CO_3^{2-} + H_3O^+$$

$$MDEAH^+ + H_2O \rightleftharpoons MDEA + H_3O^+$$

$$2\,H_2O \rightleftharpoons H_3O^+ + OH^-$$

$$H_2S_{(aq.)} + H_2O \rightleftharpoons SH^- + H_3O^+$$

$$SH^- + H_2O \rightleftharpoons S^{2-} + H_3O^+$$

stoichiometry, μ_i^0, μ_i^{ex}, $K_{j,des}$ ⟶ speciation in the liquid phase
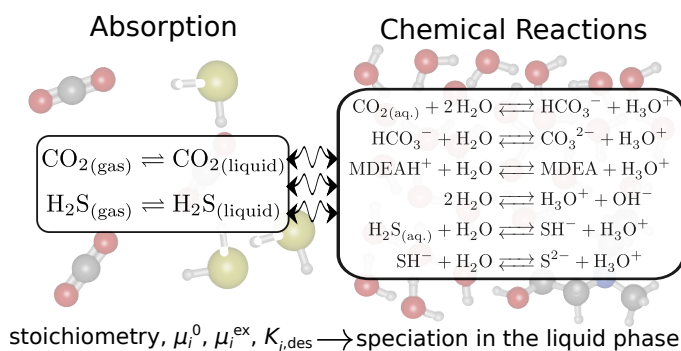
CASpy, a Python solver for gas absorption and chemical reaction equilibria in the liquid phase is developed. The computed CO_2 isotherms in aqueous MDEA solutions show excellent accuracy when the reaction equilibrium constants from literature are used. Binary CO_2/H_2S absorption in aqueous MDEA solutions is examined, revealing major challenges. The limitations of free energy and quantum chemistry calculations in predicting reaction equilibria are analyzed.

3.1. Introduction

Accurately solving chemical reaction equilibria is a challenging numerical problem with significant importance to many industrial processes [134, 195] such as steam reforming of methane and formic acid [137], and acid gas (CO_2 and H_2S) capture from flue gas or natural gas streams [104, 196]. Solving chemical reaction equilibrium allows us to have access to the speciation, i.e., the concentration of each species at equilibrium, which often requires tedious experimental spectroscopic measurements [197–199]. It is very challenging to solve the chemical reaction equilibria of systems without reliable experimental data [200]. Although free energy calculations using molecular simulations and quantum chemistry calculations are very advantageous in this case, it is crucial to explore their limitations. Two thermodynamic properties are crucial to solve reaction equilibria accurately using free energy and quantum chemistry calculations: (1) the excess chemical potential μ_i^{ex} and (2) the standard state ideal gas chemical potential μ_i^0. μ_i^{ex} describes the affinity of species i with the surrounding medium, and the affinity of reactants and reaction products to the solvent influences chemical equilibria [134]. The activity coefficient of species i (γ_i) also describes the affinity of species i with the surrounding medium, and μ_i^{ex} is related to γ_i [201–203] as:

$$\gamma_i = \frac{\rho_i}{X_i \rho_{0i}} \exp\left[\frac{\mu_i^{ex} - \mu_{i0}^{ex}}{RT}\right] \tag{3.1}$$

where ρ_i is the number density of species i, X_i is the mole fraction of species i, ρ_{0i} is the reference number density of the pure solvent (in the same units as ρ_i), and μ_{i0}^{ex} is the excess chemical potential of species i in pure solvent with respect to an ideal gas reference frame. Using free energy calculations, the values of μ_i^{ex} can be computed [96, 97, 104, 196]. μ_i^0 of reactants and reaction products also influence chemical equilibria since μ_i^0 is related to the molar Gibbs free energy of the pure substance i [77] (see Appendix B). Quantum chemistry calculations can be used to compute μ_i^0 [104, 196, 204]. A methodology for computing chemical reaction equilibrium constants using free energy and quantum chemistry calculations have been already established in literature [104, 105, 204–206].

The chemical reaction equilibrium in a solvent can be solved using Reaction Ensemble MC (RxMC) simulation [115, 117, 123, 151, 152]. In RxMC simulations, reactants and products of a reaction can be interconverted through insertions and deletions of molecules to compute the speciation at chemical equilibrium [82, 96, 115]. Smith and Qi [205] described a novel algorithm called Reaction Ensemble Molecular Dynamics (REMD) to predict chemical reaction equilibria in MD simulations. In REMD simulations, the Gibbs free energy is iteratively minimized by changing the composition in the simulation box. Smith and Qi [205] investigated reactive $N_2/O_2/NO$ and $N_2/H_2/NH_3$ systems using the REMD algorithm. The compositions obtained using the REMD algorithm agreed with experiments and simulations from literature.

Noroozi et al. [206] developed a methodology for the calculation of chemical reaction equilibrium constants in the liquid phase using molecular simulations and quantum chemistry calculations and investigated CO_2 absorption in aqueous MEA.

In this study, it was reported that predicting the concentration of minor species such as the bicarbonate ion HCO_3^- or free CO_2 in the solution, and the CO_2 isotherms in aqueous MEA solutions are very challenging. Noroozi et al. [104] also computed the equilibrium constants for the reactions of 7 different primary/secondary alkanolamines and CO_2, and the carbamated alkanolamine dissociation reaction for these 7 primary/secondary alkanolamines. Although the equilibrium constants and the concentration of minor species at equilibrium computed by Noroozi et al [104] did not always agree with the values from literature, the CO_2 absorption isotherms showed a reasonable agreement with experimental isotherms from literature. In another study, Noroozi et al. [204] computed the values of pK_a of protonated alkanolamine dissociation reactions for 29 different alkanolamine species using three different methods: (1) quantum chemistry calculations at three different levels of theory (Hartree-Fock (HF) [69], second order Møller-Plesset perturbation theory (MP2) [70], and Becke's three parameter hybrid exchange functional with Lee-Yang-Parr correlation functional (B3LYP) [207, 208]), (2) the SMD continuum solvent method, and (3) the AM1-BCC point charge assignment method. These authors [204] showed that none of the investigated methods can predict the values of pK_a that consistently agree with experiments. Noroozi et al. [105] determined a new force field for the hydronium ion (H_3O^+) by fitting the computed pK_a to the experimental pK_a of a well-known system (CO_2/MEA/water). Using this force field for H_3O^+, the values of pK_a for 77 different alkanolamines were predicted. The authors showed that the predicted values of pK_a have an average absolute deviation of 0.72 in units of pK_a (i.e., an absolute deviation of 1.66 in units of $\ln[K]$ since $\ln[K] = \ln[10] \times pK_a$) from the experimental values in literature. The average absolute deviation of 1.66 $\ln[K]$ units corresponds to a change of ca. 5.25 times in units of K, and this is too high to accurately compute the speciation in systems that are very sensitive to the value of the protonated amine dissociation reaction equilibrium constant. Therefore, it is important to investigate the limitations of the method.

In this chapter, we present the chemical reaction equilibrium solver in Python called CASpy (https://github.com/omoultosEthTuDelft/CASpy) and use it to solve binary (and single-component) CO_2 and H_2S absorption isotherms in aqueous MDEA solutions. We study the absorption of CO_2 and H_2S in aqueous MDEA solutions because it is relevant to biogas upgrading [209] and acid gas (CO_2 and H_2S) removal from natural gas [49, 50, 210–212]. Molecular simulation is a natural choice for this application as simulations allow studies without the difficulty of working with H_2S (due to safety and environmental concerns) [7], and eliminate the low accuracy of experiments at low partial pressures of acid gases [53, 213]. For this purpose, we first derive an expression for the equilibrium constant as a function of μ_i^{ex} and μ_i^0 of species i, temperature, and volume using a mole fraction-based equilibrium constant and develop software to solve chemical reaction equilibria in combination with absorption. A schematic representation of the scheme of our chemical reaction equilibrium solver is shown in Fig. 3.1. The species in the gas phase absorb into the liquid phase where the chemical reactions occur. We assume that the volume of the liquid phase and μ_i^{ex} of the species do not change with

3
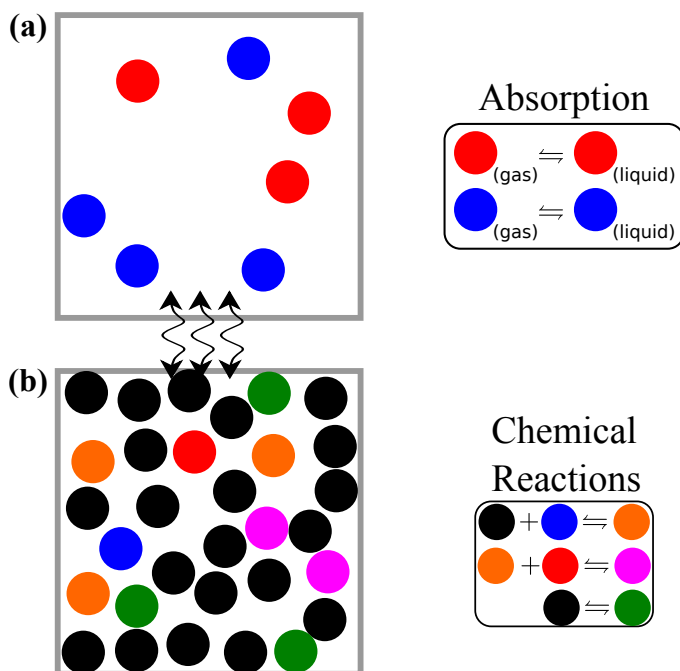
Figure 3.1: Schematic representation of our chemical reaction equilibrium solver. (a) Different species in the gas phase are absorbed by (b) the liquid phase where the absorbed species undergo chemical reactions. Given the stoichiometry of the reactions in the liquid phase, the values of μ_i^{ex} and μ_i^0 of species, and/or the desired equilibrium constants of the reactions in the liquid phase, CASpy computes the speciation in the liquid phase at equilibrium. The partial pressures of the species in the gas phase at equilibrium can also be computed using the concentrations and excess chemical potentials of these species in the liquid phase.

composition, and compute the speciation in the liquid phase at equilibrium using the reaction stoichiometry, the values of μ_i^{ex} and μ_i^0, and/or the desired equilibrium constants. CASpy can be used for any reaction network in liquid phase. We present the accuracy of the solver using two case studies: (1) CO_2/MDEA/water and (2) H_2S/CO_2/MDEA/water. We showcase the accuracy and precision of the solver by comparing the computed CO_2 isotherms in aqueous MDEA with experimental isotherms from literature, and by comparing the speciation at equilibrium for the CO_2/MDEA/water system with the respective experimental data. We also compared the binary absorption isotherms of H_2S and CO_2 in aqueous MDEA with the available data from literature. To assess the sensitivity of the absorption isotherms, we also computed the equilibrium constant of the protonated MDEA dissociation reaction using two different force fields, the General Amber Force Field (GAFF) [95] and the OPLS-AA force field [88, 89]. We use these equilibrium constants to compute CO_2 isotherms in aqueous MDEA solutions and compare the computed isotherms with experimental data. We quantify the sensitivity of μ_i^{ex} and the equilibrium constant for protonated MDEA dissociation reaction to the point charges of the species.

3.2. Methodology

3.2.1. Chemical Reaction Equilibrium Solver

The equilibrium of a chemical reaction occurs when the sum of chemical potentials of the reaction products times the stoichiometric coefficient of the reaction products is equal to that of the reactants at constant temperature and pressure (Eq. (1.1)) [134]. For the remainder of this chapter, we consider the stoichiometric coefficients of the reaction products positive, while the reactants have negative stoichiometric coefficients. The chemical potentials of solutes are calculated using an ideal gas reference frame using Eq. (1.2) [96]. Note that different reference states can be used to compute chemical potentials [214]. In this chapter, we use ρ_0 as reference state for chemical potentials to be consistent with our previous work [96, 97]. Other definitions for the chemical potential using different reference states can also be used to compute chemical reaction equilibria with the methodology described in this chapter [215]. However, a conversion of reference states will be required. The chemical potential of the solvent (μ_s) in a solution is computed with the ideal gas reference state using [134]:

$$\mu_s = \mu_s^0 + \mu_s^{ex} + RT\ln\left[\frac{\rho_{pure}}{\rho_0}\right] - RT\left(\frac{1-X_s}{X_s}\right) \qquad (3.2)$$

where ρ_{pure} is the number density of the pure solvent and X_s is the mole fraction of the solvent s in the solution ($X_s = N_s/N_{total}$ where N_{total} is the sum of number of molecules of all species in the solution including the solvent). The term $RT\left(\frac{1-X_s}{X_s}\right)$ in Eq. (3.2) originates from the Gibbs-Duhem equation at constant temperature and pressure [216].

The equilibrium constant of reaction j (K_j) can be defined using the mole fraction of each species in the solution as:

$$K_j = \prod_{i=1}^{N_{species}} X_i^{\nu_{i,j}} \qquad (3.3)$$

where X_i is the mole fraction of species i. Using the equilibrium condition of Eq. (1.1), we derive the desired equilibrium condition of reaction j ($K_{j,des}$) as a function of μ_i^0, μ_i^{ex}, T and volume V as:

$$K_{j,des} = \exp\left[-\left(\sum_{i=1}^{N_{species}} \frac{\nu_{i,j}(\mu_i^0 + \mu_i^{ex})}{RT} + \nu_{s,j}\ln\left[\frac{\rho_{pure}}{\rho_0}\right]\right) + \nu_{s,j}\left(\frac{1-X_s}{X_s}\right)\right]$$
$$\left(\frac{V\rho_0}{\sum_{i=1}^{N_{species}} N_i}\right)^{\nu_{total\ solute,j}} X_s^{\nu_{s,j}} \qquad (3.4)$$

where $\nu_{s,j}$ is the stoichiometric coefficient of the solvent in reaction j and $\nu_{total\ solute,j}$ is the sum of stoichiometric coefficients of the solutes (all species except for the solvent) in reaction j. This means that at chemical equilibrium, $K_j = K_{j,des}$. A detailed

derivation of Eq. (3.4) is provided in Appendix B. The required values of μ_i^0 and μ_i^{ex} to calculate $K_{j,\text{des}}$ can be computed using quantum chemistry calculations and molecular simulations, respectively. Eq. (3.4) implies that the mole fraction of the solvent X_s is constant. In CASpy, we solve the value of X_s iteratively. This means that a new $K_{j,\text{des}}$ is computed based on the new mole fraction of the solvent after solving for the speciation of the system at equilibrium. This is performed until the difference between the new mole fraction of the solvent and the old mole fraction no longer changes. In practice, the difference the speciation between solving the value of X_s iteratively and assuming a constant value of X_s is very small. Using the computed speciation in liquid phase at equilibrium, the partial pressure of the gas species i (P_i) can be computed using:

$$P_i = \frac{N_i k_{\text{B}} T}{V \exp\left[\frac{-\mu_i^{\text{ex}}}{RT}\right]} \tag{3.5}$$

where N_i is the number of molecules of species i in the liquid phase, V is the volume of the liquid phase which is constant, and k_{B} is the Boltzmann constant. Alternatively, using CASpy, the total pressure and the composition of the gas phase can be imposed, and the solver computes the speciation in the liquid phase (and the absorbed amount). Note that when the total pressure and the composition of the gas phase are imposed, the mass balance equations for the gases should not be used since there is mass transfer from the infinite gas phase to the liquid phase. Also, the addition of non-reactive gases (such as N_2 or CH_4 in aqueous MDEA solutions) will not influence the outcome of our model.

In this chapter, we use the "least_squares" function as implemented in Scipy [217] library in Python to solve for the speciation (the number of molecules or concentration of each species in the solution) of liquid phase at equilibrium. "least_squares" is a function for solving nonlinear equations with the least squares method. This requires an objective function to be defined. The objective function is computed by summing the squares of the values of individual equations (residuals). CASpy runs until the value of each residual is lower than 10^{-10} to ensure that the global minimum of the objective function is obtained. CASpy can be used to compute the speciation in any reactive liquid phase. The objective function is constructed using the following residuals:

$$\frac{\ln\left[K_j\right] - \ln\left[K_{j,\text{des}}\right]}{\ln\left[K_{j,\text{des}}\right]} = 0, \quad \text{for all reactions} \tag{3.6}$$

$$\frac{N_{i,\text{total}} - \left(\sum_{k=1}^{N_{\text{balance,species}}} N_k\right)}{N_{i,\text{total}}} = 0, \quad \text{for all mass balance equations} \tag{3.7}$$

$$\frac{\sum_{i=1}^{N_{\text{species}}} q_i N_i}{\sum_{i=1}^{N_{\text{species}}} |q_i| N_i} = 0, \quad \text{for charge neutrality} \tag{3.8}$$

where $N_{\text{balance,species}}$ is the number of species included in the mass balance equation, q_i is the net charge of species i, and N_{species} is the total number of species in

the solution. Note that including charge neutrality (Eq. (3.8)) to our set of equations is necessary because we use molecule-based balance equations (Eq. (3.7)) and the net charge of each molecule is fixed. With element-based balance equations (i.e., carbon, oxygen, hydrogen, and nitrogen balances), the charge neutrality would not be required as long as the net charge of each element is fixed. However, the stoichiometry of each molecule and ion should be known with the element-based balance equations. To generalize our solver, we used molecule-based balance equations with the addition of the charge neutrality. An example input file and the detailed explanation of the input file are provided in Appendix B.

3.2.2. Case Studies

As a case study for CASpy, we investigate the binary CO_2 and H_2S absorption from an ideal gas phase to aqueous MDEA. In the CO_2/MDEA/water system, there are four chemical reactions [212]:

$$CO_{2(aq.)} + 2\,H_2O \rightleftarrows HCO_3^- + H_3O^+ \tag{R1}$$

$$HCO_3^- + H_2O \rightleftarrows CO_3^{2-} + H_3O^+ \tag{R2}$$

$$MDEAH^+ + H_2O \rightleftarrows MDEA + H_3O^+ \tag{R3}$$

$$2\,H_2O \rightleftarrows H_3O^+ + OH^- \tag{R4}$$
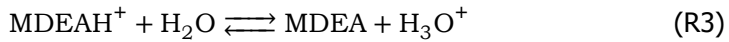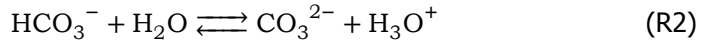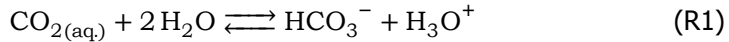
By combining reaction R1 and the reverse reaction R3 ($-$R3), we can obtain the reaction between CO_2, MDEA, and water ($CO_{2(aq.)} + H_2O + MDEA \rightleftarrows MDEAH^+ + HCO_3^-$). There are 8 species in the CO_2/MDEA/water system, including the reaction products. These species are the free CO_2, water (solvent), HCO_3^-, H_3O^+, CO_3^{2-}, MDEA, $MDEAH^+$, and OH^-. The equilibrium constants for each of these reactions can be computed using Eq. (3.3), and the equilibrium follows from $K_j = K_{j,\text{des}}$. In this work, the values of $K_{j,\text{des}}$ for the reactions R1, R2, and R4 are computed using the correlations provided by Plakia et al. [212] since these reactions are present in systems where CO_2 is absorbed by an aqueous solution of any primary, secondary, or tertiary alkanolamine. We computed the desired equilibrium constant of the $MDEAH^+$ dissociation reaction ($K_{R3,\text{des}}$) either by using the correlation provided by Plakia et al. [212], or by performing MC simulations and quantum chemistry calculations. The correlations to compute mole fraction-based equilibrium constants reported by Plakia et al. [212] are listed in Table B.4 of Appendix B. Note that the logarithm of an equilibrium constant (pK_a) can be converted to natural logarithm of the equilibrium constant ($\ln\left[K_{j,\text{des}}\right]$) using $\ln\left[K_{j,\text{des}}\right] = \ln\left[10\right]pK_a$. For this system, four additional equations must be satisfied at equilibrium: the MDEA balance, CO_2 balance, water balance, and charge neutrality. The MDEA balance equals:

$$N_{\text{MDEA,total}} - (N_{\text{MDEA}} + N_{\text{MDEAH}^+}) = 0 \tag{3.9}$$

The water balance equals:

$$N_{\text{H}_2\text{O,total}} - \left(N_{\text{H}_2\text{O}} + N_{\text{H}_3\text{O}^+} + N_{\text{OH}^-}\right) = 0 \tag{3.10}$$

The CO_2 balance equals:

$$N_{CO_2,total} - \left(N_{CO_{2(aq.)}} + N_{HCO_3^-} + N_{CO_3^{2-}}\right) = 0 \qquad (3.11)$$

Finally, charge neutrality of the system is formulated as:

$$\sum_{i=1}^{N_{species}} q_i N_i = 0 \qquad (3.12)$$

Thus, for the CO_2/MDEA/water system, we have 8 different species and 8 equations to satisfy.

With the addition of H_2S, two additional reactions are added to the reaction network which are [218]:

$$H_2S_{(aq.)} + H_2O \rightleftharpoons SH^- + H_3O^+ \qquad (R5)$$

$$SH^- + H_2O \rightleftharpoons S^{2-} + H_3O^+ \qquad (R6)$$
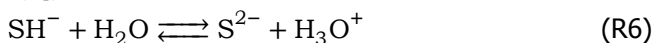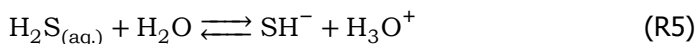
By combining reaction R5 and the reverse reaction R3 (−R3), we obtain the reaction between H_2S and MDEA ($H_2S_{(aq.)}$ + MDEA $\rightleftharpoons$ MDEAH$^+$ + SH$^-$). While the combination of reactions R5 and R3 is kinetically favorable [219], our reaction network (reactions R1–R6) is thermodynamically consistent, meaning that we can compute the equilibrium constant of the combined reaction of reactions R5 and R3 using the equilibrium constants of reactions R5 and R3 ($K_{R5-R3} = \frac{K_{R5}}{K_{R3}}$). Note that this is also valid for the combined reaction of reactions R1 and R3. The addition of the component H_2S to the CO_2/MDEA/water system leads to an additional equation for the H_2S balance. The H_2S balance equals:

$$N_{H_2S,total} - \left(N_{H_2S_{(aq.)}} + N_{SH^-} + N_{S^{2-}}\right) = 0 \qquad (3.13)$$

With the addition of H_2S to the CO_2/MDEA/water system, we have 3 additional species in the solution. These species are the free H_2S, bisulfide ion SH$^-$, and sulfide ion S^{2-}. We also have 3 more equations to solve which are: $K_{R5} = K_{R5,des}$, $K_{R6} = K_{R6,des}$, and the H_2S balance. In summary, in the H_2S/CO_2/MDEA/water system, we have 11 different species and 11 equations to satisfy.

The objective function for CO_2/MDEA/water systems is defined as an array of

Eq. (3.6) and the following residuals:

$$\frac{N_{\text{MDEA,total}} - (N_{\text{MDEA}} + N_{\text{MDEAH}^+})}{N_{\text{MDEA,total}}} = 0 \tag{3.14}$$

$$\frac{N_{\text{H}_2\text{O,total}} - (N_{\text{H}_2\text{O}} + N_{\text{H}_3\text{O}^+} + N_{\text{OH}^-})}{N_{\text{H}_2\text{O,total}}} = 0 \tag{3.15}$$

$$\frac{N_{\text{CO}_2\text{,total}} - \left(N_{\text{CO}_{2\text{(aq.)}}} + N_{\text{HCO}_3^-} + N_{\text{CO}_3^{2-}}\right)}{N_{\text{CO}_2\text{,total}}} = 0 \tag{3.16}$$
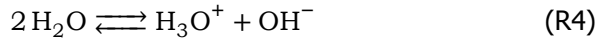
$$\frac{\sum_{i=1}^{N_{\text{species}}} q_i N_i}{\sum_{i=1}^{N_{\text{species}}} |q_i| N_i} = 0 \tag{3.17}$$

The objective function for $\text{H}_2\text{S}/\text{CO}_2/\text{MDEA}/\text{water}$ systems is defined as an array of Eq. (3.6), Eq. (3.14)–Eq. (3.17), and an additional residual for H_2S balance in the system:

$$\frac{N_{\text{H}_2\text{S,total}} - \left(N_{\text{H}_2\text{S}_{\text{(aq.)}}} + N_{\text{SH}^-} + N_{\text{S}^{2-}}\right)}{N_{\text{H}_2\text{S,total}}} = 0 \tag{3.18}$$

Each residual in the objective functions should be equal to 0 at equilibrium. Note that each residual in the objective functions (Eq. (3.6)–Eq. (3.8)) is normalized to make sure that the residuals are of similar magnitudes. We also need to scale the initial guess for the speciation to unity to ensure that the numerical solver will deal with variables of similar magnitudes [220]. Otherwise, there is a ca. 12 orders of magnitude difference between the concentration of the most scarce species in the solution (H_3O^+) and the concentration of the most abundant one (water). This would make it challenging to numerically find a solution at equilibrium. For this purpose, at the start of our calculations, the variable array is divided by itself (element-wise) and kept in the memory (scaling factors). While computing the residuals, we scale the variable array back by multiplying the solution with the scaling factors stored in the memory. In our calculations, we use 10^{-15} as both termination tolerance for individual variables (number of species of each species) and for the residuals. The tolerances are sufficiently low since we use normalized residuals (Eq. (3.6)–Eq. (3.8)).

3.2.3. Monte Carlo Simulation

We perform MC simulations in the *NPT* ensemble to compute the values of μ_i^{ex}. To this purpose, we use Brick-CFCMC [96, 97, 123], an open source state-of-the-art MC simulation software for computing phase– and reaction equilibria. In CFCMC, the so called "fractional" molecule groups are used to insert or delete molecules from the simulation box. A "fractional" molecule group can contain multiple molecules and/or ions as long as it is charge neutral. The interactions between the "fractional" molecule group and the surrounding molecules are scaled using a parameter called λ. At $\lambda = 0$, the "fractional" molecule group has no interactions with the surrounding molecules while at $\lambda = 1$, the "fractional" molecule group has full interactions

with the surrounding molecules [114, 115, 117, 157]. There are two different methods implemented in Brick-CFCMC to compute μ_i^{ex}. The details of these methods are explained in Appendix B. In this chapter, we compute μ_i^{ex} using thermodynamic integration [82, 97, 164] using Eq. (2.1). For thermodynamic integration, we compute the values of the term $\langle \partial U / \partial \lambda \rangle$ for 50 equidistant and fixed values of λ, along with $\lambda = 10^{-6}$ and $\lambda = 1 - 10^{-6}$ to increase the accuracy of the thermodynamic integration. In these simulations, a simulation box of 300 water molecules and a single fractional group were used. Initial configurations were created by randomly inserting molecules to a simulation box with a length of 20.8 Å. The random insertion of molecules into the simulation box causes atomic overlaps and these overlaps were eliminated by 10^3 initialization cycles in which only single molecule translation and single molecule rotation trial moves were performed. The initialization cycles were followed by 10^6 equilibration cycles and 10^6 production cycles. For every MC cycle, N MC trial moves were performed where N is the number of molecules in the simulation box. In the equilibration and production cycles, single molecule translations (48.49%), single molecule rotations (48.49%), hybrid MD/MC translations (0.01%), hybrid MD/MC rotations (0.01%) [97], volume changes (1%), bond bending (1%), and torsion (1%) trial moves were performed with fixed probabilities. The time step and the number of time steps for hybrid MD/MC trial moves were set as 5 fs and 2 MD cycles, respectively. In the MC simulations, a 10 Å distance was used as the LJ cutoff distance and analytic tail corrections [83] were applied. The electrostatic potential was computed using the Ewald summation [182]. We set the Ewald summation parameters to 10 Å and 0.32 Å^{-1} for the cutoff radius and the damping parameter, respectively. After the MC simulations, a spline was fitted to the values of $\langle \partial U / \partial \lambda \rangle$ as a function of λ and the spline was integrated from $\lambda = 0$ to $\lambda = 1$ to compute μ_i^{ex} (Eq. (2.1)). The computed values of μ_i^{ex} were not corrected for the finite-size effects since the corrections were found insignificant [103, 221].

The TIP3P [222] force field was used to model water in this chapter. We used this force field because the μ_i^{ex} of water computed using the TIP3P agrees with experimental μ_i^{ex} much better than the μ_i^{ex} computed using the TIP4P or the TIP5P force fields [138]. In Brick-CFCMC, the value of $\langle \partial U / \partial \lambda \rangle$ can only be computed for a charge-neutral group of "fractional" molecules. For this purpose, we included a rigid HCO_3^- molecule to the fractional group of either $MDEAH^+$ or H_3O^+. The choice of counter ion does not matter because the value of μ_i^{ex} of the counter ion cancels out when we compute $K_{\text{R3,des}}$ using Eq. (3.4) (see Table B.2 for all fractional molecule groups used in this chapter). For flexible MDEA, $MDEAH^+$, and (rigid) HCO_3^- we used either the General Amber Force Field (GAFF) [95] with Restrained Electrostatic Potential Surface (RESP) fitted point charges (see the next subsection for the details of RESP fitting) or the OPLS-AA force field [88, 89] with 1.14*CM1A point charges [223]. The parameters for the OPLS-AA force field with 1.14*CM1A point charges were generated using the LibParGen web server [223]. For H_3O^+ ions, we used the force field developed by Noroozi et al. [105]. We used the TraPPE [90] and the force field from Kristóf and Lizsi [224] for CO_2 and H_2S molecules, respectively. Details of all used force fields can be found in Appendix C (Appendices C.1.2, C.3, C.4.1, C.5.1, C.7, C.8.1 to C.8.2, C.9.1 and C.9.2). The force field parameters for unlike

LJ interactions were computed using Lorentz-Berthelot mixing rules [83] except for the TraPPE CO_2 and TIP3P water molecules. The LJ interactions between TraPPE CO_2 and TIP3P water molecules were computed using the optimized potential for CO_2/H_2O mixtures developed by Orozco et al. [225] (see Table C.10 of Appendix C).

3.2.4. Quantum Chemistry Calculations

In this chapter, we perform quantum chemistry calculations using the Gaussian09 software [78] to compute the values of μ_i^0 for the MDEAH$^+$ ion, the MDEA molecule, the H_3O^+ ion, and water. As the MDEAH$^+$ ion and the MDEA molecule have many different conformers (molecules with different spatial arrangements), we first conducted a conformer search for these molecules [226]. We optimized the structure of 5 different conformers for both MDEAH$^+$ and MDEA with the Gaussian-4 (G4) composite method [227] and chose the conformers with the minimum free energy. The molecular partition function computed in these calculations were used to compute μ_i^0. Details on computing μ_i^0 using quantum chemistry calculations are explained in Appendix B. We also compute the electrostatic potential energy grid of the conformers at the minimum free energy using the Merz-Kollman scheme [228] at the HF [69] level of theory with a 6–31G* basis set. The computed electrostatic potential energy grids are used in a two-step Restrained Electrostatic Potential Surface (RESP) fitting with the Antechamber package [229] to compute the point charges of these molecules for the GAFF [95].

3.3. Results and Discussion

3.3.1. Absorption of CO_2 in Aqueous MDEA Solutions

As a first case study, we investigate CO_2 absorption in aqueous MDEA. Based on the definition of mole fraction-based reaction equilibrium constant (Eq. (3.3)), we assume an ideal solution where the activity coefficients of all species are constant. The activity coefficients of species can be computed from μ_i^{ex} in the solution and μ_i^{ex} in pure solvent [201–203]. In principle, the activity coefficients of species can be computed using an activity coefficient model or iteratively [230, 231]. The latter means that a new set of μ_i^{ex} can be calculated based on the speciation computed using the values of μ_i^{ex} at infinite dilution, and this can be performed until the differences between the old values and new values of μ_i^{ex} no longer change. However, it was previously shown that the speciation obtained by the ideal solution assumption and the non-ideal case are very similar for CO_2 absorption in aqueous alkanolamine solutions [104]. We implemented the specific ion interaction theory (SIT) [232, 233] with our chemical reaction equilibrium solver to test if the ideal solution assumption differs from the non-ideal case. The results show that the differences are indeed very small. Therefore, the results presented in this chapter are obtained with the ideal solution assumption. In these calculations, we use the experimental values of $K_{j,\mathrm{des}}$ provided by Plakia et al. [212] for all 4 reactions in CO_2/MDEA/water system (R1–R4) at 313.15 K (see Table B.4 for the correlations). To compute the partial pressure of CO_2 using the concentration of free CO_2 in the

3
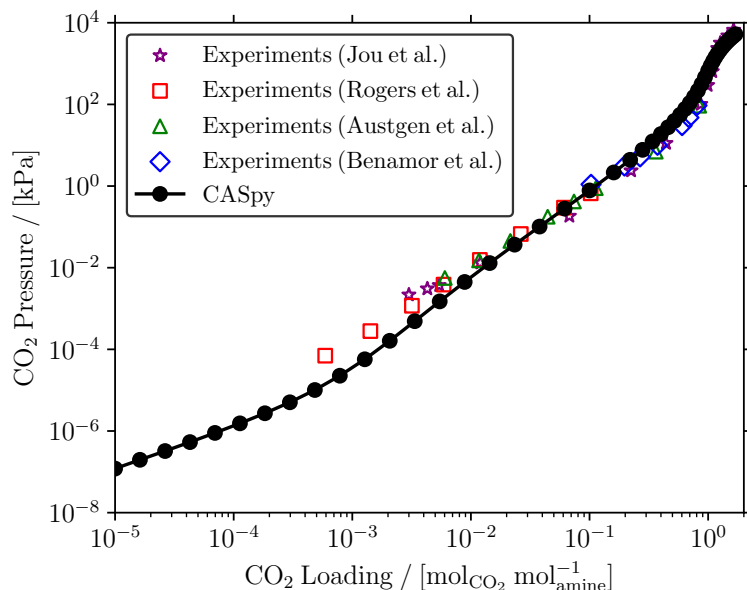
Figure 3.2: Comparison of the calculated CO_2 isotherm and experimental CO_2 isotherms [234–237] in 23 wt.% MDEA/water solutions at 313.15 K. Note that the experimental values of $K_{j,\text{des}}$ provided by Plakia et al. [212] were used for all reactions in the CO_2/MDEA/water system (R1–R4) in the calculations with the solver (Table B.4).

liquid phase at equilibrium (Eq. (3.5)), we computed the value of μ_i^{ex} for CO_2 in water at 313.15 K and 1 bar. The values of μ_i^{ex} for CO_2 in water as a function of temperature are listed in Table B.5 of Appendix B. To validate that CASpy yields the correct solutions at equilibrium, we investigate the sum of the square of the residuals ($\sum_{i=1}^{N_{\text{obj}}} A_i^2$ where N_{obj} is the number of residuals in the objective function and A_i is the value of residual i) as a function of the CO_2 loading in the solution. Our results show that the sum of the squared residuals is 0 within machine precision for all CO_2 loadings. This means that the solutions computed by CASpy are at chemical equilibrium. Fig. 3.2 shows the computed CO_2 pressure as a function of the CO_2 loading along with the experimental CO_2 isotherms from literature [234–237] in 23 wt.% MDEA/water solutions at 313.15 K.

It is clearly shown that the computed CO_2 pressures are in excellent agreement with the experiments from the literature. Fig. 3.2 also shows that the computed CO_2 pressures are slightly lower than the experimental pressures at low loadings ($<10^{-2}$ mol_{CO_2} $\text{mol}_{\text{amine}}^{-1}$). This may be because the experiments at low pressures of CO_2 are less accurate than the experiments at higher CO_2 pressures [53, 213]. Motivated by this excellent agreement, we also compare experimental [197] and calculated speciations in CO_2 loaded 23 wt.% MDEA/water solutions at 313.15 K. Fig. 3.3 shows the experimental speciation from literature [197] and the calculated speciation as a function of CO_2 loading in 23 wt.% MDEA/water at 313.15 K. The

comparison of the speciations shows that the calculated concentrations of MDEA, MDEAH$^+$, and HCO$_3^-$ agree well with the experimental measurements for all CO$_2$ loadings. However, this is not the case for the concentration of free CO$_2$ and the carbonate ion CO$_3^{2-}$. For CO$_3^{2-}$, the calculated concentration at the lowest loading agrees well with the experimental measurements, while the CO$_3^{2-}$ concentrations are underpredicted for higher loadings. Jakobsen et al.[197] state that the measured CO$_3^{2-}$ concentrations are most likely overestimated at high CO$_2$ loadings. This was shown by the excess negative charge that Jakobsen et al.[197] reported. An excess negative charge means that the net charge of the system is not zero but negative, so the concentration of CO$_3^{2-}$ is overestimated. For the free CO$_2$ concentration, the chemical reaction equilibrium solver slightly overpredicts the only experimental measurement that Jakobsen et al.[197] reported. However, these authors state that the measured free CO$_2$ concentration may be underestimated due to the chemical exchange between the species at equilibrium complicating the integration of the NMR spectra.

3.3.2. Binary Absorption of CO$_2$ and H$_2$S in Aqueous MDEA Solutions

As a second case study, we investigate the binary absorption of CO$_2$ and H$_2$S in aqueous MDEA. To this purpose, we computed the values of μ_i^{ex} for H$_2$S in water as a function of temperature at 1 bar. The values of μ_i^{ex} for H$_2$S in water as a function of temperature are listed in Table B.5. We computed the CO$_2$ and H$_2$S isotherms in 50 wt.% MDEA/water solutions at 323.15 K and fixed H$_2$S and CO$_2$ loadings, respectively. Note that all values of the residuals in these calculations were 0 within machine precision, thus, the solutions correspond to chemical equilibrium. Dicko et al. [54] performed a modeling study on the CO$_2$ and H$_2$S isotherms in aqueous MDEA solutions for fixed H$_2$S and CO$_2$ loadings, respectively. These authors also reported experimental H$_2$S isotherms in aqueous MDEA solutions at fixed CO$_2$ loadings. Fig. 3.4 shows the comparison between the calculated absorption isotherm of CO$_2$ (and H$_2$S) in 50 wt.% MDEA/water solution at 313.15 K and fixed H$_2$S (and CO$_2$) loading, and modeling (and experimental) data from Dicko et al. [54]. Fig. 3.4(a) shows that with increasing loading of H$_2$S, CO$_2$ pressure also increases. The same behavior can be seen for H$_2$S pressures as a function of CO$_2$ loading in Fig. 3.4(b). This effect is more prominent at low acid gas loadings. Fig. 3.4 also shows that the calculated CO$_2$ isotherms at fixed H$_2$S loading are in agreement with the modeling results from Dicko et al. [54] at higher CO$_2$ loadings. At lower loadings (total acid gas loading < 1 $\mathrm{mol_{acid\,gas}\,mol_{amine}^{-1}}$), the results from the two models deviate significantly. For H$_2$S isotherms, Fig. 3.4(b) shows that the calculated H$_2$S isotherms in 50 wt.% MDEA/water solution at fixed CO$_2$ loadings do not agree well with the experimental results by Dicko et al. [54]. The sequential binary absorption of CO$_2$ first and H$_2$S second approach by Dicko et al. [54] may be the reason for the difference between our H$_2$S isotherms and experimental results. It is important to note that there may be CO$_2$ evaporating in the second part of the measurement due to the competitive absorption with H$_2$S. We modified our solver so we can

quantify this effect. Details of this correction are explained in Appendix B. The CO_2 loading and H_2S pressure were computed as a function of H_2S loading using the modified solver. Fig. B.1 of Appendix B shows the CO_2 loading as a function of H_2S loading during H_2S absorption. Our results show that CO_2 indeed evaporates from the solution to the gas phase during H_2S absorption [54]. The amount of evaporated CO_2 is the lowest at the lowest CO_2 loading. For the initial CO_2 loading of 0.093 $mol_{CO_2} \, mol_{amine}^{-1}$, the decrease in the CO_2 loading is 0.6–26.9% of the initial amount while for the highest CO_2 loading, the decrease is 9.5–44.7% of the initial CO_2 loading. Fig. B.2 shows the H_2S isotherms for the fixed CO_2 loading assumption, by the effect of evaporating CO_2, and the experimental results from Dicko et al. [54]. Fig. B.2 of Appendix B show that the H_2S pressure decreases for fixed H_2S loadings when we account for the evaporation of CO_2. This is because there is less CO_2 in the solution for H_2S to compete with. The decrease in H_2S pressure is 0.6–5.9% for the initial CO_2 loading of 0.093 $mol_{CO_2} \, mol_{amine}^{-1}$, while the decrease in H_2S pressure is between 21.6–37.6% for the highest initial CO_2 loading (i.e., 0.706 $mol_{CO_2} \, mol_{amine}^{-1}$).

Even after accounting for the effect of CO_2 evaporation during H_2S loading, the computed H_2S isotherms still do not agree well with the experimental results from Dicko et al. [54]. For example, Dicko et al. [54] measured the H_2S pressure as 680 kPa for a CO_2 loading of 0.706 $mol_{CO_2} \, mol_{amine}^{-1}$ and a H_2S loading of 0.645 $mol_{H_2S} \, mol_{amine}^{-1}$ in 50 wt.% MDEA/water solution at 323.15 K, while the computed H_2S pressure is 1887 kPa at the same conditions. Even when there is no CO_2 in the solution (CO_2 loading = 0 $mol_{CO_2} \, mol_{amine}^{-1}$), the calculated H_2S isotherm does not agree with the experimental results from Dicko et al. [54] except for the data point at the lowest H_2S loading. For a H_2S loading of 0.884 $mol_{H_2S} \, mol_{amine}^{-1}$, the calculated pressure of H_2S is 996 kPa, while the experimental H_2S pressure is 278 kPa. This may be because of two reasons; (1) we use experimental values of $K_{j,\text{des}}$ for all reactions (R1–R6) reported by Plakia et al. [212]. However, these parameters were not fitted to binary absorption of CO_2 and H_2S in aqueous MDEA. Thus, experimental values of $K_{j,\text{des}}$ may be less accurate for the conditions we are investigating. (2) We use the μ_i^{ex} of infinitely diluted H_2S in water at 323.15 K to compute H_2S pressure using Eq. (3.5). This means that we assume that the μ_i^{ex} of CO_2 and H_2S do not change with the increasing concentration of CO_2, H_2S, and different ions (see R1–R6). We tested this assumption by computing the μ_i^{ex} of CO_2 for different CO_2 loadings in 23 wt.% MDEA/water solutions at 313.15 K using the speciations reported in Fig. 3.3. Fig. B.3 of Appendix B shows that the difference between the μ_i^{ex} of CO_2 at the highest CO_2 loading (1 $mol_{CO_2} \, mol_{amine}^{-1}$) and the lowest CO_2 loading (10^{-5} $mol_{CO_2} \, mol_{amine}^{-1}$) is well within the chemical accuracy (1 kcal mol^{-1} = 4.18 kJ mol^{-1}) [191].
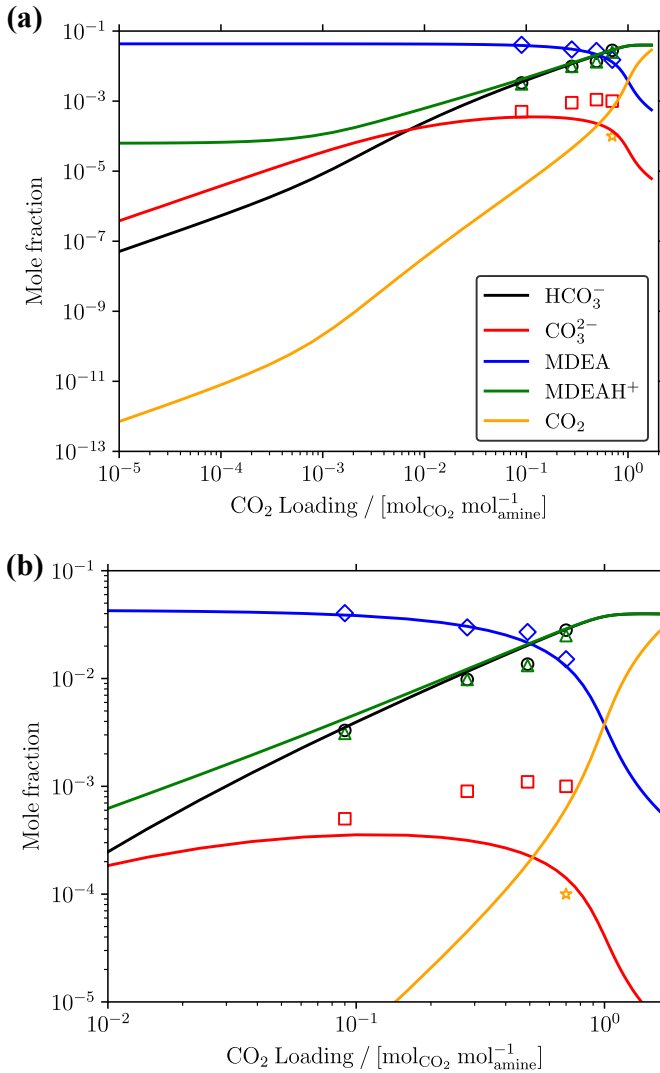
Figure 3.3: Comparison of the calculated and experimental [197] speciations of CO_2 loaded 23 wt.% MDEA/water solutions at 313.15 K for CO_2 loading ranges between (a) 10^{-5}–1.7 $mol_{CO_2}\,mol_{amine}^{-1}$ and (b) 10^{-2}–1.7 $mol_{CO_2}\,mol_{amine}^{-1}$. Open symbols represent the experimental speciation reported by Jakobsen et al.[197]; $\square$: CO_3^{2-}, $\star$: CO_2, $\diamond$: MDEA, $\triangle$: MDEAH$^+$, $\circ$: HCO$_3^-$. Note that the experimental values of $K_{j,\mathrm{des}}$ provided by Plakia et al. [212] were used for all reactions in the CO_2/MDEA/water system (R1–R4) in our calculations (Table B.4). The color coding in (b) follows that of (a).

3

(a)

(b)
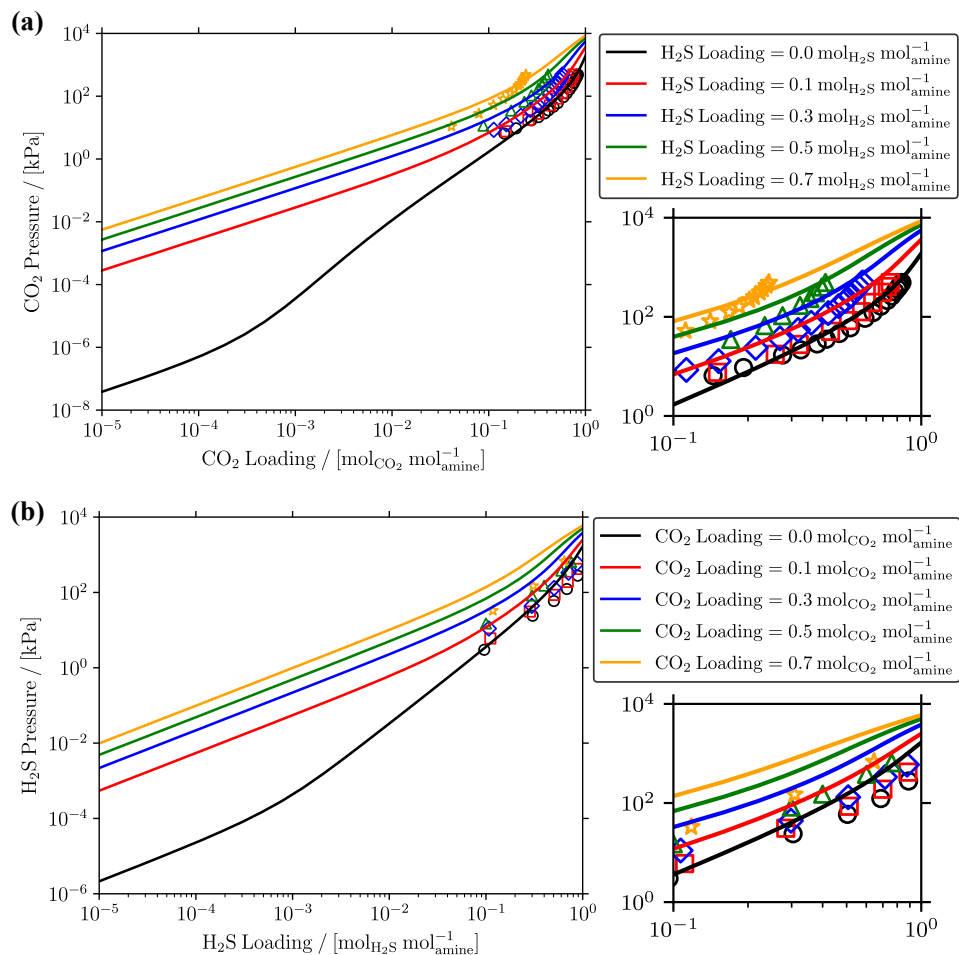
Figure 3.4: Absorption isotherms of (a) CO_2 and (b) H_2S in 50 wt.% MDEA/water solutions at 313.15 K and fixed H_2S and CO_2 loadings, respectively. Open symbols represent modeling and experimental results from Dicko et al. [54] for (a) and (b), respectively. The color coding for the open symbols follows that of the solid lines. The figures below the legends show the CO_2 (H_2S) pressures in kPa for a CO_2 (H_2S) loading range between 0.1 to 1 $mol_{CO_2} \, mol_{amine}^{-1}$ ($mol_{H_2S} \, mol_{amine}^{-1}$). Note that the experimental values of $K_{j,des}$ provided by Plakia et al. [212] were used for all reactions in $H_2S/CO_2/MDEA$/water system (R1–R6) for the calculations in the solver (Table B.4).

Table 3.1: Natural logarithms of the computed values of $K_{R3,des}$ (reaction R3) for the GAFF and OPLS-AA force field and natural logarithm of the experimental value [212] of $K_{R3,des}$ at 313.15 K.

	$\ln[K_{R3,des}]$	Source
GAFF	-34.80	This chapter
OPLS-AA	-24.91	This chapter
Experimental	-23.04	Plakia et al.[212]

3

3.3.3. Sensitivity and Limitations of the Method

We tested the sensitivity of computed CO_2 pressures in aqueous MDEA solutions to the computed values μ_i^0 and μ_i^{ex} by computing $K_{j,des}$ of the MDEAH$^+$ dissociation reaction (R3) using Eq. (3.4). We used either the GAFF [95] with point charges fitted with RESP or the OPLS-AA force field [88, 89] with 1.14*CM1A point charges [223] for MDEAH$^+$ and MDEA. For water, we used the TIP3P force field [222], while we used the optimized force field by Noroozi et al. [105] for the H$_3$O$^+$ ions. Using CFCMC simulations and thermodynamic integration [97], we computed the μ_i^{ex} of MDEAH$^+$ (HCO$_3$$^-$ as the counter ion), MDEA, H$_3$O$^+$ (HCO$_3$$^-$ as the counter ion), and water. We also computed the μ_i^0 of MDEAH$^+$, MDEA, H$_3$O$^+$, and water using quantum chemistry calculations. The values of μ_i^{ex} and μ_i^0 of MDEAH$^+$, MDEA, H$_3$O$^+$, and water are listed and compared with the available data from literature in Table B.6 and Table B.7 of Appendix B. We also listed the values of μ_i^0 and the atomization energies ($D_{0,i}$) computed with different quantum chemistry composite methods in Table B.8. The computed values of μ_i^0 show that different quantum chemistry composite methods result in very similar values of μ_i^0 as the standard deviations are between 1.5–2.6 k_BT. Note that every 1 k_BT unit change in values of μ_i^0 corresponds to a change of ca. 1 in terms of $\ln[K_{j,des}]$ (Eq. (3.4)). Also, Table B.6 shows that the calculated values of μ_i^0 agree with the values computed using the JANAF tables [135, 136] within 6–8 k_BT for charge neutral molecules (water and CO_2), while the difference between the values of μ_i^0 computed using quantum chemistry calculations and JANAF tables [135, 136] for ions (H$_3$O$^+$ and OH$^-$) are between 5–17 k_BT. Since the standard deviation between the values of μ_i^0 computed using different quantum chemistry composite methods in Gaussian09 [78] is low and the G4 method is one of the most accurate methods [227], we use the G4 method to compute the values of μ_i^0 for the remainder of this chapter. We compared the values of μ_i^{ex} computed using MC simulations with available experimental data from literature and values of μ_i^{ex} computed from Henry constant of species in water (Table B.7). Our results show that the computed values of μ_i^{ex} agree with the available data from literature within the chemical accuracy (1 kcal mol^{-1} = 4.18 kJ mol^{-1}) [191]. Using the computed values of μ_i^{ex} and μ_i^0, we computed the equilibrium constant of the MDEAH$^+$ dissociation reaction $K_{R3,des}$ at 313.15 K (Eq. (3.4)). The natural logarithms of the computed values of $K_{R3,des}$ for different force fields are listed in Table 3.1.

Our results show that the computed $K_{R3,des}$ using the OPLS-AA force field [88, 89] with point charges derived from 1.14*CM1A [223] agrees well with the experimental [212] value, while the value computed using GAFF [95] with RESP fitted point charges differs from the experiments. Noroozi et al. [204] computed the pK_a of protonated amine dissociation reactions for 29 different alkanolamine species at 298.15 K and 1 bar. To make the results of Noroozi et al. [204] comparable with our study, we convert the values of pK_a these authors report to the units of $\ln\left[K_{j,des}\right]$ ($\ln\left[K_{j,des}\right] = \ln\left[10\right]pK_a$). Noroozi et al. [204] compared the values of pK_a computed using GAFF with RESP fitted point charges, SMD continuum solvent simulations, and GAFF with the semiempirical AM1-BCC charge model with experimental values of pK_a from literature. For the RESP fitting, these authors computed the electrostatic potential of the species at 3 different levels of theory using quantum chemical calculations. The authors showed that although some calculated values of pK_a agree with the experimental data within 1 pK_a unit, none of the investigated methods is consistently successful in accurately predicting pK_a of protonated amine dissociation reactions. For example, Noroozi et al. [204] computed the value of $\ln\left[K_{j,des}\right]$ of protonated MDEA dissociation reaction between 28.1–31.5 while the experimental value from literature is 23.8 [238] at 298.15 K. Noroozi et al. [204] also showed that the deviations in computed values of pK_a are quite large for some alkanolamines. For example, these authors computed the value of $\ln\left[K_{j,des}\right]$ of protonated tris(hydroxymethyl)aminomethane (THMAM) dissociation reaction between 9.9–20.7 while the experimental value from literature is 22.7 at 298.15 K.

To test the sensitivity of CO_2 isotherm in aqueous MDEA solution to the value of $K_{R3,des}$, we computed CO_2 isotherm in 23 wt.% MDEA/water solution at 313.15 K using the values of μ_i^0 computed from quantum chemistry calculations and the values of μ_i^{ex} computed using thermodynamic integration. Fig. 3.5 shows the CO_2 isotherms computed using $K_{R3,des}$ from OPLS-AA force field, GAFF, and the experimental correlation from Plakia et al. [212], and experimental CO_2 isotherms from literature [234–237] as a function of CO_2 loading. When $K_{R3,des}$ computed with GAFF ($\ln\left[K_{R3,des}\right] = -34.80$) is used, the computed CO_2 pressures are significantly underestimated at low CO_2 loadings ($< 1 \ mol_{CO_2} \ mol_{amine}^{-1}$), while at high loadings ($> 1 \ mol_{CO_2} \ mol_{amine}^{-1}$), the computed CO_2 pressures agree well with the experimental isotherms. The computed CO_2 pressures were underestimated at low CO_2 loadings because lower values of $K_{R3,des}$ mean that reaction R3 is dominated by the species on the left side of the reaction (MDEAH$^+$ and H_2O) (Eq. (3.3)). This means that the CO_2 dissociation reaction (reaction R1) proceeds towards the right side of the reaction more freely, so more CO_2 is absorbed by the solution (in the form of HCO_3^-, and consequently CO_3^{2-}) at low CO_2 loadings. This results in the underestimation of the CO_2 isotherm at low loadings of CO_2 computed using $K_{R3,des}$ from GAFF. When $K_{R3,des}$ computed with the OPLS-AA force field is used, the agreement between the computed and experimental CO_2 isotherms is much better than GAFF but still differs from the experimental isotherms. At the lowest CO_2 loading (10^{-5} $mol_{CO_2} \ mol_{amine}^{-1}$), the CO_2 pressure computed using $K_{R3,des}$ from the experimental
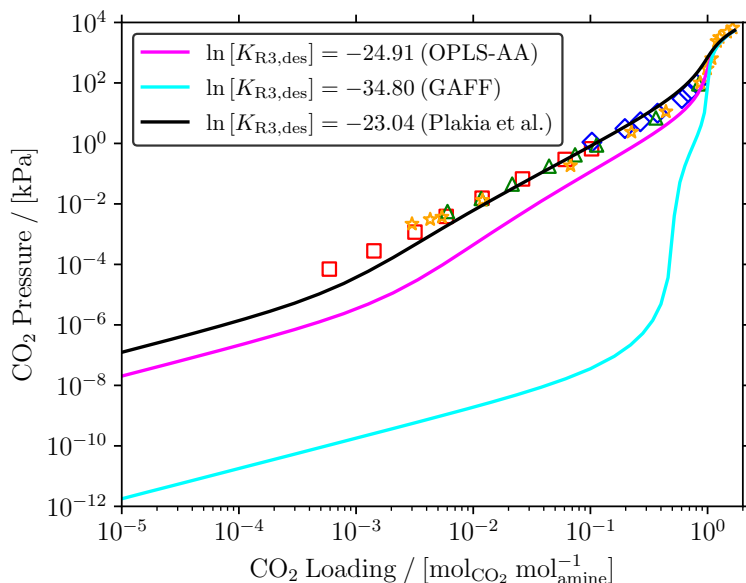
Figure 3.5: Comparison of experimental CO_2 isotherms [234–237] and the calculated CO_2 isotherms obtained using $K_{R3,des}$ from the OPLS-AA force field [88, 89], the GAFF [95], and the experimental correlation from Plakia et al. [212] in 23 wt.% MDEA/water solution at 313.15 K. Note that experimental values of $K_{j,des}$ provided by Plakia et al. [212] were used for reactions R1, R2, and R4 in CO_2/MDEA/water system while for reaction R3, we used $K_{R3,des}$ from OPLS-AA force field, GAFF, or experimental correlation from Plakia et al. [212]. The solid lines represent the CO_2 isotherms computed with CASpy while the empty symbols represent CO_2 isotherms from literature [234–237]. The color codes of the empty points (experiments) follow those in Fig. 3.2.

correlation reported by Plakia et al. [212] is ca. 6 times higher than the CO_2 pressure computed using $K_{R3,des}$ from the OPLS-AA force field. At a higher CO_2 loading (5×10^{-3} $mol_{CO_2} mol_{amine}^{-1}$), the CO_2 pressure computed using $K_{R3,des}$ from the experimental correlation reported by Plakia et al. [212] is ca. 16 times higher than the CO_2 pressure computed using $K_{R3,des}$ from the OPLS-AA force field. The isotherms computed using the GAFF and OPLS-AA force field agree well with the experimental CO_2 isotherms at high CO_2 loadings. This is because the limit of chemical CO_2 absorption in aqueous MDEA solutions is the CO_2 loading of 1 $mol_{CO_2} mol_{amine}^{-1}$ (due to the one-to-one stoichiometry between CO_2 and MDEA in reactions R1–R4). Further analyses showed that an accuracy of 0.1 $k_B T$ in the computed values of μ_i^0 is needed to predict values of P_{CO_2} within 10% of the ones computed using the equilibrium constant from the experimental correlation reported by Plakia et al. [212] at low CO_2 loadings. At loadings higher than 1 $mol_{CO_2} mol_{amine}^{-1}$, we only have physical absorption of CO_2 in the solution. This can also be seen with the changing slope of the CO_2 isotherms at CO_2 loadings higher than 1 $mol_{CO_2} mol_{amine}^{-1}$. The only parameter affecting the amount of physically absorbed CO_2 in our model is the μ_i^{ex} of CO_2. This shows that we predict the μ_i^{ex} of CO_2 in water correctly,

therefore, all the isotherms agree with the experimental CO_2 isotherms at high CO_2 loadings. All in all, Fig. 3.5 shows that the computed CO_2 isotherms are sensitive to the changes in the equilibrium constant of reaction R3 ($K_{R3,des}$). Even with a reasonable prediction of the value of $K_{R3,des}$ ($\ln\left[K_{R3,des}\right]$ (OPLS-AA) $= -24.91$ vs. $\ln\left[K_{R3,des}\right]$ (Plakia et al.) $= -23.04$) from quantum chemistry calculations and MC simulations, the CO_2 isotherms computed are quite different.

To investigate absorption at low pressures, we derived an expression for the Henry constant of CO_2 in aqueous MDEA solutions. Details of derivation of the expression for the Henry constant of CO_2 are shown in Appendix B. The Henry constants computed using the expression we derived and computed using the slope of the CO_2 isotherm (the one with $K_{R3,des}$ from Plakia et al. [212]) show an excellent agreement since the Henry constant computed using the expression we derived is $0.0162\ \mathrm{kPa\,mol_{amine}\,mol_{CO_2}^{-1}}$ and the Henry constant computed using the slope of the CO_2 isotherm is $0.0149\ \mathrm{kPa\,mol_{amine}\,mol_{CO_2}^{-1}}$. We also validated the expression for the Henry constant of CO_2 in aqueous MDEA solutions using the speciation obtained from CASpy. Table B.3 of Appendix B shows the excellent agreement between the speciation computed using the Henry constant expression we derived and the speciation computed numerically with our solver. This means that the expression derived for the Henry constant of CO_2 in aqueous MDEA solutions can be used to accurately compute absorption at low pressures.

To test the sensitivity of computed values of $K_{R3,des}$ to point charges, we computed μ_i^{ex} of $MDEAH^+$ (and HCO_3^- as counter ion), H_3O^+ (and HCO_3^- as counter ion), and MDEA with point charge scaling factors (χ) of 0.9, 0.8, and 0.7 at 313.15 K. For example, $\chi = 0.9$ means that all the point charges in the molecule were multiplied by 0.9. Fig. 3.6 shows the computed values of μ_i^{ex} and the computed values of $\ln\left[K_{R3,des}\right]$ for GAFF with RESP fitted point charges and OPLS-AA force field with 1.14*CM1A point charges as a function of χ at 313.15 K. The parameters of the linear regression fits in Fig. 3.6 are tabulated in Table B.9 and Table B.10 of Appendix B. The results show that for both force fields, the values of μ_i^{ex} are very sensitive to the point charges. For GAFF with RESP fitted point charges, the value of μ_i^{ex} for $MDEAH^+ + HCO_3^-$ increases by 95.63 kJ mol^{-1} (36.73 k_BT) when $\chi = 0.9$ is used instead of the unscaled point charges. The change in the value of μ_i^{ex} for $H_3O^+ + HCO_3^-$ is even more sensitive to the point charges (also seen in Table B.9 with a lower slope). The value of μ_i^{ex} for $H_3O^+ + HCO_3^-$ increases by 155.53 kJ mol^{-1} (59.74 k_BT) when $\chi = 0.9$ is used instead of $\chi = 1.0$. Our results also show that $\ln\left[K_{R3,des}\right]$ is very sensitive to the changes in the point charges. For OPLS-AA force field with 1.14*CM1A point charges, the computed value of $\ln\left[K_{R3,des}\right]$ changes from -24.91 to -42.19 if only the point charges of the ions in reaction R3 are scaled, and to -45.15 if the point charges of MDEA are scaled as well. All in all, Fig. 3.6 show that we need force fields with very accurate point charges to be able to accurately compute CO_2 isotherms in aqueous alkanolamines. Polarizable force fields are usually more accurate than classical force fields [239–246] because the ability to accurately quantify electrostatic interactions is essential (Fig. 3.6). However, polarizable force fields are not implemented widely in the software packages, and are

(a)

(b)

(c)

(d)
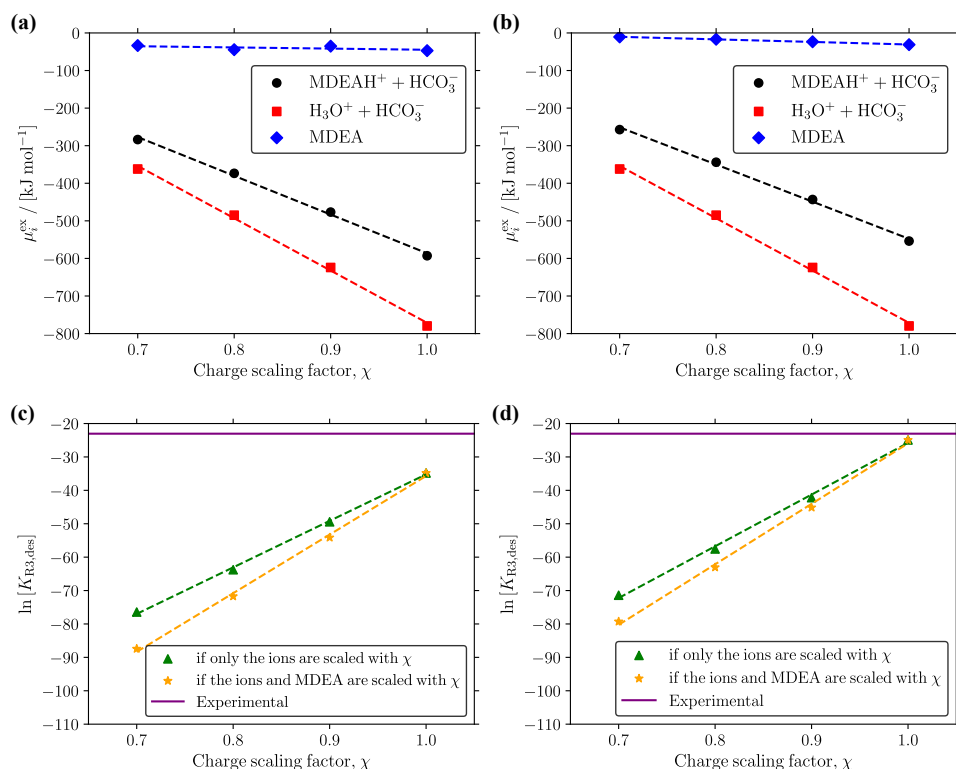
Figure 3.6: (a,b) Values of μ_i^{ex} of the species in reaction R3, and (c,d) values of $\ln\left[K_{\text{R3,des}}\right]$ for (a,c) the GAFF with RESP fitted point charges (Appendices C.8.1 and C.9.1) and (b,d) the OPLS-AA force field with 1.14*CM1A point charges (Appendices C.8.2 and C.9.2) as a function of the point charge scaling factor χ at 313.15 K. The dashed lines in all subfigures represent the linear regression fits to the values of μ_i^{ex} (the fit parameters are tabulated in Table B.9 and Table B.10).

usually computationally more expensive and less transferable than classical force fields [247, 248].

3.4. Conclusions

We derived an expression for a mole fraction-based equilibrium constant as a function of μ_i^{ex}, μ_i^0 and T, and developed an open-source chemical reaction equilibrium solver in Python called CASpy for absorption of gases to reactive solutions, assuming that the values of μ_i^{ex} and the liquid phase volume V are constant. CASpy can be used to compute the concentrations of the species in any reactive liquid phase, for example, aqueous alkanolamine solutions for CO_2 and H_2S capture, and CO_2 capture in an aqueous solution for the electrochemical conversion of CO_2. We first validated that CASpy yields the correct numerical solution at chemical equilibrium. Our results showed that the computed solutions are at chemical equilibrium since the sum of all residuals were 0 within machine precision. We computed

CO_2 isotherms in 23 wt.% MDEA/water solutions at 313.15 K using experimental equilibrium constants from literature [212] for all reactions (R1–R4) and compared the computed isotherms with experimental isotherms from literature. The results are in excellent agreement with the experiments. We compared the computed speciation in the CO_2/MDEA/water system with the experimental speciation from literature [197], showing an excellent agreement. For low pressures, we derived and validated an analytic expression for the Henry constant of CO_2 in aqueous MDEA solutions. We computed binary CO_2 and H_2S absorption isotherms in 50 wt.% MDEA/water solutions at 323.15 K using experimental equilibrium constants from literature [212] for all reactions (R1–R6). The computed CO_2 isotherms in the H_2S/CO_2/MDEA/water system show a good agreement with another modeling study from literature [54], however, the computed H_2S isotherm in H_2S/CO_2/MDEA/water system did not agree well with experimental isotherms by Dicko et al. [54]. As these authors first performed CO_2 absorption and then H_2S absorption in a 50 wt.% MDEA/water solution, and did not account for the CO_2 evaporating in the H_2S absorption part of the experiment, we also estimated the amount of evaporated CO_2 by making some modifications to our solver. The H_2S isotherm computed considering the effect of evaporating CO_2 agreed better with the experimental results [54] than the H_2S isotherm computed without considering the effect of evaporating CO_2. However, agreement with the experimental results from Dicko et al. [54] is lacking. This implies that the experimental equilibrium constants [212] from literature were not suitable for H_2S/CO_2/MDEA/water systems and the equilibrium constants of the reactions in H_2S/CO_2/MDEA/water systems need to be refitted. We tested the sensitivity of the computed CO_2 isotherms in aqueous MDEA solutions to the computed values of μ_i^{ex} and μ_i^0 by computing these values for the MDEAH$^+$ dissociation reaction (R3) in water at 313.15 K and 1 bar using MC simulations and quantum chemistry calculations. Two different force fields for MDEAH$^+$ and MDEA were used in the MC simulations (GAFF [95] and OPLS-AA [88, 89]). Using the computed values of μ_i^{ex} and μ_i^0 and Eq. (3.4), we computed the value of $K_{\mathrm{R3,des}}$ at 313.15 K. The value of $K_{\mathrm{R3,des}}$ computed using the OPLS-AA force field ($\ln\left[K_{\mathrm{R3,des}}\right]$ (OPLS-AA) $= -24.91$) showed a good agreement with the experimental value ($\ln\left[K_{\mathrm{R3,des}}\right]$ (Plakia et al.[212])$= -23.04$) from literature while the value of $K_{\mathrm{R3,des}}$ computed using the GAFF ($\ln\left[K_{\mathrm{R3,des}}\right]$ (GAFF) $= -34.80$) differed from the experimental value. We computed the CO_2 isotherms in 23 wt.% MDEA/water solutions at 313.15 K using the experimental equilibrium constants from literature [212] for reactions R1, R2, and R4, while we used either $K_{\mathrm{R3,des}}$ computed using the GAFF or the OPLS-AA force field. Results showed that the computed CO_2 isotherms are in an excellent agreement with the experimental isotherms at high CO_2 loadings (> 1 $\mathrm{mol_{CO_2}}$ $\mathrm{mol_{amine}^{-1}}$). However, the difference between the computed CO_2 isotherms and the experimental isotherms is quite large for lower CO_2 loadings (< 1 $\mathrm{mol_{CO_2}}$ $\mathrm{mol_{amine}^{-1}}$). Even with a good agreement between the value of $K_{\mathrm{R3,des}}$ computed using the OPLS-AA force field and the experimental value of $K_{\mathrm{R3,des}}$ from literature, the computed CO_2 pressures were 6 and 12 times lower than the experimental isotherms at 10^{-5} $\mathrm{mol_{CO_2}}$ $\mathrm{mol_{amine}^{-1}}$ and 5×10^{-3} $\mathrm{mol_{CO_2}}$ $\mathrm{mol_{amine}^{-1}}$,

respectively. This shows that the CO_2 isotherm in aqueous MDEA solutions is very sensitive to the value of $K_{R3,des}$. Furthermore, we computed the values of μ_i^{ex} and $K_{R3,des}$ for the GAFF and OPLS-AA force field and for charge scaling factor χ of 0.9, 0.8, and 0.7. Our results showed that even with 10% change in the point charges, the changes in the values of μ_i^{ex} and $K_{R3,des}$ were very large. The value of μ_i^{ex} for $MDEAH^+ + HCO_3^-$ has increased by ca. 37 k_BT from $\chi = 1.0$ to $\chi = 0.9$, while the value of μ_i^{ex} for $H_3O^+ + HCO_3^-$ has increased by ca. 60 k_BT. The value of $\ln\left[K_{R3,des}\right]$ computed using the GAFF has decreased from -34.80 to -49.42 when charges are scaled by $\chi = 0.9$ while the value of $\ln\left[K_{R3,des}\right]$ computed using the OPLS-AA force field decreased from -24.91 to -42.19. Our results showed that force fields with accurate point charges are required to be able to solve chemical reaction equilibrium accurately. Further research must be conducted to develop accurate point charge assignment methods, while exploring alternative approaches such as the development of polarizable force fields.

3

4

Transport Properties of Mixtures of Acid Gases with Aqueous Monoethanolamine Solutions
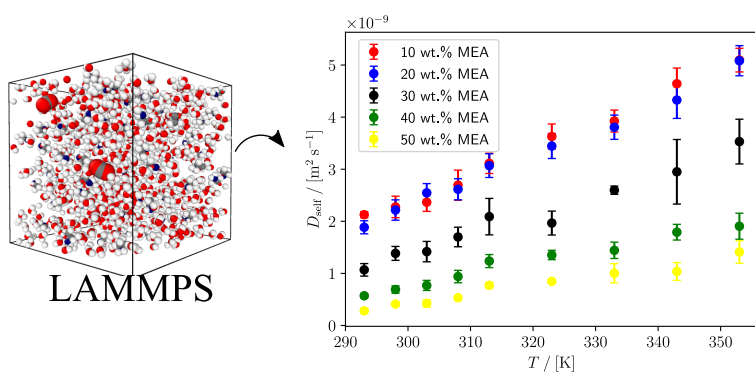
The effects of temperature and MEA concentration on acid gas self-diffusivity in aqueous MEA solutions are investigated. MEA point charges are scaled by a factor of 0.8, validated using viscosities and self-diffusivities. Computed self-diffusivities of CO_2 and H_2S reveal significant dependencies on temperature and MEA concentration.

4.1. Introduction

Force field-based MD simulations have been extensively used to predict diffusion coefficients of different solutes such as alkylbenzenes, ketones, and water in various solvents [249, 250]. This simulation method requires an accurate description of the interaction between the molecules of the solute and the solvent i.e., interaction potentials that describe the interactions between the molecules accurately. The advantage of MD simulations is that reactions in the system can be "switched off", thereby eliminating the need for a model molecule in the experimental studies. Although MD simulations have been very promising and are widely used for this purpose [56, 251], we currently have limited knowledge of the diffusion coefficients of CO_2 and H_2S and their temperature dependence in solutions with different concentrations of alkanolamine in the solvent. The diffusivity of acid gases in pure water has been studied extensively [144, 145, 252]. A comprehensive literature review on studies examining the transport properties of acid gases in aqueous alkanolamine solutions using MD simulations is presented in Section 1.2.3.

In this chapter, we compute self-diffusion coefficients (D_{self}) for CO_2 and H_2S in aqueous MEA solutions for a wide range of temperatures and MEA concentrations in the solution. We studied aqueous MEA solutions because it is considered as an industry benchmark solvent [253] and it is also used in other applications such as CO_2 capture from flue gas [254]. We first computed the density of pure MEA solution for the temperature range 293–353 K. It turns out that with the standard force fields from literature, the results did not agree with the experimental density values from literature. We then scaled the force field parameters of MEA molecules to find the optimum scaling factor that best describes the experimental densities of the solvent. We validated this set of parameters by calculating the viscosities and D_{self} of pure MEA and 30 wt.% MEA/water solution and compared these values to experimental values from literature. We used the validated force field for MEA to compute the self-diffusivities of CO_2 and H_2S at infinite dilution for a temperature range of 293–353 K and MEA concentrations ranging from of 10–50 wt.% in the solvent. The results we provide will be useful for more accurate modelling in the process simulations, and will guide the design and development of acid gas removal process.

4.2. Simulation Details

MC simulations were performed to compute solvent densities using the open source MC software, Brick-CFCMC [96, 97, 123]. For MEA molecules, the OPLS-AA [88, 89] force field was used for intermolecular LJ interactions because it was optimized for amines. Partial charges computed from quantum mechanical calculations were used for electrostatic interactions of the MEA molecules. Quantum chemical calculations were performed using the Gaussian09 [78] software at second order Møller-Plesset perturbation theory (MP2) [70] level using the 6-311+G(2d,2p) basis set. We then multiply either the energy (ε) parameters of the LJ interactions of MEA molecule or the point charges of the MEA molecule with a scaling factor χ to scale the interactions of this molecule. For water molecules, the SPC/E [188] force field was used.

The SPC/E force field is known to predict the transport properties of water accurately [255]. For CO_2 molecules, the TraPPE [90] force field was used. The interactions between the TraPPE CO_2 molecules and the SPC/E water molecules were computed using the optimized intermolecular potential for CO_2/H_2O developed by Orozco et al. [225]. For H_2S molecules, the force field developed by Kristóf and Liszi [224] was used. All force field parameters for these molecules can be found in Appendix C (Appendices C.1.1, C.3, C.4.1 and C.10). LJ parameters of the interactions of different types of atoms except the interactions between CO_2 and water molecules [225] were computed using Lorentz-Berthelot mixing rules [83]. All molecules in the molecular simulations were kept rigid. It was shown that the rigidity of small molecules (length of MEA molecule $\approx 3\,\text{Å}$) does not significantly affect the dynamics in MD simulations [83]. Initial configurations were generated in a cubic simulation box with a length of 25.5 Å using Packmol [256]. For initialization, equilibration and production stages, 10^4, 10^5 and 10^5 MC cycles were performed, respectively. In MC cycles, the number of trial moves is equal to the number of molecules in the simulation box. These moves were the translation of a randomly selected molecule (49.5%), the rotation of a randomly selected molecule (49.5%) and attempting to change the volume of the simulation box (1%). In these simulations, LJ interactions were truncated at 12 Å and analytic tail corrections [83] were applied. To compute the electrostatic interactions, the Ewald summation [182] was used with a precision of 10^{-6}. Standard deviations for densities of pure MEA and 30 wt.% MEA/water solutions were computed using block averaging over the densities computed in the production stage of the MC simulations.

Initial configurations for the MD simulations were generated with a box length of 50 Å using Packmol [256]. The number of MEA and water molecules used for different concentrations of MEA in the solution are listed in Table 4.1. Two molecules of CO_2 or H_2S were used to compute the self-diffusivity of these species. The MD simulations start with an equilibration period of 0.5 ns with a timestep of 1 fs in the *NPT* ensemble using the Nosé-Hoover thermostat and barostat. After this equilibration, the temperature was equilibrated in the *NVT* ensemble using the Nosé-Hoover thermostat for another 0.5 ns. In the production stage, the simulations were run for 100 ns in the *NVE* ensemble with a timestep of 1 fs. In these simulations, LJ interactions were truncated at 12 Å. Analytic tail corrections [83] were applied to account for the long-range interactions. Electrostatic interactions were computed using the Particle-Particle Particle-Mesh (PPPM) method with a relative precision of 10^{-5}. MD simulations to compute viscosities and self-diffusivities were performed using the LAMMPS [130] package (version 3 March 2020) with the On-the-Fly Calculation of Transport Properties (OCTP) [257] plugin. The computed self-diffusion coefficients were corrected for the finite-size effects using [258–261]:

$$D_i = D_i^{\text{MD}} + \frac{\xi k_{\text{B}} T}{6\pi\eta L} \tag{4.1}$$

where D_i is the self-diffusivity of species i in the thermodynamic limit, D_i^{MD} is the self-diffusivity of species i computed from the MD simulation, ξ is a constant equal to 2.837297 for a cubic simulation box, k_{B} is the Boltzmann constant, T is the ab-

Table 4.1: Number of MEA and water molecules in MD simulations for different concentrations of MEA in the MEA/water solutions.

MEA concentration / [wt.%]	Number of MEA molecules	Number of water molecules	Average Box Size at 313 K / [Å]
10	25	775	29.1
20	55	745	29.8
30	81	646	29.9
40	123	627	30.5
50	159	541	30.8

4

solute temperature, η is the viscosity computed from MD simulation, and L is the length of the simulation box. It is important to note that the computed self-diffusion coefficients of the acid gases are practically equal to transport diffusion coefficients because the acid gases are at low loading [262]. The standard deviations of the self-diffusion coefficients and the viscosities were computed from ten independent simulations starting from different initial configurations. The computed radial distribution functions (RDFs) are center-of-mass RDFs.

4.3. Results and Discussion
4.3.1. Densities and Viscosities of Aqueous MEA Solutions
LJ interaction parameters for MEA were taken from the OPLS-AA force field [88, 89]. The point charges of MEA were computed using quantum chemical calculations as discussed in the previous section. Generic force fields such as OPLS-AA and point charges calculated using quantum chemical calculations may require scaling (with different methods) [263–268]. The reason for this is that point charges calculated using quantum chemical calculations typically overestimate electrostatic interactions [190, 263, 266, 267, 269, 270]. To test the performance of the force field for MEA, we computed the density of a pure MEA solution and a 30 wt.% MEA/water solution for a temperature range of 293–353 K using MC simulations. Comparison between computed and experimental densities [271–273] are shown in Fig. 4.1. Results showed that computed densities using this force field do not agree well with experimental measurements [271–273]. This is because strong polarization and charge transfer in these solutions are not well produced by this force field [264]. We scaled the energy (ε) parameter of the LJ potential and the point charges of the MEA molecule by multiplying either ε or the point charges with a scaling factor, χ. Fig. 4.1 shows the densities of pure MEA solvent and 30 wt.% MEA/water solution as a function of temperature and χ. Results show that changing the LJ potential does not affect the densities of both pure MEA and 30 wt.% MEA/water solution significantly, while scaling the point charges significantly affects the density of these solutions. Fig. 4.2 shows that scaling the LJ ε parameter of the MEA atoms by

Figure 4.1: Comparison of simulated and experimental [271–273] densities of (a,b) pure MEA and (c,d) 30 wt.% MEA/water solutions as a function of temperature. Subfigures (a) and (c) show the scaling of LJ ε parameters of the MEA molecules while subfigures (b) and (d) show the scaling of the point charges of the MEA molecules. Red: $\chi = 1.00$; blue: $\chi = 0.95$; green: $\chi = 0.90$; orange: $\chi = 0.85$; purple: $\chi = 0.80$; brown: $\chi = 0.75$; cyan: $\chi = 0.70$; black: experiments [271], blue: experimental correlation [272, 273]. The lines connecting the experimental data are to guide the eye.

$\chi = 0.7$ changes the density of pure MEA solution (30 wt.% MEA/water solution) by ca. 0.4% (1.1%) at 303 K. The scaling of the point charges of MEA by the same χ changes the density of pure MEA by ca 10% and the density of 30 wt.% MEA/water solution by ca. 4% (Fig. 4.1(b) and (d)). Overall, these results suggest that calculated densities of pure MEA and 30 wt.% MEA/water solutions agree well with the experimental values when the point charges of MEA are scaled by 0.8, with a maximum deviation of ca. 3% from experiments for both solutions (Fig. 4.1(b) and (d)).

Motivated by the good agreement between simulations and experiments on the densities of pure MEA and 30 wt.% MEA/water solutions, we validated the scaling factor for the point charges, i.e. $\chi = 0.80$, of MEA by computing the viscosities and self-diffusivities of MEA (D_{MEA}) and water (D_{water}) of these solutions using MD simulations for a temperature range of 293–353 K. We have used 30 wt.% MEA/water solution to validate our model for MEA because this is the most stud-
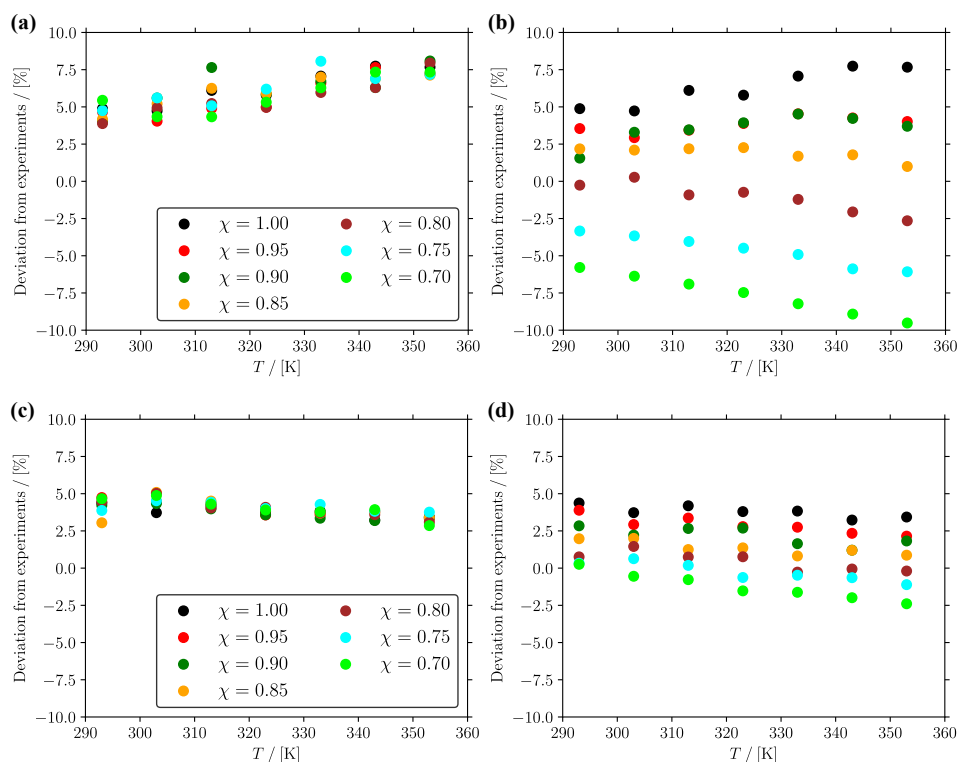
Figure 4.2: Deviation between the simulated densities of (a,b) pure MEA and (c,d) 30 wt.% MEA/water and experimental densities [271] of (a,b) pure MEA and (c,d) 30 wt.% MEA/water solutions as a function of temperature. Subfigures (a) and (c) show the scaling of LJ the ε parameters of MEA while subfigures (b) and (d) show the scaling of the point charges of MEA. In subfigures (b) and (d), color codes follow those in subfigures (a) and (c).

ied solution in literature and the industry standard for CO_2 capture [274]. It is important to note that we scaled the point charges of MEA with $\chi = 0.8$ in these simulations. Fig. 4.3 shows the comparison between the computed and experimental [271] viscosities and values of D_{MEA} and D_{water} of pure MEA and 30 wt.% MEA/water solutions. Results show that the computed and experimental viscosities of pure MEA and 30 wt.% MEA/water solutions have coefficient of determination (R^2) [24] scores of 0.98 and 0.97, respectively. Both R^2 scores show that the simulations, and therefore this set of force field parameters for MEA, agree well with the experiments on viscosity in this temperature range. We also compare the simulation results with the experimental correlation obtained from Design Institute for Physical Properties (DIPPR) [272] (Fig. 4.3(a)). The simulations agree well also with the experimental correlation obtained from the DIPPR database. For example, the computed viscosities for pure MEA (30 wt.% MEA/water) were between 26.26–2.42 (2.69–0.91) mPa s at 293–353 K. The experimental values for the same conditions vary between 24.09–2.92 and 2.91–0.77 mPa s for pure MEA

and 30 wt.% MEA/water solutions, respectively. The maximum (average) deviation between computed viscosities and experimental viscosities were computed as 17% (8.8%) and 15% (7.6%) for pure MEA and 30 wt.% MEA/water solutions, respectively. These results suggest that using the scaling factor ($\chi = 0.8$) for the point charges of MEA in these simulations can provide accurate predictions for the viscosity of MEA/water solutions. We also compared the computed values of D_{MEA} (corrected for finite-size effects using computed viscosities [259, 260]) of MEA molecules in pure MEA solution with the experimental values from literature [275]. The experimental values are 4.2×10^{-11} m^2 s^{-1}, 5.5×10^{-11} m^2 s^{-1}, and 9.3×10^{-11} m^2 s^{-1} for 288, 298, and 308 K, while the computed values of D_{MEA} are 4.5×10^{-11} m^2 s^{-1} (extrapolated slightly using an Arrhenius equation fit, R^2 for the Arrhenius fit = 0.997), 5.6×10^{-11} m^2 s^{-1}, and 1.1×10^{-10} m^2 s^{-1}, respectively. To the best of our knowledge, there is no experimental data in literature to compare D_{MEA} and D_{water} in 30 wt.% MEA/water solutions. The values of D_{MEA} molecules are 2.14-2.34 times larger than the values of D_{MEA} in 30 wt.% MEA/water solutions. Also, the results show that the values of D_{MEA} are an order of magnitude higher in 30 wt.% MEA/water solution than that in a pure MEA solution. This indicates stronger MEA-MEA interactions than MEA-water interactions.

4.3.2. Diffusivities of CO_2, H_2S, MEA, and Water in Aqueous MEA Solutions

To obtain a fundamental understanding of the transport mechanism of CO_2 and H_2S in MEA/water solutions with different MEA concentrations, we computed self-diffusivities of CO_2 (D_{CO_2}), H_2S (D_{H_2S}), water, and MEA molecules in 10–50 wt.% MEA/water solutions at infinite dilution and 1 bar for a temperature range of 293–353 K using MD simulations. Fig. 4.4 shows the values of D_{CO_2} and D_{H_2S} in pure water [144, 252] and 10–50 wt.% MEA/water solutions as a function of temperature and MEA concentration. Fig. 4.5 shows the computed values of D_{MEA} and D_{water} as a function of temperature and MEA concentration. We first compare computed values of D_{CO_2} with D_{CO_2} obtained using CO_2/N_2O analogy [277]. Mandal et al. [277] estimated values of D_{CO_2} in 30 wt.% MEA/water solution as 1.61×10^{-9} m^2 s^{-1}, 1.74×10^{-9} m^2 s^{-1}, and 2.14×10^{-9} m^2 s^{-1} at 293, 303, and 313 K, respectively. The computed values of D_{CO_2} at infinite dilution in 30 wt.% MEA/water solution are 1.1×10^{-9} m^2 s^{-1}, 1.4×10^{-9} m^2 s^{-1}, and 2.1×10^{-9} m^2 s^{-1} at 293, 303, and 313 K, respectively. These results show that simulated values of D_{CO_2} are slightly underestimated for the temperatures 293 K and 303 K, while at 313 K the computed value of D_{CO_2} agrees with the value obtained using CO_2/N_2O analogy [277].
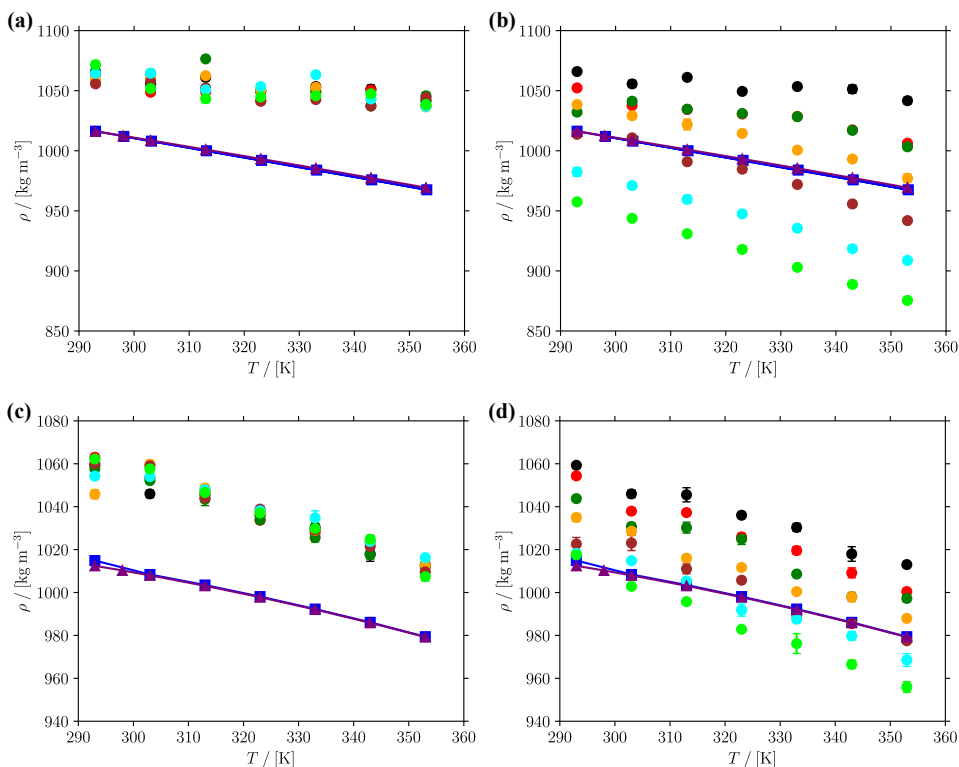
4
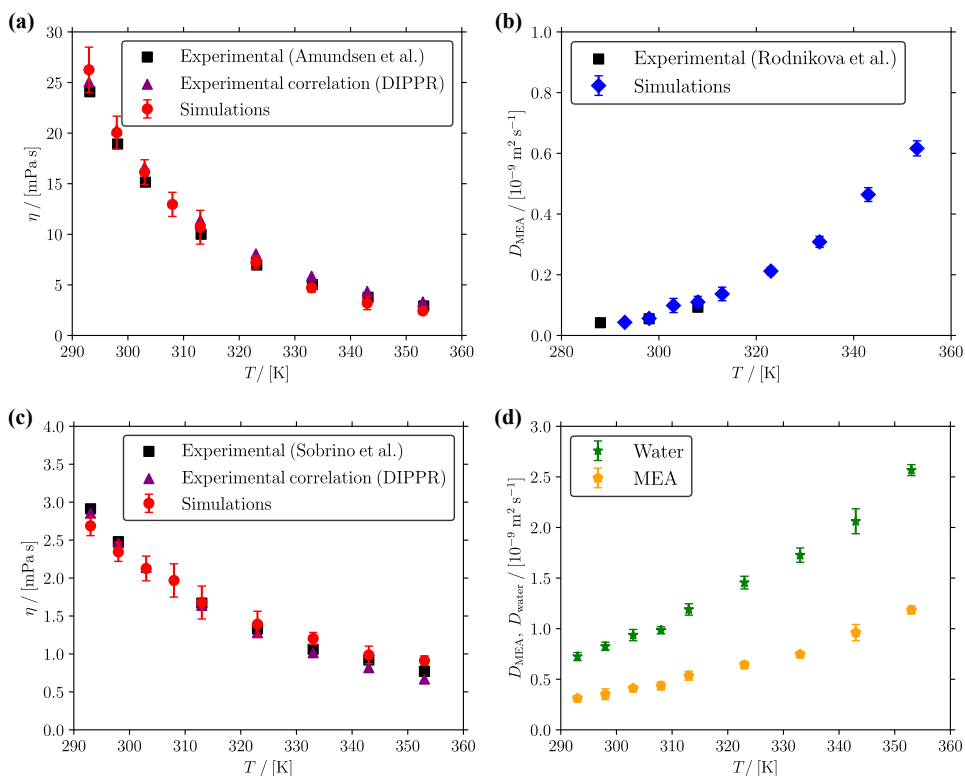
Figure 4.3: Comparison of simulated and experimental [271–273, 276] viscosities of (a) pure MEA and (c) 30 wt.% MEA/water solution as a function of temperature. The values of (b) D_{MEA} in pure MEA, and (d) D_{MEA} and D_{water} in 30 wt.% MEA/water solution as a function of temperature.
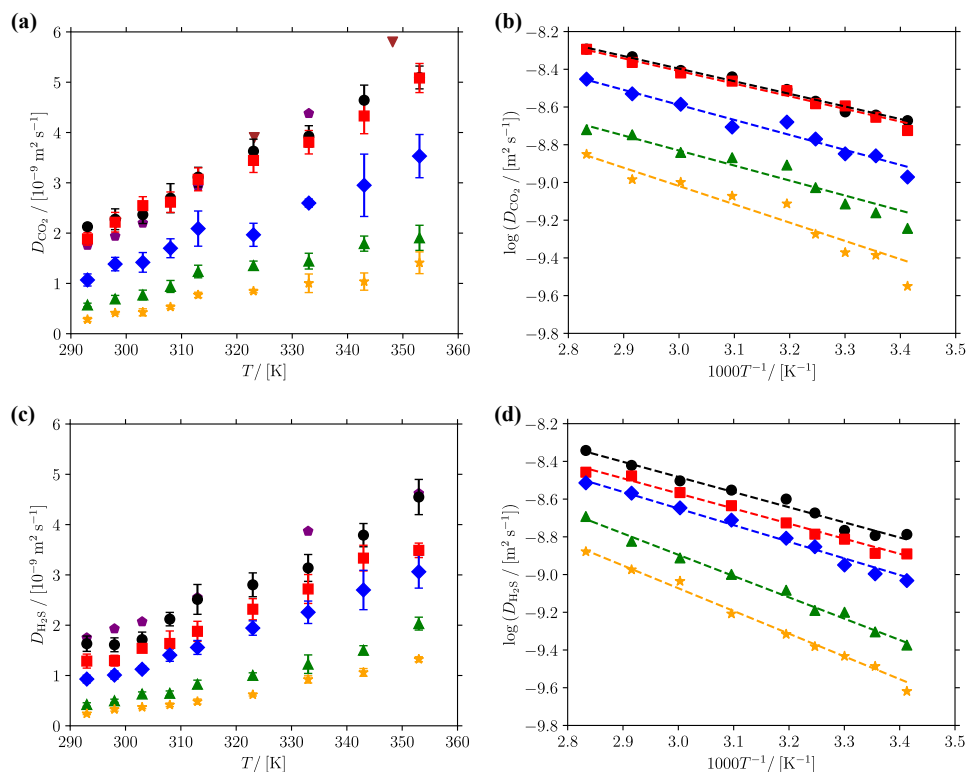
Figure 4.4: Values of (a) D_{CO_2} and (c) D_{H_2S} in pure water [144, 252] and 10–50 wt.% MEA/water solutions as a function of temperature. Subfigures (b) and (d) show the Arrhenius plots of subfigures (a) and (c), respectively. Dashed lines represent the Arrhenius fits of the values of D_{CO_2} and D_{H_2S}. Color code: black: 10 wt.% MDEA/water; red: 20 wt.% MDEA/water; blue: 30 wt.% MDEA/water; green: 40 wt.% MDEA/water; orange: 50 wt.% MDEA/water; purple: pure water [252]; brown: pure water [144].

4
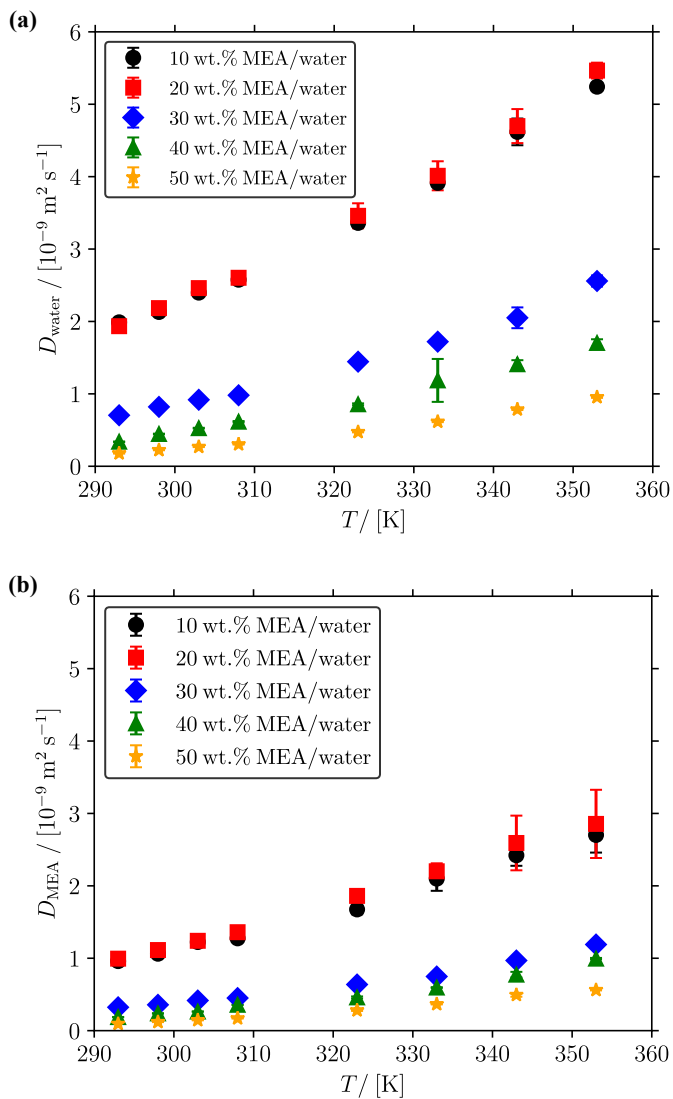
Figure 4.5: Computed values of (a) D_{water} and (b) D_{MEA} as a function of temperature and MEA concentration in the solution.

Our results show that the values of D_{CO_2} and D_{H_2S} increase with increasing temperature. Fig. 4.4 also shows that the values of D_{CO_2} is larger than D_{H_2S} at the same conditions. Although H_2S has a lower molar mass ($M_{H_2S} = 34.1\,g\,mol^{-1}$) than CO_2 ($M_{CO_2} = 44.01\,g\,mol^{-1}$), the values of D_{H_2S} are lower because it can form hydrogen bonds with both water and MEA molecules, and the H_2S molecule is more spherical than the linear CO_2 molecule [278]. Also, the results show that with the increasing concentration of MEA in the solution, the values of both D_{CO_2} and D_{H_2S} in these solutions decrease. The value of D_{CO_2} (D_{H_2S}) at 293 K decreases by a factor of 7.6 (6.8) from 10 wt.% MEA to 50 wt.% MEA while at 353 K, these values decrease by a factor of 3.6 (3.4) times. The temperature dependency of the values of D_{CO_2} and D_{H_2S} decreases with increasing MEA concentration in the solution. The same temperature dependency can also be observed in the values of D_{water} and D_{MEA} (Fig. 4.5). The slope of the self-diffusivities as a function of temperature in a 10 wt.% solution is 3.0 and 2.7 times higher than 50 wt.% solution for CO_2 and H_2S, respectively. Also, the self-diffusivities change significantly for both acid gases from 40 wt.% solution to 30 wt.%, especially at low temperatures. However, the changes in the self-diffusivities of both acid gases are not as significant from 50 wt.% to 40 wt.%. For example, the value of D_{H_2S} at 293 K increases by 2.2 times from 40 wt.% solution to 30 wt.% solution while it only increases by a factor of 1.7 from 50 wt.% to 40 wt.%. This effect of MEA concentration on the self-diffusivities decreases with the increasing temperature as the value of D_{H_2S} increases 1.5 times both from 40 wt.% to 30 wt.% and from 50 wt.% to 40 wt.% at 353 K. For CO_2, water and MEA, there is also a significant effect of concentration on the self-diffusivities from 30 wt.% MEA/water solution to 20 wt.% MEA/water solution (Fig. 4.4(a) and Fig. 4.5). We fit the values of D_{CO_2} and D_{H_2S} to an Arrhenius equation using:

$$D_i = D_0 \exp\left[-\frac{E_A}{RT}\right] \tag{4.2}$$

where D_i is the self-diffusivity of species i, D_0 is the pre-exponential factor, E_A is the activation energy for diffusion, R is the ideal gas constant, and T is the absolute temperature. Fig. 4.4(b,d) shows the Arrhenius fits of the values of D_{CO_2} and D_{H_2S}. Table 4.2 shows Arrhenius fit parameters of the values of D_{CO_2} and D_{H_2S}. Table 4.2 show that the values of E_A for diffusion for both acid gases increases with increasing MEA concentration in the solution. This was also indicated by slower acid gas dynamics (Fig. 4.4) with increasing MEA concentration. We also fit the values of D_{CO_2} and D_{H_2S} to the Speedy-Angell power equation [279]:

$$D_i = D_0 \left(\frac{T}{T_s} - 1\right)^m \tag{4.3}$$

where T_s is the singularity temperature, and the Vogel-Tamann-Fulcher (VTF) equation [280]:

$$D_i = \exp\left[\frac{-\alpha}{T - \beta} - \gamma\right] \tag{4.4}$$

Table 4.2: Arrhenius equation (Eq. (4.2)) fit parameters (pre-exponential factor (D_0) and activation energy (E_A)) and coefficient of determinations (R^2) for the values of D_{CO_2} and D_{H_2S} in MEA/water solutions with different MEA concentrations. The values of D_{CO_2} and D_{H_2S} were fitted for a temperature range of 293–353 K.

	MEA concentration / [wt.%]	D_0 / [m^2 s^{-1}]	E_A / [kJ mol^{-1}]	R^2
D_{CO_2}	10	4.05×10^{-7}	12.79	0.989
	20	3.98×10^{-7}	12.82	0.988
	30	6.28×10^{-7}	15.23	0.970
	40	3.59×10^{-7}	15.23	0.947
	50	7.77×10^{-7}	18.57	0.944
D_{H_2S}	10	8.41×10^{-7}	15.36	0.985
	20	6.76×10^{-7}	15.31	0.985
	30	9.84×10^{-7}	16.86	0.991
	40	3.10×10^{-6}	21.61	0.991
	50	3.48×10^{-6}	23.06	0.992

where α, β, and γ are the fit parameters. Tables 4.3 to 4.4 show the Speedy-Angell power equation and the VTF equation fit parameters for the values of D_{CO_2} and D_{H_2S}. Fig. 4.6 shows the Speedy-Angell and VTF fits for the values of D_{CO_2} and D_{H_2S} in aqueous MEA solutions. The pressure and temperature dependent form of the Speedy-Angell power equation has been shown to be able to predict the CO_2 diffusivity in water very accurately [145]. Our results show that the Speedy-Angell power equation has the highest coefficients of determination (R^2) for the values of D_{CO_2} and D_{H_2S} between the Arrhenius, Speedy-Angell and VTF equations.

Table 4.3: Speedy-Angell power equation [279] (Eq. (4.3)) fit parameters (D_0, T_S and m) and coefficient of determinations (R^2) for the values of D_{CO_2} and D_{H_2S} in MEA/water solutions for different MEA concentrations. The values of D_{CO_2} and D_{H_2S} were fitted for a temperature range of 293–353 K.

	MEA concentration / [wt.%]	D_0 / [m^2 s^{-1}]	T_S / [K]	m	R^2
D_{CO_2}	10	1.27×10^{-8}	238.84	1.23	0.991
	20	1.25×10^{-8}	241.44	1.19	0.990
	30	8.63×10^{-9}	220.23	1.80	0.971
	40	4.80×10^{-9}	282.68	0.65	0.978
	50	4.33×10^{-9}	280.31	0.87	0.961
D_{H_2S}	10	4.31×10^{-10}	120.58	3.57	0.985
	20	1.11×10^{-8}	245.76	1.36	0.988
	30	1.08×10^{-8}	258.05	1.26	0.997
	40	3.63×10^{-35}	0.2031	7.94	0.992
	50	6.78×10^{-9}	234.98	2.37	0.993

Table 4.4: Vogel-Tamann-Fulcher (VTF) equation [280] (Eq. (4.4)) fit parameters (α, β, γ) and coefficient of determinations (R^2) for the values of D_{CO_2} and D_{H_2S} in MEA/water solutions for different MEA concentrations. The values of D_{CO_2} and D_{H_2S} were fitted for a temperature range of 293–353 K.

	MEA concentration / [wt.%]	α	β	γ	R^2
D_{CO_2}	10	385.62	161.30	17.08	0.992
	20	432.29	151.94	16.97	0.990
	30	861.74	101.79	16.04	0.971
	40	78.726	254.40	19.28	0.979
	50	133.60	243.50	19.22	0.960
D_{H_2S}	10	3069.55	-93.855	12.35	0.985
	20	367.787	179.11	17.33	0.989
	30	300.548	199.11	17.65	0.997
	40	208598	-2604.8	-50.49	0.992
	50	804.827	150.63	16.46	0.993

4
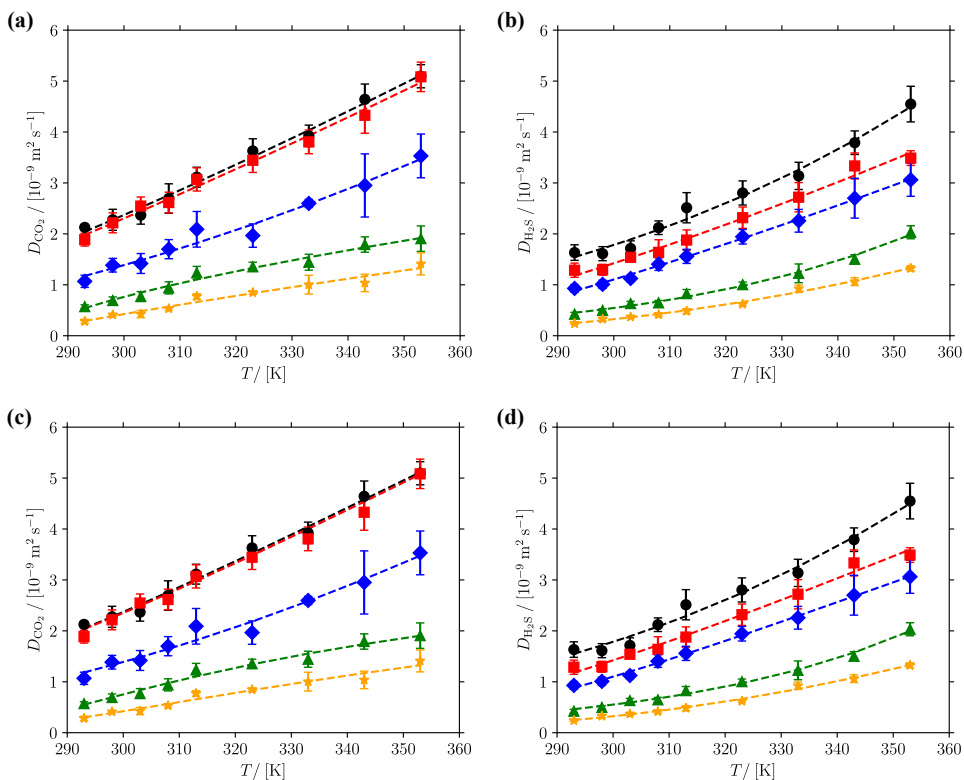
Figure 4.6: Computed values of (a,c) D_{CO_2} and (b,d) D_{H_2S} as a function of temperature and MEA concentration in the solution. The dashed lines represent the fits to (a,b) Speedy-Angell power equation [279] (Eq. (4.3)) and (c,d) VTF equation [280] (Eq. (4.4)). Color code: black: 10 wt.% MDEA/water; red: 20 wt.% MDEA/water; blue: 30 wt.% MDEA/water; green: 40 wt.% MDEA/water; orange: 50 wt.% MDEA/water.

4.3.3. Structure of Aqueous CO_2/H_2S/MEA Mixtures

Fig. 4.7 shows RDFs of CO_2 and H_2S with water and MEA molecules as a function of the MEA concentration in MEA/water solutions. For the MEA concentrations, the peak positions of CO_2-MEA and H_2S-MEA RDFs are similar. However, the results show that the intensity of the first peaks in CO_2-MEA and H_2S-MEA RDFs increases with decreasing MEA concentration in the solution. These results indicate that acid gas-MEA interactions are stronger with respect to the decreasing MEA concentration in the solutions. In the CO_2-water RDF, it can be observed that the first peak gets widened and more intense with increasing MEA concentration in the solution. In the H_2S-water RDF, the first peak positions do not change while the intensities of the first peak show a trend of decreasing with increasing MEA concentration in the solution. These results mainly indicate a weaker interaction between H_2S and water molecules with respect to the increase in the concentration of MEA in the solutions. The second peaks in H_2S-water RDFs slightly change position in the solutions with different MEA concentration. Intensities of the second peak in H_2S-water RDF also change with changing MEA concentration in the solution. The intensity decreases from 10 to 40 wt.% while it increases from 30 to 40 wt.%. Overall, our results show that the MEA concentration in aqueous MEA solutions significantly affects the acid gas-MEA and acid gas-water interactions. The RDFs we computed indicate that both acid gas-MEA interactions and acid gas-water interactions will become weaker with increasing MEA concentration in the solution. With weaker interactions with the surrounding molecules, we would expect that values of D_{CO_2} and D_{H_2S} increase with increasing MEA concentration. However, Fig. 4.4 shows that self-diffusivities decrease significantly with increasing MEA concentration in the solution. This is because of increased viscosity of the solution with increasing MEA concentration [273], i.e. self-diffusivities of every molecule type in the solution decrease (Fig. 4.4 and Fig. 4.5) with increasing MEA concentration.

4
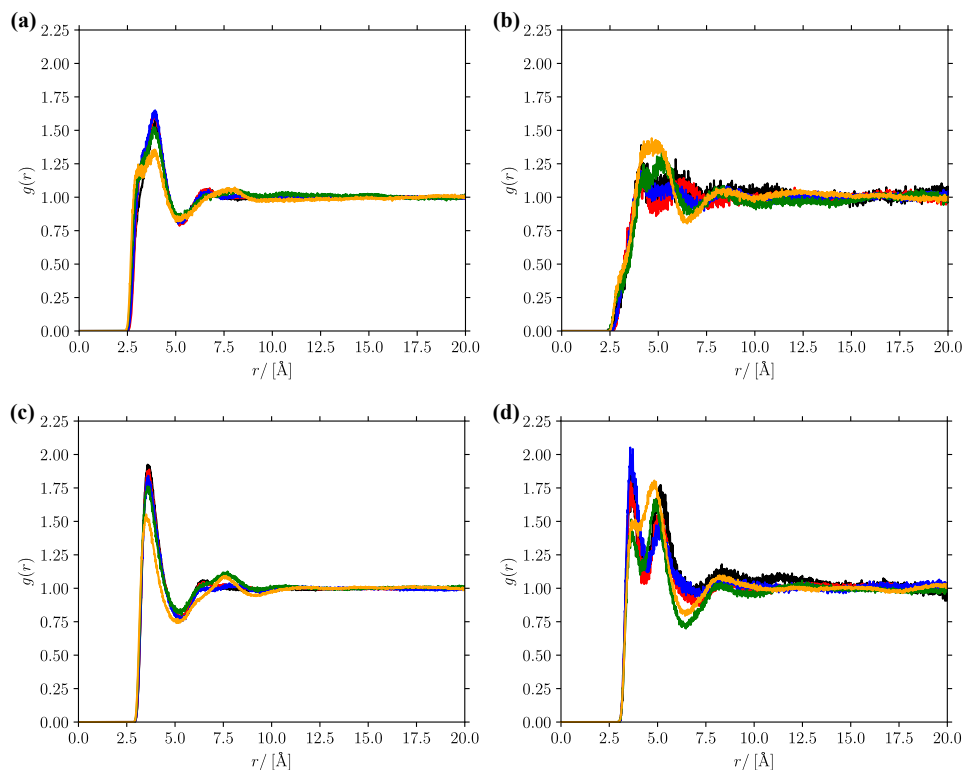
Figure 4.7: Radial distribution functions of (a) CO_2-MEA, (b) CO_2-water, (c) H_2S-MEA, and (d) H_2S-water for 10–50 wt.% MEA/water solutions at 293 K and 1 bar. Color code: black: 10 wt.% MDEA/water; red: 20 wt.% MDEA/water; blue: 30 wt.% MDEA/water; green: 40 wt.% MDEA/water; orange: 50 wt.% MDEA/water.

4.4. Conclusions

We investigated the effect of temperature and MEA concentration on D_{CO_2} and D_{H_2S} in aqueous MEA solutions. For this purpose, we computed densities of pure MEA and 30 wt.% MEA/water solutions as a function of temperature and the scaling factor for point charges of MEA (χ). We showed that scaling factor $\chi = 0.80$ can be used to obtain a good agreement between molecular simulations and experiments from literature. We validated this scaling factor by computing viscosities and self-diffusivities of pure MEA and 30 wt.% MEA/water solutions at 293–353 K. The scaling factor of $\chi = 0.80$ was validated by comparing the computed and experimental viscosities and the self-diffusivities of pure MEA and 30 wt.% MEA/water solutions. We computed the values of D_{CO_2} and D_{H_2S} at infinite dilution, at 293–353 K and 1 bar, for 10–50 wt.% MEA/water solutions. The results showed that the values of D_{CO_2} and D_{H_2S} significantly depends on the MEA concentration in the solution. It is also shown that the values of D_{CO_2} are larger than the values of D_{H_2S} despite molecular weight of CO_2 (44.01 g mol^{-1}) being higher than that of H_2S (34.1 g mol^{-1}).

4

5

Densities, Viscosities, and Diffusivities of Aqueous CO$_2$/H$_2$S/MDEA Mixtures
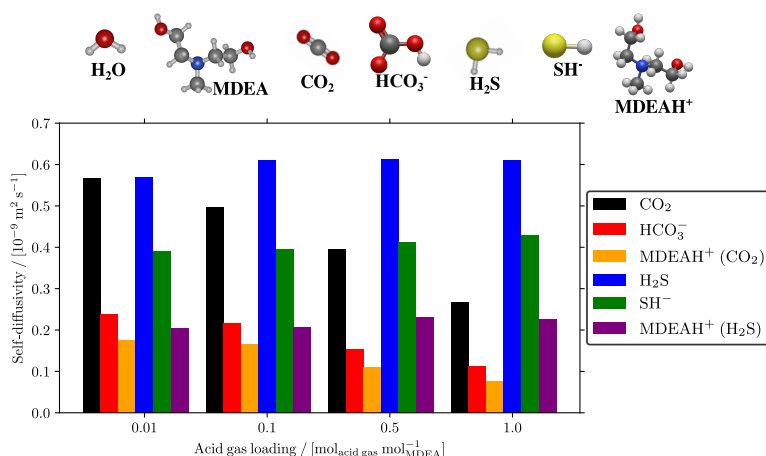
Exploring self-diffusivities of CO$_2$ and H$_2$S in aqueous MDEA solutions reveals significant temperature and concentration dependencies, demonstrating distinct diffusion behavior due to the differences in intermolecular interactions of CO$_2$ and H$_2$S. CO$_2$-loaded solutions show decreased self-diffusivities with increasing CO$_2$ loading, unlike H$_2$S-loaded solutions that remain unaffected by the loading of H$_2$S.

5.1. Introduction

MDEA is a tertiary amine solvent that is primarily used in gas treating applications for the removal of CO_2 and H_2S from natural gas streams [7, 281]. Aqueous solutions of MDEA are selective towards H_2S compared to CO_2 [282, 283]. This makes them ideal to be used in acid gas removal from natural gas streams as the specifications for H_2S concentration in natural gas is much lower than CO_2 concentration. MDEA has a relatively low vapor pressure, and is thermally stable, enhancing the regenerability of the solvent in acid gas removal processes [284–286]. As a tertiary amine, MDEA does not form carbamates with CO_2, therefore has a lower energy requirement in the regeneration (desorption) processes, making it an economically viable option [287, 288]. The versatility and effectiveness of MDEA in acid gas capture, coupled with its favorable thermodynamic properties, makes it a preferred choice in the gas processing industry for achieving strict purity standards in natural gas production and liquefaction.

In this chapter, the self-diffusion coefficients of CO_2 and H_2S in aqueous MDEA solutions are computed for a wide range of temperatures and MDEA concentrations. To validate the accuracy of the interaction potentials for the aqueous solutions of acid gases, we first computed self-diffusion coefficients of CO_2 and H_2S in pure water. Next, we computed the densities of aqueous MDEA solutions for a temperature range of 288–333 K and an MDEA concentration range of 10–50 wt.% MDEA and compared our results with experimental data from literature. By introducing a scaling factor of 0.9 to the point charges of MDEA, we show that we can accurately compute the density of aqueous MDEA solutions. To validate the force field selection for MDEA, we compute viscosities of aqueous MDEA solutions for a temperature range of 288–333 K and an MDEA concentration range of 10–50 wt.% MDEA, and compare the computed viscosities with experimental data from literature. We further validated the force field for MDEA by computing the self-diffusion coefficient of MDEA and comparing it with available data from literature. Next, the self-diffusion coefficients of CO_2 and H_2S in aqueous MDEA solutions are computed for a temperature range of 288–333 K and an MDEA concentration range of 10–50 wt.% MDEA. Using radial distribution functions of the acid gases, water, and MDEA, we investigated the structural changes in the solutions as a function of MDEA concentration. Finally, we investigated the diffusivities of the acid gases and the reaction products from acid gas absorption in aqueous MDEA solutions (bicarbonate (HCO_3^-), bisulfide (SH^-), and protonated MDEA ($MDEAH^+$) ions) as a function of acid gas loading in 50 wt.% MDEA/water solutions at 313 K. The accurate knowledge of the self-diffusivities of the reaction products in acid gas loaded aqueous MDEA solutions is important since this shows how the mass transfer of these species change with changing acid gas loading [289–292]. Our results will be helpful in the optimization of an acid gas removal unit of a plant treating natural gas and biogas, and we anticipate that our study will motivate further research in computing transport properties of acid gases and the reaction products from acid gas absorption in aqueous alkanolamine solutions.

5.2. Simulation Details

All MD simulations in this chapter are performed using LAMMPS (version 2 June 2022) [130] on the DelftBlue supercomputer [293]. The widely used TIP4P/2005 classical force field [94] is used to model water. For CO_2 and H_2S, we use the TraPPE force field [90, 294]. For the interactions between water and CO_2, we used the cross-interaction parameters optimized by Orozco et al. [225]. In our simulations, water, CO_2, and H_2S are considered nearly-rigid by using strong bond-stretching and bond-bending potentials. For water, CO_2, and H_2S molecules, bond-stretching and bond-bending coefficients are set to $1000\,\text{kcal}\,\text{Å}^{-2}$ and $1000\,\text{kcal}$, respectively (see Table C.34 and Table C.35 for the functional forms of these potentials). For the LJ and bonded (bonds, angles, and dihedrals) interactions of MDEA, MDEAH^{+}, HCO$_3$$^{-}$, and SH^{-}, the OPLS-AA force field [88, 89] is utilized. We used two sets of parameters for the N–C–C–O dihedral of MDEA as the parameters for this dihedral are not available in the OPLS-AA force field: (1) the parameters from Cornell et al. [295] and (2) the parameters from Orozco et al. [296]. The difference in the development of the parameters from Cornell et al. [295] and Orozco et al. [296] is that the first one was parameterized for proteins, nucleic acids, and organic molecules, while the latter was parameterized for alkanolamines by adjusting the densities, vapor pressures, excess enthalpies, and viscosities of six different alkanolamines which is more relevant to the system of our interest.

The point charges of MDEA, MDEAH^{+}, HCO$_3$$^{-}$, and SH^{-} molecules are computed using quantum chemical calculations performed with Gaussian09 [78] with the 6-311+G(2d,2p) basis set at the second order Møller-Plesset perturbation (MP2) [70] level of theory, by means of a Natural bond orbital (NBO) analysis [297, 298]. To obtain accurate densities for aqueous MDEA solutions, the point charges of MDEA molecules are scaled by 0.9 after comparison with experimental data from literature, in line with the previous work on the effect of the scaled charges on transport properties of molecules/ions [194, 270, 299–301]. Note that the charge scaling factor validated for aqueous alkanolamine solutions can be used to obtain accurate densities and viscosities of pure alkanolamine solutions as we showed in our previous study [5]. To obtain accurate densities and viscosities for CO_2/H_2S-loaded aqueous MDEA solutions, we scaled the point charges of the reaction products from CO_2 (MDEAH^{+} and HCO$_3$$^{-}$) and H_2S (MDEAH^{+} and SH^{-}) absorption by 0.90 and 0.75, respectively. The point charges of water, CO_2, and H_2S are not scaled. For this purpose, we use a scaling factor χ_j^i, where i shows the parameter that is scaled and j represents the specific interaction or molecule for the scaling. For example, a scaling factor of $\chi_{\text{MDEA}}^q = 0.9$ means that the point charges of MDEA molecule were scaled (multiplied) by 0.9. Note that there are more fundamental methods to adjust the point charges (and therefore the dipole moment) of the molecules with point charges computed by quantum chemistry such as the Quantum Mechanical Bespoke approach [302], the Polarization-Consistent Approach [302], and the Self-Consistent Electrostatic Embedding approach [303]. However, in this chapter, we adopted scaling the point charges of the molecules as it has shown to produce accurate self-diffusivities [148, 162, 301, 304–306] and to be consistent with

Table 5.1: Number of MDEA and water molecules in MD simulations for different concentrations of MDEA in aqueous MDEA solutions. The average simulation box sizes are computed at 313 K and 1 bar.

MDEA concentration / [wt.%]	Number of MDEA molecules	Number of water molecules	Average box size / [Å]
0	0	700	27.6
10	12	688	28.4
20	25	675	29.4
30	43	657	30.1
40	64	636	31.5
50	92	608	32.6

5

our previous work [301]. All force field parameters are tabulated in Appendix C (Appendices C.1.3, C.3, C.4.2, C.5.2, C.6, C.8.3 and C.9.3).

The LJ interactions of unlike atom types are computed using the Lorentz-Berthelot mixing rules [82] unless specified otherwise. In all MD simulations, the LJ interactions are truncated at 12 Å and analytic tail corrections [83] are applied to energies and pressures. Electrostatic interactions are computed using the PPPM method with a relative precision of 10^{-5}. The 1-4 LJ and electrostatic intramolecular interactions are scaled by a factor of 0.5 [88, 89].

The initial configurations for MD simulations were generated by randomly inserting molecules in a cubic simulation box with a size of 45–55 Å, depending on the MDEA concentration in the solution. The number of molecules of water and MDEA for all systems studied are shown in Table 5.1. The composition of the simulation box for the acid gas-loaded 50 wt.% MDEA/water solutions at 313 K is computed using CASpy [5], an open-source software for computing speciation at reaction equilibrium that we recently developed (Chapter 3). To this purpose, we followed the procedure explained in ref. [5] and computed the composition in CO_2-loaded 50 wt.% MDEA/water solutions and H_2S-loaded 50 wt.% MDEA/water solutions using the correlations for experimental reaction equilibrium constants reported by Plakia et al. [212]. The compositions of the simulation box of of CO_2-loaded 50 wt.% MDEA/water solution and H_2S-loaded 50 wt.% MDEA/water solutions at 313 K are reported in Table 5.2 and Table 5.3, respectively.

To compute the self-diffusivities of CO_2 (D_{CO_2}) or H_2S (D_{H_2S}), two solute molecules are used to improve statistics. Although two molecules of free CO_2 or H_2S are higher than the solubility of CO_2 or H_2S in the aqueous MDEA solutions [5], we did not encounter any agglomeration of these species in the time period of our MD simulations. Note that the computed self-diffusion coefficients of the acid gases are practically equal to transport diffusion coefficients since CO_2 and H_2S are at the infinite dilution limit [307]. We start the MD simulations with an equilibration stage of 0.5 ns with a timestep of 1 fs in the *NPT* ensemble. The Nosé-Hoover thermostat (with a coupling constant of 10 fs) and barostat (with a coupling constant of 1000 fs)

Table 5.2: Number of MDEA, HCO_3^-, $MDEAH^+$, and water molecules in CO_2-loaded 50 wt.% MDEA/water solutions at 313 K as a function of CO_2 loading in the solution. To compute the self-diffusivities of CO_2, we also have two molecules of CO_2 in the solution. In these simulations, the point charges of MDEA are scaled by 0.9, and the point charges of $MDEAH^+$ and HCO_3^- are scaled by either 0.9 or 0.75. The point charges of CO_2 and water are not scaled. The average simulation box sizes are computed at 313 K and 1 bar.

CO_2 loading / [mol_{CO_2} mol_{MDEA}^{-1}]	0.01	0.1	0.5	1.0
N_{MDEA} (molar mass = 119.163 g mol^{-1})	150	205	153	29
$N_{HCO_3^-}$ (molar mass = 61.02 g mol^{-1})	1	21	148	272
N_{MDEAH^+} (molar mass = 120.17 g mol^{-1})	1	21	148	272
N_{H_2O} (molar mass = 18.02 g mol^{-1})	1000	1500	2000	2000
Average box size / [Å]	38.5	44.3	49.8	50.9

Table 5.3: Number of MDEA, SH^-, $MDEAH^+$, and water molecules in H_2S-loaded 50 wt.% MDEA/water solutions at 313 K as a function of H_2S loading in the solution. In these simulations, the point charges of MDEA are scaled by 0.9, and the point charges of $MDEAH^+$ and SH^- are scaled by either 0.9 or 0.75. To compute the self-diffusivities of H_2S, we also have two molecules of H_2S in the solution. The point charges of H_2S and water are not scaled. The average simulation box sizes are computed at 313 K and 1 bar.

H_2S loading / [mol_{H_2S} mol_{MDEA}^{-1}]	0.01	0.1	0.5	1.0
N_{MDEA} (molar mass = 119.163 g mol^{-1})	224	203	156	48
N_{SH^-} (molar mass = 33.07 g mol^{-1})	2	23	146	254
N_{MDEAH^+} (molar mass = 120.17 g mol^{-1})	2	23	146	254
N_{H_2O} (molar mass = 18.02 g mol^{-1})	1500	1500	2000	2000
Average box size / [Å]	44.0	44.2	49.3	49.9

are used to maintain constant temperature and pressure, respectively. Consecutively, another equilibration stage of 1 ns with a timestep of 1 fs is performed in the *NVT* ensemble. Finally, production runs of 20 ns are performed in the *NVE* ensemble to compute all properties of interest.

The OCTP plugin [257] in LAMMPS is used to compute viscosities, self-diffusivities, and center-of-mass radial distribution functions (RDFs). The OCTP plugin [257] computes transport properties with the order-*n* [82, 308] algorithm using Einstein relations. The center-of-mass RDFs computed by the OCTP plugin are corrected for finite-size effects [257]. For details about these computations the reader is referred to Ref. [257]. In this chapter, all reported self-diffusivities are corrected for finite-size effects using Eq. (4.1) [258–261]. Note that the computed viscosities do not show any finite-size effects [258, 259, 309]. The standard deviations for densities, viscosities, and self-diffusion coefficients are computed from seven independent simulations each one starting from a different initial configuration. The average

and the uncertainties of the RDFs shown in this chapter are computed from five independent simulations. To quantify the agreement between the computed values (of density, viscosity, and diffusivity) and experimental values from literature, the coefficient of determination (R^2) scores are computed using:

$$R^2 = 1 - \frac{\sum_{i=1}^{n}(y_{i,\text{exp}} - y_{i,\text{sim}})^2}{\sum_{i=1}^{n}(y_{i,\text{exp}} - \bar{y}_{\text{exp}})^2} \tag{5.1}$$

where n is the number of data points, $y_{i,\text{exp}}$ is the experimental value from literature, $y_{i,\text{sim}}$ is the computed value, and $\bar{y}_{\text{exp}}$ is the arithmetic average of the experimental values from literature. An R^2 score of 1 means that the agreement between simulations and experiments is perfect.

5.3. Results and Discussion

5.3.1. Densities and Viscosities of Aqueous MDEA Solutions

To validate the force fields for water, CO_2, and H_2S, we first compute the values of D_{CO_2} and D_{H_2S} in pure water. Fig. 5.1 shows the comparison between the computed and experimental [310, 311] self-diffusivities D_{CO_2} and D_{H_2S} in pure water as a function of temperature. Our results show that the computed values of D_{CO_2} and D_{H_2S} in pure water are in excellent agreement with the experimental results from literature [310, 311] as the maximum deviations are 12% and 10% for D_{CO_2} and D_{H_2S}, respectively. This shows that the force fields chosen for CO_2, H_2S, and water accurately describe the interactions in aqueous solutions of CO_2 and H_2S.

Therefore, we proceeded with investigating the accuracy of the OPLS-AA force field [88, 89] (with point charges computed by quantum chemistry calculations) for MDEA. We used two different sets of parameters for N–C–C–O dihedrals of MDEA molecule as the parameters for this dihedral are not available in the OPLS-AA force field: (1) from Cornell et al. [295], and (2) from Orozco et al. [296]. The main difference between these two sets of parameters for N–C–C–O dihedral is that the parameters from Cornell et al. [295] was developed for proteins, nucleic acids, and organic molecules, while the parameters from Orozco et al. [296] was developed for alkanolamines. Note that the dihedral reported by Orozco et al. [296] is ca. 2.5 times stiffer than the dihedral reported by Cornell et al. [295] (Fig. 5.2). We computed the densities of aqueous MDEA solutions as a function of temperature and MDEA concentration in the solution using $\chi_{\text{MDEA}}^{q} = 1.0$. Fig. 5.3 shows the comparison between the computed and experimental [310] densities of aqueous MDEA solutions. Our results show that the computed densities are significantly overestimated and the deviations between the computed and experimental densities increase with increasing MDEA concentration in the solution. As it has been shown that the point charges computed using quantum chemical calculations typically overestimate electrostatic interactions and the scaled point charges provide a better representation of the potential energy surface of the molecules/ions [190, 263, 266, 267, 269, 270, 312], we scaled the point charges of MDEA by 0.9 ($\chi_{\text{MDEA}}^{q} = 0.9$).

(a)

(b)
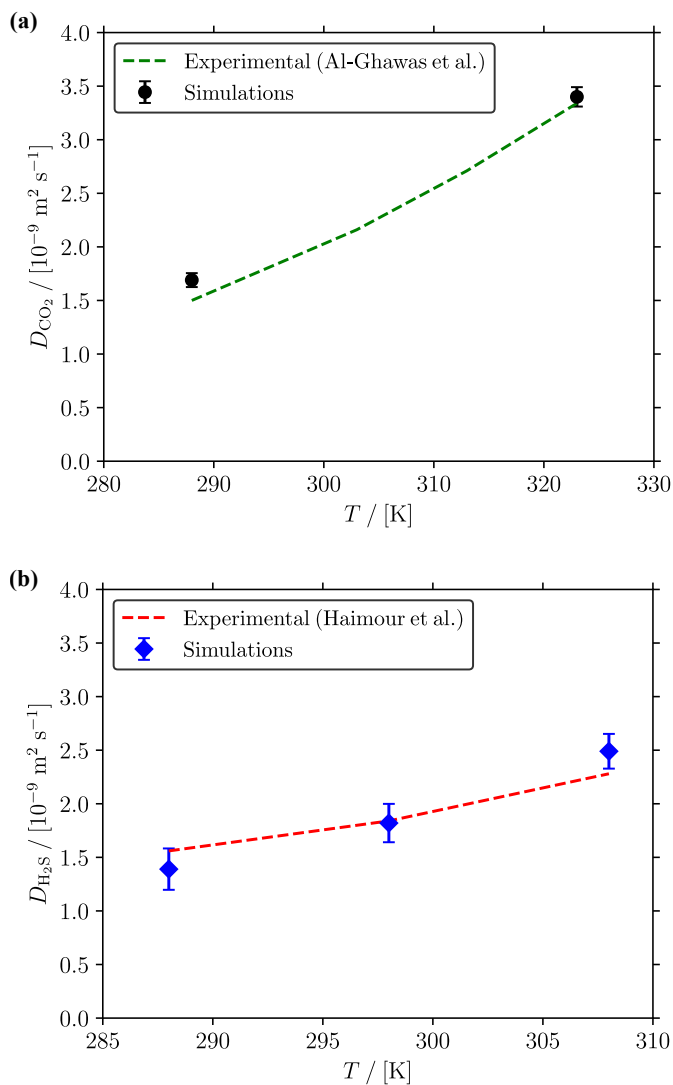
Figure 5.1: Computed and experimental [310, 311] values of (a) D_{CO_2} and (b) D_{H_2S} in pure water as a function of temperature at 1 bar. The self-diffusivities are corrected for finite-size effects using Eq. (4.1). For CO_2 and H_2S, TraPPE [90, 294] force field (Appendices C.3 and C.4.2) is used while the TIP4P/2005 [94] force field (Appendix C.1.3) is used for water.
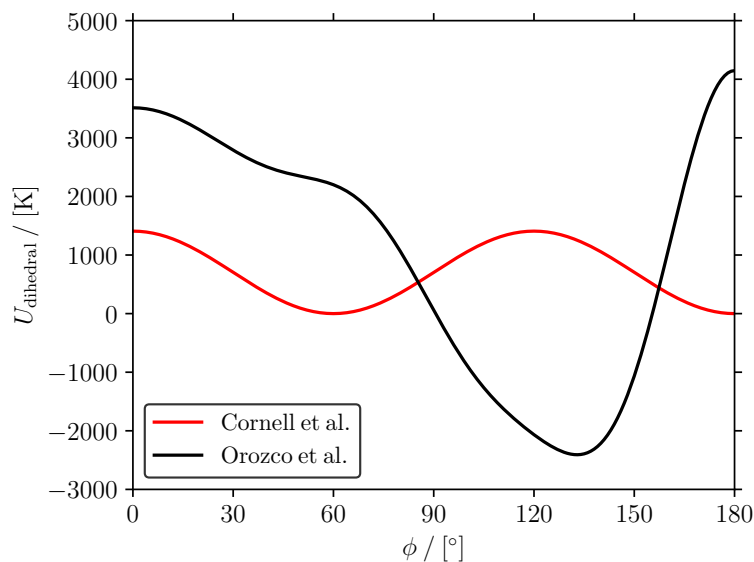
Figure 5.2: Dihedral potential energy as a function of dihedral angle for N–C–C–O dihedral in MDEA. The red curve represent the dihedral potential from Cornell et al. [295] (Table C.36) while the black curve represent the dihedral potential from Orozco et al. [296] (Table C.37).
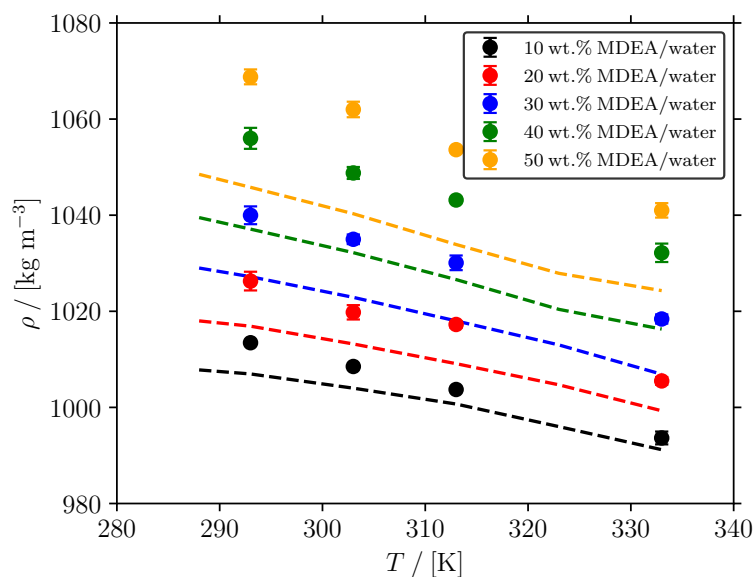
Figure 5.3: Computed and experimental [310] densities of aqueous MDEA solutions as a function of temperature at 1 bar. Note that the point charges of MDEA are not scaled, i.e. $\chi^q_{\mathrm{MDEA}} = 1$ and the parameters from Cornell et al. [295] are used for the N–C–C–O dihedral in MDEA (Table C.36). Dashed lines represent experimental results from Al-Ghawas et al. [310].

5

Fig. 5.4 shows the computed and experimental densities of aqueous MDEA solutions (with $\chi^q_{\text{MDEA}} = 0.9$) for the temperature range 288–333 K at 1 bar. Our results show that the computed densities using both sets of parameters for the N–C–C–O dihedral agree very well with the experimental densities from literature [310] with a maximum deviation of 1.3%. The deviation between the experimental data and the computed densities using the parameters from Cornell et al. [295] is 0.1–0.5% (Fig. 5.4(a)), while the respective deviation is between 0.2–1.3% when the parameters from Orozco et al. [296] are used (Fig. 5.4(b)). The deviations between simulated and experimental densities from literature for both dihedral parameters are larger than the standard errors as the standard errors for calculated values of densities are ca. 0.05%. For the dihedral parameters from Orozco et al. [296], the difference between the computed and experimental densities increases with increasing MDEA concentration in the solution. As the densities computed using both set of parameters are in excellent agreement (with a maximum deviation of 1.3%) with experimental data from literature [310], we computed viscosities of aqueous MDEA solutions and compared them with available data from literature.

Fig. 5.4(c) and Fig. 5.4(d) show the comparison between the computed (using the same two dihedral parameters discussed earlier) and experimental [310] viscosities of aqueous MDEA solutions for an MDEA concentration range of 10–50 wt.% MDEA and a temperature range of 288–333 K. Our results show that the viscosities computed using both set of parameters for N–C–C–O dihedral underestimate experimental [310] viscosities of aqueous MDEA solutions. The viscosities computed using the parameters from Orozco et al. [296] underestimate experimental results [310] (average absolute deviation of 8.4%) less as the density of aqueous MDEA solutions are higher (due to the 2.5 times stiffer N–C–C–O dihedral, see Fig. 5.2) compared to the ones obtained using the parameters from Cornell et al. [295] (average absolute deviation of 13.3%). Note that the average absolute deviation for the viscosities computed using the dihedral parameters from Cornell et al. [295] are larger than the average standard error of 8.3% while the average standard error for viscosities computed using the dihedral parameters from Orozco et al. [296] (8.7%) is slightly higher than the average absolute deviation between simulations and experimental values from literature. To quantify the agreement between the simulations and experimental values from literature, we also computed the R^2 scores. Our findings show that the viscosities computed using parameters from Cornell et al. [295] for the N–C–C–O dihedral of MDEA and experimental results [310] have an R^2 of 0.88, while the R^2 score of the viscosities computed using N–C–C–O dihedral parameters optimized by Orozco et al. [296] and experimental results [310] is 0.98. Indicatively, the viscosities computed using the N–C–C–O dihedral parameters from Cornell et al. [295] are between 0.6–1.4 mPa s and 2.4–10.7 mPa s at 288–333 K for 10 wt.% MDEA/water and 50 wt.% MDEA/water solutions, respectively. The viscosities computed using the N–C–C–O parameters from Orozco et al. [296] vary between 0.6–1.7 mPa s and 2.7–13.6 mPa s at 288 − 333 K for 10 wt.% MDEA/water and 50 wt.% MDEA/water solutions, respectively. For the same temperature range, experimental viscosities [310] are between 0.6–1.7 mPa s and 2.7–14.9 mPa s for 10 wt.% MDEA/water and 50 wt.%
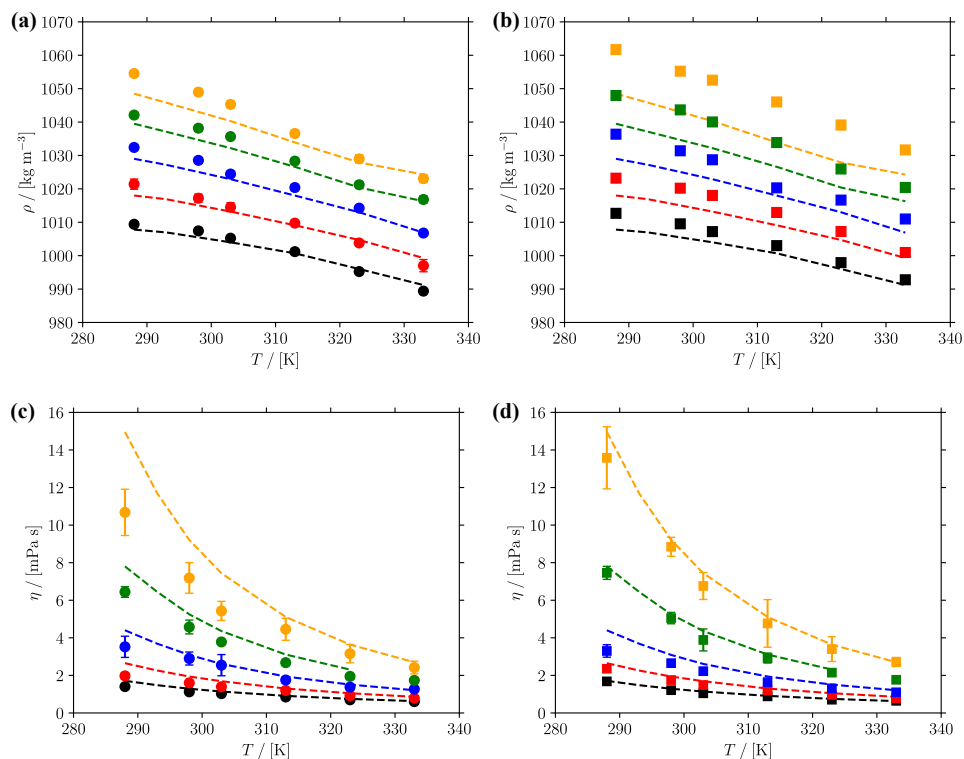
Figure 5.4: Computed and experimental [310] (a,b) densities and (c,d) viscosities of aqueous MDEA solutions as a function of temperature at 1 bar. (a,c) show the densities and viscosities computed using the parameters from Cornell et al. [295] for N–C–C–O dihedral of MDEA (Table C.36); (b,d) show the densities and viscosities computed using the N–C–C–O dihedral parameters from Orozco et al. [296] (Table C.37). Note that the point charges of MDEA are scaled with 0.9, i.e. $\chi^q_{\mathrm{MDEA}} = 0.9$. Dashed lines represent experimental results from Al-Ghawas et al. [310]. Color code: black: 10 wt.% MDEA/water; red: 20 wt.% MDEA/water; blue: 30 wt.% MDEA/water; green: 40 wt.% MDEA/water; orange: 50 wt.% MDEA/water.

MDEA/water solutions, respectively. Both the R^2 scores and deviations from experiments show that the simulations agree well with experiments from literature when the parameters from Orozco et al. [296] for N–C–C–O dihedral are used to predict viscosities of aqueous MDEA solutions.

5.3.2. Diffusivities of MDEA, CO_2, and H_2S in Aqueous MDEA Solutions

We further investigate the transport properties of aqueous MDEA solutions by computing the self-diffusion coefficients of MDEA (D_{MDEA}) in the solution. Fig. 5.5 shows the values of D_{MDEA} computed using the two different sets of parameters for N–C–C–O dihedral for MDEA concentrations in the range of 10-50 wt.%, and the comparison with experimental data from Snijder et al. [313] and MD simulation

data from Yiannourakou et al. [7] (with the PCFF+ force field reported in ref [314]) for 30 wt.% MDEA/water solutions. As expected, our data show that D_{MDEA} decreases with increasing MDEA concentration in the solution (Fig. 5.5). The values of D_{MDEA} in the 10 wt.% MDEA/water solution is ca. 3–9 and 3–6 times higher compared to the 50 wt.% MDEA/water solution for the values computed using the parameters from Cornell et al. [295] and Orozco et al. [296], respectively, for the temperature range 288–333 K. Fig. 5.5(a) shows that the values of D_{MDEA} computed using the parameters from Cornell et al. [295] for the N–C–C–O dihedral are in agreement with the experimental results from Snijder et al. [313] and computational results from Yiannourakou et al. [7] (with an R^2 score of 0.80) for 30 wt.% MDEA/water solutions except for the data point at 333 K. The value of D_{MDEA} computed using the parameters from Cornell et al. [295] for N–C–C–O dihedral is $7.94 \times 10^{-10}\,m^2\,s^{-1}$ at 333 K while the experimental value for the same temperature is $9.2 \times 10^{-10}\,m^2\,s^{-1}$. As shown in Fig. 5.5(b), the values of D_{MDEA} computed using the parameters from Orozco et al. [296] agree very well with the experimental and MD data from literature [7, 313] ($R^2 = 0.94$). The values of D_{MDEA} computed using the optimized N–C–C–O dihedral parameters from Orozco et al. [296] are between 3.92×10^{-10}–$8.89 \times 10^{-10}\,m^2\,s^{-1}$ in 30 wt.% MDEA/water solution at 303–333 K, while the experimental values [313] for the same temperature range and solution vary between 4.6×10^{-10}–$9.2 \times 10^{-10}\,m^2\,s^{-1}$. This shows that the N–C–C–O dihedral parameters from Orozco et al. [296] perform better than the ones by Cornell et al. [295]. Based on the force field validation for the densities (Fig. 5.4(a,b)), viscosities (Fig. 5.4(c,d)) and D_{MDEA}, we hereafter adopt the parameters by Orozco et al. [296] for the N–C–C–O dihedral MDEA to compute the diffusivities of the acid gases in aqueous MDEA solutions.

Interestingly, MDEA diffuses slightly faster in 30 wt.% MDEA/water solutions at 333 K ($D_{MDEA} = 8.89 \times 10^{-10}\,m^2\,s^{-1}$) compared to MEA in 30 wt.% MEA/water solutions ($D_{MEA} = 7.54 \times 10^{-10}\,m^2\,s^{-1}$) from our previous study [301] despite the similar viscosities of both solutions (1.1 mPa s for 30 wt.% MDEA/water solutions while 1.2 mPa s for 30 wt.% MEA/water solutions [301] at 333 K). Although one would expect the opposite since MEA is smaller and lighter than MDEA (molar masses of MDEA and MEA are 119.163 g mol^{-1} and 61.08 g mol^{-1}, respectively), comparing solutions with same alkanolamine weight percentages may be misleading as the mole fractions of these components in these solutions are quite different (mole fraction of MDEA (X_{MDEA}) = 0.06 in 30 wt.% MDEA/water solution while mole fraction of MEA (X_{MEA}) = 0.11 in 30 wt.% MEA/water solution). Fig. 5.6 compares D_{MDEA} and D_{MEA} [301] for similar mole fractions of alkanolamine ($X_{MDEA} = 0.13$ in 50 wt.% MDEA/water vs. $X_{MEA} = 0.11$ in 30 wt.% MEA/water solution) in the solution as a function of temperature. Compared to a similar mole fraction of MDEA in MDEA/water solutions, MEA molecules diffuse ca. 2–4 times faster in 30 wt.% MEA/water solutions than MDEA molecules in 50 wt.% MDEA/water solutions for a temperature range of 288–333 K.
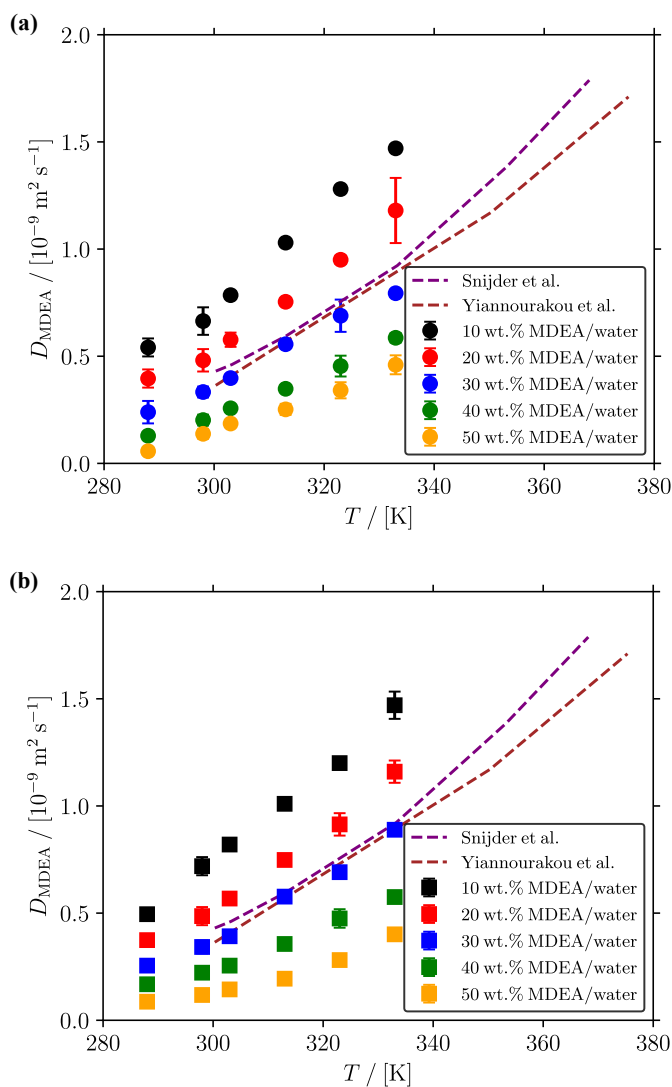
Figure 5.5: Computed and experimental [7, 313] self-diffusivities D_{MDEA} in aqueous MDEA solutions as a function of temperature at 1 bar. (a) shows the values of D_{MDEA} computed using the parameters from Cornell et al. [295] for N–C–C–O dihedral of MDEA while (b) shows the values of D_{MDEA} computed using the N–C–C–O dihedral from Orozco et al. [296]. Note that the point charges of MDEA are scaled by 0.9, i.e. $\chi^{q}_{\mathrm{MDEA}} = 0.9$, and all self-diffusivities are corrected for finite-size effects using Eq. (4.1). Dashed lines represent experimental results in 30 wt.% MDEA/water solutions from Snijder et al. [313] (purple) and simulation results from Yiannourakou et al. [7] (brown).
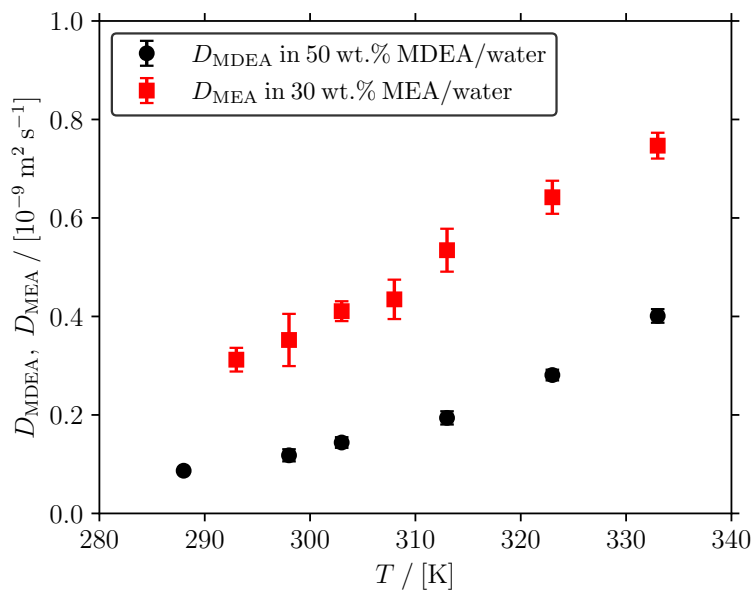
Figure 5.6: Comparison between the computed values of D_{MDEA} in 50 wt% MDEA/water solution and D_{MEA} in 30 wt.% MEA/water solution [5] as a function of temperature at 1 bar. The self-diffusivities are corrected for finite-size effects using Eq. (4.1). The point charges of MDEA and MEA [5] are scaled by 0.9 and 0.8, respectively. We compare the values of D_{MDEA} in a 50 wt% MDEA/water solution and the values of D_{MEA} in a 30 wt.% MEA/water solution because MDEA and MEA have similar mole fractions in these solutions ($X_{\mathrm{MDEA}} = 0.13$ in 50 wt.% MDEA/water solutions and $X_{\mathrm{MEA}} = 0.11$ in 30 wt.% MEA/water solutions).

We compute the values of D_{CO_2} and D_{H_2S} as a function of MDEA concentration in the solution and temperature using MD simulations. Fig. 5.7 shows the simulation results and comparisons with the available experimental data from literature [310]. To the best of our knowledge, no experimental or modeling data on the diffusivity of D_{H_2S} in aqueous MDEA solutions have been reported. Using the CO_2/N_2O analogy [55, 56] (by measuring the diffusivity of N_2O), Al-Ghawas et al. [310] estimated the values of D_{CO_2} to be in the ranges 1.2×10^{-9}–3.1×10^{-9} $m^2\,s^{-1}$ and 3.8×10^{-10}–1.7×10^{-9} $m^2\,s^{-1}$ in 10 wt.% MDEA/water and 50 wt.% MDEA/water solutions, respectively, at temperatures ranging from 288 to 323 K. For the same temperature range, we computed D_{CO_2} to be 1.29×10^{-9}–2.87×10^{-9} $m^2\,s^{-1}$ and 3.54×10^{-10}–9.50×10^{-10} $m^2\,s^{-1}$ in 10 wt.% MDEA/water and 50 wt.% MDEA/water solutions, respectively. This clearly shows that our data are in agreement with the values of D_{CO_2} estimated using CO_2/N_2O analogy [310]. Note that Chen et al. [56] investigated the validity of CO_2/N_2O analogy by computing the Henry coefficients and self-diffusivities of CO_2 and N_2O in water, ethanol, *n*-heptane, and aqueous MEA solutions, and concluded that the assumption holds for 30 wt.% MEA/water solutions at 303 K. Also, Kohns et al. [57] stated that the analogy is valid for CO_2 in pure water and ethanol, while it is not valid for CO_2 in binary mixtures of water and ethanol. We also compare the computed values of D_{CO_2} and D_{H_2S} in aqueous MDEA solutions with the ones in aqueous MEA solutions from our previous study [301]. Fig. 5.8 shows the comparison of D_{CO_2} and D_{H_2S} in aqueous MDEA and aqueous MEA solutions. When solutions with similar mole fractions of MDEA and MEA are compared, CO_2 diffuses ca. 1–3 times slower in aqueous MDEA solutions than in aqueous MEA solutions. For example, we computed D_{CO_2} as 5.19×10^{-10}–9.50×10^{-10} $m^2\,s^{-1}$ at 298–323 K in 50 wt.% MDEA/water solution while the respective value in 30 wt.% MEA/water solution at the same temperature range is 1.38×10^{-9}–2.00×10^{-9} $m^2\,s^{-1}$. This is expected since the viscosity of 50 wt.% MDEA/water solution is ca. 3 times higher than the viscosity of 30 wt.% MEA/water solution at 298–323 K and the self-diffusivities of solutes depend highly on the viscosity of the solution. The comparison of the self-diffusivities D_{H_2S} in MEA/water and MDEA/water solutions (Fig. 5.8(b)) shows a similar difference between the two solutions, i.e. H_2S diffuses ca. 2 times faster in 30 wt.% MEA/water solutions than in 50 wt.% MDEA/water solutions.
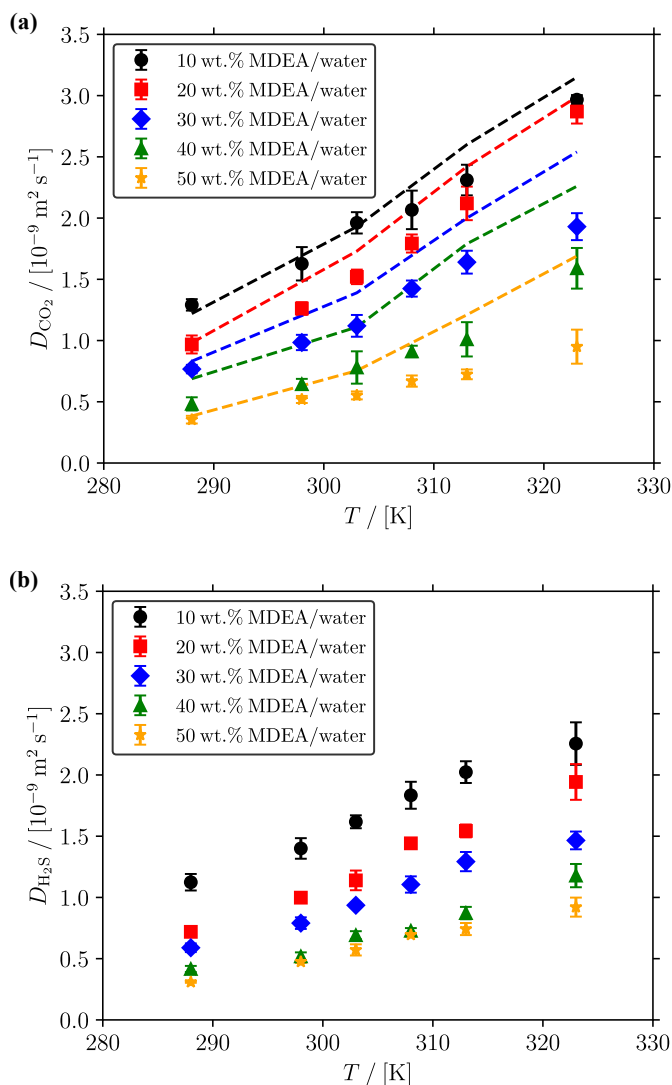
Figure 5.7: Computed and experimental [310] (a) self-diffusivities of CO_2 and (b) computed self-diffusivities of H_2S in aqueous MDEA solutions as a function of temperature and MDEA concentration at 1 bar. Note that the point charges of MDEA are scaled with 0.9, i.e. $\chi^q_{MDEA} = 0.9$, and all self-diffusivities are corrected for finite-size effects using Eq. (4.1). The TraPPE force field [90, 294] was used for CO_2 and H_2S (Appendices C.3 and C.4.2). In (a), dashed lines represent experimental results from Al-Ghawas et al. [310]. The color code for dashed lines follows that of symbols.

5
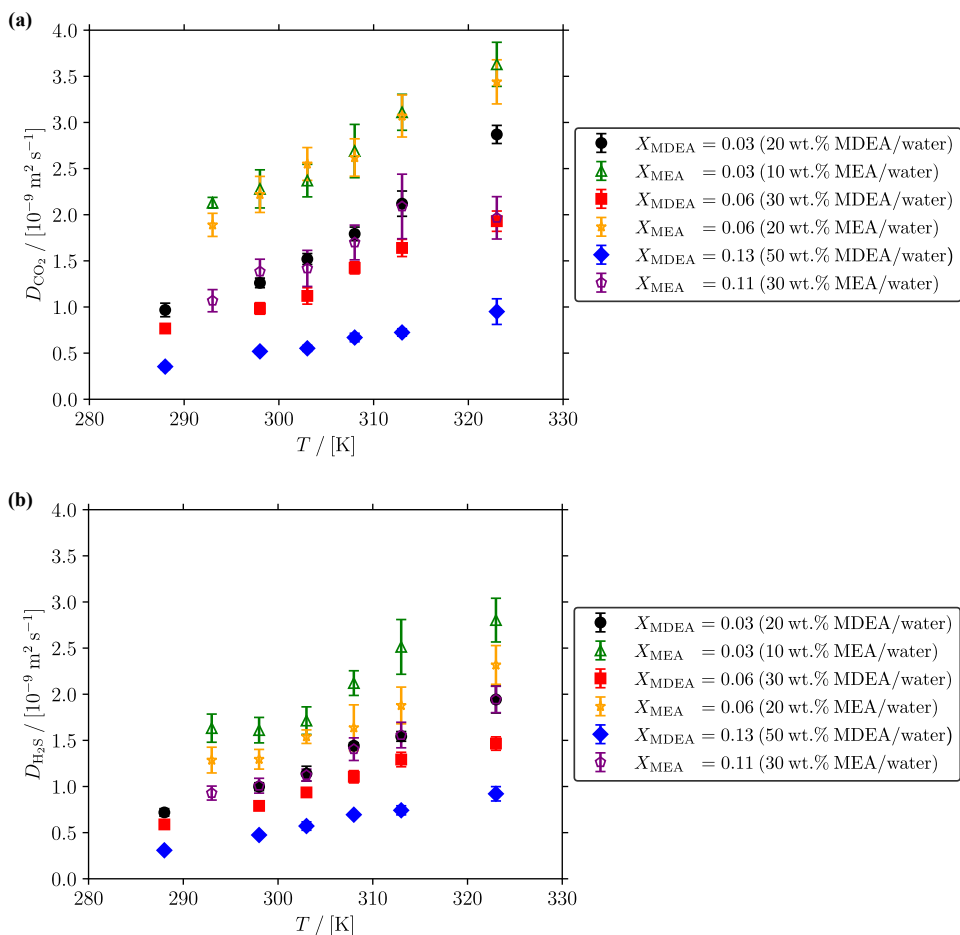
Figure 5.8: Comparison of (a) self-diffusities of CO_2 D_{CO_2} and (b) the self-diffusities of H_2S D_{H_2S} in aqueous MDEA (this study) and MEA [5] solutions as a function of temperature at 1 bar. The self-diffusivities are corrected for finite-size effects using Eq. (4.1). The point charges of MDEA and MEA [5] are scaled by 0.9 and 0.8, respectively. Note that due to the difference in the molar weights of MDEA and MEA, different weight percentages of MDEA and MEA can correspond to a similar molar fraction. For example, $X_{MDEA} = 0.03$ in 20 wt.% MDEA/water solutions while $X_{MEA} = 0.03$ in 10 wt.% MDEA/water solutions.

As shown in Fig. 5.7, the self-diffusivities D_{CO_2} in aqueous MDEA solutions are slightly larger than the self-diffusivities D_{H_2S} at the same conditions. Note that the differences between the computed values of D_{CO_2} and D_{H_2S} are statistically important as the differences are larger than the error bars. H_2S diffuses slower in aqueous MDEA solutions despite its lower molar mass ($M_{H_2S} = 34.1\,g\,mol^{-1}$ vs. $M_{CO_2} = 44.01\,g\,mol^{-1}$) compared to CO_2 because H_2S can form hydrogen bonds with both water and MDEA molecules [278, 301, 315, 316] and it is a more spherical molecule than CO_2. The values of both D_{CO_2} and D_{H_2S} decrease with increasing MDEA concentration in the solution. For example, both CO_2 and H_2S diffuse ca. 3.5 times faster in 10 wt.% MDEA/water solutions than in 50 wt.% MDEA/water solutions. Our results also show that the temperature dependency of D_{CO_2} and D_{H_2S} changes significantly with MDEA concentration in the solution. The slope of D_{CO_2} (D_{H_2S}) as a function of temperature is 2.6 (1.8) times higher in 10 wt.% MDEA/water solution than in the 50 wt.% MDEA/water solution. The same trend can also be seen in the values of D_{CO_2} estimated by Al-Ghawas et al. [310] using the CO_2/N_2O analogy.

The temperature dependence of the self-diffusion coefficients can be described with an Arrhenius equation [5] (Eq. (4.2)), the Speedy-Angell power equation [279] (Eq. (4.3)), or the VTF equation [280] (Eq. (4.4)). We fit the values of D_{CO_2} and D_{H_2S} to an Arrhenius equation [5] (Eq. (4.2)), the Speedy-Angell power equation [279] (Eq. (4.3)), and the VTF equation [280] (Eq. (4.4)) for an MDEA concentration range of $10 - 50$ wt.% MDEA and a temperature range of 288–323 K. The functional forms of these equations are shown in the Supplementary Material. Tables 5.4 to 5.6 show Arrhenius fit, Speedy-Angell, and VTF equation parameters for D_{CO_2} and D_{H_2S}. The activation energies for diffusion (E_A) for both CO_2 and H_2S increase with MDEA concentration in the solution which also indicates slower diffusion of CO_2 and H_2S with increasing MDEA concentration (see Table 5.4).

5.3.3. Structure of Aqueous $CO_2/H_2S/MDEA$ Mixtures

In Fig. 5.9, the center-of-mass RDFs of CO_2 and H_2S with water and MDEA are shown at 313 K and 1 bar. Our findings show that as the MDEA concentration in the solution increases, the first and second peaks in both CO_2-MDEA and H_2S-MDEA RDFs shift to lower values of intermolecular distance, indicating stronger interactions between acid gases and MDEA. However, the intensities of the first peaks in H_2S-MDEA RDFs are higher than those of CO_2-MDEA RDFs, indicating stronger H_2S-MDEA interactions than CO_2-MDEA interactions. The same trend is observed for the CO_2-water and H_2S-water RDFs, where the position of the first and second peaks shift to lower values with increasing MDEA concentration, and the intensities of the first peaks in H_2S-water RDFs are higher than those of CO_2-MDEA RDFs. Overall, these findings suggest that H_2S has stronger interactions with the surrounding molecules (MDEA and water) than CO_2. This is probably the reason why H_2S diffuses slower than CO_2 in aqueous MDEA solutions (Fig. 5.7).

Table 5.4: Arrhenius (Eq. (4.2)) fit parameters (pre-exponential factors (D_0) and activation energies (E_A)) and coefficients of determinations (R^2) for the values of D_{CO_2} and D_{H_2S} in aqueous MDEA solutions with different MDEA concentrations. The values of D_{CO_2} and D_{H_2S} were fitted for a temperature range of 288–323 K.

	MDEA concentration / [wt.%]	D_0 / [m^2 s^{-1}]	E_A / [kJ mol^{-1}]	R^2
D_{CO_2}	10	2.71×10^{-6}	18.33	0.991
	20	3.51×10^{-5}	25.28	0.997
	30	4.97×10^{-6}	21.02	0.975
	40	5.78×10^{-5}	28.28	0.981
	50	2.25×10^{-6}	20.87	0.991
D_{H_2S}	10	6.79×10^{-7}	15.24	0.976
	20	5.59×10^{-6}	21.34	0.986
	30	2.34×10^{-6}	19.70	0.972
	40	8.82×10^{-6}	23.98	0.988
	50	3.04×10^{-6}	21.68	0.973

5.3.4. Densities, Viscosities, and Diffusivities of Acid Gas-Loaded Aqueous MDEA Solutions

The densities, viscosities, and self-diffusivities of the reaction products are of primary importance in the optimization of the mass transfer in acid gas loaded aqueous MDEA solutions [289–292]. Here, we investigate the densities, viscosities and self-diffusivities of CO_2 and H_2S loaded aqueous MDEA solutions at 313 K as this is a typical temperature in acid gas removal units [42]. We compute the densities of CO_2- or H_2S-loaded 50 wt.% MDEA/water solutions at 313 K by using two different scaling factors for the point charges of the reaction products of CO_2 absorption (MDEAH$^+$ and HCO$_3^-$) and H_2S absorption (MDEAH$^+$ and SH$^-$), see Table 5.2 and Table 5.3: $\chi^q_{products} = 0.90$ and $\chi^q_{products} = 0.75$. Note that for the point charges of MDEA, we use $\chi^q_{MDEA} = 0.90$ in all simulations. Fig. 5.10 shows the comparison between the computed and experimental [317–319] densities of CO_2- and H_2S-loaded 50 wt.% MDEA/water solutions at 313 K and 1 bar. Our findings show that the computed densities of CO_2-loaded solutions agree well with the experimental data from literature [317] when the point charges of the reaction products (MDEAH$^+$ and HCO$_3^-$) are scaled by 0.90. When the point charges of the reaction products (MDEAH$^+$ and HCO$_3^-$) are scaled by 0.90, the computed densities show an average absolute deviation of 0.8% and a maximum deviation of 1.2%. When a scaling factor of 0.75 is used for the point charges of MDEAH$^+$ and HCO$_3^-$, the computed densities of CO_2-loaded solutions agree less well with the experimental data [317] with an average absolute deviation of 1.3% and a maximum deviation of 3%. However, following the trend in experimental densities of CO_2-loaded solutions in Fig. 5.10, it is clear that a scaling factor of 0.9 for the reaction products results

Table 5.5: Speedy-Angell power equation [279] (Eq. (4.3)) fit parameters (D_0, T_S and m) and coefficient of determinations (R^2) for the values of D_{CO_2} and D_{H_2S} in aqueous MDEA solutions for different MDEA concentrations. The values of D_{CO_2} and D_{H_2S} were fitted for a temperature range of 288–323 K.

	MDEA concentration / [wt.%]	D_0 / [$m^2\,s^{-1}$]	T_S / [K]	m	R^2
D_{CO_2}	10	3.07×10^{-28}	0.710	7.14	0.992
	20	3.36×10^{-47}	0.045	9.84	0.999
	30	1.30×10^{-8}	238.659	1.82	0.979
	40	5.80×10^{-46}	0.155	10.98	0.984
	50	4.31×10^{-9}	205.738	2.70	0.992
D_{H_2S}	10	7.78×10^{-9}	263.827	0.82	0.989
	20	1.30×10^{-8}	252.324	1.49	0.991
	30	7.27×10^{-9}	265.252	1.04	0.985
	40	1.51×10^{-35}	0.537	9.32	0.989
	50	4.34×10^{-9}	273.395	0.91	0.995

5

in more accurate computed densities than a scaling factor of 0.75 at CO_2 loading of 1 $mol_{CO_2}\,mol_{amine}^{-1}$. The computed densities of H_2S-loaded 50 wt.% MDEA/water solutions have average absolute deviations of 3.6% and 1%, and maximum deviations of 4.3% and 2% when scaling factors of $\chi^q_{products} = 0.90$ and $\chi^q_{products} = 0.75$ are used, respectively. Our findings show that a scaling factor of $\chi^q_{products} = 0.90$ results in accurately predicted densities for CO_2-loaded 50 wt.% MDEA/water solutions, while the computed densities of H_2S-loaded solution have a better agreement with the experimental data [318, 319] when a scaling factor of $\chi^q_{products} = 0.75$ is used.

We compute the viscosities of CO_2 and H_2S-loaded 50 wt.% MDEA/water solutions at 313 K and 1 bar using two different scaling factors for the point charges of reaction products from CO_2 and H_2S absorption, $\chi^q_{products} = 0.90$ and $\chi^q_{products} = 0.75$, and compared the computed viscosities with experimental data from literature [318–320]. Fig. 5.11 shows the comparison between the computed and experimental [318–320] viscosities of acid gas-loaded 50 wt.% MDEA/water solutions at 313 K and 1 bar. For CO_2-loaded solutions, our findings show that the computed viscosities agree well with the experimental data from Pinto et al. [320] when a scaling factor of $\chi^q_{products} = 0.90$ is used, capturing the increasing viscosity of the solutions with increasing CO_2 loading. However, the computed viscosities are significantly underestimated when $\chi^q_{products} = 0.75$ is used, especially at high CO_2 loadings. The computed viscosities of H_2S-loaded 50 wt.% MDEA/water solutions agree well when a scaling factor of $\chi^q_{products} = 0.75$, while a scaling factor of $\chi^q_{products} = 0.90$ results in significant overestimation of the computed viscosities. Our simulations also capture the effect of slightly decreasing viscosity of the solutions with increasing H_2S loading. Therefore, we decided to compute the self-diffusivities of free

Table 5.6: Vogel-Tamann-Fulcher (VTF) equation [280] (Eq. (4.4)) fit parameters (α, β, γ) and coefficient of determinations (R^2) for the values of D_{CO_2} and D_{H_2S} in aqueous MDEA solutions for different MDEA concentrations. The values of D_{CO_2} and D_{H_2S} were fitted for a temperature range of 288–323 K.

	MDEA concentration / [wt.%]	α	β	γ	R^2
D_{CO_2}	10	1.88×10^4	-5.92×10^2	-9.30×10^{-1}	0.992
	20	9.02×10^5	-5.02×10^3	-1.49×10^2	0.999
	30	3.67×10^2	1.91×10^2	1.73×10^1	0.979
	40	3.01×10^8	-9.18×10^4	-3.25×10^3	0.988
	50	1.14×10^3	1.01×10^2	1.57×10^1	0.992
D_{H_2S}	10	1.19×10^2	2.28×10^2	1.86×10^1	0.990
	20	2.97×10^2	2.03×10^2	1.76×10^1	0.991
	30	1.44×10^2	2.31×10^2	1.88×10^1	0.986
	40	3.36×10^6	-1.02×10^4	-2.98×10^2	0.989
	50	1.03×10^2	2.46×10^2	1.95×10^1	0.995

5

CO_2, $MDEAH^+$, and HCO_3^- in CO_2-loaded 50 wt.% MDEA/water solutions using a scaling factor of $\chi^q_{products} = 0.90$, while using a scaling factor of $\chi^q_{products} = 0.75$ for the MD simulations of H_2S-loaded solutions. The reason for scaling down the point charges of the reaction products of H_2S absorption ($MDEAH^+$ and SH^-) to a greater extent compared to those of the reaction products of CO_2 absorption ($MDEAH^+$ and HCO_3^-) may be attributed to quantum chemistry calculations overestimating the electrostatic interactions of SH^- ion more than the electrostatic interactions of HCO_3^- ion. This may be due to the greater polarity of SH^- ion compared to the HCO_3^- ion.

Fig. 5.12 shows the computed self-diffusivities of free CO_2, free H_2S, and the reaction products of CO_2 or H_2S absorption in 50 wt.% MDEA/water solutions at 313 K and 1 bar. To the best of our knowledge, the data of self-diffusivities of the reaction products in CO_2 or H_2S loaded aqueous MDEA solutions reported here are the first in literature. For CO_2-loaded aqueous MDEA solution, our results show that for free CO_2, HCO_3^-, and $MDEAH^+$, the self-diffusivities show a decreasing trend with increasing CO_2 loading. For all species, the self-diffusivities in CO_2-loaded 50 wt.% MDEA/water solutions decrease by ca. 50% from a CO_2 loading of 0.01 mol_{CO_2} mol^{-1}_{amine} to 1 mol_{CO_2} mol^{-1}_{amine}. This is expected since the viscosities of the CO_2-loaded solutions increase with increasing CO_2 loading (Fig. 5.11(a)). However, the self-diffusivities of free H_2S, SH^-, and $MDEAH^+$ are not affected by the changes in H_2S loading. The self-diffusivities of H_2S and H_2S related reaction products also follow the same trend as the viscosities of H_2S-loaded 50 wt.% MDEA/water solutions (Fig. 5.11(b)) and the viscosities of H_2S-loaded solutions also showed minimal change with changing H_2S loading. Our results indicate that the absorption of CO_2 slows down with increasing CO_2 loading whereas the absorption of H_2S does not exhibit the same behavior. This may be due the linear shape of the SH^- ion (as opposed to the spherical HCO_3^- ion) and a speculative proposition: a proton hopping
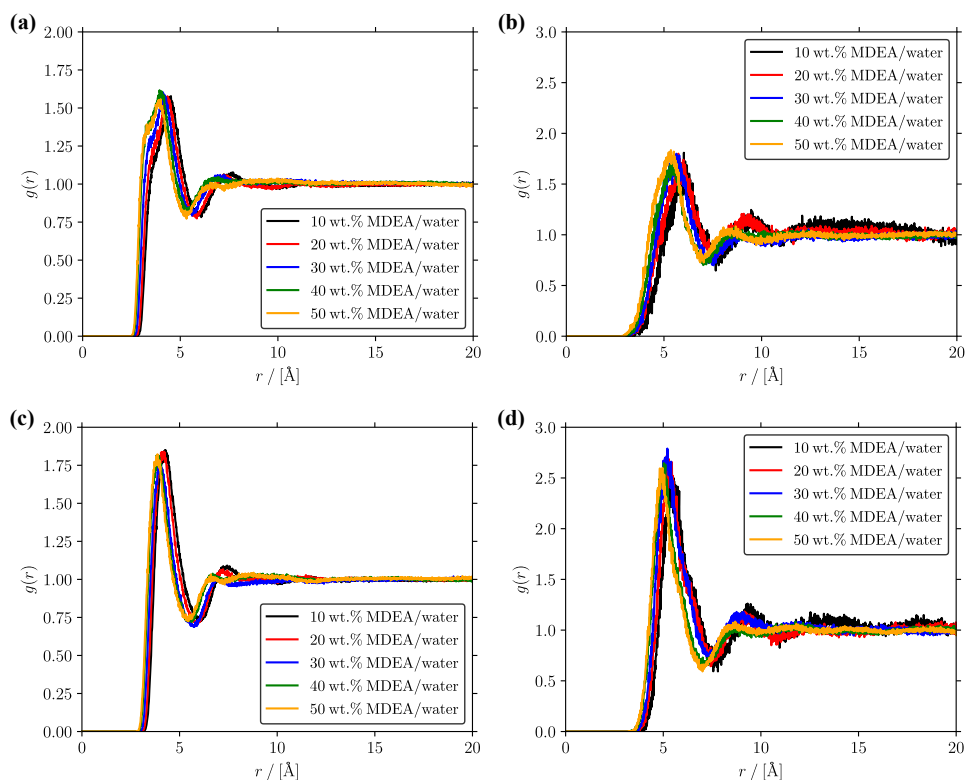
Figure 5.9: Radial distribution functions of (a) CO_2–water, (b) CO_2–MDEA, (c) H_2S–water, and (d) H_2S–MDEA at 313 K and 1 bar. For water, the TIP4P/2005 force field [94] (Appendix C.1.3) was used while for MDEA, we used OPLS-AA force field [88, 89] with point charges computed from quantum chemistry (Appendix C.8.3). Note that the point charges of MDEA are scaled by 0.9, i.e. $\chi^q_{\mathrm{MDEA}} = 0.9$. For CO_2 and H_2S, the TraPPE force field [90, 294] (Appendices C.3 and C.4.2) was used.

mechanism between SH^- and H_2S molecules where there is a proton exchange between the ion and the molecule [321–323].

5
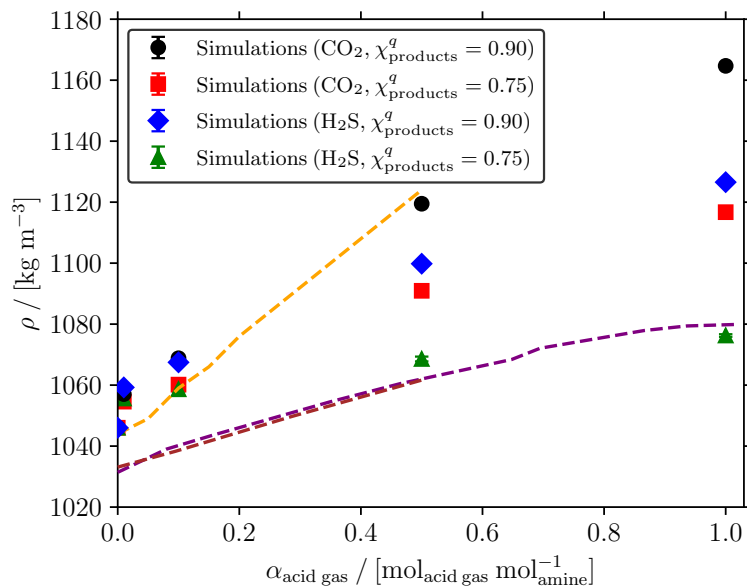
Figure 5.10: Densities of acid-gas loaded 50 wt.% MDEA/water solutions as a function of acid gas loading at 313 K and 1 bar. The orange dashed line represents experimental densities of CO_2-loaded 50 wt.% MDEA solutions from Weiland et al. [317], while the purple and brown dashed lines represent experimental densities of H_2S-loaded 50 wt.% MDEA/water solutions from Shoukouhi et al. [318] and Rinker et al. [319], respectively. Note that the point charges of MDEA are scaled by 0.9, i.e. $\chi^q_{\text{MDEA}} = 0.9$. The point charges of the reaction products of CO_2 absorption ($MDEAH^+$ and HCO_3^-) and H_2S absorption ($MDEAH^+$ and SH^-) are scaled by either 0.9 or 0.75, i.e. $\chi^q_{\text{products}} = 0.9$ or $\chi^q_{\text{products}} = 0.75$. For CO_2 and H_2S, the TraPPE force field [90, 294] (Appendices C.3 and C.4.2) was used.
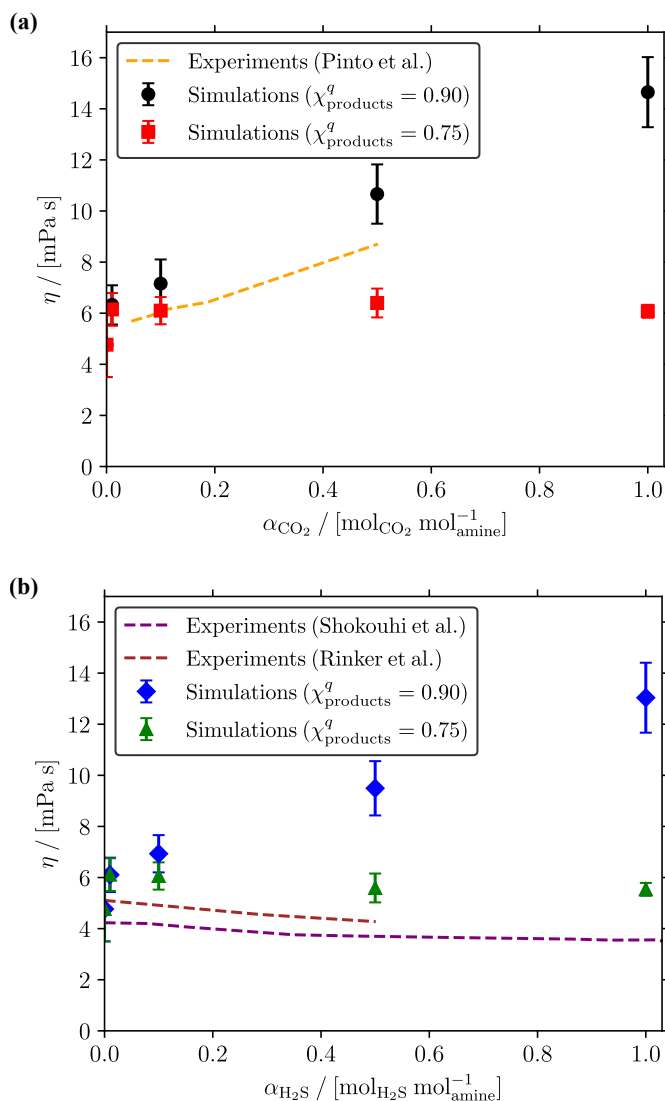
Figure 5.11: Comparison of the computed and experimental [318–320] viscosities of (a) CO_2-loaded and (b) H_2S-loaded 50 wt.% MDEA/water solutions as a function of acid gas loading at 313 K and 1 bar. Note that the point charges of MDEA are scaled with 0.9, i.e. $\chi^q_{MDEA} = 0.9$. The point charges of the reaction products of CO_2 absorption ($MDEAH^+$ and HCO_3^-) and H_2S absorption ($MDEAH^+$ and SH^-) are scaled by either 0.9 or 0.75, i.e. $\chi^q_{products} = 0.9$ or $\chi^q_{products} = 0.75$. For CO_2 and H_2S, the TraPPE force field [90, 294] (Appendices C.3 and C.4.2) was used.

5
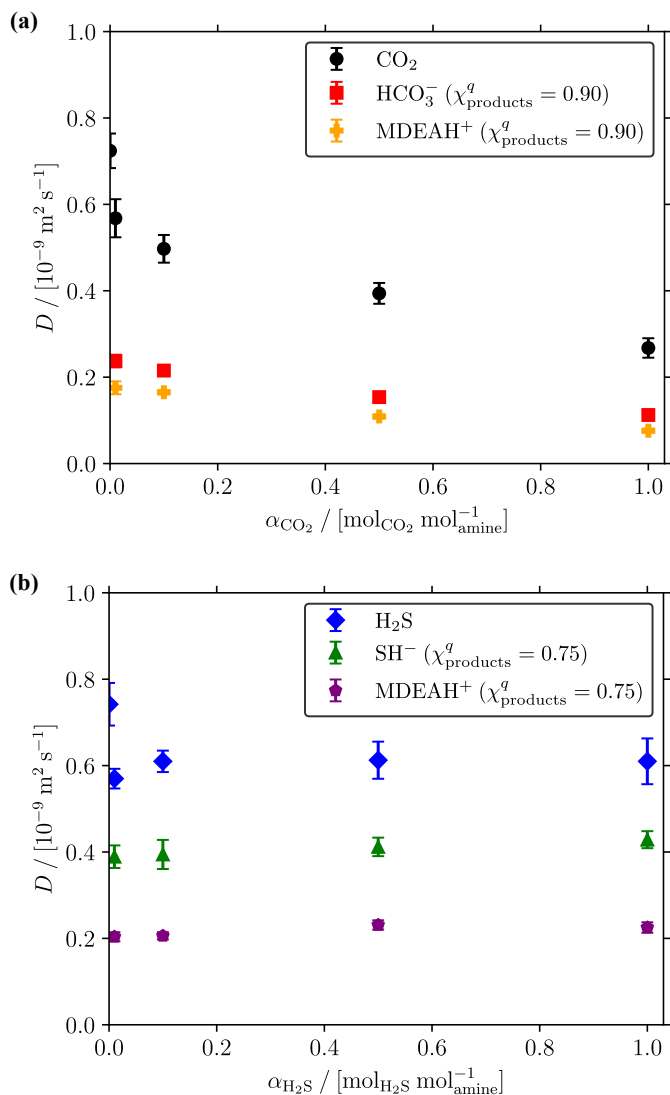
Figure 5.12: Self-diffusivities of free acid gases and the reaction products from acid gas absorption in (a) CO_2-loaded and (b) H_2S-loaded 50 wt.% MDEA/water solutions as a function of acid gas loading at 313 K and 1 bar. Note that the point charges of MDEA are scaled with 0.9, i.e. $\chi^q_{MDEA} = 0.9$. The point charges of the reaction products of CO_2 absorption ($MDEAH^+$ and HCO_3^-) and H_2S absorption ($MDEAH^+$ and SH^-) are scaled by 0.9 and 0.75, respectively. All self-diffusivities are corrected for finite-size effects using Eq. (4.1). For CO_2 and H_2S, the TraPPE force field [90, 294] (Appendices C.3 and C.4.2) was used.

5.4. Conclusions

In this chapter, the effects of temperature and MDEA concentration in aqueous MDEA solutions on the values of the self-diffusivities D_{CO_2} and D_{H_2S} were investigated using classical MD simulations. First, we computed the densities of aqueous MDEA solutions for a temperature range of 288–333 K and an MDEA concentration of $10 - 50$ wt.% MDEA using two different sets of parameters for the N–C–C–O dihedral in MDEA, showing excellent agreement with experimental data from literature. We also computed the viscosities of aqueous MDEA solutions and showed that the computed viscosities agree well with experimental results from literature when the dihedral parameters from Orozco et al. [296] and a point charge scaling factor of 0.9 for MDEA are used. To validate that the diffusion of MDEA molecules are accurately captured in the MD simulations, we computed D_{MDEA} in aqueous MDEA solutions for a wide range of temperatures and MDEA concentrations and compared our data with available data in literature, showing a good agreement. Next, we computed D_{CO_2} and D_{H_2S} in aqueous MDEA solutions. Our findings showed that both CO_2 and H_2S diffuse 3.5 times faster in 10 wt.% MDEA/water solutions than in 50 wt.% MDEA/water solutions and H_2S diffuse slower than CO_2 in aqueous MDEA solutions. We also investigated the RDFs between CO_2, H_2S, water, and MDEA molecules and showed that the interactions between H_2S and the surrounding molecules are stronger than those between CO_2 and the surrounding molecules which explains why H_2S diffuse slower than CO_2 in these solutions. Our results also showed that the interactions between the acid gases and surrounding molecules are stronger with increasing MDEA concentration in the solution. Finally, we investigated the impact of acid gas loading on the densities, viscosities and self-diffusivities (of acid gases and reaction products) in 50 wt.% MDEA/water solutions at 313 K and 1 bar. The densities, viscosities, and self-diffusivities in the acid gas loaded aqueous MDEA solutions are important for the modeling of the mass transfer in loaded solutions. Comparing the computed densities and viscosities of CO_2 and H_2S-loaded solutions with experimental data from literature showed that two different point charge scaling factors are needed to accurately compute the densities and viscosities of acid gas-loaded aqueous MDEA solutions. When a scaling factor of 0.90 for the point charges of reaction products of CO_2 absorption ($MDEAH^+$ and HCO_3^-) and a scaling factor of 0.75 for those of H_2S absorption ($MDEAH^+$ and SH^-) are used, we showed that the viscosities of CO_2-loaded aqueous MDEA solutions increase with increasing CO_2 loading while the viscosities do not show a significant change with changing H_2S loading in H_2S-loaded solutions. For the first time in literature, we computed the self-diffusivities of free CO_2, HCO_3^-, and $MDEAH^+$ in CO_2-loaded 50 wt.% MDEA/water solutions, and free H_2S, SH^-, and $MDEAH^+$ in H_2S-loaded 50 wt.% MDEA/water solutions at 313 K. Our results showed that the self-diffusivities in CO_2-loaded solutions significantly decrease with increasing CO_2 loading while the self-diffusivities in H_2S-loaded solutions did not change significantly with changing H_2S loading in the solution which indicates that CO_2 absorption slows down with increasing CO_2 loading while this is not the case for H_2S absorption.

5

6

Conclusions

In this thesis, we have demonstrated the effectiveness of molecular simulations as a practical approach for the computation of VLEs and transport properties of acid gases in aqueous alkanolamine solutions. These simulations overcome experimental challenges associated with measuring very low partial pressures of acid gases and diffusivities of acid gases in reactive solvents. Our predictions play a crucial role in the design and optimization of absorption-based acid gas removal processes. For computing transport properties, our investigations have revealed that the existing methods (i.e., classical force field-based MD simulations) can be used to accurately predict diffusivities of acid gases and the reaction products from acid gas absorption in aqueous alkanolamine solutions (Chapters 4 and 5). We introduced novel methods to accurately predict excess chemical potentials of ionic and/or polar species (via thermodynamic integration, Chapter 2) and speciation/VLE of acid gases in aqueous alkanolamine solutions (using CASpy, an open-source solver for chemical reaction equilibrium, Chapter 3) for reaction equilibria and VLE calculations.

The results of this thesis emphasize a critical limitation of molecular simulations using classical force fields, particularly for predicting reaction equilibrium via free energy and quantum chemistry calculations. Predicting the equilibrium constant of the MDEAH$^+$ dissociation reaction in acid gas absorption in aqueous MDEA solutions exemplifies the sensitivity of reaction equilibrium to the computed values of the excess chemical potentials μ_i^{ex} (via free energy calculations) and standard state ideal gas chemical potentials μ_i^0 (via quantum chemistry calculations). In the CO$_2$/MDEA/water system, even an uncertainty of $1 \ln[K]$ unit in the reaction equilibrium constant of the MDEAH$^+$ dissociation reaction leads to ca. 2.5 times differences in computed values of the partial pressure of CO$_2$ (P_{CO_2}) at low loadings of CO$_2$. This uncertainty translates to an uncertainty of $1 k_{\mathrm{B}}T$ unit ($\approx 2.6 \, \mathrm{kJ \, mol^{-1}}$ at 313.15 K) in the computed values of μ_i^{ex} and μ_i^0 (Eq. (3.4)). As the absolute values of μ_i^0 are higher than those of μ_i^{ex} by 2-3 orders of magnitude and the uncertainty in the values of μ_i^0 computed with different quantum chemistry methods is significant (in the order of $1 k_{\mathrm{B}}T$) (Appendix B), we emphasize the crucial need for a benchmark study to identify the most accurate quantum chemistry level of theory or composite method to accurately compute the values of μ_i^0. Our investigation of the performance of two generic force fields, OPLS-AA and GAFF, in predicting the equilibrium constant of the MDEAH$^+$ dissociation reaction showed the pivotal role

of force field selection and, more specifically, the accuracy of point charges on the computed values of μ_i^{ex} (with statistical uncertainties in the order of 0.02 $k_{\text{B}}T$). The concept of chemical accuracy (1 kcal mol^{-1} = 4.18 kJ mol^{-1}) was introduced in 1999 to align the precision of computational chemistry with experimental measurements of energies, such as heats of formation and ionization energies [63]. This concept continues to be used as a benchmark for precision in computational chemistry today [74, 324–327]. As an example, let us assume a maximum of 10% uncertainty in the computed values of P_{CO_2} in CO$_2$/MDEA/water mixture at 313.15 K and low loadings of CO$_2$ (<10^{-3} mol$_{\text{CO}_2}$ mol$_{\text{amine}}^{-1}$). To achieve this level of accuracy, an uncertainty of 0.1 $\ln[K]$ units in the predicted value of the equilibrium constant of the MDEAH$^+$ dissociation reaction in this mixture is necessary. An uncertainty of 0.1 $\ln[K]$ units in the equilibrium constant corresponds to 0.1 $k_{\text{B}}T$ units ($\approx$ 0.26 kJ mol^{-1} at 313.15 K, an order of magnitude lower than the chemical accuracy of 4.18 kJ mol^{-1}) in the computed values of μ_i^0 and μ_i^{ex}. Consequently, the concept of chemical accuracy becomes arbitrary in predicting reaction equilibria for complex systems, highlighting the need for significantly higher accuracies such as 0.1 $k_{\text{B}}T$ for truly predictive simulations.

Transport properties of acid gases in aqueous alkanolamine solutions such as viscosities and diffusivities are also very sensitive to the point charges of molecules/ions. A point charge scaling factor, i.e., a multiplication factor applied to all point charges in a molecule/ion to capture the electrostatic interactions more accurately (as the point charges from quantum chemistry calculations typically overestimate electrostatic interactions) [148, 148, 166, 267, 268, 312], plays a crucial role in the accuracy of computed transport properties. From a point charge scaling factor of 0.90 to 0.75, the computed viscosities of CO$_2$- and H$_2$S-loaded aqueous MDEA solutions show a decrease of ca. 60% at a high acid gas loading (1 mol$_{\text{acid gas}}$ mol$_{\text{amine}}^{-1}$). This is also the case for the diffusivities of the reaction products (HCO$_3^-$ and SH$^-$) from acid gas absorption in aqueous MDEA solutions, as the same change in the point charge scaling factors results in a ca. 3 times increase in the computed diffusivities. The computed densities have a more modest sensitivity, changing by ca. 4% for the same range of point charge scaling factors. Therefore, using transport properties such as viscosities and diffusivities in force field validation is crucial for accurately predicting transport properties of acid gases in aqueous alkanolamine solutions.

This thesis shows that the accuracy of classical force fields depends on rigorous validation and system-specific scaling factors, thereby posing a challenge to the predictive power of molecular simulations in reaction equilibria and transport properties. Classical force fields, considering electrostatic interactions as fixed point charges, provide a rough approximation of dynamic molecular systems, where electron density, consequently electrostatic interactions, of a molecule/ion depends on the electron density of the surrounding atoms. Addressing this limitation, polarizable force fields emerge as a more accurate solution [239–246], albeit with increased computational expense. Implementation of polarizable force fields in both MC and MD codes, as well as extension to cover a broader range of species, remains a crucial area for future research. Additionally, alternative approaches, such

as *ab initio* molecular dynamics simulations and machine learning-based force field development, offer promising avenues [328]. These methods may provide more accurate solutions to interactions between molecules. While high computational costs restrict their use to short timescales and smaller systems, the ever-growing computational power positions these methods as increasingly relevant tools in the near future.

Appendix A

A.1. Implementation of Thermodynamic Integration

In this section, the details of the implementation of thermodynamic integration in Brick-CFCMC are explained. In the CFCMC method [114–116, 123, 157], the interactions of the fractional molecule group are scaled using a scaling factor λ. The fractional molecule group has no interactions with the surrounding molecules when $\lambda = 0$, and has full interactions when $\lambda = 1$. The ensemble average of the derivative of potential energy with respect to λ can be used to calculate the excess chemical potential of species i according to [82, 164]:

$$NVT \text{ ensemble}: \quad \mu_i^{\text{ex}} = \int_0^1 d\lambda \left\langle \frac{\partial A}{\partial \lambda} \right\rangle_{NVT} = \int_0^1 d\lambda \left\langle \frac{\partial U}{\partial \lambda} \right\rangle_{NVT} \tag{A1.1}$$

$$NPT \text{ ensemble}: \quad \mu_i^{\text{ex}} = \int_0^1 d\lambda \left\langle \frac{\partial G}{\partial \lambda} \right\rangle_{NPT} = \int_0^1 d\lambda \left\langle \frac{\partial U}{\partial \lambda} \right\rangle_{NPT} \tag{A1.2}$$

LJ and electrostatic interactions are scaled independently with two different scaling factors, λ_{LJ} and λ_{el}, respectively. Both λ_{LJ} and λ_{el} are a function of λ in such a way that they are both zero when $\lambda = 0$ and both are unity when $\lambda = 1$. For the implementation of the thermodynamic integration, we need to develop a scaling scheme that uses continuous functions λ_{LJ} and λ_{el} so that the integration of Eqs. (A1.1) and (A1.2) can be performed. Both λ_{LJ} and λ_{el} and the derivatives of these functions with respect to λ are required to be continuous functions. In Brick-CFCMC, The following equations provide the expressions used to compute λ_{LJ} and λ_{el}, respectively:

$$\lambda_{\text{LJ}} = \begin{cases} \frac{20}{9}\lambda & 0.0 < \lambda < 0.4, \\ 1 - \frac{100}{9}(\lambda - \frac{1}{2})^2 & 0.4 < \lambda < 0.5, \\ 1 & 0.5 < \lambda < 1.0 \end{cases} \tag{A1.3}$$

$$\lambda_{\text{el}} = \begin{cases} 0 & 0.0 < \lambda < 0.5, \\ \frac{100}{9}(\lambda - \frac{1}{2})^2 & 0.5 < \lambda < 0.6, \\ \frac{-11}{9} + \frac{20}{9}\lambda & 0.6 < \lambda < 1.0 \end{cases} \tag{A1.4}$$

Fig. 2.2 shows λ_{LJ} and λ_{el} as a function of λ. With this scaling scheme, electrostatic interactions are not "switched on" before the LJ interactions are at full strength ($\lambda_{\text{LJ}} = 1$) [178]. This is chosen to avoid any overlap between the atoms of the fractional group and other atoms. In this way, we protect the electrostatic interaction sites using the LJ interactions in order to avoid atomic overlaps. This scaling scheme can be easily modified in the source code (file: interactionlambda.f). It is

important to note that both λ_{LJ} and λ_{el} should be continuous functions of λ, and that λ_{el} should be zero when $\lambda_{\mathrm{LJ}} < 1$. The value of $\frac{\partial U}{\partial \lambda}$ is computed by using the chain rule:

$$\frac{\partial U}{\partial \lambda} = \frac{\partial U_{\mathrm{LJ}}}{\partial \lambda_{\mathrm{LJ}}} \frac{\partial \lambda_{\mathrm{LJ}}}{\partial \lambda} + \frac{\partial U_{\mathrm{el}}}{\partial \lambda_{\mathrm{el}}} \frac{\partial \lambda_{\mathrm{el}}}{\partial \lambda} \tag{A1.5}$$

The terms $\frac{\partial \lambda_{\mathrm{LJ}}}{\partial \lambda}$ and $\frac{\partial \lambda_{\mathrm{el}}}{\partial \lambda}$ in Eq. (A1.5) are computed using Eq. (A1.3) and Eq. (A1.4). Note that with these definitions, $\frac{\partial U}{\partial \lambda} = 0$ at $\lambda = 0.5$. The terms $\frac{\partial U_{\mathrm{LJ}}}{\partial \lambda_{\mathrm{LJ}}}$ and $\frac{\partial U_{\mathrm{el}}}{\partial \lambda_{\mathrm{el}}}$ are computed after every MC trial move and we keep track of these quantities during the MC simulation. This bookkeeping is implemented to avoid any additional computational cost. In the next two subsections, exact analytic expressions are presented for the computation of $\frac{\partial U_{\mathrm{LJ}}}{\partial \lambda_{\mathrm{LJ}}}$ and $\frac{\partial U_{\mathrm{el}}}{\partial \lambda_{\mathrm{el}}}$.

A.1.1. Lennard-Jones Interactions

Intermolecular Lennard-Jones Interactions

The intermolecular LJ energy between interaction site i of molecule m and interaction site j of molecule n is computed using:

$$U_{\mathrm{LJ},ij} = 4\epsilon_{ij}\left[\left(\frac{\sigma_{ij}}{r_{ij}}\right)^{12} - \left(\frac{\sigma_{ij}}{r_{ij}}\right)^{6}\right] \tag{A1.6}$$

where ϵ_{ij} is the minimum of the LJ potential between sites i and j, σ_{ij} is the distance where the LJ potential between sites i and j is zero, and r_{ij} is the distance between sites i and j. When a site belonging to a fractional molecule group (as the fractionals in Brick-CFCMC can be consist of multiple number of molecules) is involved, the intermolecular LJ energy between site i of molecule m and site j of molecule n is computed using a softcore potential [329]:

$$U_{\mathrm{LJ},ij} = 4\epsilon_{ij}\lambda_{\mathrm{LJ,t}}\left[\left(\frac{1}{Y}\right)^{12/c} - \left(\frac{1}{Y}\right)^{6/c}\right] \tag{A1.7}$$

where the total interaction scaling parameter is computed using the value of λ_{LJ} of sites m and n ($\lambda_{\mathrm{LJ,t}} = \lambda_{\mathrm{LJ},m}\lambda_{\mathrm{LJ},n}$), and

$$Y = \alpha_{\mathrm{LJ}}(1 - \lambda_{\mathrm{LJ,t}})^{b} + (r_{ij}/\sigma_{ij})^{c} \tag{A1.8}$$

The values of α_{LJ}, b and c can be adjusted [114]. In Brick-CFCMC, the default values for these parameters are 0.5, 1 and 6, respectively, as this choice of α_{LJ}, b and c showed the lowest statistical variance of the computed free energies and highest efficiency [178, 330]. The derivative with respect to $\lambda_{\mathrm{LJ},m}$ is:

$$\frac{\partial U_{\mathrm{LJ},ij}}{\partial \lambda_{\mathrm{LJ},m}} = 4\epsilon_{ij}\lambda_{\mathrm{LJ},n}\left(\frac{1}{Y}\right)^{6/c}\left[\left(\frac{1}{Y}\right)^{6/c} - 1 + \frac{6\lambda_{\mathrm{LJ,t}}b\alpha_{\mathrm{LJ}}}{cY}(1 - \lambda_{\mathrm{LJ,t}})^{b-1}\left(2\left(\frac{1}{Y}\right)^{6/c} - 1\right)\right] \tag{A1.9}$$

After every MC trial move, the values of both U and $\frac{\partial U_{\mathrm{LJ},ij}}{\partial \lambda_{\mathrm{LJ},m}}$ are updated so that $\frac{\partial U}{\partial \lambda}$ is immediately obtained without having to consider all pairwise interactions (only particles with modified coordinates are considered).

Tail Corrections

Tail corrections account for the interactions of the molecules beyond the cutoff radius by adding an average energy contribution to the potential energy of the system [82, 96]. The tail correction energy of a system is computed as [82, 83, 96]:

$$U_{\mathrm{LJ}}^{\mathrm{tail}} = \frac{1}{2} \sum_{i,j} \frac{16\pi N_i N_j \epsilon_{ij}}{V} \left(\frac{\sigma_{ij}^{12}}{9 r_{\mathrm{cut}}^9} - \frac{\sigma_{ij}^6}{3 r_{\mathrm{cut}}^3} \right) \tag{A1.10}$$

where the sum ranges over all atom types in the system, N_i and N_j are the numbers of atoms of types i and j, respectively (excluding atoms of fractional molecules), and V is the volume of the simulation box. The factor $1/2$ accounts for double counting of the interactions.

In Brick-CFCMC, the fractional molecule interactions are added to the tail correction energy by substituting $N_i \rightarrow N_i + \lambda_{\mathrm{LJ},m} \times N_{m,i}$ and $N_j \rightarrow N_j + \lambda_{\mathrm{LJ},n} \times N_{n,j}$ in Eq. (A1.10), where $N_{m,i}$ and $N_{n,j}$ are the numbers of atoms of types i and j within fractional molecules m and n, respectively [96]. The derivative with respect to $\lambda_{\mathrm{LJ},m}$ can be calculated as:

$$\frac{\partial U_{\mathrm{LJ}}^{\mathrm{tail}}}{\partial \lambda_{\mathrm{LJ},m}} = \frac{1}{2V} \sum_{i,j} \left[16\pi \epsilon_{ij} (N_j N_{m,i} + \lambda_{\mathrm{LJ},n} N_{m,i} N_{n,j}) \left[\left(\frac{\sigma_{ij}^{12}}{9 r_{\mathrm{cut}}^9} \right) - \left(\frac{\sigma_{ij}^6}{3 r_{\mathrm{cut}}^3} \right) \right] \right] \tag{A1.11}$$

A.1.2. Electrostatic Interactions

The analytic expressions for $\frac{\partial U_{\mathrm{el}}}{\partial \lambda_{\mathrm{el}}}$ of electrostatic potentials may seem trivial at first sight because for linear charge scaling $\frac{\partial U_{\mathrm{el}}}{\partial \lambda_{\mathrm{el}}}$ is proportional to λ_{el} [128, 129]. It is important to note that such a scaling may result in numerical instabilities and atomic overlaps as the attractive electrostatic interactions are usually much stronger than the repulsive part of LJ interactions. The electrostatic interaction potentials for the fractional molecule groups are defined in Brick-CFCMC in such a way that they have an offset parameter (Q) to avoid any atomic overlaps. Therefore, the computation of $\frac{\partial U_{\mathrm{el}}}{\partial \lambda_{\mathrm{el}}}$ will require more complex expressions. The next three subsections present the analytic expressions of $\frac{\partial U_{\mathrm{el}}}{\partial \lambda_{\mathrm{el}}}$ for the Ewald summation [182], the Wolf method [179], and the damped and shifted version of the Wolf method [180].

Ewald Summation

The Ewald summation consists of a real-space part, exclusion part, self-energy part, and Fourier-space part [182, 331, 332]. The real-space part is a damped electrostatic potential for the short-ranged interactions. The exclusion accounts

for all intramolecular interactions for which electrostatic interactions should not be considered (i.e., between atoms that interact with a bonded interaction potential such as bond-stretching or bond-bending). The self-energy part considers the self-electrostatic energy of all charges, and the Fourier-space part handles the long-range electrostatic interactions by using a Fourier transform. The real-space energy of the Ewald summation between sites i and j of molecules m and n is computed as:

$$U_{\text{real},ij} = q_i q_j \frac{\text{erfc}(\alpha_{\text{el}} r_{ij})}{r_{ij}} \tag{A1.12}$$

where α_{el} is the damping parameter, $\text{erfc}(x)$ is the complementary error function and r_{ij} is the distance between the interaction sites i and j. If one of the sites involved in the interaction belongs to a fractional molecule group, then the real-space energy of the Ewald summation is computed as:

$$U_{\text{real},ij} = \lambda_{\text{el,t}} q_i q_j \frac{\text{erfc}(\alpha_{\text{el}}(r_{ij} + Q))}{r_{ij} + Q} \tag{A1.13}$$

where the total fractional scaling factor for electrostatic interactions is computed by multiplying the electrostatic interaction scaling factors of molecules m and n ($\lambda_{\text{el,t}} = \lambda_{\text{el},m}\lambda_{\text{el},n}$). Q is the offset parameter computed as:

$$Q = \beta_{\text{el}}(1 - \lambda_{\text{el,t}}) \tag{A1.14}$$

where β_{el} is equal to 0.01 Å. In this way, there is no divergence of the interaction potential, even when $r_{ij} = 0$. The exclusion term of the Ewald summation between atoms i and j in molecule m is obtained using [119, 181]:

$$U_{\text{exclusion},ij} = q_i q_j \frac{\text{erfc}(\alpha_{\text{el}} r_{ij}) - 1}{r_{ij}} \tag{A1.15}$$

When a fractional molecule is involved, the exclusion term is computed as follows:

$$U_{\text{exclusion},ij} = \lambda_{\text{el,t}} q_i q_j \frac{\text{erfc}(\alpha_{\text{el}}(r_{ij} + Q)) - 1}{r_{ij} + Q} \tag{A1.16}$$

The self-energy term of the Ewald summation is computed as:

$$U_{\text{self}} = \frac{-\alpha_{\text{el}}}{\sqrt{\pi}} \sum_n \sum_i \lambda_{\text{el},n}^2 q_{i,n}^2 \tag{A1.17}$$

where index n runs over all the molecules in the simulation box and index i runs over all atoms in molecule n, and $\lambda_{\text{el,t}} = \lambda_{\text{el},m}^2$. The Fourier-space term of the Ewald summation is computed as [182]:

$$U_{\text{Fourier}} = \frac{1}{V} \sum_{\mathbf{k}} F(\mathbf{k}) \Big[\Big(\sum_i \lambda_{\text{el},i} q_i \cos(i\mathbf{k}.\mathbf{r}_i) \Big)^2 + \Big(\sum_i \lambda_{\text{el},i} q_i \sin(i\mathbf{k}.\mathbf{r}_i) \Big)^2 \Big] \tag{A1.18}$$

in which indices $\mathbf{k}$ and i run over all k-vectors (except for the zero wavevector $\mathbf{k} = (0, 0, 0)$ [82]) and all atoms in the system, respectively, and:

$$F(\mathbf{k}) = \frac{4\pi}{|\mathbf{k}|^2} \exp\left[\frac{|\mathbf{k}|^2}{4\alpha_{\text{el}}}\right] \tag{A1.19}$$

In Eq. (A1.18), the terms $\lambda_{\text{el},i}$ are the electrostatic interaction scaling factors of atoms i. These terms were added to this equation to account for the contribution of the fractional molecules to the Fourier-space part of the Ewald summation. The values of $\lambda_{\text{el},i}$ are set to 1 for atoms of whole molecules (i.e., molecules that always have a full interaction strength with the surrounding molecules [96]) and for sites belonging to fractional molecules, $\lambda_{\text{el},i} = \lambda_{\text{el}}$.

The bookkeeping for the real-space and exclusion parts of the Ewald summation is similar to the bookkeeping of the LJ interactions as these are all pairwise interactions [82]. The bookkeeping of the self-energy term is trivial as this term does not depend on the atomic positions. The bookkeeping of the Fourier-space part of the Ewald summation is more complicated as it is not a pairwise interaction. In Brick-CFCMC, the bookkeeping for the Fourier-space term of the Ewald summation is performed according to Ref. [331]. During the simulation, we keep track of the values of the terms in $\sum_i \lambda_{\text{el},i} q_i \cos(i\mathbf{k}.\mathbf{r}_i)$ and $\sum_i \lambda_{\text{el},i} q_i \sin(i\mathbf{k}.\mathbf{r}_i)$ of Eq. (A1.18). For each wavevector $\mathbf{k}$, this requires the storage of two floats. After every MC trial move, the values of the terms in $\sum_i \lambda_{\text{el},i} q_i \cos(i\mathbf{k}.\mathbf{r}_i)$ and $\sum_i \lambda_{\text{el},i} q_i \sin(i\mathbf{k}.\mathbf{r}_i)$ are updated by adding the contribution of the new configuration and subtracting the contribution of the old configuration. This updating is performed for each wavevector seperately.

The derivative of the real-space part of the Ewald summation with respect to the scaling factor of (fractional) molecule m $\lambda_{\text{el},m}$ is obtained as:

$$\frac{\partial U_{\text{real},ij}}{\partial \lambda_{\text{el},m}} = \lambda_n q_i q_j \left[\frac{\text{erfc}(\alpha_{\text{el}}(r_{ij} + Q))}{r_{ij} + Q} + \lambda_{\text{el}}\left(X(r_{ij})\right)\right] \tag{A1.20}$$

where $X(r_{ij})$ is computed using:

$$X(r) = \frac{\beta_{\text{el}}}{(r + Q)^2}\left[(r + Q)\left(\frac{2\alpha_{\text{el}}}{\sqrt{\pi}}\right)\exp\left[-\alpha_{\text{el}}^2(r + Q)^2\right] + \text{erfc}(\alpha_{\text{el}}(r + Q))\right] \tag{A1.21}$$

The derivative of the exclusion part of the Ewald summation with respect to $\lambda_{\text{el},m}$ is calculated according to:

$$\frac{\partial U_{\text{exclusion},ij}}{\partial \lambda_{\text{el},m}} = 2\lambda_{\text{el},m} q_i q_j \left[\frac{\text{erfc}(\alpha_{\text{el}}(r_{ij} + Q))}{r_{ij} + Q} + \lambda_{\text{el,t}}\left(X(r_{ij})\right) - \frac{r_{ij} + Q + \lambda_{\text{el,t}}\beta_{\text{el}}}{(r_{ij} + Q)^2}\right]$$
$$\tag{A1.22}$$

where $X(r)$ follows from Eq. (A1.21). The derivative of the self-energy part with respect to $\lambda_{\text{el},m}$ of fractional molecule m becomes:

$$\frac{\partial U_{\text{self}}}{\partial \lambda_{\text{el},m}} = 2\lambda_{\text{el},m} \frac{-\alpha_{\text{el}}}{\sqrt{\pi}} \sum_j q_j^2 \tag{A1.23}$$

in which the index j runs over all atoms in the fractional molecule m. The derivative of the Fourier-space part of the Ewald summation with respect to $\lambda_{\text{el},m}$ is:

$$\frac{\partial U_{\text{Fourier}}}{\partial \lambda_{\text{el},m}} = \frac{2}{V} \sum_{\mathbf{k}} F(\mathbf{k}) \Bigg[(\sum_i \lambda_{\text{el},i} q_i \cos(i\mathbf{k}.\mathbf{r}_i)) \times (\sum_j q_j \cos(i\mathbf{k}.\mathbf{r}_j))) +$$

$$(\sum_i \lambda_{\text{el},i} q_i \sin(i\mathbf{k}.\mathbf{r}_i)) \times (\sum_j q_j \sin(i\mathbf{k}.\mathbf{r}_j))) \Bigg] \tag{A1.24}$$

in which indices k, i and j run over all k-vectors (except for the zero wavevector $\mathbf{k} = (0,0,0)$), all atoms in the system, and all atoms of molecule m, respectively. $F(\mathbf{k})$ follows Eq. (A1.19) and V is the volume of the simulation box. The bookkeeping for the computation of $\frac{\partial U_{\text{Fourier}}}{\partial \lambda_{\text{el},m}}$ is performed in the same way as the bookkeeping for the Fourier-space energy of the Ewald summation. The values of the terms in $(\sum_i \lambda_{\text{el},i} q_i \cos(i\mathbf{k}.\mathbf{r}_i)) \times (\sum_j q_j \cos(i\mathbf{k}.\mathbf{r}_j))$ and $(\sum_i \lambda_{\text{el},i} q_i \sin(i\mathbf{k}.\mathbf{r}_i)) \times (\sum_j q_j \sin(i\mathbf{k}.\mathbf{r}_j))$ are calculated at the start of the simulation and stored in memory. The values of the terms in $(\sum_i \lambda_{\text{el},i} q_i \cos(i\mathbf{k}.\mathbf{r}_i)) \times (\sum_j q_j \cos(i\mathbf{k}.\mathbf{r}_j))$ and $(\sum_i \lambda_{\text{el},i} q_i \sin(i\mathbf{k}.\mathbf{r}_i)) \times (\sum_j q_j \sin(i\mathbf{k}.\mathbf{r}_j))$ are updated after every MC trial move by subtracting the contribution of the old configuration and adding the contribution of the new configuration. This is done for each wavevector. Because this is performed only for the atoms that have different positions in the old and the new configurations, this does not lead to any additional computational cost.

Wolf Method
The Wolf method uses the strong screening of the electrostatic interactions in a system to calculate electrostatic potential energy [179]. Because of this strong screening, it works very well for dense (liquid) systems [333, 334] while it does not work well for the less dense (gas) systems due to less effective screening of electrostatics [119, 331]. All interactions in the Wolf method are either pairwise interactions (real-space and exclusion parts) or constant (self-energy part) and no Fourier transform is involved. This makes this method computationally more efficient than the Ewald summation [119]. The short ranged real-space electrostatic energy between site i of molecule m and site j of molecule n is computed as:

$$U_{\text{real},ij} = q_i q_j \left[\frac{\text{erfc}(\alpha_{\text{el}} r_{ij})}{r_{ij}} - \frac{\text{erfc}(\alpha_{\text{el}} r_{\text{cut}})}{r_{\text{cut}}} \right] \tag{A1.25}$$

where $\text{erfc}(x)$ is the complementary error function ($\text{erfc}(x) = 1 - \text{erf}(x)$), r_{ij} is the distance between sites i and j, r_{cut} is the cutoff radius, and α_{el} is the damping parameter. When a site of a fractional molecule group is involved in this type of

interaction, the following expression is used to compute the real-space electrostatic energy between site i of molecule m and site j of molecule n.

$$U_{\text{real},ij} = \lambda_{\text{el,t}} q_i q_j \left[\frac{\text{erfc}(\alpha_{\text{el}}(r_{ij} + Q))}{r_{ij} + Q} - \frac{\text{erfc}(\alpha_{\text{el}}(r_{\text{cut}} + Q))}{r_{\text{cut}} + Q} \right] \qquad (\text{A1.26})$$

in which $\lambda_{\text{el,t}} = \lambda_{\text{el},m}\lambda_{\text{el},n}$, and the offset term Q is computed using Eq. (A1.14). The derivative of the real-space part of the Wolf method with respect to $\lambda_{\text{el},m}$ is obtained as:

$$\frac{\partial U_{\text{real},ij}}{\partial \lambda_{\text{el},m}} = \lambda_n q_i q_j \left[\frac{\text{erfc}(\alpha_{\text{el}}(r_{ij} + Q))}{r_{ij} + Q} - \frac{\text{erfc}(\alpha_{\text{el}}(r_{\text{cut}} + Q))}{r_{\text{cut}} + Q} + \lambda_{\text{el,t}} \left(X(r_{ij}) - X(r_{\text{cut}}) \right) \right]$$
$$(\text{A1.27})$$

where the term $X(r)$ follows from Eq. (A1.21).
The exclusion term of the Wolf method between sites i and j of molecule m is computed as:

$$U_{\text{exclusion},ij} = q_i q_j \left[\frac{\text{erfc}(\alpha_{\text{el}} r_{ij}) - 1}{r_{ij}} - \frac{\text{erfc}(\alpha_{\text{el}} r_{\text{cut}})}{r_{\text{cut}}} \right] \qquad (\text{A1.28})$$

When molecule m is in a fractional molecule group, the following expression is used for the exclusion term:

$$U_{\text{exclusion},ij} = \lambda_{\text{el,t}} q_i q_j \left[\frac{\text{erfc}(\alpha_{\text{el}}(r_{ij} + Q)) - 1}{r_{ij} + Q} - \frac{\text{erfc}(\alpha_{\text{el}}(r_{\text{cut}} + Q))}{r_{\text{cut}} + Q} \right] \qquad (\text{A1.29})$$

in which $\lambda_{\text{el,t}} = \lambda_{\text{el},m}^2$, and the derivative with respect to $\lambda_{\text{el},m}$ is calculated from:

$$\frac{\partial U_{\text{exclusion},ij}}{\partial \lambda_{\text{el},m}} = 2\lambda_{\text{el},m} q_i q_j \left[\frac{\text{erfc}(\alpha_{\text{el}}(r_{ij} + Q))}{r_{ij} + Q} - \frac{\text{erfc}(\alpha_{\text{el}}(r_{\text{cut}} + Q))}{r_{\text{cut}} + Q} + \right.$$
$$\left. \lambda_{\text{el,t}} \left(X(r_{ij}) - X(r_{\text{cut}}) \right) - \frac{r_{ij} + Q + \lambda_{\text{el}}\beta_{\text{el}}}{(r_{ij} + Q)^2} \right] \qquad (\text{A1.30})$$

The self-energy term of the Wolf method is computed from:

$$U_{\text{self}} = - \left(\frac{\text{erfc}(\alpha_{\text{el}} r_{\text{cut}})}{2r_{\text{cut}}} + \frac{\alpha_{\text{el}}}{\sqrt{\pi}} \right) \sum_n \sum_i \lambda_{\text{el},n}^2 q_{i,n}^2 \qquad (\text{A1.31})$$

where index n runs over all molecules in the simulation box and index i runs over all atoms in molecule n. The derivative for the self-energy term of the Wolf method is computed as follows:

$$\frac{\partial U_{\text{self}}}{\partial \lambda_{\text{el},m}} = -2\lambda_{\text{el},m} \left(\frac{\text{erfc}(\alpha_{\text{el}} r_{\text{cut}})}{2r_{\text{cut}}} + \frac{\alpha_{\text{el}}}{\sqrt{\pi}} \right) \sum_j q_j^2 \qquad (\text{A1.32})$$

where index j runs over all atoms in fractional molecule m.

Damped and Shifted Version of the Wolf Method

The Wolf method can be used to accurately calculate electrostatic interactions, however, artificial structuring, i.e., unphysical arrangement of particles due to inaccurately described electrostatic interactions, around the cutoff distance is a potential problem [203, 335–337]. Fennell and Gezelter [180] solved this issue with a modification to the real-space term of the Wolf method. The real-space electrostatic energy between site i of molecule m and site j of molecule n in the damped and shifted (DSF) version of the Wolf method is computed as [119, 181]:

$$U_{\text{real},ij} = q_i q_j \left[\frac{\text{erfc}(\alpha_{\text{el}} r_{ij})}{r_{ij}} - \frac{\text{erfc}(\alpha_{\text{el}} r_{\text{cut}})}{r_{\text{cut}}} + \left(\frac{\text{erfc}(\alpha_{\text{el}} r_{\text{cut}})}{r_{\text{cut}}^2} + \frac{2\alpha_{\text{el}}}{\sqrt{\pi}} \frac{\exp[-\alpha_{\text{el}}^2 r_{\text{cut}}^2]}{r_{\text{cut}}} (r_{ij} - r_{\text{cut}}) \right) \right] \quad \text{(A1.33)}$$

where $\text{erfc}(x)$ is the complementary error function, r_{ij} is the distance between the sites i and j, r_{cut} is the cutoff radius, and α_{el} is the damping parameter. In this way, both $U_{\text{real},ij}$ and its derivative with respect to r_{ij} are continuous around r_{cut}. When either one or both of the sites involved in the interaction belong to a fractional molecule group, the real-space term in DSF Wolf method is computed from:

$$U_{\text{real},ij} = \lambda_{\text{el,t}} q_i q_j \left[\frac{\text{erfc}(\alpha_{\text{el}} (r_{ij} + Q))}{r_{ij} + Q} - \frac{\text{erfc}(\alpha_{\text{el}} (r_{\text{cut}} + Q))}{r_{\text{cut}} + Q} + \left(\frac{\text{erfc}(\alpha_{\text{el}} r_{\text{cut}})}{r_{\text{cut}}^2} + \frac{2\alpha_{\text{el}}}{\sqrt{\pi}} \frac{\exp[-\alpha_{\text{el}}^2 r_{\text{cut}}^2]}{r_{\text{cut}}} (r_{ij} - r_{\text{cut}}) \right) \right] \quad \text{(A1.34)}$$

where the term Q follows from Eq. (A1.14). The total scaling factor for electrostatic interactions $\lambda_{\text{el,t}}$ is calculated using the value of λ_{el} of the molecules m and n as $\lambda_{\text{el,t}} = \lambda_{\text{el},m} \lambda_{\text{el},n}$. The derivative of the DSF real-space term with respect to λ_m is calculated using:

$$\frac{\partial U_{\text{real},ij}^{\text{DSF}}}{\partial \lambda_{\text{el},m}} = \lambda_{\text{el},n} q_i q_j \left[\frac{\text{erfc}(\alpha_{\text{el}} (r_{ij} + \beta_{\text{el}}(1 - \lambda_{\text{el,t}})))}{r_{ij} + \beta_{\text{el}}(1 - \lambda_{\text{el,t}})} - \frac{\text{erfc}(\alpha_{\text{el}} (r_{\text{cut}} + \beta_{\text{el}}(1 - \lambda_{\text{el,t}})))}{r_{\text{cut}} + \beta_{\text{el}}(1 - \lambda_{\text{el,t}})} + \left(\frac{\text{erfc}(\alpha_{el} r_{\text{cut}})}{r_{\text{cut}}^2} + \frac{2\alpha_{el}}{\sqrt{\pi}} \frac{\exp[-\alpha_{el}^2 r_{\text{cut}}^2]}{r_{\text{cut}}} \right) (r_{ij} - r_{\text{cut}}) + \lambda_{\text{el,t}} \left(X(r_{ij}) - X(r_{\text{cut}}) \right) \right]$$

$$\text{(A1.35)}$$

where the term $X(r)$ follows from Eq. (A1.21). The exclusion term of the DSF version of the Wolf method between sites i and j of the molecule m is computed using:

$$U_{\text{exclusion},ij} = q_i q_j \left[\frac{\text{erfc}(\alpha_{\text{el}} r_{ij}) - 1}{r_{ij}} - \frac{\text{erfc}(\alpha_{\text{el}} r_{\text{cut}})}{r_{\text{cut}}} \right] \qquad \text{(A1.36)}$$

The exclusion term of DSF version of the Wolf method between sites i and j of molecule m, when m is a fractional molecule, is computed as:

$$U_{\text{exclusion},ij} = \lambda_{\text{el,t}} q_i q_j \left[\frac{\text{erfc}(\alpha_{\text{el}}(r_{ij} + Q)) - 1}{r_{ij} + Q} - \frac{\text{erfc}(\alpha_{\text{el}}(r_{\text{cut}} + Q))}{r_{\text{cut}} + Q} \right] \qquad \text{(A1.37)}$$

where $\lambda_{\text{el,t}} = \lambda_{\text{el},m}^2$. The derivative of the DSF exclusion term with respect to $\lambda_{\text{el},m}$ is calculated from:

$$\begin{aligned}
\frac{\partial U_{\text{exclusion},ij}}{\partial \lambda_{\text{el},m}} = 2\lambda_{\text{el},m} q_i q_j \bigg[& \frac{\text{erfc}(\alpha_{\text{el}}(r_{ij} + Q))}{r_{ij} + Q} - \frac{\text{erfc}(\alpha_{\text{el}}(r_{\text{cut}} + Q))}{r_{\text{cut}} + Q} + \\
& \lambda_{\text{el,t}} \left(X(r_{ij}) - X(r_{\text{cut}}) \right) - \frac{r_{ij} + Q + \lambda_{\text{el}} \beta_{\text{el}}}{(r_{ij} + Q)^2} \bigg] \qquad \text{(A1.38)}
\end{aligned}$$

where $X(r)$ follows from Eq. (A1.21). The self-energy term of DSF version of the Wolf method is computed as:

$$U_{\text{self}} = -\left(\frac{\text{erfc}(\alpha_{\text{el}} r_{\text{cut}})}{2 r_{\text{cut}}} + \frac{\alpha_{\text{el}}}{\sqrt{\pi}} \right) \sum_n \sum_i \lambda_{n,\text{el}}^2 q_{i,n}^2 \qquad \text{(A1.39)}$$

in which n runs over all molecules in the system and i runs over all atoms in molecule n. The derivative of the self-energy term with respect to $\lambda_{\text{el},m}$ of fractional molecule m becomes:

$$\frac{\partial U_{\text{self}}}{\partial \lambda_{\text{el},m}} = -2\lambda_{\text{el},m} \left(\frac{\text{erfc}(\alpha_{\text{el}} r_{\text{cut}})}{2 r_{\text{cut}}} + \frac{\alpha_{\text{el}}}{\sqrt{\pi}} \right) \sum_j q_j^2 \qquad \text{(A1.40)}$$

in which index j runs over all atoms in fractional molecule m.

A.2. Implementation of Hybrid Monte Carlo Trial Moves

The hybrid trial moves use a short Molecular Dynamics (MD) trajectory to simultaneously displace or rotate all molecules inside the simulation box. These trial moves are more efficient than the single-molecule trial moves in inducing a collective motion in the fluid [83, 173, 175] as in hybrid methods, the configurational space is explored along the trajectory of the natural motion of the system. This is because The interaction potential to generate the short MD trajectories does not need to be the actual interaction potential. It can be another interaction potential still resembling the actual one but computationally cheaper [82, 173].

A.2.1. Hybrid MC/MD Translation Trial Moves

In the hybrid MC translation trial move, a short MD simulation in the *NVE* ensemble is performed with a specified time step (Δt) and trajectory length (N_{step}). Although there are no restrictions on the choice of Δt and N_{step}, these parameters influence the efficiency of the sampling. It is therefore recommended that the optimal values of these parameters are chosen from short test runs, such that an average acceptance probability of ca. 50% and a maximum average displacement per unit of CPU time are achieved. All molecules are kept rigid, and the hybrid translation trial move is performed collectively (for all molecules) using the center of mass motion. To integrate the equations of motion, the velocity Verlet algorithm [184, 185] is used, which is time reversible and area-preserving (symplectic) [82, 338, 339]. It is important that the integration algorithm is time reversible as the classical equations of motion are time reversible and symplectic as the exact trajectories are known to conserve volume in phase space to provide reliable long time trajectories. The hybrid translation trial move is performed as follows [82, 176, 185, 340]:

1. Center of mass velocity vectors, $\mathbf{v}_i$, are randomly generated for each molecule i, where the vector components are drawn from a normal distribution with the mean value equal to 0 and a variance of 1.

2. The kinetic energy of translation of the old configuration is calculated as:

$$K_{\text{old}}^{\text{trans}} = \sum_{i=1}^{N} \frac{1}{2} m_i \mathbf{v}_{i,\text{old}}^2 \tag{A2.1}$$

   where i is the molecule number, N is the total number of molecules in the system, and m_i is the mass of molecule i.

3. All velocities are scaled by the factor $\sqrt{3Nk_{\text{B}}T/2K_{\text{old}}^{\text{trans}}}$ which adjusts the kinetic energy of the system according to the equipartition theorem [83]. The kinetic energy of the system ($K_{\text{old}}^{\text{trans}}$) is then recomputed using Eq. (A2.1).

4. The resultant force, $\mathbf{F}_i$, acting on each molecule i is computed. To reduce the computational costs, an approximation can be used for $\mathbf{F}_i$ (rather than its precise value), e.g., obtained from a computationally cheaper method, e.g., the damped and shifted version of the Wolf method instead of the Ewald summation. In principle, such an approximation would maintain a correct phase-space sampling [82].

5. The velocities of all molecules are updated to a half time step:

$$\mathbf{v}_{i,\text{old}} = \mathbf{v}_{i,\text{old}} + \frac{\mathbf{F}_i}{2m_i}\Delta t \qquad \text{(A2.2)}$$

6. The center-of-mass position vectors of all molecules are updated:

$$\mathbf{r}_{i,\text{new}} = \mathbf{r}_{i,\text{old}} + \mathbf{v}_{i,\text{old}}\Delta t \qquad \text{(A2.3)}$$

7. Using the new center-of-mass positions ($\mathbf{r}_{i,\text{new}}$), all atomic coordinates are updated.

8. The resultant forces on all molecules are recomputed based on the new atomic positions $\mathbf{r}_{i,\text{new}}$.

9. The velocities are updated to the full time step:

$$\mathbf{v}_{i,\text{new}} = \mathbf{v}_{i,\text{old}} + \frac{\mathbf{F}_i}{2m_i}\Delta t \qquad \text{(A2.4)}$$

10. For an MD trajectory of length N_{step}, steps 5-9 are repeated for $N_{\text{step}} - 1$ times.

11. The kinetic energy of the new configuration is calculated as:

$$K_{\text{new}}^{\text{trans}} = \sum_{i=1}^{N} \frac{1}{2}m_i\mathbf{v}_{i,\text{new}}^2 \qquad \text{(A2.5)}$$

12. The trial move is accepted or rejected according to the following acceptance rule [82]:
$$\text{acc}(\text{o} \rightarrow \text{n}) = \min\left(1, \exp[-\beta(\Delta U + \Delta K^{\text{trans}})]\right) \qquad \text{(A2.6)}$$

where o and n denote the old and new (initial and final) configurations on the MD trajectory, and ΔU and ΔK^{trans} are the differences in potential energy and translational kinetic energy, respectively, between the old and new configurations. β is defined as $1/(k_{\text{B}}T)$, where k_{B} is the Boltzmann constant, and T is the absolute temperature. It is important to note that U is the actual potential of the system, not the one used to compute the forces acting on particles as explained in point 4.

A.2.2. Hybrid MC/MD Rotation Trial Moves

In the hybrid rotation trial move, collective rotation of molecules as rigid bodies is performed using a short MD simulation in the *NVE* ensemble. The time step size (Δt) and trajectory length (N_{step}) of this MD run are chosen to maximize the efficiency of the sampling. For the rigid body rotation of molecules, the velocity Verlet-based algorithm of Miller et al. [186] (NOSQUISH) is used, which is symplectic and time reversible. At every time step, all molecules are rotated according to the total torque acting on the molecules, and only intermolecular interactions are taken into account to compute the forces and torques.

In the first step, the moment of inertia tensor, $\mathbf{I}_i$, of each molecule i about its center of mass is computed. To obtain the principal moments of inertia, the eigenvalues and eigenvectors of the inertia tensors are computed using the Jacobi method [341]. The computed eigenvectors indicate the direction of the principal axes, and the corresponding eigenvalues determine the values of inertia moments in these directions. The body frame of reference is taken to be the principal axes of each molecule, denoted by $\hat{x}$, $\hat{y}$, and $\hat{z}$, whereas the laboratory frame axes are specified by x, y, and z. The principal (diagonalized) moment of inertia tensor of molecule i is denoted by $\hat{\mathbf{I}}_i$, and its diagonal elements (eigenvalues of the $\mathbf{I}_i$ tensor), are represented by $\hat{I}_{\hat{x}\hat{x},i}$, $\hat{I}_{\hat{y}\hat{y},i}$, and $\hat{I}_{\hat{z}\hat{z},i}$. The principal axes are set such that $I_{\hat{x}\hat{x},i} > I_{\hat{y}\hat{y},i} > I_{\hat{z}\hat{z},i}$. The quaternion 4-vector, $\mathbf{q}_i^{(4)} = (q_{0,i} \ q_{1,i} \ q_{2,i} \ q_{3,i})^{\mathrm{T}}$ is then computed for the body frame of each molecule i, based on the direction of the principal axes. Subsequently, the rotation matrix, $\mathbf{R}_i$, for each molecule i is calculated according to:

$$\mathbf{R}_i = \begin{pmatrix} q_{0,i}^2 + q_{1,i}^2 - q_{2,i}^2 - q_{3,i}^2 & 2(q_{1,i}q_{2,i} - q_{0,i}q_{3,i}) & 2(q_{1,i}q_{3,i} + q_{0,i}q_{2,i}) \\ 2(q_{1,i}q_{2,i} + q_{0,i}q_{3,i}) & q_{0,i}^2 - q_{1,i}^2 + q_{2,i}^2 - q_{3,i}^2 & 2(q_{2,i}q_{3,i} - q_{0,i}q_{1,i}) \\ 2(q_{1,i}q_{3,i} - q_{0,i}q_{2,i}) & 2(q_{2,i}q_{3,i} + q_{0,i}q_{1,i}) & q_{0,i}^2 - q_{1,i}^2 - q_{2,i}^2 + q_{3,i}^2 \end{pmatrix} \tag{A2.7}$$

In the algorithm outlined here, a variable X computed in the body frame is denoted by $\hat{X}$, whereas it lacks the hat symbol when designated in the laboratory frame. The following steps are performed in the hybrid rotation trial move [186, 340, 342]:

1. Angular velocity vectors, $\hat{\omega}_i$, are randomly generated for every molecule i in its body frame, where each component of the angular velocity ($\omega_{\hat{x},i}$, $\omega_{\hat{y},i}$, and $\omega_{\hat{z},i}$) is obtained from a normal distribution with mean and variance values of 0 and 1, respectively.

2. The rotational kinetic energy of the system in the old configuration is computed according to:

$$K_{\text{old}}^{\text{rot}} = \sum_{i=1}^{N} \frac{1}{2} (I_{\hat{x}\hat{x},i} \hat{\omega}_{\hat{x},i}^2 + I_{\hat{y}\hat{y},i} \hat{\omega}_{\hat{y},i}^2 + I_{\hat{z}\hat{z},i} \hat{\omega}_{\hat{z},i}^2) \tag{A2.8}$$

   where i is the molecule number, and N is the total number of molecules in the system.

3. Similar to the hybrid translation trial move, the angular velocities of all molecules are scaled by a factor of $\sqrt{3Nk_{\mathrm{B}}T/2K_{\mathrm{old}}^{\mathrm{rot}}}$ to yield the correct temperature and kinetic energy. The rotational kinetic energy ($K_{\mathrm{old}}^{\mathrm{rot}}$) is then recomputed using Eq. (A2.8).

4. The positions of each atom j in molecule i, with respect to the center-of-mass of i, are computed in the body frame, using the inverse of the rotation matrix of molecule i:

$$\hat{\mathbf{r}}_{ji} = \mathbf{R}_i^{-1}\mathbf{r}_{ji} \tag{A2.9}$$

where $\mathbf{r}_{ji}$ is the position vector of atom j in molecule i, with respect to the center-of-mass of i, in the laboratory frame.

5. The resultant torque vector on each molecule i with N_i atoms, $\mathbf{T}_i$, is calculated about its center of mass in the laboratory frame:

$$\mathbf{T}_i = \sum_{j=1}^{N_i} \sum_k \left[\mathbf{r}_{ji} \times \mathbf{F}_{jk}\right] \tag{A2.10}$$

in which the indices j and k run over all atoms in molecule i and atoms in all other molecules except i, respectively. $\mathbf{r}_{ji}$ is the position vector of atom j with respect to the center-of-mass of molecule i, and $\mathbf{F}_{jk}$ denotes the force vector acting upon atom j of molecule i by atom k of another molecule. An approximate value of the force can be used in Eq. (A2.10) to reduce the computational costs.

6. The resultant torque on each molecule i in its body frame, $\hat{\mathbf{T}}_{\mathbf{i}}$, is computed using the transposed rotation matrix:

$$\hat{\mathbf{T}}_i = \mathbf{R}_i^{\mathrm{T}}\mathbf{T}_i \tag{A2.11}$$

7. The 4-vector quaternion torque of each molecule i in its body frame, $\hat{\mathbf{T}}_{\mathbf{q},i}^{(4)}$, is computed according to:

$$\hat{\mathbf{T}}_{\mathbf{q},i}^{(4)} = 2\mathbf{M}_i\hat{\mathbf{T}}_i^{(4)} \tag{A2.12}$$

where $\hat{\mathbf{T}}_i^{(4)} = (0 \ \hat{T}_{\hat{x},i} \ \hat{T}_{\hat{y},i} \ \hat{T}_{\hat{z},i})^{\mathrm{T}}$ is the 4-vector torque on molecule i in its body frame, and $\hat{T}_{\hat{x},i}$, $\hat{T}_{\hat{y},i}$, and $\hat{T}_{\hat{z},i}$ as the components of the $\hat{\mathbf{T}}_i$ vector. $\mathbf{M}_i$ is a matrix consisting of the quaternion components of the body frame of molecule i:

$$\mathbf{M}_i = \begin{pmatrix} q_{0,i} & -q_{1,i} & -q_{2,i} & -q_{3,i} \\ q_{1,i} & q_{0,i} & -q_{3,i} & q_{2,i} \\ q_{2,i} & q_{3,i} & q_{0,i} & -q_{1,i} \\ q_{3,i} & -q_{2,i} & q_{1,i} & q_{0,i} \end{pmatrix}$$

8. The angular momentum of every molecule i, $\hat{\mathbf{L}}_i$ is computed in its body frame using the principal moment of inertia tensor and the angular velocity:

$$\hat{\mathbf{L}}_i = \hat{\mathbf{I}}_i \hat{\omega}_i \tag{A2.13}$$

9. The 4-vector conjugate quaternion momentum of each molecule i, $\mathbf{P}_{\mathbf{q},i}^{(4)}$, is computed as:

$$\mathbf{P}_{\mathbf{q},i}^{(4)} = 2\mathbf{M}_i \hat{\mathbf{L}}_i^{(4)} \tag{A2.14}$$

where $\hat{\mathbf{L}}_i^{(4)} = (0 \ \hat{L}_{\hat{x},i} \ \hat{L}_{\hat{y},i} \ \hat{L}_{\hat{z},i})^{\mathrm{T}}$ is the 4-vector angular momentum of molecule i in its body frame, and $\hat{L}_{\hat{x},i}$, $\hat{L}_{\hat{y},i}$, and $\hat{L}_{\hat{z},i}$ are the components of the $\hat{\mathbf{L}}_i$ vector. For simplicity, the 4-vectors $\mathbf{P}_{\mathbf{q},i}^{(4)}$ and $\mathbf{q}_i^{(4)}$ are denoted by $\mathbf{P}_{\mathbf{q},i}$ and $\mathbf{q}_i$, respectively, in the following steps.

10. The quaternion momentum of every molecule i is updated to a half time step:

$$\mathbf{P}_{\mathbf{q},i}\left(t + \frac{\Delta t}{2}\right) = \mathbf{P}_{\mathbf{q},i}(t) + \frac{\Delta t}{2}\hat{\mathbf{T}}_{\mathbf{q},i}(t) \tag{A2.15}$$

11. The following steps in Eqs. (A2.16) to (A2.25) are repeated for m times (e.g., $m = 10$ [340]). A larger value of m increases the accuracy of the scheme at the expense of a larger computational cost [342]. For each molecule i, the quaternions are updated to the full time step:

$$\mathbf{P}_{\mathbf{q},i} \rightarrow \cos(\phi_3 \delta t/2)\mathbf{P}_{\mathbf{q},i} + \sin(\phi_3 \delta t/2)\mathbf{D_3}\mathbf{P}_{\mathbf{q},i} \tag{A2.16}$$
$$\mathbf{q}_i \rightarrow \cos(\phi_3 \delta t/2)\mathbf{q}_i + \sin(\phi_3 \delta t/2)\mathbf{D_3}\mathbf{q}_i \tag{A2.17}$$
$$\mathbf{P}_{\mathbf{q},i} \rightarrow \cos(\phi_2 \delta t/2)\mathbf{P}_{\mathbf{q},i} + \sin(\phi_2 \delta t/2)\mathbf{D_2}\mathbf{P}_{\mathbf{q},i} \tag{A2.18}$$
$$\mathbf{q}_i \rightarrow \cos(\phi_2 \delta t/2)\mathbf{q}_i + \sin(\phi_2 \delta t/2)\mathbf{D_2}\mathbf{q}_i \tag{A2.19}$$
$$\mathbf{P}_{\mathbf{q},i} \rightarrow \cos(\phi_1 \delta t)\mathbf{P}_{\mathbf{q},i} + \sin(\phi_1 \delta t)\mathbf{D_1}\mathbf{P}_{\mathbf{q},i} \tag{A2.20}$$
$$\mathbf{q}_i \rightarrow \cos(\phi_1 \delta t)\mathbf{q}_i + \sin(\phi_1 \delta t)\mathbf{D_1}\mathbf{q}_i \tag{A2.21}$$
$$\mathbf{P}_{\mathbf{q},i} \rightarrow \cos(\phi_2 \delta t/2)\mathbf{P}_{\mathbf{q},i} + \sin(\phi_2 \delta t/2)\mathbf{D_2}\mathbf{P}_{\mathbf{q},i} \tag{A2.22}$$
$$\mathbf{q}_i \rightarrow \cos(\phi_2 \delta t/2)\mathbf{q}_i + \sin(\phi_2 \delta t/2)\mathbf{D_2}\mathbf{q}_i \tag{A2.23}$$
$$\mathbf{P}_{\mathbf{q},i} \rightarrow \cos(\phi_3 \delta t/2)\mathbf{P}_{\mathbf{q},i} + \sin(\phi_3 \delta t/2)\mathbf{D_3}\mathbf{P}_{\mathbf{q},i} \tag{A2.24}$$
$$\mathbf{q}_i(t + \Delta t) \rightarrow \cos(\phi_3 \delta t/2)\mathbf{q}_i + \sin(\phi_3 \delta t/2)\mathbf{D_3}\mathbf{q}_i \tag{A2.25}$$

where $\delta t = \Delta t/m$, $\phi_k = (\mathbf{P}_{\mathbf{q},i}^{\mathrm{T}}\mathbf{D}_k\mathbf{q}_i)/(4\hat{I}_{kk,i})$ (for $k = 1, 2, 3$), in which $\hat{I}_{11,i} = \hat{I}_{\hat{x}\hat{x},i}$, $\hat{I}_{22,i} = \hat{I}_{\hat{y}\hat{y},i}$, and $\hat{I}_{33,i} = \hat{I}_{\hat{z}\hat{z},i}$, and:

$$\mathbf{D_1}\mathbf{q}_i = (-q_{1,i} \quad q_{0,i} \quad q_{3,i} \quad -q_{2,i})^{\mathrm{T}} \tag{A2.26}$$
$$\mathbf{D_2}\mathbf{q}_i = (-q_{2,i} \quad -q_{3,i} \quad q_{0,i} \quad q_{1,i})^{\mathrm{T}} \tag{A2.27}$$
$$\mathbf{D_3}\mathbf{q}_i = (-q_{3,i} \quad q_{2,i} \quad -q_{1,i} \quad q_{0,i})^{\mathrm{T}} \tag{A2.28}$$

$\mathbf{D}_k\mathbf{P}_{\mathbf{q},i}$ ($k = 1, 2, 3$) are similarly computed, where the quaternion components are replaced by the corresponding components of the quaternion momenta:

$$\mathbf{D}_1\mathbf{P}_{\mathbf{q},i} = (-P_{q,1,i} \quad P_{q,0,i} \quad P_{q,3,i} \quad -P_{q,2,i})^{\mathrm{T}} \tag{A2.29}$$

$$\mathbf{D}_2\mathbf{P}_{\mathbf{q},i} = (-P_{q,2,i} \quad -P_{q,3,i} \quad P_{q,0,i} \quad P_{q,1,i})^{\mathrm{T}} \tag{A2.30}$$

$$\mathbf{D}_3\mathbf{P}_{\mathbf{q},i} = (-P_{q,3,i} \quad P_{q,2,i} \quad -P_{q,1,i} \quad P_{q,0,i})^{\mathrm{T}} \tag{A2.31}$$

12. The new rotation matrix $\mathbf{R}_i$ is computed for each molecule i, using Eq. (A2.7), based on the new quaternions obtained after applying Eqs. (A2.16) to (A2.25).

13. The new positions of atoms are computed using the new rotation matrix:

$$\mathbf{r}_{ji} = \mathbf{R}_i\hat{\mathbf{r}}_{ji} \tag{A2.32}$$

where $\mathbf{r}_{ji}$ and $\hat{\mathbf{r}}_{ji}$ are the position vectors of atom j in molecule i, with respect to the center-of-mass of i, in the laboratory and body frames ($\hat{\mathbf{r}}_{ji}$ is computed in step 4), respectively. Using $\mathbf{r}_{ji}$ and the center-of-mass coordinates, the positions of the atoms are updated.

14. The angular momentum and angular velocity of every molecule i are updated to a half time step:

$$\hat{\mathbf{L}}_i^{(4)} = \frac{1}{2}\mathbf{M}_i^{-1}\mathbf{P}_{\mathbf{q},i}$$
$$\hat{\omega}_{k,i} = \hat{L}_{k,i}/\hat{I}_{kk,i} \quad (k = 1, 2, 3) \tag{A2.33}$$

in which $k = 1$, $k = 2$, and $k = 3$ correspond to the $\hat{x}$, $\hat{y}$, and $\hat{z}$ axes, respectively.

15. The new torques in laboratory frame and body frame, as well as the new quaternion torques are computed at half time step, as demonstrated in steps 5-7.

16. The quaternion momentum of each molecule i is updated from a half time step (output of step 11) to a full time step:

$$\mathbf{P}_{\mathbf{q},i}(t + \Delta t) = \mathbf{P}_{\mathbf{q},i}(t + \frac{\Delta t}{2}) + \frac{\Delta t}{2}\hat{\mathbf{T}}_{\mathbf{q},i}(t + \frac{\Delta t}{2}) \tag{A2.34}$$

17. The new angular momenta and angular velocities are computed for all molecules at a full time step, similar to step 14.

18. For an MD trajectory of length N_{step}, steps 10-17 are repeated for $N_{\text{step}} - 1$ times.

19. The new rotational kinetic energy of the system, $K_{\text{new}}^{\text{rot}}$, is computed based on the final angular velocities:

$$K_{\text{new}}^{\text{rot}} = \sum_{i=1}^{N} \frac{1}{2}(\hat{I}_{\hat{x}\hat{x},i}\hat{\omega}_{\hat{x},i}^2 + \hat{I}_{\hat{y}\hat{y},i}\hat{\omega}_{\hat{y},i}^2 + \hat{I}_{\hat{z}\hat{z},i}\hat{\omega}_{\hat{z},i}^2) \qquad (A2.35)$$

where i is the molecule number and N is the total number of molecules in the system.

20. The trial move is accepted or rejected according to the acceptance rule [82]:

$$\text{acc(o} \rightarrow \text{n)} = \min\left(1, \exp[-\beta(\Delta U + \Delta K^{\text{rot}})]\right) \qquad (A2.36)$$

where o and n denote the old and new (initial and final) configurations on the MD trajectory, and ΔU and ΔK^{rot} are the differences in potential energy and rotational kinetic energy, respectively, between the old and new configurations. β is defined as $1/(k_{\text{B}}T)$, where k_{B} is the Boltzmann constant, and T is the absolute temperature. For more details on this rigid body dynamics integrator, the reader is referred to Refs. [186, 342].

Appendix B

B.1. Derivation of an Expression for Mole Fraction-based Reaction Equilibrium Constants

Our aim is to derive an expression for the reaction equilibrium constant K as a function of the standard ideal gas chemical potential of species i (μ_i^0), the excess chemical potential of species i (μ_i^{ex}), and the absolute temperature T. As an example, let us assume a reaction $A + S \rightleftharpoons B + C$ where S is the solvent. Using Eqs. (1.1), (1.2) and (3.2), we can write [134]:

$$
\nu_{A,j}\mu_A^0 + \nu_{A,j}\mu_A^{\text{ex}} + \nu_{A,j}RT\ln\left[\frac{\rho_A}{\rho_0}\right]
$$
$$
+ \nu_{B,j}\mu_B^0 + \nu_{B,j}\mu_B^{\text{ex}} + \nu_{B,j}RT\ln\left[\frac{\rho_B}{\rho_0}\right]
$$
$$
+ \nu_{C,j}\mu_C^0 + \nu_{C,j}\mu_C^{\text{ex}} + \nu_{C,j}RT\ln\left[\frac{\rho_C}{\rho_0}\right] \tag{B.1}
$$
$$
+ \nu_{S,j}\mu_S^0 + \nu_{S,j}\mu_S^{\text{ex}} + \nu_{S,j}RT\ln\left[\frac{\rho_{\text{pure}}}{\rho_0}\right] - \nu_{S,j}RT\left(\frac{1-X_S}{X_S}\right) = 0
$$

For an arbitrary chemical reaction, this can be rewritten as:

$$
\exp\left[-\left(\sum_{i=1}^{N_{\text{species}}}\frac{\nu_{i,j}(\mu_i^0 + \mu_i^{\text{ex}})}{RT} + \nu_{s,j}\ln\left[\frac{\rho_{\text{pure}}}{\rho_0}\right]\right)\right](V\rho_0)^{\nu_{\text{total,solute},j}} =
$$
$$
\exp\left[-\nu_{s,j}\left(\frac{1-X_S}{X_S}\right)\right]\prod_{i=1}^{N_{\text{solute}}}N_i^{\nu_{i,j}} \tag{B.2}
$$

where N_{solute} is the number of solutes (excluding the solvent) in the reaction, N_i is the number molecules of the species i, $\nu_{s,j}$ are the stoichiometric coefficient of the solvent in reaction j, and $\nu_{\text{total,solute},j}$ is the sum of the stoichiometric coefficients of all solutes in reaction j ($\sum_{i=1}^{N_{\text{solute}}}\nu_{i,j}$). We define the equilibrium constant of reaction j as:

$$
K_j' = \exp\left[-\nu_{S,j}\left(\frac{1-X_S}{X_S}\right)\right]\prod_{i=1}^{N_{\text{solute}}}N_i^{\nu_{i,j}} \tag{B.3}
$$

The left side of the Eq. (B.2) can be used to compute the desired equilibrium constant K_{des}' as a function of μ_i^0, μ_i^{ex}, T, and V.

$$K'_{j,\text{des}} = \exp\left[-\left(\sum_{i=1}^{N_{\text{species}}} \frac{v_{i,j}(\mu_i^0 + \mu_i^{\text{ex}})}{RT} + v_{\text{S},j}\ln\left[\frac{\rho_{\text{pure}}}{\rho_0}\right]\right)\right](V\rho_0)^{v_{\text{total,solute},j}} \quad \text{(B.4)}$$

Using the values of μ_i^0 (computed by quantum chemical calculations [82, 96]), μ_i^{ex} (computed by Monte Carlo simulations [82, 96, 97]), T, V, and ρ_{pure}, we can compute the equilibrium constant K'_{des} for any reaction.

The equilibrium constants can also be defined with the number molecules of each species or the mole fraction of each species:

$$K_j = \prod_{i=1}^{N_{\text{species}}} X_i^{v_{i,j}} \quad \text{(B.5)}$$

where X_i is the mole fraction of species i. Note that the summation in Eq. (B.5) includes the solvent mole fraction and originates from defining the chemical potential of the species using a pure-liquid reference state [197]:

$$\mu_i = \mu_i^* + RT\ln[X_i\gamma_i] \quad \text{(B.6)}$$

where γ_i is the activity coefficient of species i and μ_i^* is the reference chemical potential of the pure component i in the liquid phase. γ_i is incorporated into K_j in our calculations and assumed constant. To convert K'_j to K_j, we divide the right-hand side of Eq. (B.5) with the right-hand side of Eq. (B.3) so:

$$K_j = K'_j \frac{X_{\text{s}}^{v_{\text{s},j}}}{\exp\left[-v_{\text{s},j}\left(\frac{1-X_{\text{s}}}{X_{\text{s}}}\right)\right]\left(\sum_{i=1}^{N_{\text{species}}} N_i\right)^{v_{\text{total,solute},j}}} \quad \text{(B.7)}$$

The desired equilibrium constant K_j ($K_{j,\text{des}}$) as a function of μ^0, μ^{ex}, T, and V can be computed as:

$$K_{j,\text{des}} = \exp\left[-\left(\sum_{i=1}^{N_{\text{species}}} \frac{v_{i,j}(\mu_i^0 + \mu_i^{\text{ex}})}{RT} + v_{\text{s},j}\ln\left[\frac{\rho_{\text{pure}}}{\rho_0}\right]\right) + v_{\text{s},j}\left(\frac{1-X_{\text{s}}}{X_{\text{s}}}\right)\right]$$
$$\left(\frac{V\rho_0}{\sum_{i=1}^{N_{\text{species}}} N_i}\right)^{v_{\text{total,solute},j}} X_{\text{s}}^{v_{\text{s},j}} \quad \text{(B.8)}$$

This means that $K_{j,\text{des}} = K_j$ at equilibrium. $K_{j,\text{des}}$ can be constant or it can be solved iteratively for changing values of X_{s}. In CASpy, we solve $K_{j,\text{des}}$ iteratively for changing values of X_{s}. That means that we compute new values of X_{s} and $K_{j,\text{des}}$ in every iteration of the solver and this is continued until the difference between the new X_{s} and the old X_{s} no longer changes ($< 10^{-3}$).

B.2. Input File for the Chemical Reaction Equilibrium Solver CASpy

In this section, we explain the input file for CASpy in detail. For this purpose, we used the CO_2/MDEA/water system as a case study. The reactions (Reactions R1–R4 of Chapter 3) and the mass balance equations (Eqs. (3.9) to (3.12)) involved in this system are shown in the Methods section of Chapter 3. Note that the input file should be in the same directory with **main.py** and **functions.py** for solver to perform properly. An example input file for CO_2/MDEA/water system (see Section 3.2.2 for details of this system) is:

```
Temperature (K)
313.15
Number of Species
8
C0 (initial guess) / [mol/dm3]
1.0e-10 3.0e-10 1.0e-10 55.0638 2.500E-05 1.0e-10 1.0e-10 2.5
Names of species
HCO3- H3O+  CO3--  H2O  CO2  OH-  MDEAH+  MDEA
Charges
-1 1 -2 0 0 -1 1 0
Name of the solvent
H2O
Pure Density of the Solvent / [mol/dm3]
55.0638
mu^0 species / [kJ/mol] (only for the calculation of K_j,des)
0.0 -338.21 0.0 -965.23 0.0 0.0 -7428.61 -7758.70
mu^ex species / [kJ/mol] (only for the calculation of K_j,des)
0.0 -771.50 0.0 -27.83 0.0 0.0 -586.34 -43.77
Impose Ptotal and gas composition? (T=True or F=False)
F
Ptotal / [kPa] (only used if Ptotal and gas composition is imposed)
0.0
Gas phase species
CO2
Gas phase composition (only used if Ptotal and gas composition is imposed)
1
mu^ex gases / [kJ/mol]
0.41013
Ctotal,gas / [mol/dm3] (Total concentration of the gases in liquid phase)
2.5E-05 4.06E-05 6.6E-05 1.07E-04 1.74E-04 2.82E-04 4.58E-04 7.44E-04
Number of Reactions
4
Stoichiometry
1 1 0 -2 -1 0 0 0
-1 1 1 -1 0 0 0 0
0 1 0 -1 0 0 -1 1
0 1 0 -2 0 1 0 0
ln(K) for reactions (if QMMC then computed using K_des expression)
-18.34 -27.55 QMMC -39.21
Number of mass balance equations (excluding charge neutrality)
3
Balances
1 3 5
7 8
2 4 6
```

The lines in the input file represent the following:

- Temperature: The absolute temperature.

- Number of Species: Number of species in the liquid phase.

- C0 (initial guess): Initial guess of the composition in the liquid phase. This is a list of initial concentrations of species in mol dm^{-3}. In our example, we used a lean solvent (only MDEA and water in the solution) as our initial guess. Note that none of the concentrations in the initial guess should be zero (due to the boundaries we use in our solver), instead, one can input a very low concentration. If any concentration in the initial guess is inputted zero or lower than zero (≤ 0), then it is changed by 10^{-10} mol dm^{-3}. Although the solver works if the initial guess does not satisfy charge neutrality, we recommend an initial guess that satisfies charge neutrality for quicker results. The solver does not print a warning if charge neutrality is not satisfied by the initial guess and will continue to run.

- Names of species: Names of the species in the liquid phase.

- Charges: Net charges of the molecules/ions in the liquid phase.

- Name of the solvent: The name of the solvent.

- Pure Density of the Solvent: Density of the pure solvent in mol dm^{-3}. The name of the solvent and the pure density of the solvent are used to compute the desired equilibrium constants of reactions using Eq. (B.8).

- mu^0 species: A list of the values of μ_i^0 in kJ mol^{-1} for the species involved in reactions. Only used if the equilibrium constants are computed using Eq. (B.8). See Table B.6 for the values of μ_i^0 used in this example.

- mu^ex species: A list of the values of μ_i^{ex} in kJ mol^{-1} for the species involved in reactions. Only used if the equilibrium constants are computed using Eq. (B.8). See Tables B.7 and B.9 for the values of μ_i^{ex} used in this example.

- Impose Ptotal and gas composition? (T=True or F=False): Are the total gas pressure and the gas composition imposed in the calculation? If True, the solver assumes an infinite gas phase and the speciations are computed for all Ptotal (in kPa) listed in the next line. If the total gas pressure and gas composition are imposed, no mass balance equation is used for the species in the gas phase since there is mass transfer from the infinite gas phase to the liquid phase.

- Ptotal / [kPa] (only used if Ptotal and gas composition is imposed): The list of total gas pressures. Used only if the total gas pressure and gas composition are imposed to compute the partial pressures of the species in the gas phase.

- **Gas phase species**: The names of the species in the gas phase.

- **Gas phase composition (only used if Ptotal and gas composition is imposed)**: The composition of the gas phase. The values in this list are normalized so the values sum up to 1.

- **mu^ex gases / [kJ/mol]**: The values of μ_i^{ex} for the gas phase species in the solvent.

- **Ctotal,gas / [mol/dm3] (Total concentration of the gases in liquid phase)**: A list of concentrations on the gas phase species in the liquid phase in $\mathrm{mol\,dm^{-3}}$. Only used if the total gas pressure and gas composition are not imposed.

- **Number of Reactions**: Number of reactions in the liquid phase.

- **Stoichiometry**: The stoichiometric coefficients of all species for each reaction. See Section 3.2.2 for the reactions in CO$_2$/MDEA/water system.

- **ln(K) for reactions**: The mole fraction-based equilibrium constants (Eq. (3.3)) for each reaction in the liquid phase. In case the desired equilibrium constant should be computed using Eq. (B.8), the input should be "QMMC".

- **Number of mass balance equations**: Number of mass balance equations.

- **Balances**: A list of species involved in each mass balance equation. For example, the line "1 3 5" shows that the species at the first, third and fifth place in the names line (HCO_3^-, CO_3^{2-}, and CO_2) are included in the first mass balance equation (CO_2 balance). See Section 3.2.2 for the mass balance equations in CO$_2$/MDEA/water system.

The output from CASpy is printed on a file called "output.log" on the same directory as the input file. First, the initial conditions are printed in the output file. Then, for each solution (i.e. for each gas concentration listed under "Ctotal,gas / [mol/dm3]"), CASpy prints:

- the total gas concentration for this solution as C_i where i is the name of the gas species,

- maximum residual in the objective function,

- names of the species in the solution as specified in the input file,

- concentrations of each species at chemical equilibrium,

- mole fractions of each species at chemical equilibrium,

- the desired reaction equilibrium constants for the reactions specified in the input file,

- the actual reaction equilibrium constants computed using the mole fractions of the species,

- and the values of the residuals corresponding to mass balance equations and charge neutrality.

B.3. Computing μ_i^0 and μ_i^{ex}

B.3.1. Computing μ_i^0 using Quantum Chemistry Calculations

Quantum chemistry calculations [82, 96] or thermodynamic data sets such as the JANAF tables [135, 136] can be used to compute molecular partition functions of isolated molecules. Molecular partition functions can be used to compute heat capacities, internal energies, or chemical potentials of species [77, 96]. In this section, we explain how to obtain the standard ideal gas chemical potential of species using the Gaussian09 software [78]. For more detail on molecular partition functions, the reader is referred to Refs. [77, 96]. The standard ideal gas chemical potential can be computed using the molecular partition function using [77, 96]:

$$\mu_i^0 = -RT \ln \left[\frac{q_{0,i}}{\rho_0 \Lambda_i^3} \right] - D_{0,i} \tag{B.9}$$

where μ_i^0 is the standard ideal gas chemical potential of species i, R is the ideal gas constant, T is the absolute temperature, $q_{0,i}$ is the molecular partition function (excluding the translational part) of the molecule with the ground state energy of the molecule is taken as zero [96], ρ_0 is the reference number density of 1 molecule Å^{-3}, Λ_i is the thermal de Broglie wavelength of molecule i, and $D_{0,i}$ is the atomization energy of molecule i, which is the energy required to break all bonds in the molecule [343] ($D_{0,i} > 0$). The atomization energy of molecule i can be computed using [78, 96]:

$$D_{0,i} = \sum_{j=1}^{N_{\text{atoms},i}} y_j \varepsilon_{\text{e},j} - \varepsilon_{\text{e},i} - \varepsilon_{\text{ZPE},i} \tag{B.10}$$

where $N_{\text{atoms},i}$ is the number of atoms in the molecule i, y_j is the number of atoms of type j in molecule i, $\varepsilon_{\text{e},j}$ is the electronic energy of the atom of type j, $\varepsilon_{\text{e},i}$ is the electronic energy of molecule i, and $\varepsilon_{\text{ZPE},i}$ is the zero point vibrational energy of molecule i (the vibrational energy at the ground state). The definition of μ_i^0 in Eq. (B.9) is consistent with the reference state of the chemical potential used in the definitions of Eq. (1.2) and Eq. (3.2) of Chapter 3. As explained in Chapter 3, other definitions of the reference state of the chemical potential are also possible.

It should be noted that Gaussian09 [78] does not print the electronic energies of individual atoms when the energy of a molecule is computed. Therefore, the electronic energies of individual atoms must be computed separately. It is also important that the zero point energy is included in the electronic energy computed by Gaussian09, so the zero point energy should not be subtracted from the electronic energies of the individual atoms (Eq. (B.10)). Also, larger molecules such as MDEA

and MEA has many different conformers with different ground state energies. A conformer search must be performed for these type of molecules to obtain the free energies of conformers. Although the conformers with similar free energies can be accounted using a "lumping" procedure [344], we only use the conformer with minimum free energy since the differences between the free energy of the conformer with minimum free energy and the free energies of the other conformers are large ($\gg 1\, k_B T$). The standard state ideal chemical potential of a molecule can be computed using Gaussian09 (with the `Freq` keyword). However, Gaussian09 uses a different reference state ($P_0 = 1\,\mathrm{bar}$) than Brick-CFCMC ($\rho_0 = 1$ molecule Å^{-3}). The standard state ideal gas chemical potential at the Gaussian09 reference state (μ_i^G) can be computed using:

$$\mu_i^G = -RT \ln\left[\frac{q_{0,i} k_B T}{P_0 \Lambda_i^3}\right] - D_{0,i} \tag{B.11}$$

Also in Eq. (B.11), $q_{0,i}$ is used with the ground state energy of the molecule as a reference. The value of the term $\frac{q_{0,i} k_B T}{P_0 \Lambda_i^3}$ and its natural logarithm can be computed by Gaussian09 [78] when frequency calculations are enabled (with the `Freq` keyword). The logarithm term in Eq. (B.11) is printed by Gaussian09 [78] in the thermochemistry section of the output file. The line "`Total V=0`" in the table where "Q" is tabulated shows the term $\frac{q_{0,i} k_B T}{P_0 \Lambda_i^3}$ and its natural logarithm. We can use this value tabulated in the thermochemistry section of Gaussian09 output directly in Eq. (B.11). To use the values of μ_i^G computed by Gaussian09 in CASpy (or Brick-CFCMC [96, 97, 123]), a conversion is needed to the correct reference state. The conversion from μ_i^G (Eq. (B.11)) to μ_i^0 (Eq. (B.9)) can be performed using:

$$\mu_i^0 = \mu_i^G + RT \ln\left[\frac{k_B T \rho_0}{P_0}\right] \tag{B.12}$$

As an example, we will compute the value of μ_i^0 for water at 313.15 K. We optimized and computed free energy of water at 313.15 K using the G4 method. Below the input file to compute the value of μ_i^0 for water (including an geometry optimization step) using Gaussian09 [78] can be found:

```
%Chk=h2o.chk
#p G4 Opt Freq pop=(nbo,esp) Temperature=313.15 Volume

H2O

0 1
O          0.00000         -0.11195          0.00000
H         -0.78304          0.49423          0.00000
H          0.78304          0.49423          0.00000
```

We show a small part of the Gaussian09 [78] output below.

```
...
-------------------
- Thermochemistry -
-------------------
Temperature   313.150 Kelvin.  Pressure   1.00000 Atm.
Atom    1 has atomic number  8 and mass  15.99491
Atom    2 has atomic number  1 and mass   1.00783
Atom    3 has atomic number  1 and mass   1.00783
Molecular mass:    18.01056 amu.
Principal axes and moments of inertia in atomic units:
1         2         3
Eigenvalues --    2.26052   4.11754   6.37806
X            0.00000   0.00000   1.00000
Y            1.00000   0.00000   0.00000
Z            0.00000   1.00000   0.00000
This molecule is an asymmetric top.
Rotational symmetry number  2.
Rotational temperatures (Kelvin)    38.31594    21.03534    13.57997
Rotational constants (GHZ):       798.37555   438.30579   282.96103
Zero-point vibrational energy     56124.9 (Joules/Mol)
13.41416 (Kcal/Mol)
Vibrational temperatures:   2405.69  5472.96  5621.88
(Kelvin)

Zero-point correction=                           0.021377
Thermal correction to Energy=                    0.024355
Thermal correction to Enthalpy=                  0.025347
Thermal correction to Gibbs Free Energy=         0.002646
Sum of electronic and zero-point Energies=           -76.404700
Sum of electronic and thermal Energies=              -76.401722
Sum of electronic and thermal Enthalpies=            -76.400730
Sum of electronic and thermal Free Energies=         -76.423431

E (Thermal)            CV                S
KCal/Mol      Cal/Mol-Kelvin   Cal/Mol-Kelvin
Total                 15.283            6.016            45.490
Electronic             0.000            0.000             0.000
Translational          0.933            2.981            34.852
Rotational             0.933            2.981            10.629
Vibrational           13.416            0.054             0.008
Q              Log10(Q)         Ln(Q)
Total Bot      0.693662D-01     -1.158852        -2.668356
Total V=0      0.159514D+09      8.202800        18.887645
Vib (Bot)      0.435059D-09     -9.361452       -21.555540
Vib (V=0)      0.100046D+01      0.000200         0.000461
Electronic     0.100000D+01      0.000000         0.000000
Translational  0.339657D+07      6.531040        15.038276
Rotational     0.469418D+02      1.671560         3.848908

...
Temperature=              313.150000 Pressure=             1.000000
E(ZPE)=                     0.021065 E(Thermal)=           0.024044
E(CCSD(T))=               -76.207699 E(Empiric)=          -0.027788
DE(Plus)=                 -0.012885 DE(2DF)=              -0.074805
E(Delta-G3XP)=            -0.085401 DE(HF)=               -0.009735
G4(0 K)=                 -76.397249 G4 Energy=            -76.394271
G4 Enthalpy=             -76.393279 G4 Free Energy=       -76.415980
```

Table B.1: Electronic energies (ε_e) of the individual atoms related to Chapter 3 computed using Gaussian09 with G4 composite method.

Atom	ε_e / kJ mol^{-1}
H	-1.313×10^3
O	-1.970×10^5
N	-1.433×10^5
C	-9.933×10^4

```
58    1\1\GINC-C061\Mixed\G4\G4\H2O1\XXX\17-Jun-2022\0\\#p G4 Opt Freq po
59    p=(nbo,esp) Temperature=313.15 Volume\\H2O\\0,1\O,0,0.,-0.1042712687,0
60    .\H,0,-0.7563319142,0.4903906343,0.\H,0,0.7563319142,0.4903906343,0.\\
61    Version=EM64L-G09RevB.01\State=1-A1\MP2/GTBas1=-76.1967582\MP4/GTBas1=
62    -76.2072004\CCSD(T)/G3Bas1=-76.2076993\MP2/GTBas2=-76.2095143\MP4/GTBa
63    s2=-76.2200856\MP2/GTBas3=-76.2673009\MP4/GTBas3=-76.2820058\HF/GTLarg
64    eXP=-76.0573671\MP2/GTLargeXP=-76.3654584\HF/GFHFB1=-76.0648885\HF/GFH
65    FB2=-76.0666683\G4=-76.3972495\FreqCoord=0.,-0.1970441413,0.,-1.429260
66    1835,0.926703997,0.,1.4292601835,0.926703997,0.\PG=C02V C2(O1),SGV(H2
67    )\NImag=0\\0.66772935,0.,0.45904202,0.,0.,-0.00003485,-0.33386467,0.1
68    9890011,0.,0.36695722,0.26249795,-0.22952101,0.,-0.23069903,0.21793357
69    ,0.,0.,0.00001743,0.,0.,-0.00009409,-0.33386467,-0.19890011,0.,-0.0330
70    9255,-0.03179892,0.,0.36695722,-0.26249795,-0.22952101,0.,0.03179892,0
71    .01158744,0.,0.23069903,0.21793357,0.,0.,0.00001743,0.,0.,0.00007667,0
72    .,0.,-0.00009409\\0.,-0.00012296,0.,0.00010199,0.00006148,0.,-0.000101
73    99,0.00006148,0.\\\@
74    Job cpu time:  0 days  0 hours  0 minutes 27.4 seconds.
75    File lengths (MBytes):  RWF=      18 Int=      0 D2E=      0 Chk=      3
76    Scr=      1
77    Normal termination of Gaussian 09 at Fri Jun 17 15:41:48 2022.
78    ----------------------------------------------------------------------
```

The Gaussian09 [78] output shows that the natural logarithm of the term $\frac{q_{0,i}(T)k_B T}{P_0 \Lambda^3}$ ($P_0 = 1$ bar) is computed as 18.89 (the line with "Total V=0" in thermochemistry section of the output, line 43), the electronic energy (including the zero-point energy) of the molecule is computed as -76.40 Hartree (-2.01×10^5 kJ mol^{-1}) (line 56). From separate calculations, we computed the electronic energy of a hydrogen atom and an oxygen atom as -0.50 Hartree (-1.31×10^3 kJ mol^{-1}) and -75.05 Hartree (-1.97×10^5 kJ mol^{-1}) at 313.15 K, respectively (Table B.1). Using Eq. (B.10), we computed the atomization energy $D_{0,\text{water}}$ as 916.06 kJ mol^{-1}. Using Eq. (B.11), and Eq. (B.12), we compute the μ_i^0 of water as -965.23 kJ mol^{-1} at 313.15 K.

B.3.2. Computing μ_i^0 using the JANAF Tables

Thermodynamic data sets such as the JANAF tables can also be used to compute μ_i^0 of a molecule. The JANAF tables provide thermodynamic functions and parameters such as the Gibbs free energy, the enthalpy of formation, and heat capacity [135, 136] as a function of temperature. As explained in the previous section, we use

the ground state energy as the reference state in our calculations, so the Gibbs free energy values should be shifted to the enthalpy at $T = 0\,\mathrm{K}$. JANAF tables use the same reference state as Gaussian09 ($P_0 = 1\,\mathrm{bar}$). Therefore, we use the same symbol for the standard state ideal gas chemical potential computed using the JANAF tables as the standard state ideal gas chemical potential computed using Gaussian09 (μ_i^{G}). Note that μ_i^{G} should be converted to μ_i^0 using Eq. (B.12) to use the correct reference state in Brick-CFCMC [96, 97] or CASpy. The standard ideal gas chemical potential of a molecule can be computed in terms of the entries in JANAF tables using [96]:

$$\mu_i^G = [G_i^0(T) - H_i^0(T_{\mathrm{r}})] - [H_i^0(0\,\mathrm{K}) - H_i^0(T_{\mathrm{r}})] - D_{0,i} \tag{B.13}$$

where G_i^0 is the standard ideal gas Gibbs free energy of molecule i, H_i^0 is the standard enthalpy of molecule i, T is the absolute temperature, and T_{r} is the reference temperature ($T_{\mathrm{r}} = 298.15\,\mathrm{K}$ for the JANAF tables). The terms $-[G_i^0(T) - H_i^0(T_{\mathrm{r}})]/T$ and $[H_i^0(T) - H_i^0(T_{\mathrm{r}})]$ reported in the JANAF tables can be used to compute the terms $[G_i^0(T) - H_i^0(T_{\mathrm{r}})]$ and $[H_i^0(0\,\mathrm{K}) - H_i^0(T_{\mathrm{r}})]$ in Eq. (B.13). The atomization energy $D_{0,i}$ can also be computed using the JANAF tables using the difference between the enthalpy of formation of the molecule and the enthalpy of formation of the individual atoms [96]:

$$D_{0,i} = \sum_{j=1}^{N_{\mathrm{atoms},i}} y_j \Delta_f H_j^0(0\,\mathrm{K}) - \Delta_f H_i^0(0\,\mathrm{K}) \tag{B.14}$$

where $N_{\mathrm{atoms},i}$ is the number of atoms in molecule i, y_j denotes the number of atoms of type j in molecule i, and $\Delta_f H^0$ is the enthalpy of formation as tabulated in the JANAF tables. As an example, we compute μ_i^0 of water at $313.15\,\mathrm{K}$. The terms $-[G_i^0(T) - H_i^0(T_{\mathrm{r}})]/T$ and $[H_i^0(0\,\mathrm{K}) - H_i^0(T_{\mathrm{r}})]$ are reported as $188.87\,\mathrm{J\,K^{-1}\,mol^{-1}}$ and $-9.904\,\mathrm{kJ\,mol^{-1}}$ for water, respectively. Also, $\Delta_f H_{\mathrm{H_2O}}^0(0\,\mathrm{K})$, $\Delta_f H_{\mathrm{H}}^0(0\,\mathrm{K})$, and $\Delta_f H_{\mathrm{O}}^0(0\,\mathrm{K})$ are listed in the JANAF tables as $-238.921\,\mathrm{kJ\,mol^{-1}}$, $216.035\,\mathrm{kJ\,mol^{-1}}$, and $246.79\,\mathrm{kJ\,mol^{-1}}$, respectively. Using the values of $\Delta_f H_i^0(0\,\mathrm{K})$ and Eq. (B.14), we computed the atomization energy $D_{0,\mathrm{water}}$ as $917.84\,\mathrm{kJ\,mol^{-1}}$. The $D_{0,\mathrm{water}}$ computed using quantum chemical calculations ($916.06\,\mathrm{kJ\,mol^{-1}}$) is in excellent agreement with the $D_{0,\mathrm{water}}$ computed using the JANAF tables. More accurate values of $D_{0,i}$ with more accurate quantum chemistry composite methods can be obtained, as the value of μ_i^0 is sensitive to the value of $D_{0,i}$ (Eq. (B.9)). Using Eq. (B.13) and Eq. (B.12), we computed μ_i^0 of water as $-986.83\,\mathrm{kJ\,mol^{-1}}$. The difference between the value of μ_i^0 computed using quantum chemistry ($-965.23\,\mathrm{kJ\,mol^{-1}}$, see the previous section) and the value of μ_i^0 computed using JANAF tables is ca. $21\,\mathrm{kJ\,mol^{-1}}$ which is well beyond the chemical accuracy of $4.18\,\mathrm{kJ\,mol^{-1}}$ ($1\,\mathrm{kcal\,mol^{-1}}$). More accurate values of μ_i^0 can be obtained using other quantum chemistry composite methods (methods that combine results of several calculations at different levels of theory or basis sets for high accuracy) which is beyond the scope of this thesis [345].

B.3.3. Computing μ_i^{ex} using Brick-CFCMC

Brick-CFCMC is an open source Monte Carlo simulation software to compute the phase and reaction equilibria [96, 97]. Brick-CFCMC uses the efficient Continuous Fractional Component Monte Carlo (CFCMC) method [96, 97, 114, 115, 123, 157] for molecule insertions and deletions which allows us to compute partial molar properties and μ_i^{ex}. The CFCMC method uses a so-called "fractional" molecule group to compute partial molar properties and the values of μ_i^{ex}. An interaction scaling factor λ is used to scale the interactions of the fractional molecule group with the surrounding molecules. At $\lambda = 1$, the fractional molecule group has full interactions with the surrounding molecules while at $\lambda = 0$, the fractional molecule group has no interactions with the surrounding molecules. To compute μ_i^{ex}, we can use two different methods implemented in Brick-CFCMC. The first method is the "probability" route and it uses the probability distribution of the interaction scaling factor λ at $\lambda = 1$ and $\lambda = 0$ to compute μ_i^{ex} (Eq. (1.3)) [96, 97]. This method requires a flat distribution of (observed) λ and this is obtained using a biasing function [96, 97, 114, 115, 123, 157]. A rule of thumb for the flat distribution of λ is that the difference between the maximum and minimum probabilities should be lower than 20%. The second method is thermodynamic integration [97]. In thermodynamic integration, we use the average value of the derivative of the potential energy with respect to λ, $\left\langle \frac{\partial U}{\partial \lambda} \right\rangle$, and compute μ_i^{ex} using [82, 97]:

$$\mu_i^{ex} = \int_0^1 d\lambda \left\langle \frac{\partial U}{\partial \lambda} \right\rangle_{NPT} \tag{B.15}$$

It is very challenging to obtain a flat probability distribution of λ in a single simulation for large and/or polar molecules [97]. As mentioned in Section 3.2, we need to compute μ_i^{ex} of ionic and/or large molecules such as the hydronium ion (H_3O^+) and the protonated MDEA ion ($MDEAH^+$). Using thermodynamic integration, a flat probability distribution of λ is not required since $\left\langle \frac{\partial U}{\partial \lambda} \right\rangle$ term can be computed from independent MC simulations at different and fixed values of λ. Therefore, the thermodynamic integration as implemented in Brick-CFCMC is used to compute μ_i^{ex} in Chapter 3. The term $\left\langle \frac{\partial U}{\partial \lambda} \right\rangle$ can only be computed for one charge-neutral fractional group [96, 97]. The fractional group can consist of multiple molecules or ions. In Chapter 3, we computed the μ_i^{ex} of the reactants and reaction products of $MDEAH^+$ dissociation reaction. As the fractional group should be charge-neutral, an HCO_3^- ion is added to the fractional groups. For example, μ_i^{ex} of the reactants of the $MDEAH^+$ dissociation reaction (reaction R3 of Chapter 3) can be computed using a fractional group consisting of one $MDEAH^+$ ion, one H_2O molecule, and one HCO_3^- ion. μ_i^{ex} of reaction products of $MDEAH^+$ dissociation reaction can be computed using a fractional group consisting of one MDEA molecule, one H_3O^+ ion, and one HCO_3^- ion. In this way, we can compute the difference between μ_i^{ex} of $MDEAH^+ + H_2O$ and μ_i^{ex} of $MDEA + H_3O^+$ (because the excess chemical potential of HCO_3^- cancels out).

Table B.2: The list of fractional groups for which we computed μ_i^{ex} and the molecules included in the fractional groups.

Fractional group name	Molecules or ions included in fractional group
MDEA	MDEA
H_2O	H_2O
CO_2	CO_2
H_2S	H_2S
$MDEAH^+ + HCO_3^-$	$MDEAH^+$ and HCO_3^-
$H_3O^+ + HCO_3^-$	H_3O^+ and HCO_3^-

B.4. Accounting for CO_2 Evaporation in Sequential Absorption of CO_2 (First) and H_2S (Second)

Dicko et al. [54] measured binary absorption of CO_2 and H_2S sequentially. In their measurements, Dicko et al. [54] first loaded 50 wt.% MDEA/water solution with fixed loadings of CO_2 and then loaded H_2S to the CO_2 loaded solution. Dicko et al. [54] assumed that the CO_2 loading in the solution does not change during H_2S absorption. However, CO_2 may evaporate from the solution to the gas phase as the presence of H_2S may shift the equilibrium between CO_2 in the gas phase and free CO_2 in the liquid phase. For multi-component absorption, our chemical reaction equilibrium solver was designed to compute simultaneous absorption of all components in the gas phase. To account for the CO_2 evaporation effect in the experiments by Dicko et al. [54], we modified our solver so it also computes the amount of evaporated CO_2 to the gas phase during loading with H_2S. In these calculations, we first computed the speciation of a CO_2 loaded 50 wt.% MDEA/water solution at 323.15 K for fixed loadings of CO_2 (CO_2 loadings of 0.093, 0.306, 0.510, and 0.706 $\mathrm{mol_{CO_2}\ mol_{amine}^{-1}}$) as explained in Section 3.2. Next, we computed the speciation of the H_2S/CO_2/MDEA/water system using the speciation obtained in the previous computation as an initial guess. For computing the speciation of the H_2S/CO_2/MDEA/water system at equilibrium, we have 11 variables (N_i) and 11 equations to solve. To account for the effect of CO_2 evaporation in the experiments of Dicko et al. [54], we have one more variable additional to the concentrations of the species in liquid phase (N_i), which is the amount of CO_2 evaporated to the gas phase ($N_{CO_2,\mathrm{gas}}$). As a result of this, the CO_2 balance in the system has an additional term $N_{CO_2,\mathrm{gas}}$. The CO_2 balance in the H_2S/CO_2/MDEA/water system changes from Eq. (3.16) to:

$$N_{\mathrm{CO_2,total}} - \left(N_{\mathrm{CO_2_{(aq.)}}} + N_{\mathrm{HCO_3^-}} + N_{\mathrm{CO_3^{2-}}} + N_{\mathrm{CO_2,gas}} \right) = 0 \qquad (B.16)$$

We also have an additional equation derived using the chemical equilibrium between the free CO_2 absorbed in the liquid solution and the CO_2 evaporated to the gas phase

and the equilibrium condition (Eq. (1.1)):
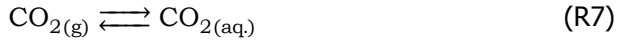
$$CO_{2(g)} \rightleftharpoons CO_{2(aq.)} \tag{R7}$$

The chemical equilibrium between the free CO_2 absorbed in the liquid solution and the CO_2 evaporated to the gas phase can be shown as:

$$\frac{RTN_{CO_2,gas}}{V_{gas}} = \frac{N_{CO_{2(aq.)}} RT}{V_{liquid} \exp\left[\frac{-\mu_{CO_2}^{ex}}{RT}\right]} \tag{B.17}$$

which results in:

$$\frac{N_{CO_2,liquid}}{N_{CO_2,gas}} = \frac{V_{liquid}}{V_{gas}} \exp\left[\frac{-\mu_{CO_2,liquid}^{ex}}{RT}\right] \tag{B.18}$$

where $N_{CO_2,liquid}$ represent the number of molecules of free CO_2 in liquid phase, V_{liquid} is the volume of the liquid phase, V_{gas} is the volume of the gas phase, and $\mu_{CO_2,liquid}^{ex}$ is the excess chemical potential of CO_2 in liquid phase. Note that we used $\frac{V_{liquid}}{V_{gas}} = 0.3$ in these calculations to mimic the conditions in the experiments by Dicko et al. [54]. In total, we have 12 variables and 12 equations to solve in computing the speciation of the $H_2S/CO_2/MDEA/water$ system while accounting for the effect of evaporating CO_2 during sequential H_2S absorption. We solved the speciation in this system using a numerical least squares solver for nonlinear equations. Fig. B.1 shows the CO_2 loading in 50 wt.% MDEA/water solution at 323.15 K as a function of H_2S loading during H_2S absorption and comparison with the fixed loading assumption. Results show that the amount of evaporated CO_2 is the highest for the highest initial CO_2 loaded solution. For the solution with initial CO_2 loading of 0.093 $mol_{CO_2} mol_{amine}^{-1}$, the decrease in CO_2 loading is between 0.6–26.9% of the initial loading (5.58×10^{-4}–2.50×10^{-2} $mol_{CO_2} mol_{amine}^{-1}$). The decrease in the CO_2 loading is between 9.5–44.6% of the initial CO_2 loading (6.71×10^{-2}–3.14×10^{-1} $mol_{CO_2} mol_{amine}^{-1}$) for the solution with the highest initial CO_2 loading (0.706 $mol_{CO_2} mol_{amine}^{-1}$) Fig. B.2 shows the partial pressures of H_2S as a function of the H_2S loading at 323.15 K for the fixed CO_2 loading assumption (no CO_2 evaporation), by quantifying the effect of CO_2 evaporation, and experimental results from Dicko et al. [54]. The computed H_2S partial pressures for fixed CO_2 loading assumptions are always higher than the H_2S partial pressures computed quantifying the effect of CO_2 evaporation. This is expected because there is a lower amount of CO_2 for H_2S to compete when we take the effect of CO_2 evaporation into account, so H_2S can be absorbed by the solution at lower pressures. However, even with the decrease in H_2S partial pressures, the computed H_2S isotherms does not agree with the experimental isotherms [54].
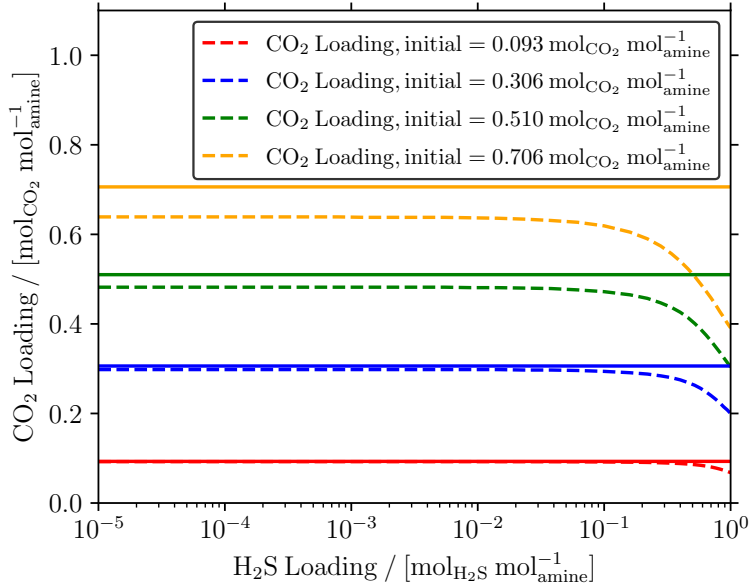
Figure B.1: Calculated CO_2 loadings as a function of the H_2S loadings during H_2S absorption in CO_2 loaded 50 wt.% MDEA/water solutions at 323.15 K. The dashed lines show the CO_2 loading after the correction (desorption of CO_2 due to absorption of H_2S) while solid lines show the fixed CO_2 loading assumption.
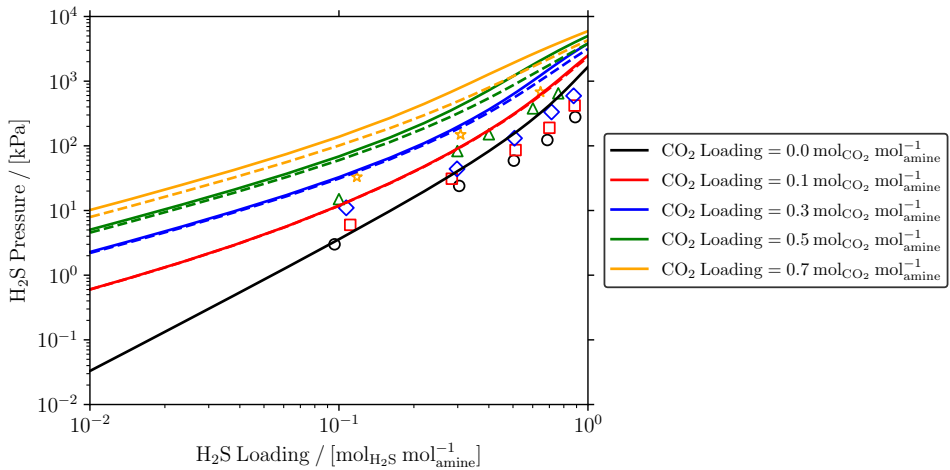
Figure B.2: H_2S pressure as a function of H_2S loading. Solid lines represent simultaneous absorption of CO_2 and H_2S while dashed lines represent sequential absorption of CO_2 and then H_2S (accounting for the effect of evaporated CO_2). Empty symbols represent the experimental results from Dicko et al. [54]. Color codings for solid lines, dashed lines, and empty symbols follow the color coding in the legend.
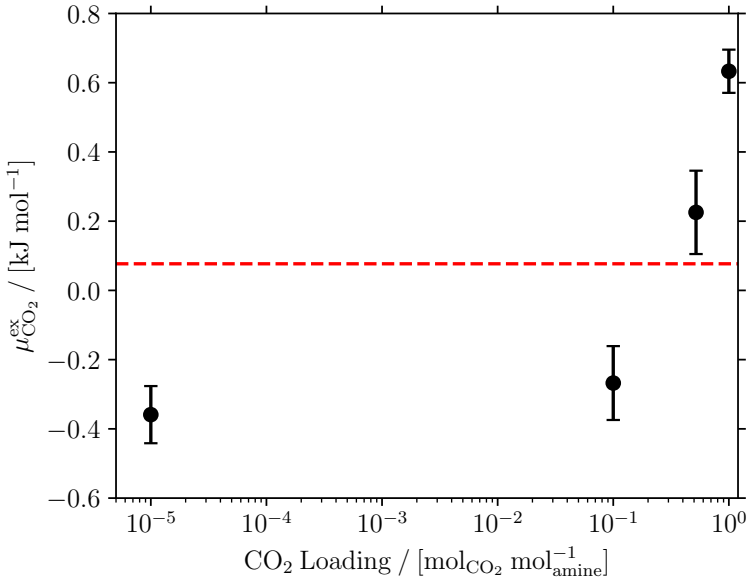
Figure B.3: The values of $\mu_{CO_2}^{ex}$ for CO_2 as a function of CO_2 loading in 23 wt.% MDEA/water solutions at 313.15 K. To compute the values of μ_i^{ex} for CO_2 for different CO_2 loadings, we changed the composition of the simulation boxes to the speciations reported in Fig. 3.3. The dashed line represents the computed value of μ_i^{ex} for CO_2 in pure water at 313.15 K.

B.5. Derivation of an Expression for the Henry Constant of CO_2 in Aqueous MDEA Solutions

Our aim is to derive an approximate expression for the Henry constant of CO_2 in aqueous MDEA solutions as a function of the equilibrium constants (K) of reactions R1–R4 of Chapter 3. The Henry constant of CO_2 in aqueous MDEA solutions ($K_{CO_2}^H$) can be expressed as:

$$K_{CO_2}^H = \lim_{P_{CO_2} \to 0} \frac{P_{CO_2}}{X_{CO_2,\text{total}}} \tag{B.19}$$

where P_{CO_2} is the partial pressure of CO_2 in the gas phase and $X_{CO_2,\text{total}}$ is the total mole fraction of the free CO_2, HCO_3^-, and CO_3^{2-} ($X_{CO_2,\text{total}} = X_{CO_2} + X_{HCO_3^-} + X_{CO_3^{2-}}$). There is already an expression to compute P_{CO_2} (Eq. (3.5)), so we need to derive an expression for $X_{CO_2,\text{total}}$. As P_{CO_2} approaches 0, we assume that the solution is only composed of water and MDEA ($X_{MDEA} + X_{H_2O} = 1$) and the net charge of the OH^- ion is the only negative charge in the solution that balances the positive charge from the $MDEAH^+$ ion ($X_{MDEAH^+} = X_{OH^-}$) i.e. MDEA is a weak base. By using the equilibrium constant of reaction R4 (K_{R4}) and replacing X_{OH^-}

with X_{MDEAH^+}, we obtain an expression for the mole fraction of the H_3O^+ ion:

$$X_{\text{H}_3\text{O}^+} = \frac{K_{\text{R4}} X_{\text{H}_2\text{O}}^2}{X_{\text{MDEAH}^+}} \tag{B.20}$$

By replacing the term $X_{\text{H}_3\text{O}^+}$ with Eq. (B.20) in the equilibrium constant of reaction R3 (K_{R3}), an expression to compute the mole fraction of MDEAH$^+$ is obtained:

$$X_{\text{MDEAH}^+} = \sqrt{\frac{K_{\text{R4}} X_{\text{H}_2\text{O}} X_{\text{MDEA}}}{K_{\text{R3}}}} \tag{B.21}$$

The mole fraction of free CO_2 in the solution can be computed using Eq. (3.5) and total number of molecules ($N_{\text{MDEA}} + N_{\text{H}_2\text{O}}$) as:

$$X_{\text{CO}_2} = \frac{P_{\text{CO}_2} V \exp\left[\frac{-\mu_{\text{CO}_2}^{\text{ex}}}{RT}\right]}{k_{\text{B}} T (N_{\text{MDEA}} + N_{\text{H}_2\text{O}})} \tag{B.22}$$

where V is the volume of the liquid phase, $\mu_{\text{CO}_2}^{\text{ex}}$ is the excess chemical potential of CO_2, k_{B} is the Boltzmann constant, and T is the absolute temperature. By using the equilibrium constant of reaction R1 (K_{R1}), we obtain an expression to compute the mole fraction of HCO$_3^-$ which is:

$$X_{\text{HCO}_3^-} = \frac{K_{\text{R1}} X_{\text{CO}_2} X_{\text{H}_2\text{O}}^2}{X_{\text{H}_3\text{O}^+}} \tag{B.23}$$

By using the equilibrium constant of reaction R2 (K_{R2}), we can compute the mole fraction of CO$_3^{2-}$ as:

$$X_{\text{CO}_3^{2-}} = \frac{K_{\text{R2}} X_{\text{HCO}_3^-} X_{\text{H}_2\text{O}}}{X_{\text{H}_3\text{O}^+}} \tag{B.24}$$

By summing Eq. (B.22), Eq. (B.23), and Eq. (B.24) up, an expression for $X_{\text{CO}_2,\text{total}}$ is obtained:

$$X_{\text{CO}_2,\text{total}} = \frac{P_{\text{CO}_2} V \exp\left[\frac{-\mu_{\text{CO}_2}^{\text{ex}}}{RT}\right]}{k_{\text{B}} T (N_{\text{MDEA}} + N_{\text{H}_2\text{O}})} + \frac{K_{\text{R1}} X_{\text{CO}_2} X_{\text{H}_2\text{O}}^2}{X_{\text{H}_3\text{O}^+}} + \frac{K_{\text{R2}} X_{\text{HCO}_3^-} X_{\text{H}_2\text{O}}}{X_{\text{H}_3\text{O}^+}} \tag{B.25}$$

Because we show the CO_2 pressure as a function of the CO_2 loading in our isotherms (see Fig. 3.5), we prefer to compute the Henry coefficient of CO_2 as:

$$K_{\text{CO}_2}^{\text{H}} = \lim_{P_{\text{CO}_2} \to 0} \frac{P_{\text{CO}_2}}{\alpha_{\text{CO}_2,\text{total}}} \tag{B.26}$$

where $\alpha_{\text{CO}_2,\text{total}}$ is the total loading of CO_2 in the solution in the units of $\text{mol}_{\text{CO}_2} \, \text{mol}_{\text{amine}}^{-1}$ ($\alpha_{\text{CO}_2,\text{total}} = \alpha_{\text{CO}_2} + \alpha_{\text{HCO}_3^-} + \alpha_{\text{CO}_3^{2-}}$ where α_{CO_2}, $\alpha_{\text{HCO}_3^-}$, and

Table B.3: The mole fractions of species and Henry constants of CO_2 computed using Eq. (B.20)–Eq. (B.24) and CASpy at 313.15 K and 1.2×10^{-7} kPa in 23 wt.% MDEA/water solutions

	from Eq. (B.20)–Eq. (B.24)	from CASpy
X_{MDEAH^+}	6.25×10^{-5}	6.29×10^{-5}
$X_{H_3O^+}$	1.62×10^{-13}	1.38×10^{-13}
X_{OH^-}	6.25×10^{-5}	6.21×10^{-5}
X_{CO_2}	7.10×10^{-13}	7.10×10^{-13}
$X_{HCO_3^-}$	4.35×10^{-8}	5.09×10^{-8}
$X_{CO_3^{2-}}$	2.78×10^{-7}	3.81×10^{-7}
$K_{CO_2}^H$ / kPa mol$_{amine}^{-1}$ mol$_{CO_2}^{-1}$	0.0162	0.0149

Table B.4: Correlations reported by Plakia et al. [212] to compute mole fraction-based equilibrium constants of reactions R1-R6 of Chapter 3. The mole fraction-based equilibrium constants are computed using the expression $\ln[K_j] = A + \frac{B}{T} + C \ln[T]$ where T is the absolute temperature.

Reaction	A	B	C
R1	231.465	-12092.1	-36.7816
R2	216.049	-12431.7	-35.4819
R3	-83.4914	-819.7	10.9756
R4	132.899	-13445.9	-22.4773
R5	214.582	-12995.4	-33.5471
R6	-32	-3338	0

$\alpha_{CO_3^{2-}}$ are the loadings of free CO_2, HCO_3^-, and CO_3^{2-}, respectively). The mole fractions computed using Eq. (B.22), Eq. (B.23), and Eq. (B.24) can be converted to loading α_i using:

$$\alpha_i = X_i \frac{(N_{H_2O} + N_{MDEA})}{N_{MDEA}} \tag{B.27}$$

When we evaluate Eq. (B.20)–Eq. (B.24) using the equilibrium constants of the reactions R1–R4 of Chapter 3, V, and $\mu_{CO_2}^{ex}$ at 313.15 K and 1.2×10^{-7} kPa for 23 wt.% MDEA/water solutions ($X_{H_2O} = 0.957$ and $X_{MDEA} = 0.043$), the approximate mole fractions of the species in CO_2/MDEA/water system are computed. Table B.3 shows the mole fractions of the species and the Henry constant of CO_2 in CO_2/MDEA/water system computed using Eq. (B.20)–Eq. (B.24) and our solver at 313.15 K and a low pressure of 1.2×10^{-7} kPa in 23 wt.% MDEA/water solutions. The results show that the mole fractions and Henry constant computed using Eq. (B.20)–Eq. (B.24) are in excellent agreement with the mole fractions and Henry constant computed numerically using our solver.

Table B.5: Computed μ_i^{ex} of CO_2 (TraPPE [90] force field (Appendix C.3) with optimized potential for CO_2–H_2O interactions [225] (Table C.10)) and H_2S (force field from Kristóf and Lizsi [224] (Appendix C.4.1)) in water (TIP3P [222] force field (Appendix C.1.2)) as a function of temperature at 1 bar.

	298.15 K	313.15 K	323.15 K
$\mu_{CO_2}^{\text{ex}}$ / [kJ mol^{-1}]	-0.563	0.077	0.410
$\mu_{H_2S}^{\text{ex}}$ / [kJ mol^{-1}]	-2.514	-2.025	-1.786

Table B.6: Comparison of the values of μ_i^0 and $D_{0,i}$ computed using quantum chemistry calculations (with G4 method) and JANAF tables at 313.15 K.

Species	μ_{G4}^0 / [kJ mol^{-1}]	μ_{JANAF}^0 / [kJ mol^{-1}]	$D_{0,i}^{\text{G4}}$ / [kJ mol^{-1}]	$D_{0,i}^{\text{JANAF}}$ / [kJ mol^{-1}]
MDEA	-7758.70	N/A	7625.75	N/A
MDEAH$^+$	-7428.61	N/A	7338.39	N/A
H_2O	-965.23	-986.83	916.06	917.78
H_3O^+	-338.21	-383.14	284.91	312.91
CO_2	-1657.34	-1674.24	1601.81	1597.92
OH^-	-649.47	-662.88	607.62	600.25

Table B.7: Comparison of the computed values of μ_i^{ex} in water with available data from literature and μ_i^{ex} values derived from Henry constants at 298.15 K and 1 bar.

Species	Force field	μ_i^{ex} (our calculations) / [kJ mol^{-1}]	μ_i^{ex} (literature [104]) / [kJ mol^{-1}]	μ_i^{ex} (from Henry constants) / [kJ mol^{-1}]
MDEA	GAFF [95]	-43.77	-43.01	N/A
H_2O	TIP3P [222]	-27.83	-28.09	N/A
CO_2	TraPPE [90]	-0.60	1.25	0.44 [346]
H_2S	K-L [224]	-2.63	N/A	-2.40 [347]

Table B.8: Comparison of the values of μ_i^0, $D_{0,i}$, and μ_i^G computed using different composite methods in quantum chemistry calculations at 313.15 K.

Species	μ_{G3}^0 / [kJ mol^{-1}]	μ_{G4}^0 / [kJ mol^{-1}]	$\mu_{\text{CBS-QB3}}^0$ / [kJ mol^{-1}]	μ_{G3B3}^0 / [kJ mol^{-1}]	Standard deviation
MDEA	-7756.55	-7758.7	-7760.17	-7755.58	2.05
H_2O	-964.11	-965.23	-964.48	-968.09	1.80
MDEAH$^+$	-7425.49	-7428.61	-7431.06	-7425.80	2.62
CO_2	-1655.89	-1657.34	-1659.49	-1654.16	2.26
H_3O^+	-339.33	-338.21	-336.76	-340.26	1.51
	D_0^{G3} / [kJ mol^{-1}]	D_0^{G4} / [kJ mol^{-1}]	$D_0^{\text{CBS-QB3}}$ / [kJ mol^{-1}]	D_0^{G3B3} / [kJ mol^{-1}]	Standard deviation
MDEA	7653.64	7652.75	7652.14	7652.81	0.62
H_2O	915.87	916.06	917.01	916.30	0.50
MDEAH$^+$	7338.86	7338.39	7338.59	7338.49	0.20
CO_2	1602.40	1601.81	1600.93	1601.58	0.61
H_3O^+	284.64	284.91	285.47	285.45	0.41
Species	μ_{G3}^G / [kJ mol^{-1}]	μ_{G4}^G / [kJ mol^{-1}]	$\mu_{\text{CBS-QB3}}^G$ / [kJ mol^{-1}]	μ_{G3B3}^G / [kJ mol^{-1}]	Standard deviation
MDEA	-7784.76	-7786.91	-7788.38	-7783.79	2.05
H_2O	-992.32	-993.44	-992.69	-996.30	1.80
MDEAH$^+$	-7453.70	-7456.82	-7459.27	-7454.01	2.62
CO_2	-1684.10	-1685.55	-1687.70	-1682.37	2.26
H_3O^+	-367.54	-366.42	-364.97	-368.47	1.51

Table B.9: Linear regression fit parameters of the computed values of μ_i^{ex} as a function of charge scaling factor χ. The analytic expression to compute μ_i^{ex} is: $\mu_i^{ex} = A \times \chi + B$. The values of A and B shown in this table are in $kJ\,mol^{-1}$.

	GAFF			OPLS-AA		
	A	B	R^2	A	B	R^2
μ_{MDEA}^{ex}	-31.40	-13.39	0.963	-68.24	37.51	0.999
$\mu_{MDEAH^++HCO_3^-}^{ex}$	-1030.80	444.46	0.997	-988.89	440.99	0.998
$\mu_{H_3O^++HCO_3^-}^{ex}$	-1392.01	620.51	0.997	-1392.01	620.51	0.997

Table B.10: Linear regression fit parameters of the computed values of the equilibrium constant of the $MDEAH^+$ dissociation reaction ($\ln[K_{R3,des}]$) as a function of charge scaling factor χ. The analytic expression to compute $\ln[K_{R3,des}]$ is: $\ln[K_{R3,des}] = A \times \chi + B$.

	A	B	R^2
$\ln[K_{R3,des}]$ (GAFF-only the ions are scaled)	139.24	-174.46	0.998
$\ln[K_{R3,des}]$ (GAFF-the ions and MDEA are scaled)	175.48	-211.18	0.998
$\ln[K_{R3,des}]$ (OPLS–AA-only the ions are scaled)	154.83	-180.62	0.998
$\ln[K_{R3,des}]$ (OPLS–AA-the ions and MDEA are scaled)	181.02	-206.97	0.997

Appendix C

C.1. Force Field Details for Water

C.1.1. SPC/E

This force field is used in Chapters 2 and 4 of this thesis and Refs. [97, 301].

Table C.1: The atom types and coordinates of the SPC/E [188] water molecule.

Atom type	x / [Å]	y / [Å]	z / [Å]
O	0.0000	0.000	0.000
H	-0.817	0.577	0.000
H	0.817	0.577	0.000

Table C.2: Non-bonded interaction parameters for SPC/E water [188].

Atom	ε/k_B / [K]	σ / [Å]	q / $[e^-]$
O	78.177	3.166	-0.8476
H	1.0000	1.000	0.4238

C.1.2. TIP3P

This force field is used in Chapter 3 of this thesis and reference [5].

Table C.3: The atom types and coordinates of the TIP3P [222] water molecule.

Atom type	x / [Å]	y / [Å]	z / [Å]
O	0.000	0.000	0.000
H	-0.757	0.586	0.000
H	0.757	0.586	0.000

Table C.4: Non-bonded interaction parameters for TIP3P water [222].

Atom	ε/k_B / [K]	σ / [Å]	q / $[e^-]$
O	76.5414	3.15061	-0.834
H	0.00000	0.00000	0.417

C.1.3. TIP4P/2005

This force field is used in Chapter 5 of this thesis and Ref. [348].

Table C.5: The atom types and coordinates of the TIP4P/2005 [94] water molecule. The atom type M represents the dummy charge site in the TIP4P/2005 force field.

Atom type	x / [Å]	y / [Å]	z / [Å]
O	0.00000000	0.00000000	0.00000000
H	-0.75695033	0.58588228	0.00000000
H	0.75695033	0.58588228	0.00000000
M	0.00000000	0.15000000	0.00000000

Table C.6: Force field parameters for TIP4P/2005 [94] water.

Atom	ε/k_B / [K]	σ / [Å]	q / $[e^-]$
O	81.899	3.16435	0.00000
H	0.0000	0.00000	0.52422
M	0.0000	0.00000	-1.04844

C.2. Force Field Details for NaCl

This force field is used in Chapter 2 of this thesis and Ref. [97].

Table C.7: Non-bonded interaction parameters for NaCl force field from Joung and Cheatham [189].

Atom	ε/k_B / [K]	σ / [Å]	q / $[e^-]$
Na	177.46	2.159	1.000
Cl	6.4340	4.830	-1.000

C.3. Force Field Details for CO_2

This force field is used in Chapters 3 to 5 of this thesis and Refs. [5, 301, 348].

Table C.8: The atom types and coordinates of the TraPPE [90] CO_2 molecule.

Atom type	x / [Å]	y / [Å]	z / [Å]
C	1.16	0.00	0.00
O	0.00	0.00	0.00
O	2.32	0.00	0.00

Table C.9: Non-bonded interaction parameters for TraPPE carbon dioxide [90].

Atom	ε/k_B / [K]	σ / [Å]	q / [e^-]
O	79.0	3.05	-0.35
C	27.0	2.80	0.70

Table C.10: Non-bonded interaction parameters for the optimized potential between carbon dioxide and water developed by [225].

Atoms	ε/k_B / [K]	σ / [Å]
O_{CO_2}–O_{H_2O}	79.14	3.058
C_{CO_2}–O_{H_2O}	53.04	3.052

C.4. Force Field Details for H_2S

C.4.1. Force Field from Kristóf and Lizsi

This force field is used in Chapters 3 and 4 of this thesis and Refs. [5, 301].

Table C.11: The atom types and coordinates of the H_2S molecule. The force field from Kristóf and Lizsi [224] was used. "X" designates the dummy charge in the force field. "X" site is coplanar with the S and H sites and is located at the bisector of the H–S–H angle.

Atom type	x / [Å]	y / [Å]	z / [Å]
S	0.000	0.000	0.000
H	0.964	-0.931	0.000
H	-0.964	-0.931	0.000
X	0.000	-0.186	0.000

Table C.12: Non-bonded interaction parameters for hydrogen sulfide from Kristóf and Lizsi [224]. "X" designates the dummy charge in the force field. "X" site is coplanar with the S and H sites and is located at the bisector of the H–S–H angle.

Atom	ε/k_B / [K]	σ / [Å]	q / [e^-]
S	250.0	3.73	0.40
H	0.000	0.00	0.25
X	0.000	0.00	-0.90

C.4.2. TraPPE

This force field is used in Chapter 5 of this thesis and Ref. [348].

Table C.13: The atom types and coordinates of the TraPPE [294] H_2S molecule.

Atom type	x / [Å]	y / [Å]	z / [Å]
S	0.00	0.00	0.00
H	1.34	0.00	0.00
H	-1.34	0.00	0.00

Table C.14: Force field parameters for TraPPE hydrogen sulfide [294].

Atom	ε/k_B / [K]	σ / [Å]	q / [e^-]
S	125.0	3.60	-0.28
H	50.0	2.50	0.14

C.5. Force Field Details for HCO_3^-
C.5.1. GAFF/RESP
This force field is used in Chapter 3 of this thesis and Ref. [5].

Table C.15: The atom types and coordinates of the rigid HCO_3^- ion.

Atom type	x / [Å]	y / [Å]	z / [Å]
OH	-0.724	-0.764	0.0
O	1.521	-0.541	0.0
O	0.182	1.301	0.0
C	0.446	0.096	0.0
HO	-0.306	-1.632	0.0

Table C.16: Non-bonded interaction parameters for HCO_3^-. For Lennard-Jones (LJ) interactions, the General Amber Force Field (GAFF) [95] was used. For electrostatic interactions, two-step RESP fitted point charges [229] were used. The point charges listed in this table sum up to -1.

Atom	ε/k_B / [K]	σ / [Å]	q / [e^-]
OH	105.8792	3.06469	-0.728557
O	105.6775	2.95992	-0.826268
C	43.27747	3.39967	1.057315
HO	0.000000	0.00000	0.323778

C.5.2. OPLS-AA/Quantum Chemistry
This force field is used in Chapter 5 of this thesis and Ref. [348].

Table C.17: Non-bonded interaction parameters for HCO_3^-. The OPLS-AA force field [88, 89] with point charges computed by quantum chemical calculations (MP2/6-311+G(2d,2p)) was used for HCO_3^-. The point charges listed in this table are unscaled charges, i.e. $\chi_{HCO_3^-}^q = 1.0$. The tabulated point charges sum up to exactly -1. As explained in Chapter 5, in our simulations, these point charges are scaled by 0.90 or 0.75. The atom labels are as follows: C: carbon of HCO_3^-; O1: oxygen connected to carbon in HCO_3^-; O2: oxygen connected to carbon in HCO_3^-; OH: oxygen of OH group in HCO_3^-; HO: hydrogen of OH group in HCO_3^-.

Atom	ε/k_B / [K]	σ / [Å]	q / [e^-]
C	35.190	3.55	1.15070
O1	105.58	2.96	-0.90698
O2	105.58	2.96	-0.86222
OH	85.470	3.12	-0.83705
HO	1.0000	1.00	0.45555

Table C.18: Harmonic bond stretching potential parameters for HCO_3^-. The OPLS-AA [88, 89] force field is used for HCO_3^-. To compute the bonding potentials, we use $U_{bond} = K(r - r_0)^2$ where K is the bond coefficient, r is the distance between two atoms, and r_0 is the equilibrium distance between two atoms. The atom labels are designated in the caption of Table C.17.

Bond	r_0 / [Å]	K/k_B / [K Å^{-2}]
C–O	1.250	329800.9
C–OH	1.364	226235.4
OH-HO	0.945	278018.2

Table C.19: Harmonic bond bending angle potential parameters for HCO_3^-. The OPLS-AA [88, 89] force field is used for HCO_3^-. To compute the angle potentials, we use $U_{angle} = K(\theta - \theta_0)^2$ where K is the bending strength, θ is the bending angle between three atoms, and θ_0 is the equilibrium bending angle. The atom labels are designated in the caption of Table C.17.

Angle	θ_0 / [°]	K/k_B / [K]
O–C–OH	121	40219.6
O–C–O	126	40219.6
C–OH–HO	113	17596.1

Table C.20: OPLS-AA dihedral potential parameters for HCO_3^-. The OPLS-AA [88, 89] force field is used for the dihedrals in HCO_3^-. To compute the dihedral potential for the dihedrals in this table, we use $U_{\text{dihedral}} = \frac{1}{2}K_1[1 + \cos(\phi)] + \frac{1}{2}K_2[1 - \cos(2\phi)] + \frac{1}{2}K_3[1 + \cos(3\phi)] + \frac{1}{2}K_4[1 - \cos(4\phi)]$ where $K_1..K_4$ are the dihedral coefficients and ϕ is the dihedral angle. The values of K_4 are 0 for all dihedrals listed in this table. The atom labels are designated in the caption of Table C.17.

Dihedral	K_1/k_B / [K]	K_2/k_B / [K]	K_3/k_B / [K]
O–C–OH–HO	0.0	2765.1	0.0

C.6. Force Field Details for SH$^-$

This force field is used in Chapter 5 of this thesis and Ref. [348].

Table C.21: Intermolecular force field parameters for SH$^-$. The OPLS-AA force field [88, 89] with point charges computed by quantum chemical calculations (MP2/6-311+G(2d,2p)) was used for SH$^-$. The point charges listed in this table are unscaled charges, i.e. $\chi_{\text{SH}^-}^q = 1.0$. The tabulated point charges sum up to exactly -1. As explained in Chapter 5, in our simulations, these point charges are scaled by 0.90 or 0.75.

Atom	ε/k_B / [K]	σ / [Å]	q / [e^-]
S	125.69	3.55	-1.04173
H	1.0000	1.00	0.04173

Table C.22: Harmonic bond stretching potential parameters for SH$^-$. The OPLS-AA [88, 89] force field is used for SH$^-$. To compute the bonding potentials, we use $U_{\text{bond}} = K(r - r_0)^2$ where K is the bond coefficient, r is the distance between two atoms, and r_0 is the equilibrium distance between two atoms.

Bond	r_0 / [Å]	K/k_B / [K Å^{-2}]
S–H	1.351103	502745.3

C.7. Force Field Details for H$_3$O$^+$

This force field is used in Chapter 3 of this thesis and Ref. [5].

Table C.23: The atom types and coordinates of the rigid H_3O^+ ion [105].

Atom type	x / [Å]	y / [Å]	z / [Å]
OH	-0.00044	-0.00003	0.04871
HO	-0.01990	-0.94884	-0.19579
HO	0.82552	0.44398	-0.23683
HO	-0.80407	0.47899	-0.24304

Table C.24: Non-bonded interaction parameters for H_3O^+ from Noroozi and Smith [105]. The point charges listed in this table sum up to 1.

Atom	ε/k_B / [K]	σ / [Å]	q / [e^-]
OH	76.54135	3.15061	-1.2797
HO	1.000000	1.00000	0.7599

C.8. Force Field Details for MDEA

C.8.1. GAFF/RESP

This force field is used in Chapter 3 of this thesis and Ref. [5].
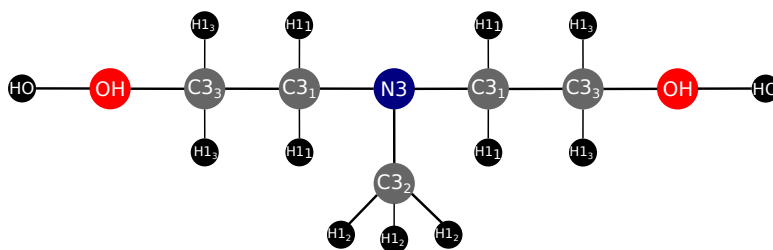
Figure C.1: Schematic representation showing atom type designations of the MDEA molecule for the GAFF with RESP fitted point charges [95, 229].

Table C.25: Non-bonded interaction parameters for MDEA. For Lennard-Jones (LJ) interactions, the General Amber Force Field (GAFF) [95] was used. For electrostatic interactions, two-step RESP fitted point charges [229] were used. The point charges of the MDEA molecule sum up to zero and are not scaled. Fig. C.1 shows the atom types designation of MDEA for the GAFF [95].

Atom	ε/k_B / [K]	σ / [Å]	q / [e^-]
OH	105.8789	3.06647	-0.715283
N3	85.54849	3.25000	-0.495858
$C3_1$	55.05302	3.39967	0.024816
$C3_2$	55.05302	3.39967	-0.041777
$C3_3$	55.05302	3.39967	0.290555
$H1_1$	7.900655	2.47135	0.060612
$H1_2$	7.900655	2.47135	0.059755
$H1_3$	7.900655	2.47135	0.015339
HO	0.000000	0.00000	0.427195

Table C.26: Bond lengths of the MDEA molecule with the General Amber Force field (GAFF) [95]. The bond lengths are fixed in MC simulations in Chapter 3.

Bond	Bond length / [Å]
OH–HO	0.96
OH–C3$_3$	1.42
N3–C3$_1$	1.46
N3–C3$_2$	1.46
C3$_1$–H1$_1$	1.09
C3$_1$–C3$_3$	1.53
C3$_2$–H1$_2$	1.09
C3$_3$–H1$_3$	1.09

Table C.27: Bending potential parameters, the equilibrium angle (θ_0) and the bending constant (K) of the MDEA molecule for the GAFF [95]. The bending potential was computed using $U_{\text{Bending}} = \frac{K}{2}(\theta - \theta_0)^2$ where K is the bending constant, θ is the bending angle, θ_0 is the bending angle at equilibrium. Fig. C.1 shows the atom types designation of MDEA for the GAFF [95].

Bending	θ_0 / [°]	K/k_{B} / [K rad^{-2}]
OH–C3$_3$–C3$_1$	110.19	67935.6
OH–C3$_3$–H1$_3$	110.26	51228.3
N3–C3$_1$–C3$_3$	111.04	66426.1
N3–C3$_1$–H1$_1$	109.88	49819.9
N3–C3$_2$–H1$_2$	109.88	49819.9
C3$_1$–N3–C3$_2$	112.35	64211.9
C3$_1$–C3$_3$–H1$_3$	109.56	46700.0
C3$_3$–OH–HO	107.26	47705.5
C3$_3$–C3$_1$–H1$_1$	109.56	46700.0
H1$_1$–C3$_1$–H1$_1$	108.46	39453.5
H1$_2$–C3$_2$–H1$_2$	108.46	39453.5
H1$_3$–C3$_3$–H1$_3$	108.46	39453.5

Table C.28: Torsion potential parameters of the MDEA molecule for the GAFF [95]. The torsion potential was computed using $U_{\text{Torsion}} = \sum_{i=0}^{5} p_i \cos^i(\phi)$ where $p_0..p_5$ are the torsion constants and ϕ is the torsion angle. Fig. C.1 shows the atom types designation of MDEA for the GAFF [95]. The values of p_4 and p_5 are zero for all torsions in the MDEA molecule.

Torsion	p_0/k_B / [K]	p_1/k_B / [K]	p_2/k_B / [K]	p_3/k_B / [K]
N3–C3$_1$–C3$_3$–OH	78.28	234.84	0.0	-313.12
OH–C3$_3$–C3$_1$–H1$_1$	125.81	-125.81	0.0	0.0
N3–C3$_1$–C3$_3$–H1$_3$	78.28	234.84	0.0	-313.12
C3$_1$–N3–C3$_1$–C3$_3$	634.07	452.9	-483.10	-603.87
C3$_1$–N3–C3$_1$–H1$_1$	150.97	452.9	0.0	-603.87
C3$_1$–N3–C3$_2$–H1$_2$	150.97	452.9	0.0	-603.87
C3$_1$–C3$_3$–OH–HO	206.32	115.74	0.0	-322.06
C3$_2$–N3–C3$_1$–C3$_3$	634.07	452.9	-483.10	-603.87
C3$_2$–N3–C3$_1$–H1$_1$	150.97	452.9	0.0	-603.87
H1$_1$–C3$_1$–C3$_3$–H1$_3$	78.28	234.84	0.0	-313.12
H1$_3$–C3$_3$–OH–HO	83.87	251.61	0.0	-335.48
HO–OH–C3$_3$–H1$_3$	83.87	251.61	0.0	-335.48

C.8.2. OPLS-AA/1.14*CM1A
This force field is used in Chapter 3 of this thesis and Ref. [5].
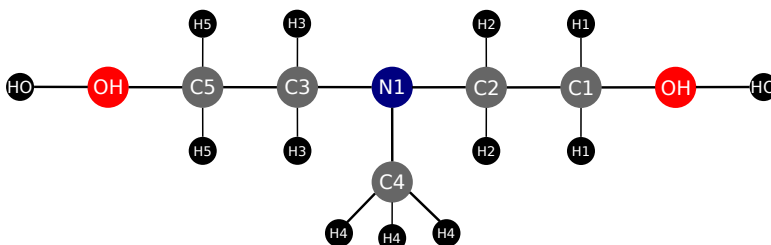
Figure C.2: Schematic representation showing atom type designations of the MDEA molecule for the OPLS-AA force field [88, 89] with 1.14*CM1A point charges [349].

Table C.29: Non-bonded interaction parameters for MDEA. For Lennard-Jones (LJ) interactions, the OPLS-AA force field [88, 89] was used. For electrostatic interactions, 1.14*CM1A point charges [349] were used. The point charges of the MDEA molecule sum up to zero and are not scaled. Fig. C.2 shows the atom types designation of MDEA for the OPLS-AA force field [88, 89].

Atom	ε/k_B / [K]	σ / [Å]	q / [e^-]
HO	0.000000	0.00	0.40770
OH	85.548491	3.12	-0.58335
C1	33.212943	3.50	0.00440
C2	33.212943	3.50	-0.01000
C3	33.212943	3.50	0.02920
C4	33.212943	3.50	-0.02180
C5	33.212943	3.50	0.00700
H1	15.096792	2.50	0.10210
H2	15.096792	2.50	0.08810
H3	15.096792	2.50	0.09900
H4	15.096792	2.50	0.08300
H5	15.096792	2.50	0.08090
N1	85.548491	3.30	-0.64670

Table C.30: Bond lengths of the MDEA molecule with the OPLS-AA force field [88, 89]. The bond lengths are fixed in MC simulations in Chapter 3.

Bond	Bond length / [Å]
HO–OH	0.96
OH–C1	1.42
C1–C2	1.53
C1–H1	1.10
C2–N1	1.46
C2–H2	1.11
N1–C3	1.46
N1–C4	1.46
C3–C5	1.53
C3–H3	1.11
C4–H4	1.11
C5–H5	1.10
C5–OH	1.42
OH–HO	0.96

Table C.31: Bending potential parameters, the equilibrium angle (θ_0) and the bending constant (K) of the MDEA molecule for the OPLS-AA force field [88, 89]. The bending potential was computed using $U_{\text{Bending}} = \frac{K}{2}(\theta - \theta_0)^2$ where K is the bending constant, θ is the bending angle, θ_0 is the bending angle at equilibrium. Fig. C.2 shows the atom types designation of MDEA for the OPLS-AA force field [88, 89].

Bending	θ_0 / [°]	K/k_{B} / [K rad^{-2}]
HO–OH–C1	108.50	55354.9
OH–C1–C2	109.50	50322.6
OH–C1–H1	109.50	35225.8
C1–C2–N1	109.47	56562.7
C1–C2–H2	110.70	37742.0
C2–N1–C3	107.20	52134.2
C2–N1–C4	107.20	52134.2
N1–C3–C5	109.47	56562.7
N1–C3–H3	109.50	35225.8
N1–C4–H4	109.50	35225.8
C3–C5–OH	109.50	50322.6
C3–C5–H5	110.70	37742.0
C5–OH–HO	108.50	55354.9
H4–C4–H4	107.80	33212.9
H3–C3–H3	107.80	33212.9
C5–C3–H3	110.70	37742.0
N1–C2–H2	109.50	35225.8
H4–C4–H4	107.80	33212.9
C5–C3–H3	110.70	37742.0
N1–C2–H2	109.50	35225.8
H5–C5–H5	107.80	33212.9
OH–C5–H5	109.50	35225.8
C2–C1–H1	110.70	37742.0
OH–C5–H5	109.50	35225.8
C2–C1–H1	110.70	37742.0
H2–C2–H2	107.80	33212.9
C3–N1–C4	107.20	52134.2
H1–C1–H1	107.80	33212.9
H4–C4–H4	107.80	33212.9

Table C.32: Torsion potential parameters of the MDEA molecule for the OPLS-AA force field [88, 89]. The torsion potential was computed using $U_{\text{Torsion}} = \frac{K_1}{2}(1 + \cos\phi) + \frac{K_2}{2}(1 - \cos2\phi) + \frac{K_3}{2}(1 + \cos3\phi) + \frac{K_4}{2}(1 - \cos4\phi)$ where $K_1..K_4$ are the torsion constants and ϕ is the torsion angle. Fig. C.2 shows the atom types designation of MDEA for the OPLS-AA force field [88, 89].

Torsion	K_1/k_B / [K]	K_2/k_B / [K]	K_3/k_B / [K]	K_4/k_B / [K]
C5–C3–N1–C2	215.17	420.00	64.47	-699.51
C5–C3–N1–C4	215.17	420.00	64.47	-699.51
C2–C1–OH–HO	-53.40	461.01	87.56	-495.17
C3–N1–C2–C1	215.17	420.00	64.47	-699.51
C4–N1–C2–H2	140.96	422.76	0.00	-563.60
C3–N1–C2–H2	140.96	422.76	0.00	-563.60
H5–C5–C3–H3	75.53	226.48	0.00	-301.89
H2–C2–C1–H1	75.53	226.48	0.00	-301.89
H5–C5–C3–H3	75.53	226.48	0.00	-301.89
H5–C5–C3–N1	-492.64	611.95	356.73	-476.04
H2–C2–C1–OH	117.75	353.24	0.00	-470.99
H4–C4–N1–C2	140.96	422.76	0.00	-563.60
H3–C3–N1–C4	140.96	422.76	0.00	-563.60
H4–C4–N1–C3	140.96	422.76	0.00	-563.60
H3–C3–N1–C2	140.96	422.76	0.00	-563.60
H4–C4–N1–C2	140.96	422.76	0.00	-563.60
H1–C1–OH–HO	88.52	265.69	0.00	-354.33
HO–OH–C5–C3	-53.40	461.01	87.56	-495.17
HO–OH–C5–H5	88.52	265.69	0.00	-354.33
N1–C2–C1–H1	-492.64	611.95	356.73	-476.04
N1–C2–C1–OH	2012.91	-2012.91	0.00	0.00
OH–C5–C3–H3	117.75	353.24	0.00	-470.99
OH–C5–C3–N1	2012.91	-2012.91	0.00	0.00

C.8.3. OPLS-AA/Quantum Chemistry
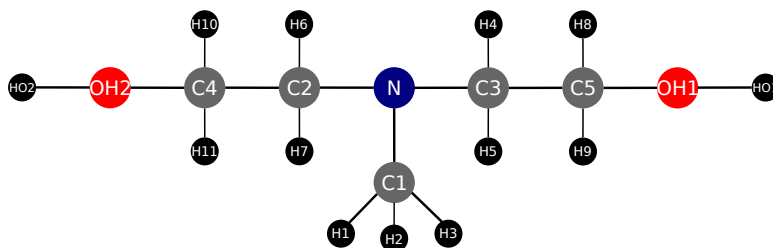This force field is used in Chapter 5 of this thesis and Ref. [348].

Figure C.3: Schematic representation showing atom type designations of the MDEA molecule for the OPLS-AA force field [88, 89] with point charges calculated using quantum chemistry calculations (MP2/6-311+G(2d,2p)). Color code: black: hydrogen; blue: nitrogen; red: oxygen; grey: carbon.

Table C.33: Intermolecular force field parameters for MDEA. The OPLS-AA force field [88, 89] with point charges computed by quantum chemical calculations (MP2/6-311+G(2d,2p)) was used for MDEA. The point charges listed in this table are unscaled charges, i.e. $\chi^q_{\mathrm{MDEA}} = 1.0$. The tabulated point charges sum up to zero. As explained in Chapter 5, in our simulations, these point charges are scaled by $\chi^q_{\mathrm{MDEA}} = 0.9$. The atom labels are defined in Fig. C.3.

Atom	ϵ/k_{B} / [K]	σ / [Å]	q / [e^-]
N	85.47	3.30	-0.63525
C1	33.18	3.50	-0.26080
C2	33.18	3.50	-0.10893
C3	33.18	3.50	-0.11385
C4	33.18	3.50	0.06446
C5	33.18	3.50	0.06972
OH1	85.47	3.12	-0.78207
OH2	85.47	3.12	-0.77757
H1	15.08	2.50	0.16784
H2	15.08	2.50	0.16269
H3	15.08	2.50	0.14238
H4	15.08	2.50	0.17381
H5	15.08	2.50	0.15235
H6	15.08	2.50	0.17490
H7	15.08	2.50	0.14150
H8	7.54	2.50	0.12994
H9	7.54	2.50	0.12320
H10	7.54	2.50	0.12901
H11	7.54	2.50	0.12130
HO1	0.50	1.00	0.46226
HO2	0.50	1.00	0.46311

Table C.34: Harmonic bond stretching potential parameters for MDEA. The OPLS-AA [88, 89] force field is used for MDEA. To compute the bonding potentials, we use $U_{\text{bond}} = K(r - r_0)^2$ where K is the bond coefficient, r is the distance between two atoms, and r_0 is the equilibrium distance between two atoms. The atom labels are defined in Fig. C.3.

Bond	r_0 / [Å]	K/k_{B} / [K Å^{-2}]
C–C	1.529	134735.7
C–H	1.090	170933.4
C–N	1.448	192048.7
C–O	1.410	160878.5
O–H	0.960	278018.2

Table C.35: Harmonic bond bending angle potential parameters for MDEA. The OPLS-AA [88, 89] force field is used for MDEA. To compute the angle potentials, we use $U_{\text{angle}} = K(\theta - \theta_0)^2$ where K is the bending strength, θ is the bending angle between three atoms, and θ_0 is the equilibrium bending angle. The atom labels are defined in Fig. C.3.

Angle	θ_0 / [°]	K/k_{B} / [K]
C–C–H	110.70	18852.9
C–C–N	109.47	28254.3
C–C–O	109.50	25137.3
C–O–H	108.50	27651.0
H–C–H	107.80	16590.6
H–C–N	109.50	17596.1
H–C–O	109.50	25137.3

Table C.36: OPLS-AA dihedral potential parameters for MDEA. The OPLS-AA [88, 89] force field is used for the dihedrals in MDEA, except for the N–C–C–O dihedral. For the N–C–C–O dihedral, we either use the parameters reported by Cornell et al. [295] or Orozco et al. [296]. To compute the dihedral potential for the dihedrals in this table, we use $U_{\text{dihedral}} = \frac{1}{2}K_1\left[1 + \cos(\phi)\right] + \frac{1}{2}K_2\left[1 - \cos(2\phi)\right] + \frac{1}{2}K_3\left[1 + \cos(3\phi)\right] + \frac{1}{2}K_4\left[1 - \cos(4\phi)\right]$ where $K_1..K_4$ are the dihedral coefficients and ϕ is the dihedral angle. The values of K_4 are 0 for all dihedrals listed in this table. The atom labels are defined in Fig. C.3.

Dihedral	K_1/k_{B} / [K]	K_2/k_{B} / [K]	K_3/k_{B} / [K]
H–C–N–C [88, 89]	0.00	0.00	281.54
C–N–C–C [88, 89]	209.14	-64.35	349.41
C–C–O–H [88, 89]	-178.98	-87.48	247.35
N–C–C–O [295]	0.00	0.00	1407.69

Table C.37: The optimized parameters for N–C–C–O dihedral from Orozco et al. [296]. All energies in this table are divided by the Boltzmann constant k_B and reported in units of K. To compute the dihedral potential for the N–C–C–O dihedral with the parameters in this table, we use $U_{\text{dihedral}} = \sum_{i=1,9} \left[a_i \cos^{i-1}(\phi) \right]$ where $a_1 .. a_9$ are the dihedral coefficients and ϕ is the dihedral angle. The atom labels are defined in Fig. C.3.

Dihedral	a_1/k_B	a_2/k_B	a_3/k_B	a_4/k_B	a_5/k_B	a_6/k_B	a_7/k_B	a_8/k_B	a_9/k_B
N–C–C–O	57.00	5889.99	1231.11	-9428.99	-6584.23	14567.26	6614.81	-11345.20	2511.20

C.9. Force Field Details for MDEAH$^+$

C.9.1. GAFF/RESP

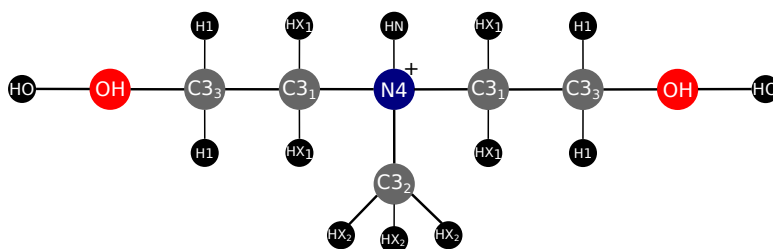This force field is used in Chapter 3 of this thesis and Ref. [5].

Figure C.4: Schematic representation showing atom type designations of the MDEAH$^+$ ion for the GAFF [95] with RESP fitted point charges [229].

Table C.38: Non-bonded interaction parameters for MDEAH$^+$. For Lennard-Jones (LJ) interactions, the General Amber Force Field (GAFF) [95] was used. For electrostatic interactions, two-step RESP fitted point charges [229] were used. The point charges of the MDEAH$^+$ molecule sum up to 1 and are not scaled. Fig. C.4 shows the atom types designation of MDEAH$^+$ for the GAFF [95].

Atom	ε/k_B / [K]	σ / [Å]	q / [e^-]
OH	105.8789	3.06647	-0.700894
N4	85.54849	3.25000	0.168263
C3$_1$	55.05302	3.39967	-0.144533
C3$_2$	55.05302	3.39967	-0.606302
C3$_3$	55.05302	3.39967	0.274300
HX$_1$	7.900655	2.47135	0.124590
HX$_2$	7.900655	2.47135	0.228587
H1	7.900655	2.47135	0.033983
HN	7.900655	2.47135	0.313387
HO	0.000000	0.00000	0.473426

Table C.39: Bond lengths of the MDEAH$^+$ ion with the General Amber Force field (GAFF) [95]. The bond lengths are fixed in MC simulations in Chapter 3.

Bond	Bond length / [Å]
OH–HO	0.96
OH–C3$_3$	1.42
N4–C3$_1$	1.51
N4_C3$_2$	1.51
N4–C3$_2$	1.51
C3$_1$–HX$_1$	1.09
C3$_1$–C3$_3$	1.53
C3$_1$–HX$_1$	1.09
C3$_2$–HX$_2$	1.09
C3$_3$–H1	1.10
N4–HN	1.03

Table C.40: Bending potential parameters, the equilibrium angle (θ_0) and the bending constant (K) of the MDEAH$^+$ ion for the GAFF [95]. The bending potential was computed using $U_{\mathrm{Bending}} = \frac{K}{2}(\theta - \theta_0)^2$ where K is the bending constant, θ is the bending angle, θ_0 is the bending angle at equilibrium. Fig. C.4 shows the atom types designation of MDEAH$^+$ for the GAFF [95].

Bending	θ_0 / [°]	K/k_{B} / [K rad^{-2}]
OH–C3$_3$–C3$_1$	110.19	67935.6
OH–C3$_3$–H1	110.26	51228.3
N4–C3$_1$–C3$_3$	114.21	64618.8
N4–C3$_1$–HX$_1$	108.01	48913.0
N4–C3$_2$–HX$_2$	108.01	48913.0
C3$_1$–N4–C3$_1$	109.66	63004.3
C3$_1$–N4–C3$_2$	109.66	63004.3
C3$_1$–N4–HN	110.11	46196.0
C3$_1$–C3$_3$–H1	109.56	46700.0
C3$_2$–N4–HN	110.11	46196.0
C3$_3$–OH–HO	107.26	47705.5
C3$_3$–C3$_1$–HX$_1$	110.56	46497.9
HX$_1$–C3$_1$–HX$_1$	109.75	39453.5
HX$_2$–C3$_2$–HX$_2$	109.75	39453.5
H1–C3$_3$–H1	108.46	39453.5

Table C.41: Torsion potential parameters of the MDEAH$^+$ ion for the GAFF [95]. The torsion potential was computed using $U_\text{Torsion} = \sum_{i=0}^{5} p_i \cos^i(\phi)$ where $p_0..p_5$ are the torsion constants and ϕ is the torsion angle. Fig. C.4 shows the atom types designation of MDEAH$^+$ for the GAFF [95]. The values of p_4 and p_5 are zero for all torsions in the MDEAH$^+$ ion.

Torsion	p_0/k_B / [K]	p_1/k_B / [K]	p_2/k_B / [K]	p_3/k_B / [K]
N4–C3$_1$–C3$_3$–OH	72.47	217.39	1308.39	-289.86
OH–C3$_3$–C3$_1$–HX$_1$	78.28	234.84	0.0	-313.12
N4–C3$_1$–C3$_3$–H1	78.28	234.84	0.0	-313.12
C3$_1$–N4–C3$_1$–C3$_3$	78.28	234.84	0.0	-313.12
C3$_1$–N4–C3$_1$–HX$_1$	78.28	234.84	0.0	-313.12
C3$_1$–N4–C3$_1$–HX$_2$	78.28	234.84	0.0	-313.12
C3$_1$–C3$_3$–OH–HO	206.32	115.74	0.0	-322.06
C3$_2$–N4–C3$_1$–C3$_3$	78.28	234.84	0.0	-313.12
C3$_2$–N4–C3$_1$–HX$_1$	78.28	234.84	0.0	-313.12
HN–N4–C3$_1$–C3$_3$	78.28	234.84	0.0	-313.12
H1–C3$_3$–C3$_1$–HX$_1$	78.28	234.84	0.0	-313.12
HX$_1$–C3$_1$–N4–HN	78.28	234.84	0.0	-313.12
HX$_1$–C3$_2$–N4–HN	78.28	234.84	0.0	-313.12
H1–C3$_3$–OH–HO	83.87	251.61	0.0	-335.48
C3$_1$–C3$_3$–OH–HO	206.32	115.74	0.0	-322.06

C.9.2. OPLS-AA/1.14*CM1A
This force field is used in Chapter 3 of this thesis and Ref. [5].
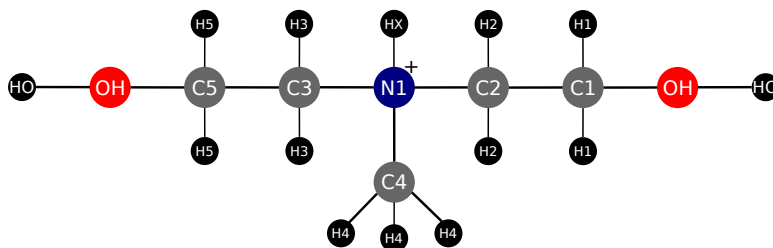

Figure C.5: Schematic representation showing atom type designations of the MDEAH$^+$ ion for the OPLS-AA force field [88, 89] with 1.14*CM1A point charges [349].

Table C.42: Non-bonded interaction parameters for MDEAH$^+$. For Lennard-Jones (LJ) interactions, the OPLS-AA force field [88, 89] was used. For electrostatic interactions, 1.14*CM1A point charges [349] were used. The point charges of the MDEAH$^+$ molecule sum up to 1 and are not scaled. Fig. C.5 shows the atom types designation of MDEAH$^+$ for the OPLS-AA force field [88, 89].

Atom	ε/k_B / [K]	σ / [Å]	q / [e^-]
HO	0.000000	0.00	0.40485
OH	85.548491	3.12	-0.54030
C1	33.212943	3.50	-0.00870
C2	33.212943	3.50	-0.10110
C3	33.212943	3.50	-0.10380
C4	33.212943	3.50	-0.15560
C5	33.212943	3.50	-0.00980
H1	15.096792	2.50	0.11010
H2	15.096792	2.50	0.14220
H3	15.096792	2.50	0.14330
H4	15.096792	2.50	0.13400
H5	15.096792	2.50	0.10990
HX	0.000000	0.00	0.36670
N1	85.548491	3.25	-0.12980

Table C.43: Bond lengths of the MDEAH$^+$ ion with the OPLS-AA force field [88, 89]. The bond lengths are fixed in MC simulations in Chapter 3.

Bond	Bond length / [Å]
HO–OH	0.96
OH–C1	1.42
C1–C2	1.53
C1–H1	1.10
C2–N1	1.51
C2–H2	1.09
N1–C3	1.51
N1–C4	1.50
N1–HX	1.03
C3–C5	1.53
C3–H3	1.09
C4–H4	1.09
C5–OH	1.41
C5–H5	1.10
OH–HO	0.96

Table C.44: Bending potential parameters, the equilibrium angle (θ_0) and the bending constant (K) of the MDEAH$^+$ ion for the OPLS-AA force field [88, 89]. The bending potential was computed using $U_{\text{Bending}} = \frac{K}{2}(\theta - \theta_0)^2$ where K is the bending constant, θ is the bending angle, θ_0 is the bending angle at equilibrium. Fig. C.5 shows the atom types designation of MDEAH$^+$ for the OPLS-AA force field [88, 89].

Bending	θ_0 / [°]	K/k_{B} / [K rad^{-2}]
HO–OH–C1	108.50	55354.9
OH–C1–C2	109.50	50322.6
OH–C1–H1	109.50	35225.8
C1–C2–N1	111.20	80516.2
C1–C2–H2	110.70	37742.0
C2–N1–C3	113.00	50322.6
C2–N1–C4	113.00	50322.6
C2–N1–HX	107.64	32357.4
N1–C3–C5	111.20	80516.2
N1–C3–H3	109.50	35225.8
N1–C4–H4	109.50	35225.8
C3–C5–OH	109.50	50322.6
C3–C5–H5	110.70	37742.0
C5–OH–HO	108.50	55354.9
C4–N1–HX	107.64	32357.4
C5–C3–H3	110.70	37742.0
OH–C5–H5	109.50	35225.8
H4–C4–H4	107.80	33212.9
N1–C2–H2	109.50	35225.8
H5–C5–H5	107.80	33212.9
C3–N1–HX	107.64	32357.4
C2–C1–H1	110.70	37742.0
C5–C3–H3	110.70	37742.0
H4–C4–H4	107.80	33212.9
H2–C2–H2	107.80	33212.9
C3–N1–C4	113.00	50322.6
H1–C1–H1	107.80	33212.9
OH–C5–H5	109.50	35225.8
H4–C4–H4	107.80	33212.9
H3–C3–H3	107.80	33212.9

Table C.45: Torsion potential parameters of the MDEAH$^+$ ion for the OPLS-AA force field [88, 89]. The torsion potential was computed using $U_{\text{Torsion}} = \frac{K_1}{2}(1 + \cos\phi) + \frac{K_2}{2}(1 - \cos2\phi) + \frac{K_3}{2}(1 + \cos3\phi) + \frac{K_4}{2}(1 - \cos4\phi)$ where $K_1..K_4$ are the torsion constants and ϕ is the torsion angle. Fig. C.5 shows the atom types designation of MDEAH$^+$ for the OPLS-AA force field [88, 89].

Torsion	K_1/k_B / [K]	K_2/k_B / [K]	K_3/k_B / [K]	K_4/k_B / [K]
C5–C3–N1–C4	365.87	-162.49	62.42	-265.69
C5–C3–N1–C2	365.87	-162.49	62.42	-265.69
C5–C3–N1–HX	87.32	261.96	0.00	-349.28
C2–C1–OH–HO	-53.40	461.01	87.56	-495.17
C4–N1–C2–C1	365.87	-162.49	62.42	-265.69
C3–N1–C2–C1	365.87	-162.49	62.42	-265.69
C4–N1–C2–H2	76.01	227.92	0.00	-303.93
C3–N1–C2–H2	76.01	227.92	0.00	-303.93
HX–N1–C2–C1	87.32	261.96	0.00	-349.28
HX–N1–C2–H2	65.67	197.01	0.00	-262.68
H5–C5–C3–H3	75.53	226.48	0.00	-301.89
H2–C2–C1–H1	75.53	226.48	0.00	-301.89
H5–C5–C3–H3	75.53	226.48	0.00	-301.89
H5–C5–C3–N1	96.58	289.86	0.00	-386.44
H2–C2–C1–OH	117.75	353.24	0.00	-470.99
H4–C4–N1–C2	76.01	227.92	0.00	-303.93
H4–C4–N1–C3	76.01	227.92	0.00	-303.93
H3–C3–N1–C4	76.01	227.92	0.00	-303.93
H3–C3–N1–C2	76.01	227.92	0.00	-303.93
H4–C4–N1–C2	76.01	227.92	0.00	-303.93
H3–C3–N1–C4	76.01	227.92	0.00	-303.93
H4–C4–N1–HX	65.67	197.01	0.00	-262.68
H3–C3–N1–HX	65.67	197.01	0.00	-262.68
H4–C4–N1–HX	65.67	197.01	0.00	-262.68
H1–C1–OH–HO	88.52	265.69	0.00	-354.33
HO–OH–C5–C3	-53.40	461.01	87.56	-495.17
HO–OH–C5–H5	88.52	265.69	0.00	-354.33
N1–C2–C1–H1	96.58	289.86	0.00	-386.44
N1–C2–C1–OH	2012.91	-2012.91	0.00	0.00
OH–C5–C3–H3	117.75	353.24	0.00	-470.99
OH–C5–C3–N1	2012.91	-2012.91	0.00	0.00

C.9.3. OPLS-AA/Quantum Chemistry
This force field is used in Chapter 5 of this thesis and Ref. [348].

Table C.46: Intermolecular force field parameters for MDEAH$^+$. The OPLS-AA force field [88, 89] with point charges computed by quantum chemical calculations (MP2/6-311+G(2d,2p)) was used for MDEAH$^+$. The point charges listed in this table are unscaled charges, i.e. $\chi^q_{\mathrm{MDEAH}^+} = 1.0$. The tabulated point charges sum up to exactly 1. As explained in Chapter 5, in our simulations, these point charges are scaled by 0.90 or 0.75. The atom labels are defined in Fig. C.6.

Atom	$\varepsilon/k_{\mathrm{B}}$ / [K]	σ / [Å]	q / [e^-]
N	85.47	3.25	-0.47548
C1	33.18	3.50	-0.30317
C2	33.18	3.50	-0.14067
C3	33.18	3.50	-0.13852
C4	33.18	3.50	-0.00517
C5	33.18	3.50	-0.00620
OH1	85.47	3.12	-0.76945
OH2	85.47	3.12	-0.76864
H1	15.08	2.50	0.21511
H2	15.08	2.50	0.20877
H3	15.08	2.50	0.20350
H4	15.08	2.50	0.20965
H5	15.08	2.50	0.20554
H6	15.08	2.50	0.20990
H7	15.08	2.50	0.20690
H8	15.08	2.50	0.18279
H9	15.08	2.50	0.15767
H10	15.08	2.50	0.18284
H11	15.08	2.50	0.15725
HO1	1.00	1.00	0.49508
HO2	1.00	1.00	0.49556
HX	1.00	1.00	0.47674
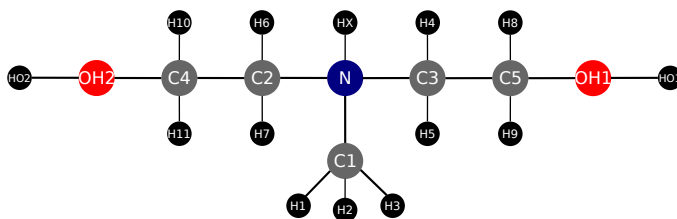
Figure C.6: Schematic representation showing atom type designations of the MDEAH$^+$ ion for the OPLS-AA force field [88, 89] with point charges calculated using quantum chemistry calculations (MP2/6-311+G(2d,2p)). Color code: black: hydrogen; blue: nitrogen; red: oxygen; grey: carbon.

Table C.47: Harmonic bond stretching potential parameters for MDEAH$^+$. The OPLS-AA [88, 89] force field is used for MDEAH$^+$. To compute the bonding potentials, we use $U_{\text{bond}} = K(r - r_0)^2$ where K is the bond coefficient, r is the distance between two atoms, and r_0 is the equilibrium distance between two atoms. The atom labels are defined in Fig. C.6.

Bond	r_0 / [Å]	K/k_{B} / [K Å^{-2}]
C–C	1.529	134735.7
C–H	1.090	170933.4
C–N	1.471	184507.5
C–O	1.410	160878.5
O–H	0.945	278018.2
N–H	1.01	218191.5

Table C.48: Harmonic bond bending angle potential parameters for MDEAH$^+$. The OPLS-AA [88, 89] force field is used for MDEAH$^+$. To compute the angle potentials, we use $U_{\text{angle}} = K(\theta - \theta_0)^2$ where K is the bending strength, θ is the bending angle between three atoms, and θ_0 is the equilibrium bending angle. The atom labels are defined in Fig. C.6.

Angle	θ_0 / [°]	K/k_{B} / [K]
C–C–H	110.70	18852.9
C–C–N	111.20	40219.6
C–C–O	109.50	25137.3
C–O–H	108.50	27651.0
C–N–C	113.00	25137.3
C–N–H	107.64	16163.3
H–C–H	107.80	16590.6
H–C–N	109.50	17596.1
H–C–O	109.50	17596.1

Table C.49: OPLS-AA dihedral potential parameters for MDEAH$^+$. The OPLS-AA [88, 89] force field is used for the dihedrals in MDEAH$^+$ except for the N–C–C–O dihedral. For the N–C–C–O dihedral, we used the parameters reported by Orozco et al. [296] (Table C.37). To compute the dihedral potential for the dihedrals in this table, we use $U_{\mathrm{dihedral}} = \frac{1}{2}K_1\left[1+\cos(\phi)\right] + \frac{1}{2}K_2\left[1-\cos(2\phi)\right] + \frac{1}{2}K_3\left[1+\cos(3\phi)\right] + \frac{1}{2}K_4\left[1-\cos(4\phi)\right]$ where $K_1..K_4$ are the dihedral coefficients and ϕ is the dihedral angle. The values of K_4 are 0 for all dihedrals listed in this table. The atom labels are defined in Fig. C.6.

Dihedral	K_1/k_B / [K]	K_2/k_B / [K]	K_3/k_B / [K]
C–C–O–H	-178.98	-87.48	247.35
C–N–C–C	722.95	-62.34	132.72
H–C–N–C	0.00	0.00	151.83
N–C–C–H	0.00	0.00	193.05
H–C–N–H	0.00	0.00	131.22
H–C–O–H	0.00	0.00	176.97
H–C–C–O	0.00	0.00	235.28
H–N–C–C	0.00	0.00	174.45
H–C–C–H	0.00	0.00	150.82

C.10. Force Field Details for MEA

This force field is used in Chapter 4 of this thesis and Ref. [301].

Table C.50: Force field parameters for MEA. For Lennard-Jones (LJ) interactions, the OPLS-AA [88, 89] force field was used while the atomic charges (corresponding to a charge neutral molecule) were computed using quantum chemical calculations. Quantum chemical calculations were performed using Gaussian09 [78] at second order Møller-Plesset perturbation theory (MP2) [70] level using the 6-311+G(2d,2p) basis set. The point charges listed in this table are scaled with $\chi^q_{\mathrm{MEA}} = 0.80$.

Atom	ε/k_B / [K]	σ / [Å]	q / [e^-]
N_T	85.600	3.30	-0.686816
H_1	1.0000	1.00	0.271816
H_2	1.0000	1.00	0.276432
C_{T1}	33.200	3.50	-0.100352
C_{T2}	33.200	3.50	0.048976
H_{T1}	7.5533	2.50	0.108248
H_{T2}	7.5533	2.50	0.133688
H_{T3}	15.107	2.50	0.099312
H_{T4}	15.107	2.50	0.106488
O_H	85.605	3.12	-0.628376
H_O	1.0000	1.00	0.370584

References

[1] J. Yu, L.-H. Xie, J.-R. Li, Y. Ma, J. M. Seminario, and P. B. Balbuena, *CO$_2$ capture and separations using MOFs: Computational and experimental studies,* Chem. Rev. **117**, 9674 (2017).

[2] National Oceanic and Atmospheric Administration, *Global climate dashboard,* (2024), https://www.climate.gov/climatedashboard, accessed on 17.01.2024.

[3] P. Erickson, M. Lazarus, and G. Piggot, *Limiting fossil fuel production as the next big step in climate policy,* Nat. Clim. Change. **8**, 1037 (2018).

[4] F.-Y. Liang, M. Ryvak, S. Sayeed, and N. Zhao, *The role of natural gas as a primary fuel in the near future, including comparisons of acquisition, transmission and waste handling costs of as with competitive alternatives,* Chem. Cent. J. **6**, S4 (2012).

[5] H. M. Polat, F. de Meyer, C. Houriez, O. A. Moultos, and T. J. H. Vlugt, *Solving chemical absorption equilibria using free energy and quantum chemistry calculations: Methodology, limitations, and new open-source software,* J. Chem. Theory Comput. **19**, 2616 (2023).

[6] J. H. Ausubel, A. Grübler, and N. Nakicenovic, *Carbon dioxide emissions in a methane economy,* Clim. Change **12**, 245 (1988).

[7] M. Yiannourakou, X. Rozanska, B. Minisini, and F. de Meyer, *Molecular simulations for improved process modeling of an acid gas removal unit,* Fluid Phase Equilib. **560**, 113478 (2022).

[8] W. F. Burgers, P. S. Northrop, H. S. Kheshgi, and J. A. Valencia, *Worldwide development potential for sour gas,* in *Energy Procedia*, Vol. 4 (Elsevier Ltd, 2011) pp. 2178–2184.

[9] A. H. Satyana, L. P. Marpaung, M. E. M. Purwaningsih, and M. K. Utama, *Regional gas geochemistry of Indonesia: genetic characterization and habitat of natural gases,* in *Proc. Indon. Petrol. Assoc., 31st Ann. Conv* (Indonesian Petroleum Association, 2007) https://www.ipa.or.id/en/publications/regional-gas-geochemistry-of-indonesia-genetic-characterization-and-habitat-of-natural-gases, accessed on 22.02.2024.

[10] G. Kang, Z. P. Chan, S. B. M. Saleh, and Y. Cao, *Removal of high concentration CO$_2$ from natural gas using high pressure membrane contactors,* Int. J. Greenh. Gas Control. **60**, 1 (2017).

[11] G. M. Dlamini, P. L. Fosbøl, and N. von Solms, *Modelling phase equilibria of sulphur compounds in mixtures relevant to carbon capture and storage with new association schemes,* Fluid Phase Equilib. **568**, 113738 (2023).

[12] J. Jiang, A. Chan, S. Ali, A. Saha, K. J. Haushalter, W.-L. M. Lam, M. Glasheen, J. Parker, M. Brenner, S. B. Mahon, H. H. Patel, R. Ambasudhan, S. A. Lipton, R. B. Pilz, and G. R. Boss, *Hydrogen sulfide—mechanisms of toxicity and development of an antidote,* Sci. Rep. **6**, 20831 (2016).

[13] S. Mokhatab, W. A. Poe, and J. Y. Mak, *Basic concepts of natural gas processing,* in *Handbook of Natural Gas Transmission and Processing*, edited by S. Mokhatab, W. A. Poe, and J. Y. Mak (Gulf Professional Publishing, 2019) 4th ed., pp. 177–189.

[14] J. Hagoort, *Fundamentals of Gas Reservoir Engineering*, 1st ed. (Elsevier, Amsterdam, The Netherlands, 1988).

[15] M. Živković, M. Ivić, D. Ivezić, and A. Madžarević, *Effect of natural gas composition on methane number: A case of gas reservoirs in serbia,* Energy Sources A: Recovery Util. Environ. Eff. **39**, 2157 (2017).

[16] G. George, N. Bhoria, S. Alhallaq, A. Abdala, and V. Mittal, *Polymer membranes for acid gas removal from natural gas,* Sep. Purif. Technol. **158**, 333 (2016).

[17] D. Turi, M. Ho, M. Ferrari, P. Chiesa, D. Wiley, and M. Romano, *CO_2 capture from natural gas combined cycles by CO_2 selective membranes,* Int. J. Greenh. Gas Control. **61**, 168 (2017).

[18] K. Maqsood, A. Mullick, A. Ali, K. Kargupta, and S. Ganguly, *Cryogenic carbon dioxide separation from natural gas: a review based on conventional and novel emerging technologies,* Rev. Chem. Eng. **30**, 453 (2014).

[19] K.-H. Park, J. W. Lee, Y. Lim, and Y. Seo, *Life cycle cost analysis of CO_2 compression processes coupled with a cryogenic distillation unit for purifying high-CO_2 natural gas,* J. CO2 Util. **60**, 102002 (2022).

[20] J. S. Eow, *Recovery of sulfur from sour acid gas: A review of the technology,* Environ. Prog. **21**, 143 (2002).

[21] Y. Wei, L. Wang, Y. Yang, L. Wen, X. Huo, L. Zhang, and M. Yang, *Molecular mechanism in the solubility reduction of elemental sulfur in H_2S/CH_4 mixtures: A molecular modeling study,* Fluid Phase Equilib. **569**, 113764 (2023).

[22] A. Haghtalab, M. Mohammadi, and Z. Fakhroueian, *Absorption and solubility measurement of CO_2 in water-based ZnO and SiO_2 nanofluids,* Fluid Phase Equilib. **392**, 33 (2015).

[23] R. L. Siegelman, P. J. Milner, E. J. Kim, S. C. Weston, and J. R. Long, *Challenges and opportunities for adsorption-based CO_2 capture from natural gas combined cycle emissions,* Energy Environ. Sci. **12**, 2161 (2019).

[24] H. M. Polat, M. Zeeshan, A. Uzun, and S. Keskin, *Unlocking CO_2 separation performance of ionic liquid/CuBTC composites: Combining experiments with molecular simulations,* Chem. Eng. J. **373**, 1179 (2019).

[25] E. Favre, *Carbon dioxide recovery from post-combustion processes: Can gas permeation membranes compete with absorption?* J. Membr. Sci. **294**, 50 (2007).

[26] M. Wang, A. Lawal, P. Stephenson, J. Sidders, and C. Ramshaw, *Post-combustion CO_2 capture with chemical absorption: A state-of-the-art review,* Chem. Eng. Res. Des. **89**, 1609 (2011).

[27] I. S. Al-Mutaz, *Removal of acid gas from natural gas: A comparison of conventional and selective membrane processes,* J. King Saud Univ. Eng. Sci. **7**, 327 (1995).

[28] A. Qayyum, U. Ali, and N. Ramzan, *Acid gas removal techniques for syngas, natural gas, and biogas clean up – a review,* Energy Sources A: Recovery Util. Environ. Eff. , 1 (2020).

[29] Y. Alcheikhhamdon and M. Hoorfar, *Natural gas purification from acid gases using membranes: A review of the history, features, techno-commercial challenges, and process intensification of commercial membranes,* Chem. Eng. Process.: Process Intensif. **120**, 105 (2017).

[30] L. Xie, J. Xu, Y. Zhang, and Y. He, *Biogas upgrading,* in *Advances in Bioenergy*, Vol. 5, edited by Y. Li and S. K. Khanal (Elsevier, 2020) pp. 309–344.

[31] S. Khairulin, M. Kerzhentsev, A. Salnikov, and Z. Ismagilov, *Basic technologies of direct catalytic oxidation of H_2S to sulfur,* J. Phys. Conf. Ser. **1749**, 012027 (2021).

[32] S. Khairulin, M. Kerzhentsev, A. Salnikov, and Z. R. Ismagilov, *Direct selective oxidation of hydrogen sulfide: Laboratory, pilot and industrial tests,* Catalysts **11**, 1109 (2021).

[33] A. Pudi, M. Rezaei, V. Signorini, M. P. Andersson, M. G. Baschetti, and S. S. Mansouri, *Hydrogen sulfide capture and removal technologies: A comprehensive review of recent developments and emerging trends,* Sep. Purif. Technol. **298**, 121448 (2022).

[34] I. Rosso, C. Galletti, M. Bizzi, G. Saracco, and V. Specchia, *Zinc oxide sorbents for the removal of hydrogen sulfide from syngas,* Ind. Eng. Chem. Res. **42**, 1688 (2003).

[35] Z. Zhao, X. Cui, J. Ma, and R. Li, *Adsorption of carbon dioxide on alkali-modified zeolite 13X adsorbents,* Int. J. Greenh. Gas Control. **1**, 355 (2007).

[36] T. Rufford, S. Smart, G. Watson, B. Graham, J. Boxall, J. D. da Costa, and E. May, *The removal of CO_2 and N_2 from natural gas: A review of conventional and emerging process technologies,* J. Pet. Sci. Eng. **94-95**, 123 (2012).

[37] E. Skylogianni, I. Mundal, D. D. Pinto, C. Coquelet, and H. K. Knuutila, *Hydrogen sulfide solubility in 50 wt% and 70 wt% aqueous methyldiethanolamine at temperatures from 283 to 393 K and total pressures from 500 to 10000 kPa,* Fluid Phase Equilib. **511**, 112498 (2020).

[38] L. Guo, Y. Wang, B. Wang, N. Wang, L. Zhang, and Y. Chen, *A simplified semi-empirical model for modeling of CO_2 solubilities in aqueous MDEA and MEA solutions,* Fluid Phase Equilib. **555**, 113352 (2022).

[39] C. Mathonat, V. Majer, A. Mather, and J.-P. Grolier, *Enthalpies of absorption and solubility of CO_2 in aqueous solutions of methyldiethanolamine,* Fluid Phase Equilib. **140**, 171 (1997).

[40] S. Bishnoi and G. T. Rochelle, *Absorption of carbon dioxide in aqueous piperazine/methyldiethanolamine,* AIChE J. **48**, 2788 (2002).

[41] S. Moioli, L. A. Pellegrini, P. Vergani, and F. Brignoli, *Study of the robustness of a low-temperature dual-pressure process for removal of CO_2 from natural gas,* Front. Chem. Sci. Eng. **12**, 209 (2018).

[42] A. A. Orlov, A. Valtz, C. Coquelet, X. Rozanska, E. Wimmer, G. Marcou, D. Horvath, B. Poulain, A. Varnek, and F. de Meyer, *Computational screening methodology identifies effective solvents for CO_2 capture,* Commun. Chem. **5**, 1 (2022).

[43] L. Peters, A. Hussain, M. Follmann, T. Melin, and M.-B. Hägg, *CO_2 removal from natural gas by employing amine absorption and membrane technology—A technical and economical analysis,* Chem. Eng. J. **172**, 952 (2011).

[44] U. S. P. R. Arachchige and M. C. Melaaen, *Aspen plus simulation of CO_2 removal from coal and gas fired power plants,* Energy Procedia **23**, 391 (2012).

[45] A. Muhammad and Y. GadelHak, *Correlating the additional amine sweetening cost to acid gases load in natural gas using Aspen HYSYS,* J. Nat. Gas. Sci. Eng. **17**, 119 (2014).

[46] N. M. Al-Lagtah, S. Al-Habsi, and S. A. Onaizi, *Optimization and performance improvement of Lekhwair natural gas sweetening plant using Aspen HYSYS,* J. Nat. Gas. Sci. Eng. **26**, 367 (2015).

[47] S. Dara and A. S. Berrouk, *Computer-based optimization of acid gas removal unit using modified CO_2 absorption kinetic models,* Int. J. Greenh. Gas Control. **59**, 172 (2017).

[48] S. Laugier and D. Richon, *New apparatus to perform fast determinations of mixture vapor–liquid equilibria up to 10 MPa and 423 K,* Rev. Sci. Instrum. **57**, 469 (1986).

[49] F.-Y. Jou, J. J. Carroll, A. E. Mather, and F. D. Otto, *Solubility of mixtures of hydrogen sulfide and carbon dioxide in aqueous N-methyldiethanolamine solutions,* J. Chem. Eng. Data **38**, 75 (1993).

[50] F. Y. Jou, F. D. Otto, and A. E. Mather, *The solubility of mixtures of H_2S and CO_2 in an MDEA solution,* Can. J. Chem. Eng. **75**, 1138 (1997).

[51] P. S. Kumar, J. A. Hogendoorn, S. J. Timmer, P. H. M. Feron, and G. F. Versteeg, *Equilibrium solubility of CO_2 in aqueous potassium taurate solutions: Part 2. experimental vle data and model,* Ind. Eng. Chem. Res. **42**, 2841 (2003).

[52] P. W. J. Derks, H. B. S. Dijkstra, J. A. Hogendoorn, and G. F. Versteeg, *Solubility of carbon dioxide in aqueous piperazine solutions,* AIChE J. **51**, 2311 (2005).

[53] P. W. J. Derks, *Carbon Dioxide Absorption in Piperazine Activated N-Methyldiethanolamine*, Ph.D. thesis, University of Twente, Netherlands (2006), URL: http://purl.utwente.nl/publications/57600, accessed on 15/02/2024.

[54] M. Dicko, C. Coquelet, C. Jarne, S. Northrop, and D. Richon, *Acid gases partial pressures above a 50wt% aqueous methyldiethanolamine solution: Experimental work and modeling,* Fluid Phase Equilib. **289**, 99 (2010).

[55] G. F. Versteeg and W. P. M. V. Swaaij, *Solubility and diffusivity of acid gases (carbon dioxide, nitrous oxide) in aqueous alkanolamine solutions,* J. Chem. Eng. Data **33**, 29 (1988).

[56] Q. Chen, S. P. Balaji, M. Ramdin, J. J. Gutiérrez-Sevillano, A. Bardow, E. Goetheer, and T. J. H. Vlugt, *Validation of the CO_2/N_2O analogy using molecular simulation,* Ind. Eng. Chem. Res. **53**, 18081 (2014).

[57] M. Kohns, S. Werth, M. Horsch, E. von Harbou, and H. Hasse, *Molecular simulation study of the CO_2-N_2O analogy,* Fluid Phase Equilib. **442**, 44 (2017).

[58] E. Sada, H. Kumazawa, and M. A. Butt, *Solubility and diffusivity of gases in aqueous solutions of amines,* J. Chem. Eng. Data **23**, 161 (1978).

[59] J. J. Ko, T. C. Tsai, C. Y. Lin, H. M. Wang, and M. H. Li, *Diffusivity of nitrous oxide in aqueous alkanolamine solutions,* J. Chem. Eng. Data **46**, 160 (2001).

[60] J. Ying and D. A. Eimer, *Measurements and correlations of diffusivities of nitrous oxide and carbon dioxide in monoethanolamine + water by laminar liquid jet,* Ind. Eng. Chem. Res. **51**, 16517 (2012).

[61] X. Yang, R. J. Rees, W. Conway, G. Puxty, Q. Yang, and D. A. Winkler, *Computational modeling and simulation of CO_2 capture by aqueous amines,* Chem. Rev. **117**, 9524 (2017).

[62] K. H. Johnson, *Quantum chemistry,* Annu. Rev. Phys. Chem. **26**, 39 (1975).

[63] J. A. Pople, *Nobel lecture: Quantum chemical models,* Rev. Mod. Phys. **71**, 1267 (1999).

[64] W. Kohn, *Nobel lecture: Electronic structure of matter—wave functions and density functionals,* Rev. Mod. Phys. **71**, 1253 (1999).

[65] S. McArdle, S. Endo, A. Aspuru-Guzik, S. C. Benjamin, and X. Yuan, *Quantum computational chemistry,* Rev. Mod. Phys. **92**, 015003 (2020).

[66] M. Head-Gordon, *Quantum chemistry and molecular processes,* J. Phys. Chem. **100**, 13213 (1996).

[67] A. Laaksonen and J. Malila, *Simulations and molecular-based theories,* in *Nucleation of Water*, edited by A. Laaksonen and J. Malila (Elsevier, 2022) pp. 83–105.

[68] R. Hoffmann, P. von Ragué Schleyer, and H. F. Schaefer, *Predicting molecules—more realism, please!* Angew. Chem. Int. Ed. **47**, 7164 (2008).

[69] C. C. J. Roothaan, *New developments in molecular orbital theory,* Rev. Mod. Phys. **23**, 69 (1951).

[70] C. Møller and M. S. Plesset, *Note on an approximation treatment for many-electron systems,* Phys. Rev. **46**, 618 (1934).

[71] P. Hohenberg and W. Kohn, *Inhomogeneous electron gas,* Phys. Rev. **136**, B864 (1964).

[72] W. Kohn and L. J. Sham, *Self-consistent equations including exchange and correlation effects,* Phys. Rev. **140**, A1133 (1965).

[73] R. G. Parr and Y. Weitao, *Density-Functional Theory of Atoms and Molecules* (Oxford University Press, New York, NY, USA, 1995).

[74] M. Bogojeski, L. Vogt-Maranto, M. E. Tuckerman, K.-R. Müller, and K. Burke, *Quantum chemical accuracy from density functional approximations via machine learning,* Nat. Commun. **11**, 5223 (2020).

[75] L. E. Ratcliff, S. Mohr, G. Huhs, T. Deutsch, M. Masella, and L. Genovese, *Challenges in large scale quantum mechanical calculations,* WIREs Comput. Mol. Sci. **7**, e1290 (2017).

[76] B. Nagy and F. Jensen, *Basis sets in quantum chemistry,* in *Reviews in Computational Chemistry* (John Wiley & Sons, Ltd, 2017) Chap. 3, pp. 93–149.

[77] D. A. McQuarrie and J. D. Simon, *Physical chemistry: A molecular approach*, 1st ed. (University Science Books, Sausalito, California, 1997).

[78] M. J. Frisch, G. W. Trucks, H. B. Schlegel, G. E. Scuseria, M. A. Robb, J. R. Cheeseman, G. Scalmani, V. Barone, B. Mennucci, G. A. Petersson, H. Nakatsuji, M. Caricato, X. Li, H. P. Hratchian, A. F. Izmaylov, J. Bloino, G. Zheng, J. L. Sonnenberg, M. Hada, M. Ehara, K. Toyota, R. Fukuda, J. Hasegawa, M. Ishida, T. Nakajima, Y. Honda, O. Kitao, H. Nakai, T. Vreven, J. A. Montgomery, Jr., J. E. Peralta, F. Ogliaro, M. Bearpark, J. J. Heyd, E. Brothers, K. N. Kudin, V. N. Staroverov, R. Kobayashi, J. Normand, K. Raghavachari, A. Rendell, J. C. Burant, S. S. Iyengar, J. Tomasi, M. Cossi, N. Rega, J. M. Millam, M. Klene, J. E. Knox, J. B. Cross, V. Bakken, C. Adamo, J. Jaramillo, R. Gomperts, R. E. Stratmann, O. Yazyev, A. J. Austin, R. Cammi, C. Pomelli, J. W. Ochterski, R. L. Martin, K. Morokuma, V. G. Zakrzewski, G. A. Voth, P. Salvador, J. J. Dannenberg, S. Dapprich, A. D. Daniels, Ö. Farkas, J. B. Foresman, J. V. Ortiz, J. Cioslowski, and D. J. Fox, *Gaussian 09 Revision E.01,* Gaussian Inc. Wallingford CT 2009.

[79] A. Rahbari, *Thermodynamics of Industrially Relevant Systems: Method Development and Applications*, Ph.D. thesis, Delft University of Technology, Netherlands (2020).

[80] F. Neese, F. Wennmohs, U. Becker, and C. Riplinger, *The ORCA quantum chemistry program package,* J. Chem. Phys. **152,** 224108 (2020).

[81] E. Aprà, E. J. Bylaska, W. A. de Jong, N. Govind, K. Kowalski, T. P. Straatsma, M. Valiev, H. J. J. van Dam, Y. Alexeev, J. Anchell, V. Anisimov, F. W. Aquino, R. Atta-Fynn, J. Autschbach, N. P. Bauman, J. C. Becca, D. E. Bernholdt, K. Bhaskaran-Nair, S. Bogatko, P. Borowski, J. Boschen, J. Brabec, A. Bruner, E. Cauët, Y. Chen, G. N. Chuev, C. J. Cramer, J. Daily, M. J. O. Deegan, T. H. Dunning, M. Dupuis, K. G. Dyall, G. I. Fann, S. A. Fischer, A. Fonari, H. Früchtl, L. Gagliardi, J. Garza, N. Gawande, S. Ghosh, K. Glaesemann, A. W. Götz, J. Hammond, V. Helms, E. D. Hermes, K. Hirao, S. Hirata, M. Jacquelin, L. Jensen, B. G. Johnson, H. Jónsson, R. A. Kendall, M. Klemm, R. Kobayashi, V. Konkov, S. Krishnamoorthy, M. Krishnan, Z. Lin, R. D. Lins, R. J. Littlefield, A. J. Logsdail, K. Lopata, W. Ma, A. V. Marenich, J. M. del Campo, D. Mejia-Rodriguez, J. E. Moore, J. M. Mullin, T. Nakajima, D. R. Nascimento, J. A. Nichols, P. J. Nichols, J. Nieplocha, A. O. de-la Roza, B. Palmer, A. Panyala, T. Pirojsirikul, B. Peng, R. Peverati, J. Pittner, L. Pollack, R. M. Richard, P. Sadayappan, G. C. Schatz, W. A. Shelton, D. W. Silverstein, D. M. A. Smith, T. A. Soares, D. Song, M. Swart, H. L. Taylor, G. S. Thomas, V. Tipparaju, D. G. Truhlar, K. Tsemekhman, T. V. Voorhis, A. Vázquez-Mayagoitia, P. Verma, O. Villa, A. Vishnu, K. D. Vogiatzis, D. Wang, J. H. Weare, M. J. Williamson, T. L. Windus, K. Woliński, A. T. Wong,

Q. Wu, C. Yang, Q. Yu, M. Zacharias, Z. Zhang, Y. Zhao, and R. J. Harrison, *NWChem: Past, present, and future,* J. Chem. Phys. **152**, 184102 (2020).

[82] D. Frenkel and B. Smit, *Understanding molecular simulation: From algorithms to applications*, 3rd ed. (Academic Press, San Diego, California, 2023).

[83] M. P. Allen and D. J. Tildesley, *Computer Simulation of Liquids*, 2nd ed. (Oxford University Press, New York, NY, USA, 2017).

[84] J. Hafner and G. Kresse, *The Vienna ab-initio simulation program VASP: An efficient and versatile tool for studying the structural, dynamic, and electronic properties of materials,* in *Properties of Complex Inorganic Solids*, edited by A. Gonis, A. Meike, and P. E. A. Turchi (Springer US, Boston, MA, 1997) pp. 69–82.

[85] D. Dubbeldam, S. Calero, D. E. Ellis, and R. Q. Snurr, *RASPA: Molecular simulation software for adsorption and diffusion in flexible nanoporous materials,* Mol. Sim. **42**, 81 (2016).

[86] Y. Nejahi, M. S. Barhaghi, G. Schwing, L. Schwiebert, and J. Potoff, *Update 2.70 to "GOMC: GPU optimized Monte Carlo for the simulation of phase equilibria and physical properties of complex fluids",* SoftwareX **13**, 100627 (2021).

[87] J. R. Maple, U. Dinur, and A. T. Hagler, *Derivation of force fields for molecular mechanics and dynamics from ab initio energy surfaces,* Proc. Natl. Acad. Sci. **85**, 5350 (1988).

[88] W. L. Jorgensen, D. S. Maxwell, and J. Tirado-Rives, *Development and testing of the OPLS all-atom force field on conformational energetics and properties of organic liquids,* J. Am. Chem. Soc. **118**, 11225 (1996).

[89] R. C. Rizzo and W. L. Jorgensen, *OPLS all-atom model for amines: Resolution of the amine hydration problem,* J. Am. Chem. Soc. **121**, 4827 (1999).

[90] J. J. Potoff and J. I. Siepmann, *Vapor–liquid equilibria of mixtures containing alkanes, carbon dioxide, and nitrogen,* AIChE J. **47**, 1676 (2001).

[91] K. M. Visscher and D. P. Geerke, *Deriving force-field parameters from first principles using a polarizable and higher order dispersion model,* J. Chem. Theory Comput. **15**, 1875 (2019).

[92] J. T. Horton, A. E. A. Allen, L. S. Dodda, and D. J. Cole, *QUBEKit: Automating the derivation of force field parameters from quantum mechanics,* J. Chem. Inf. Model **59**, 1366 (2019).

[93] M. G. Martin and J. I. Siepmann, *Transferable potentials for phase equilibria. 1. United-atom description of n-alkanes,* J. Phys. Chem. B **102**, 2569 (1998).

[94] J. L. F. Abascal and C. Vega, *A general purpose model for the condensed phases of water: TIP4P/2005,* J. Chem. Phys. **123**, 234505 (2005).

[95] J. Wang, R. M. Wolf, J. W. Caldwell, P. A. Kollman, and D. A. Case, *Development and testing of a general amber force field,* J. Comput. Chem. **25**, 1157 (2004).

[96] R. Hens, A. Rahbari, S. Caro-Ortiz, N. Dawass, M. Erdős, A. Poursaeidesfahani, H. S. Salehi, A. T. Celebi, M. Ramdin, O. A. Moultos, D. Dubbeldam, and T. J. H. Vlugt, *Brick-CFCMC: Open source software for Monte Carlo simulations of phase and reaction equilibria using the Continuous Fractional Component Method,* J. Chem. Inf. Model **60**, 2678 (2020).

[97] H. M. Polat, H. S. Salehi, R. Hens, D. O. Wasik, A. Rahbari, F. de Meyer, C. Houriez, C. Coquelet, S. Calero, D. Dubbeldam, O. A. Moultos, and T. J. H. Vlugt, *New features of the open source Monte Carlo software Brick-CFCMC: Thermodynamic integration and hybrid trial moves,* J. Chem. Inf. Model **61**, 3752 (2021).

[98] M. Ramdin, T. M. Becker, S. H. Jamali, M. Wang, and T. J. H. Vlugt, *Computing equation of state parameters of gases from Monte Carlo simulations,* Fluid Phase Equilib. **428**, 174 (2016).

[99] F. Sarrasin, P. Memari, M. Klopffer, V. Lachet, C. T. Condat, B. Rousseau, and E. Espuche, *Influence of high pressures on CH_4, CO_2 and H_2S solubility in polyethylene: Experimental and molecular simulation approaches for pure gas and gas mixtures. modelling of the sorption isotherms,* J. Membr. Sci. **490**, 380 (2015).

[100] T. Heimburg and R. Biltonen, *A Monte Carlo simulation study of protein-induced heat capacity changes and lipid-induced protein clustering,* Biophys. J. **70**, 84 (1996).

[101] G. Kronome, T. Kristóf, J. Liszi, and I. Szalai, *Heat capacities of two-centre Lennard–Jones fluids from NpT ensemble Monte Carlo simulations,* Fluid Phase Equilib. **155**, 157 (1999).

[102] M. Lagache, P. Ungerer, A. Boutin, and A. H. Fuchs, *Prediction of thermodynamic derivative properties of fluids by Monte Carlo simulation,* Phys. Chem. Chem. Phys. **3**, 4333 (2001).

[103] J. I. Siepmann, I. R. Mcdonald, and D. Frenkel, *Finite-size corrections to the chemical potential,* J. Phys. Condens. Matter **4**, 679 (1992).

[104] J. Noroozi and W. R. Smith, *Accurately predicting CO_2 reactive absorption properties in aqueous alkanolamine solutions by molecular simulation requiring no solvent experimental data,* Ind. Eng. Chem. Res. **59**, 18254 (2020).

[105] J. Noroozi and W. R. Smith, *Force-field-based computational study of the thermodynamics of a large set of aqueous alkanolamine solvents for post-combustion CO_2 capture,* J. Chem. Inf. Model **61**, 4497 (2021).

[106] A. Rahbari, R. Hens, D. Dubbeldam, and T. J. H. Vlugt, *Improving the accuracy of computing chemical potentials in CFCMC simulations,* Mol. Phys. **117**, 3493 (2019).

[107] N. Dawass, R. R. Wanderley, M. Ramdin, O. A. Moultos, H. K. Knuutila, and T. J. H. Vlugt, *Solubility of carbon dioxide, hydrogen sulfide, methane, and nitrogen in monoethylene glycol; experiments and molecular simulation,* J. Chem. Eng. Data **66**, 524 (2021).

[108] H. S. Salehi, H. M. Polat, F. de Meyer, C. Houriez, C. Coquelet, T. J. H. Vlugt, and O. A. Moultos, *Vapor pressures and vapor phase compositions of choline chloride urea and choline chloride ethylene glycol deep eutectic solvents from molecular simulation,* J. Chem. Phys. **155**, 114504 (2021).

[109] J. I. Siepmann, *A method for the direct calculation of chemical potentials for dense chain systems,* Mol. Phys. **70**, 1145 (1990).

[110] M. Laso, J. J. de Pablo, and U. W. Suter, *Simulation of phase equilibria for chain molecules,* J. Chem. Phys. **97**, 2817 (1992).

[111] D. Frenkel, G. C. A. M. Mooij, and B. Smit, *Novel scheme to study structural and thermal properties of continuously deformable molecules,* J. Phys. Condens. Matt. **4**, 3053 (1992).

[112] G. C. A. M. Mooij, D. Frenkel, and B. Smit, *Direct simulation of phase equilibria of chain molecules,* J. Phys. Condens. Matt. **4**, L255 (1992).

[113] D. Dubbeldam, A. Torres-Knoop, and K. S. Walton, *On the inner workings of Monte Carlo codes,* Mol. Sim. **39**, 1253 (2013).

[114] W. Shi and E. J. Maginn, *Continuous Fractional Component Monte Carlo: An adaptive biasing method for open system atomistic simulations,* J. Chem. Theory Comput. **3**, 1451 (2007).

[115] T. W. Rosch and E. J. Maginn, *Reaction ensemble Monte Carlo simulation of complex molecular systems,* J. Chem. Theory Comput. **7**, 269 (2011).

[116] A. Poursaeidesfahani, A. Torres-Knoop, D. Dubbeldam, and T. J. H. Vlugt, *Direct free energy calculation in the Continuous Fractional Component Gibbs Ensemble,* J. Chem. Theory Comput. **12**, 1481 (2016).

[117] A. Poursaeidesfahani, R. Hens, A. Rahbari, M. Ramdin, D. Dubbeldam, and T. J. H. Vlugt, *Efficient application of continuous fractional component Monte Carlo in the Reaction Ensemble,* J. Chem. Theory Comput. **13**, 4452 (2017).

[118] A. Rahbari, R. Hens, I. K. Nikolaidis, A. Poursaeidesfahani, M. Ramdin, I. G. Economou, O. A. Moultos, D. Dubbeldam, and T. J. H. Vlugt, *Computation of partial molar properties using continuous fractional component Monte Carlo,* Mol. Phys. **116**, 3331 (2018).

[119] R. Hens and T. J. H. Vlugt, *Molecular simulation of Vapor–Liquid equilibria using the Wolf method for electrostatic interactions,* J. Chem. Eng. Data **63**, 1096 (2017).

[120] D. Dubbeldam and R. Q. Snurr, *Recent developments in the molecular modeling of diffusion in nanoporous materials,* Mol. Sim. **33**, 305 (2007).

[121] D. Dubbeldam, K. S. Walton, T. J. H. Vlugt, and S. Calero, *Design, parameterization, and implementation of atomic force fields for adsorption in nanoporous materials,* Adv. Theory Simul. **2**, 1900135 (2019).

[122] J. K. Shah, E. Marin-Rimoldi, R. G. Mullen, B. P. Keene, S. Khan, A. S. Paluch, N. Rai, L. L. Romanielo, T. W. Rosch, B. Yoo, and E. J. Maginn, *Cassandra: An open source Monte Carlo package for molecular simulation,* J. Comput. Chem. **38**, 1727 (2017).

[123] A. Rahbari, R. Hens, M. Ramdin, O. A. Moultos, D. Dubbeldam, and T. J. H. Vlugt, *Recent advances in the continuous fractional component Monte Carlo methodology,* Mol. Sim. **47**, 804 (2021).

[124] G. Xiao, S. To, and G. Zhang, *Molecular dynamics modelling of brittle–ductile cutting mode transition: Case study on silicon carbide,* Int. J. Mach. Tools Manuf. **88**, 214 (2015).

[125] G. Xiao, M. Ren, and H. Hong, *50 million atoms scale molecular dynamics modelling on a single consumer graphics card,* Adv. Eng. Softw. **124**, 66 (2018).

[126] L. C. Pierce, R. Salomon-Ferrer, C. A. F. de Oliveira, J. A. McCammon, and R. C. Walker, *Routine access to millisecond time scale events with accelerated molecular dynamics,* J. Chem. Theory Comput. **8**, 2997 (2012).

[127] K. Lindorff-Larsen, P. Maragakis, S. Piana, and D. E. Shaw, *Picosecond to millisecond structural dynamics in human ubiquitin,* J. Phys. Chem. B **120**, 8313 (2016).

[128] E. Lindahl, M. Abraham, B. Hess, and D. van der Spoel, *GROMACS 2021.2 manual,* (2021), http://dx.doi.org/10.5281/zenodo.4723561, accessed on 15/02/2024.

[129] M. J. Abraham, T. Murtola, R. Schulz, S. Páll, J. C. Smith, B. Hess, and E. Lindahl, *GROMACS: High performance molecular simulations through multi-level parallelism from laptops to supercomputers,* SoftwareX **1-2**, 19 (2015).

[130] S. Plimpton, *Fast parallel algorithms for short-range molecular dynamics,* J. Comput. Phys. **117**, 1 (1995).

[131] R. Salomon-Ferrer, D. A. Case, and R. C. Walker, *An overview of the Amber biomolecular simulation package,* WIREs Comput. Mol. Sci. **3**, 198 (2013).

[132] D. A. Case, H. M. Aktulga, K. Belfon, D. S. Cerutti, G. A. Cisneros, V. W. D. Cruzeiro, N. Forouzesh, T. J. Giese, A. W. Götz, H. Gohlke, S. Izadi, M. Kasava-jhala, M. C. Kaymak, E. King, T. Kurtzman, T.-S. Lee, P. Li, J. Liu, T. Luchko, R. Luo, M. Manathunga, M. R. Machado, H. M. Nguyen, K. A. O'Hearn, A. V. Onufriev, F. Pan, S. Pantano, R. Qi, A. Rahnamoun, A. Risheh, S. Schott-Verdugo, A. Shajan, J. Swails, J. Wang, H. Wei, X. Wu, Y. Wu, S. Zhang, S. Zhao, Q. Zhu, T. E. Cheatham, D. R. Roe, A. Roitberg, C. Simmerling, D. M. York, M. C. Nagan, and K. M. Merz, *AmberTools,* J. Chem. Inf. Model **63**, 6183 (2023).

[133] J. C. Phillips, D. J. Hardy, J. D. C. Maia, J. E. Stone, J. V. Ribeiro, R. C. Bernardi, R. Buch, G. Fiorin, J. Hénin, W. Jiang, R. McGreevy, M. C. R. Melo, B. K. Radak, R. D. Skeel, A. Singharoy, Y. Wang, B. Roux, A. Aksimentiev, Z. Luthey-Schulten, L. V. Kalé, K. Schulten, C. Chipot, and E. Tajkhorshid, *Scalable molecular dynamics on CPU and GPU architectures with NAMD,* J. Chem. Phys. **153**, 044130 (2020).

[134] W. Smith and R. Missen, *Chemical Reaction Equilibrium Analysis: Theory and Algorithms*, 1st ed. (Wiley, New York, 1982).

[135] M. W. Chase, J. L. Curnutt, H. Prophet, R. A. McDonald, and A. N. Syverud, *JANAF thermochemical tables, 1975 supplement,* J. Phys. Chem. Ref. Data **4**, 1 (1975).

[136] M. Chase, *NIST-JANAF Thermochemical Tables*, 4th ed. (American Institute of Physics, New York, 1998).

[137] A. Rahbari, M. Ramdin, L. J. P. van den Broeke, and T. J. H. Vlugt, *Combined steam reforming of methane and formic acid to produce syngas with an adjustable H_2:CO ratio,* Ind. Eng. Chem. Res. **57**, 10663 (2018).

[138] A. Rahbari, A. Poursaeidesfahani, A. Torres-Knoop, D. Dubbeldam, and T. J. H. Vlugt, *Chemical potentials of water, methanol, carbon dioxide and hydrogen sulphide at low temperatures using continuous fractional component Gibbs Ensemble Monte Carlo,* Mol. Sim. **44**, 405 (2018).

[139] D. O. Wasik, H. M. Polat, M. Ramdin, O. A. Moultos, S. Calero, and T. J. H. Vlugt, *Solubility of CO_2 in aqueous formic acid solutions and the effect of NaCl addition: A molecular simulation study,* J. Phys. Chem. C **126**, 19424 (2022).

[140] S. Lasala, K. Samukov, H. M. Polat, V. Lachet, O. Herbinet, R. Privat, J.-N. Jaubert, O. A. Moultos, K. D. Ras, and T. J. H. Vlugt, *Application of*

thermodynamics at different scales to describe the behaviour of fast reacting binary mixtures in vapour-liquid equilibrium, Chem. Eng. J. **483**, 148961 (2024).

[141] R. Cremona, S. Delgado, A. Valtz, A. Conversano, M. Gatti, and C. Coquelet, *Density and viscosity measurements and modeling of CO_2-loaded and unloaded aqueous solutions of potassium lysinate,* J. Chem. Eng. Data **66**, 4460 (2021).

[142] S. Delgado, A. Gaunand, C. Coquelet, R. Cadours, and C. Volpi, *A new reactive absorption model using extents of reaction and activities. I. Application to alkaline-salts-CO_2 systems,* Chem. Eng. Sci. **270**, 118522 (2023).

[143] D. T. Kallikragas, A. Y. Plugatyr, and I. M. Svishchev, *High temperature diffusion coefficients for O_2, H_2, and OH in water, and for pure water,* J. Chem. Eng. Data **59**, 1964 (2014).

[144] O. A. Moultos, I. N. Tsimpanogiannis, A. Z. Panagiotopoulos, and I. G. Economou, *Atomistic Molecular Dynamics simulations of CO_2 diffusivity in H_2O for a wide range of temperatures and pressures,* J. Phys. Chem. B **118**, 5532 (2014).

[145] O. A. Moultos, I. N. Tsimpanogiannis, A. Z. Panagiotopoulos, and I. G. Economou, *Self-diffusion coefficients of the binary (H_2O + CO_2) mixture at high temperatures and pressures,* J. Chem. Therm. **93**, 424 (2016).

[146] O. A. Moultos, I. N. Tsimpanogiannis, A. Z. Panagiotopoulos, J. P. M. Trusler, and I. G. Economou, *Atomistic molecular dynamics simulations of carbon dioxide diffusivity in n-hexane, n-decane, n-hexadecane, cyclohexane, and squalane,* J. Phys. Chem. B **120**, 12890 (2016).

[147] X. Zhao, H. Jin, Y. Chen, and Z. Ge, *Numerical study of H_2, CH_4, CO, O_2 and CO_2 diffusion in water near the critical point with molecular dynamics simulation,* Comput. Math. Appl. **81**, 759 (2021).

[148] P. Habibi, A. Rahbari, S. Blazquez, C. Vega, P. Dey, T. J. H. Vlugt, and O. A. Moultos, *A new force field for OH^- for computing thermodynamic and transport properties of H_2 and O_2 in aqueous NaOH and KOH solutions,* J. Phys. Chem. B **126**, 9376 (2022).

[149] L. E. Castro-Anaya and G. A. Orozco, *Self-diffusion coefficients of amines, a molecular dynamics study,* Fluid Phase Equilib. **553**, 113301 (2022).

[150] S. M. Melnikov and M. Stein, *The effect of CO_2 loading on alkanolamine absorbents in aqueous solutions,* Phys. Chem. Chem. Phys. **21**, 18386 (2019).

[151] J. K. Johnson, A. Z. Panagiotopoulos, and K. E. Gubbins, *Reactive canonical Monte Carlo,* Mol. Phys. **81**, 717 (1994).

[152] W. R. Smith and B. Triska, *The reaction ensemble method for the computer simulation of chemical and phase equilibria. I. Theory and basic examples,* J. Chem. Phys. **100**, 3019 (1994).

[153] C. H. Turner, J. K. Brennan, M. Lísal, W. R. Smith, J. K. Johnson, and K. E. Gubbins, *Simulation of chemical reaction equilibria by the reaction ensemble Monte Carlo method: A review,* Mol. Sim. **34**, 119 (2008).

[154] A. Z. Panagiotopoulos, *Direct determination of phase coexistence properties of fluids by Monte Carlo simulation in a new ensemble,* Mol. Phys. **61**, 813 (1987).

[155] A. Panagiotopoulos, N. Quirke, M. Stapleton, and D. Tildesley, *Phase equilibria by simulation in the Gibbs ensemble,* Mol. Phys. **63**, 527 (1988).

[156] A. Z. Panagiotopoulos and M. R. Stapleton, *The Gibbs method for molecular-based computer simulations of phase equilibria,* Fluid Phase Equilib. **53**, 133 (1989).

[157] W. Shi and E. J. Maginn, *Improvement in molecule exchange efficiency in Gibbs Ensemble Monte Carlo: Development and implementation of the Continuous Fractional Component move,* J. Comput. Chem. **29**, 2520 (2008).

[158] H. S. Salehi, R. Hens, O. A. Moultos, and T. J. H. Vlugt, *Computation of gas solubilities in choline chloride urea and choline chloride ethylene glycol deep eutectic solvents using Monte Carlo simulations,* J. Mol. Liq. **316**, 113729 (2020).

[159] A. Rahbari, J. C. Garcia-Navarro, M. Ramdin, L. J. P. van den Broeke, O. A. Moultos, D. Dubbeldam, and T. J. H. Vlugt, *Effect of water content on thermodynamic properties of compressed hydrogen,* J. Chem. Eng. Data **66**, 2071 (2021).

[160] N. Dawass, J. Langeveld, M. Ramdin, E. Pérez-Gallent, A. A. Villanueva, E. J. M. Giling, J. Langerak, L. J. P. van den Broeke, T. J. H. Vlugt, and O. A. Moultos, *Solubilities and transport properties of CO_2, oxalic acid, and formic acid in mixed solvents composed of deep eutectic solvents, methanol, and propylene carbonate,* J. Phys. Chem. B **126**, 3572 (2022).

[161] K. Kobayashi and A. Firoozabadi, *Effect of branching on mutual solubility of alkane–CO_2 systems by molecular simulations,* J. Phys. Chem. B **126**, 8300 (2022).

[162] W. A. van Rooijen, P. Habibi, K. Xu, P. Dey, T. J. H. Vlugt, H. Hajibeygi, and O. A. Moultos, *Interfacial tensions, solubilities, and transport properties of the H_2/H_2O/NaCl system: A molecular simulation study,* J. Chem. Eng. Data **69**, 307 (2024).

[163] H. Kerkache, H. Hoang, P. Cézac, G. Galliéro, and S. Chabab, *The solubility of H_2 in NaCl brine at high pressures and high temperatures: Molecular simulation study and thermodynamic modeling,* J. Mol. Liq. **400**, 124497 (2024).

[164] J. G. Kirkwood, *Statistical mechanics of fluid mixtures,* J. Chem. Phys. **3**, 300 (2004).

[165] Z. Mester and A. Z. Panagiotopoulos, *Mean ionic activity coefficients in aqueous NaCl solutions from molecular dynamics simulations,* J. Chem. Phys. **142**, 044507 (2015).

[166] D. Kussainova, A. Mondal, J. M. Young, S. Yue, and A. Z. Panagiotopoulos, *Molecular simulation of liquid–vapor coexistence for NaCl: Full-charge vs scaled-charge interaction models,* J. Chem. Phys. **153**, 024501 (2020).

[167] F. Wang and D. P. Landau, *Efficient, multiple-range random walk algorithm to calculate the density of states,* Phys. Rev. Lett. **86**, 2050 (2001).

[168] S. Kumar, J. M. Rosenberg, D. Bouzida, R. H. Swendsen, and P. A. Kollman, *The weighted histogram analysis method for free-energy calculations on biomolecules. I. The method,* J. Comput. Chem. **13**, 1011 (1992).

[169] A. Grossfield, *WHAM: The weighted histogram analysis method,* http://membrane.urmc.rochester.edu/wordpress/?page_id=126, accessed on 08.06.2021.

[170] C. H. Bennett, *Efficient estimation of free energy differences from Monte Carlo data,* J. Comput. Phys. **22**, 245 (1976).

[171] M. R. Shirts and J. D. Chodera, *Statistically optimal analysis of samples from multiple equilibrium states,* J. Chem. Phys. **129**, 124105 (2008).

[172] K. Beauchamp, J. Chodera, L. Naden, M. Shirts, S. Martiniani, C. Stern, R. T. McGibbon, R. Gowers, and D. Dotson, *choderalab/pymbar,* (2019).

[173] P. Rossky, J. Doll, and H. Friedman, *Brownian dynamics as smart Monte Carlo simulation,* J. Chem. Phys. **69**, 4628 (1978).

[174] C. Pangali, M. Rao, and B. Berne, *On a novel Monte Carlo scheme for simulating water and aqueous solutions,* Chem. Phys. Lett. **55**, 413 (1978).

[175] F. Moučka, M. Rouha, and I. Nezbeda, *Efficient multiparticle sampling in Monte Carlo simulations on fluids: Application to polarizable models,* J. Chem. Phys. **126**, 224106 (2007).

[176] S. Duane, A. Kennedy, B. J. Pendleton, and D. Roweth, *Hybrid Monte Carlo,* Phys. Lett. B **195**, 216 (1987).

[177] D. Dubbeldam, S. Calero, and T. J. H. Vlugt, *iRASPA: GPU-accelerated visualization software for materials scientists,* Mol. Sim. **44**, 653 (2018).

[178] T. T. Pham and M. R. Shirts, *Identifying low variance pathways for free energy calculations of molecular transformations in solution phase,* J. Chem. Phys. **135**, 034114 (2011).

[179] D. Wolf, P. Keblinski, S. Phillpot, and J. Eggebrecht, *Exact method for the simulation of Coulombic systems by spherically truncated, pairwise r^{-1} summation,* J. Chem. Phys. **110**, 8254 (1999).

[180] C. J. Fennell and J. D. Gezelter, *Is the Ewald summation still necessary? Pairwise alternatives to the accepted standard for long-range electrostatics,* J. Chem. Phys. **124**, 234104 (2006).

[181] C. Waibel, M. S. Feinler, and J. Gross, *A modified shifted force approach to the Wolf summation,* J. Chem. Theory Comput. **15**, 572 (2018).

[182] P. Ewald, *Die berechnung optischer und elektrostatischer gitterpotentiale,* Ann. Phys. **369**, 253 (1921).

[183] D. Dotson, O. Beckstein, D. Wille, I. Kenney, Z. Wu, shuail, H. Lee, trje3733, V. Lim, M. S. Barhaghi, and W.-T. Hsu, *alchemistry/alchemlyb: 0.4.2,* (2021).

[184] L. Verlet, *Computer "Experiments" on classical fluids. I. Thermodynamical properties of Lennard-Jones molecules,* Phys. Rev. **159**, 98 (1967).

[185] W. C. Swope, H. C. Andersen, P. H. Berens, and K. R. Wilson, *A computer simulation method for the calculation of equilibrium constants for the formation of physical clusters of molecules: Application to small water clusters,* J. Chem. Phys. **76**, 637 (1982).

[186] T. Miller, M. Eleftheriou, P. Pattnaik, A. Ndirango, D. Newns, and G. Martyna, *Symplectic quaternion scheme for biophysical molecular dynamics,* J. Chem. Phys. **116**, 8649 (2002).

[187] T. J. H. Vlugt, M. Martin, B. Smit, J. I. Siepmann, and R. Krishna, *Improving the efficiency of the configurational-bias Monte Carlo algorithm,* Mol. Phys. **94**, 727 (1998).

[188] H. Berendsen, J. Grigera, and T. Straatsma, *The missing term in effective pair potentials,* J. Phys. Chem. **91**, 6269 (1987).

[189] I. S. Joung and T. E. Cheatham, *Determination of alkali and halide monovalent ion parameters for use in explicitly solvated biomolecular simulations,* J. Phys. Chem. B **112**, 9020 (2008).

[190] S. L. Perkins, P. Painter, and C. M. Colina, *Molecular Dynamic simulations and vibrational analysis of an ionic liquid analogue,* J. Phys. Chem. B **117**, 10250 (2013).

[191] G.-J. Kroes, *Towards chemically accurate simulation of molecule–surface reactions,* Phys. Chem. Chem. Phys. **14**, 14966 (2012).

[192] A. Benavides, J. Aragones, and C. Vega, *Consensus on the solubility of NaCl in water from computer simulations using the chemical potential route,* J. Chem. Phys. **144**, 124504 (2016).

[193] W. J. Hamer and Y. Wu, *Osmotic coefficients and mean activity coefficients of uni-univalent electrolytes in water at 25°C,* J. Phys. Chem. Ref. Data **1**, 1047 (1972).

[194] A. T. Celebi, T. J. H. Vlugt, and O. A. Moultos, *Structural, thermodynamic, and transport properties of aqueous reline and ethaline solutions from Molecular Dynamics simulations,* J. Phys. Chem. B **123**, 11014 (2019).

[195] F. J. Zeleznik and S. Gordon, *Calculation of complex chemical equilibria,* Ind. Eng. Chem. **60**, 27 (1968).

[196] S. P. Balaji, S. Gangarapu, M. Ramdin, A. Torres-Knoop, H. Zuilhof, E. L. V. Goetheer, D. Dubbeldam, and T. J. H. Vlugt, *Simulating the reactions of CO_2 in aqueous monoethanolamine solution by reaction ensemble Monte Carlo using the continuous fractional component method,* J. Chem. Theory Comput. **11**, 2661 (2015).

[197] J. P. Jakobsen, J. Krane, and H. F. Svendsen, *Liquid–phase composition determination in CO_2–H_2O–alkanolamine systems: An NMR study,* Ind. Eng. Chem. Res. **44**, 9894 (2005).

[198] W. Böttinger, M. Maiwald, and H. Hasse, *Online NMR spectroscopic study of species distribution in MDEA–H_2O–CO_2 and MDEA–PIP–H_2O–CO_2,* Ind. Eng. Chem. Res. **47**, 7917 (2008).

[199] R. Behrens, E. von Harbou, W. R. Thiel, W. Böttinger, T. Ingram, G. Sieder, and H. Hasse, *Monoalkylcarbonate formation in methyldiethanolamine–H_2O–CO_2,* Ind. Eng. Chem. Res. **56**, 9006 (2017).

[200] Y. Zhang and C. C. Chen, *Thermodynamic modeling for CO_2 absorption in aqueous MDEA solution with electrolyte NRTL model,* Ind. Eng. Chem. Res. **50**, 163 (2011).

[201] S. Hempel, J. Fischer, D. Paschek, and G. Sadowski, *Activity coefficients of complex molecules by molecular simulation and Gibbs-Duhem integration,* Soft Mater. **10**, 26 (2012).

[202] S. P. Balaji, S. K. Schnell, E. S. McGarrity, and T. J. H. Vlugt, *A direct method for calculating thermodynamic factors for liquid mixtures using the Permuted Widom test particle insertion method,* Mol. Phys. **111**, 287 (2013).

[203] A. Rahbari, R. Hens, S. Jamali, M. Ramdin, D. Dubbeldam, and T. J. H. Vlugt, *Effect of truncating electrostatic interactions on predicting thermodynamic properties of water–methanol systems,* Mol. Sim. **45**, 336 (2018).

[204] J. Noroozi and W. R. Smith, *Prediction of alkanolamine pKa values by combined molecular dynamics free energy simulations and ab initio calculations,* J. Chem. Eng. Data **65**, 1358 (2020).

[205] W. R. Smith and W. Qi, *Molecular simulation of chemical reaction equilibrium by computationally efficient free energy minimization,* ACS Cent. Sci. **4**, 1185 (2018).

[206] J. Noroozi and W. R. Smith, *An efficient molecular simulation methodology for chemical reaction equilibria in electrolyte solutions: Application to CO_2 reactive absorption,* J. Phys. Chem. A **123**, 4074 (2019).

[207] A. D. Becke, *Density-functional thermochemistry. III. The role of exact exchange,* J. Chem. Phys. **98**, 5648 (1993).

[208] C. Lee, W. Yang, and R. G. Parr, *Development of the Colle-Salvetti correlation-energy formula into a functional of the electron density,* Phys. Rev. B **37**, 785 (1988).

[209] J. Zhan, B. Wang, L. Zhang, B.-C. Sun, J. Fu, G.-W. Chu, and H. Zou, *Simultaneous absorption of H_2S and CO_2 into the MDEA + PZ aqueous solution in a rotating packed bed,* Ind. Eng. Chem. Res. **59**, 8295 (2020).

[210] Y. Zhang and C. C. Chen, *Modeling gas solubilities in the aqueous solution of methyldiethanolamine,* Ind. Eng. Chem. Res. **50**, 6436 (2011).

[211] P. Pal, A. AbuKashabeh, S. Al-Asheh, and F. Banat, *Role of aqueous methyldiethanolamine (MDEA) as solvent in natural gas sweetening unit and process contaminants with probable reaction pathway,* J. Nat. Gas. Sci. Eng. **24**, 124 (2015).

[212] A. Plakia and E. Voutsas, *Modeling of H_2S, CO_2 +H_2S, and CH_4 + CO_2 solubilities in aqueous monoethanolamine and methyldiethanolamine solutions,* Ind. Eng. Chem. Res. **59**, 11317 (2020).

[213] P. J. Huttenhuis, N. J. Agrawal, E. Solbraa, and G. F. Versteeg, *The solubility of carbon dioxide in aqueous N-methyldiethanolamine solutions,* Fluid Phase Equilib. **264**, 99 (2008).

[214] M. Anoua, A. Ramirez-Martinez, F. Cherblanc, and J.-C. Benet, *The use of chemical potential to describe water transfer in complex media with strong solid-liquid bonding,* Transp. Porous Media **102**, 111 (2014).

[215] S. I. Sandler, *Chemical, Biochemical, and Engineering Thermodynamics*, 4th ed. (John Wiley & Sons, Hoboken, New Jersey, 2006).

[216] A. Vegh, J. Korozs, and G. Kaptay, *Extension of the Gibbs-Duhem equation to the partial molar surface thermodynamic properties of solutions,* Langmuir **38**, 4906 (2022).

[217] P. Virtanen, R. Gommers, T. E. Oliphant, M. Haberland, T. Reddy, D. Courna-peau, E. Burovski, P. Peterson, W. Weckesser, J. Bright, S. J. van der Walt, M. Brett, J. Wilson, K. J. Millman, N. Mayorov, A. R. J. Nelson, E. Jones, R. Kern, E. Larson, C. J. Carey, İ. Polat, Y. Feng, E. W. Moore, J. VanderPlas, D. Laxalde, J. Perktold, R. Cimrman, I. Henriksen, E. A. Quintero, C. R. Harris, A. M. Archibald, A. H. Ribeiro, F. Pedregosa, P. van Mulbregt, and SciPy 1.0 Contributors, *SciPy 1.0: Fundamental Algorithms for Scientific Computing in Python,* Nat. Methods **17**, 261 (2020).

[218] P. J. G. Huttenhuis, N. J. Agrawal, and G. F. Versteeg, *Solubility of carbon dioxide and hydrogen sulfide in aqueous N-methyldiethanolamine solutions,* Ind. Eng. Chem. Res. **48**, 4051 (2009).

[219] M. Bolhàr-Nordenkampf, A. Friedl, U. Koss, and T. Tork, *Modelling selective H_2S absorption and desorption in an aqueous MDEA-solution using a rate-based non-equilibrium approach,* Chem. Eng. Process. **43**, 701 (2004).

[220] N. J. Higham, *Accuracy and Stability of Numerical Algorithms*, 2nd ed. (Society for Industrial and Applied Mathematics, Philadelphia, PA, 2002).

[221] J. M. Young and A. Z. Panagiotopoulos, *System-size dependence of elec-trolyte activity coefficients in molecular simulations,* J. Phys. Chem. B **122**, 3330 (2018).

[222] W. L. Jorgensen, J. Chandrasekhar, J. D. Madura, R. W. Impey, and M. L. Klein, *Comparison of simple potential functions for simulating liquid water,* J. Chem. Phys. **79**, 926 (1983).

[223] L. S. Dodda, I. C. D. Vaca, J. Tirado-Rives, and W. L. Jorgensen, *LigParGen web server: an automatic OPLS-AA parameter generator for organic ligands,* Nucleic Acids Res. **45**, W331 (2017).

[224] T. Kristóf and J. Liszi, *Effective Intermolecular Potential for Fluid Hydrogen Sulfide,* J. Phys. Chem. B **101**, 5480 (1997).

[225] G. A. Orozco, I. G. Economou, and A. Z. Panagiotopoulos, *Optimization of intermolecular potential parameters for the CO_2/H_2O mixture,* J. Phys. Chem. B **118**, 11504 (2014).

[226] L. Fang, E. Makkonen, M. Todorovic, P. Rinke, and X. Chen, *Efficient amino acid conformer search with bayesian optimization,* J. Chem. Theory Comput. **17**, 4906–4912 (2021).

[227] L. A. Curtiss, P. C. Redfern, and K. Raghavachari, *Gaussian-4 theory,* J. Chem. Phys. **126**, 84108 (2007).

[228] B. H. Besler, K. M. Merz, and P. A. Kollman, *Atomic charges derived from semiempirical methods,* J. Comput. Chem. **11**, 431 (1990).

[229] J. Wang, W. Wang, P. A. Kollman, and D. A. Case, *Automatic atom type and bond type perception in molecular mechanical calculations,* Journal of Molecular Graphics and Modelling , 247 (2006).

[230] G. D. R. Matos, G. Calabrò, and D. L. Mobley, *Infinite dilution activity coefficients as constraints for force field parametrization and method development,* J. Chem. Theory Comput. **15**, 3066 (2019).

[231] J. Damay, F. Jirasek, M. Kloft, M. Bortz, and H. Hasse, *Predicting activity coefficients at infinite dilution for varying temperatures by matrix completion,* Ind. Eng. Chem. Res. **60**, 14564 (2021).

[232] E. A. Guggenheim and J. C. Turgeon, *Specific interaction of ions,* Trans. Faraday Soc. , 747 (1955).

[233] G. Puxty and M. Maeder, *A simple chemical model to represent CO_2–amine–H_2O vapour–liquid-equilibria,* Int. J. Greenh. Gas Control. **17**, 215 (2013).

[234] F. Y. Jou, A. E. Mather, and F. D. Otto, *Solubility of H_2S and CO_2 in aqueous methyldiethanolamine solutions,* Ind. Eng. Chem. Process Des. Dev. **21**, 539 (1982).

[235] W. J. Rogers, J. A. Bullin, and R. R. Davison, *FTIR measurements of acid-gas–methyldiethanolamine systems,* AIChE J. **44**, 2423 (1998).

[236] D. M. Austgen, G. T. Rochelle, and C. C. Chen, *Model of vapor-liquid equilibria for aqueous acid gas-alkanolamine systems. 2. Representation of H_2S and CO_2 solubility in aqueous MDEA and CO_2 solubility in aqueous mixtures of MDEA with MEA or DEA,* Ind. Eng. Chem. Res. **30**, 543 (1991).

[237] A. Benamor and M. K. Aroua, *Modeling of CO_2 solubility and carbamate concentration in DEA, MDEA and their mixtures using the Deshmukh–Mather model,* Fluid Phase Equilib. **231**, 150 (2005).

[238] A. V. Rayer, K. Z. Sumon, L. Jaffari, and A. Henni, *Dissociation constants (pKa) of tertiary and cyclic amines: Structural and temperature dependences,* J. Chem. Eng. Data **59**, 31 (2014).

[239] T. A. Halgren and W. Damm, *Polarizable force fields,* Curr. Opin. Struct. Biol. **11**, 236 (2001).

[240] A. Warshel, M. Kato, and A. V. Pisliakov, *Polarizable force fields: History, test cases, and prospects,* J. Chem. Theory Comput. **3**, 2034 (2007).

[241] L. P. Wang, J. Chen, and T. V. Voorhis, *Systematic parametrization of polarizable force fields from quantum chemistry data,* J. Chem. Theory Comput. **9**, 452 (2013).

[242] H. Jiang, Z. Mester, O. A. Moultos, I. G. Economou, and A. Z. Panagiotopoulos, *Thermodynamic and transport properties of H_2O + NaCl from polarizable force fields,* J. Chem. Theory Comput. **11**, 3802 (2015).

[243] H. Jiang, O. A. Moultos, I. G. Economou, and A. Z. Panagiotopoulos, *Gaussian-charge polarizable and nonpolarizable models for CO_2,* J. Phys. Chem. B **120**, 984 (2016).

[244] H. Jiang, O. A. Moultos, I. G. Economou, and A. Z. Panagiotopoulos, *Hydrogen-bonding polarizable intermolecular potential model for water,* J. Phys. Chem. B **120**, 12358 (2016).

[245] K. Goloviznina, J. N. C. Lopes, M. C. Gomes, and A. A. Pádua, *Transferable, polarizable force field for ionic liquids,* J. Chem. Theory Comput. **15**, 5858 (2019).

[246] Z. Jing, C. Liu, S. Y. Cheng, R. Qi, B. D. Walker, J. P. Piquemal, and P. Ren, *Polarizable force fields for biomolecular simulations: Recent advances and applications,* Annu. Rev. Biophys. **48**, 371 (2019).

[247] C. M. Baker, *Polarizable force fields for Molecular Dynamics simulations of biomolecules,* Wiley Interdisc. Rev. Comput. Mol. Sci. **5**, 241 (2015).

[248] P. Pandey, A. H. Aytenfisu, A. D. Mackerell, and S. S. Mallajosyula, *Drude polarizable force field parametrization of carboxylate and N-acetyl amine carbohydrate derivatives,* J. Chem. Theory Comput. **15**, 4982 (2019).

[249] R. V. Vaz, J. R. Gomes, and C. M. Silva, *Molecular dynamics simulation of diffusion coefficients and structural properties of ketones in supercritical CO_2 at infinite dilution,* J. Supercrit. Fluids **107**, 630 (2016).

[250] J. Wang, H. Zhong, H. Feng, W. Qiu, and L. Chen, *Molecular dynamics simulation of diffusion coefficients and structural properties of some alkylbenzenes in supercritical carbon dioxide at infinite dilution,* J. Chem. Phys. **140**, 104501 (2014).

[251] X. Rozanska, E. Wimmer, and F. de Meyer, *Quantitative kinetic model of CO_2 absorption in aqueous tertiary amine solvents,* J. Chem. Inf. Model **61**, 1814 (2021).

[252] A. Tamimi, E. B. Rinker, and O. C. Sandall, *Diffusion coefficients for hydrogen sulfide, carbon dioxide, and nitrous oxide in water over the temperature range 293–368 k,* J. Chem. Eng. Data **39**, 330 (1994).

[253] S. Y. Oh, M. Binns, H. Cho, and J. K. Kim, *Energy minimization of MEA-based CO_2 capture process,* Appl. Energy **169**, 353 (2016).

[254] T. L. Sønderby, K. B. Carlsen, P. L. Fosbøl, L. G. Kiørboe, and N. von Solms, *A new pilot absorber for CO_2 capture from flue gases: Measuring and modelling capture with MEA solution,* Int. J. Greenh. Gas Control. **12**, 181 (2013).

[255] I. N. Tsimpanogiannis, O. A. Moultos, L. F. Franco, M. B. M. Spera, M. Erdős, and I. G. Economou, *Self-diffusion coefficient of bulk and confined water: a critical review of classical molecular simulation studies,* Mol. Sim. **45**, 425 (2019).

[256] L. Martinez, R. Andrade, E. G. Birgin, and J. M. Martínez, *PACKMOL: A package for building initial configurations for molecular dynamics simulations,* J. Comput. Chem. **30**, 2157 (2009).

[257] S. H. Jamali, L. Wolff, T. M. Becker, M. de Groen, M. Ramdin, R. Hartkamp, A. Bardow, T. J. H. Vlugt, and O. A. Moultos, *OCTP: A Tool for On-the-Fly Calculation of Transport Properties of Fluids with the Order-n Algorithm in LAMMPS,* J. Chem. Inf. Model **59**, 1290 (2019).

[258] I.-C. Yeh and G. Hummer, *System-size dependence of diffusion coefficients and viscosities from Molecular Dynamics simulations with periodic boundary conditions,* J. Phys. Chem. B **108**, 15873 (2004).

[259] S. H. Jamali, L. Wolff, T. M. Becker, A. Bardow, T. J. H. Vlugt, and O. A. Moultos, *Finite-Size Effects of Binary Mutual Diffusion Coefficients from Molecular Dynamics,* J. Chem. Theory Comput. **14**, 2667 (2018).

[260] A. T. Celebi, S. H. Jamali, A. Bardow, T. J. H. Vlugt, and O. A. Moultos, *Finite-size effects of diffusion coefficients computed from Molecular Dynamics: a review of what we have learned so far,* Mol. Sim. **47**, 831 (2021).

[261] S. H. Jamali, A. Bardow, T. J. H. Vlugt, and O. A. Moultos, *Generalized form for finite-size corrections in mutual diffusion coefficients of multicomponent mixtures obtained from equilibrium Molecular Dynamics simulation,* J. Chem. Theory Comput. **16**, 3799 (2020).

[262] R. Krishna and J. A. Wesselingh, *The Maxwell-Stefan approach to mass transfer,* Chem. Eng. Sci. **52**, 861 (1997).

[263] A. T. Celebi, N. Dawass, O. A. Moultos, and T. J. H. Vlugt, *How sensitive are physical properties of choline chloride-urea mixtures to composition changes: Molecular Dynamics simulations and Kirkwood-Buff theory,* J. Chem. Phys. **154**, 184502 (2021).

[264] A. Chaumont, E. Engler, and R. Schurhammer, *Is charge scaling really mandatory when developing fixed-charge atomistic force fields for deep eutectic solvents?* J. Phys. Chem. B **124**, 7239 (2020).

[265] A. González De Castilla, J. P. Bittner, S. Müller, S. Jakobtorweihen, and I. Smirnova, *Thermodynamic and transport properties modeling of deep eutectic solvents: A review on g^E-models, equations of state, and Molecular Dynamics,* J. Chem. Eng. Data **65**, 943 (2020).

[266] V. V. Chaban, I. V. Voroshylova, and O. N. Kalugin, *A new force field model for the simulation of transport properties of imidazolium-based ionic liquids,* Phys. Chem. Chem. Phys. **13**, 7910 (2011).

[267] S. Blazquez, I. M. Zeron, M. M. Conde, J. L. Abascal, and C. Vega, *Scaled charges at work: Salting out and interfacial tension of methane with*

electrolyte solutions from computer simulations, Fluid Phase Equilib. **513**, 112548 (2020).

[268] I. M. Zeron, J. L. Abascal, and C. Vega, *A force field of Li^+, Na^+, K^+, Mg^{2+}, Ca^{2+}, Cl^-, and SO_4^{2-} in aqueous solution based on the TIP4P/2005 water model and scaled charges for the ions,* J. Chem. Phys. **151**, 134504 (2019).

[269] H. Liu, E. Maginn, A. E. Visser, N. J. Bridges, and E. B. Fox, *Thermal and transport properties of six ionic liquids: An experimental and Molecular Dynamics study,* Ind. Eng. Chem. Res. **51**, 7242 (2012).

[270] S. L. Perkins, P. Painter, and C. M. Colina, *Experimental and computational studies of choline chloride-based deep eutectic solvents,* J. Chem. Eng. Data **59**, 3652 (2014).

[271] T. G. Amundsen, L. E. Øi, and D. A. Eimer, *Density and viscosity of monoethanolamine + water + carbon dioxide from (25 to 80) °C,* J. Chem. Eng. Data **54**, 3096 (2009).

[272] W. V. Wilding, T. A. Knotts, N. F. Giles, and R. L. Rowley, *DIPPR® Data Compilation of Pure Chemical Properties* (AIChE, New York, NY, 2020).

[273] M. Sobrino, E. I. Concepción, Á. Gómez-Hernández, M. C. Martín, and J. J. Segovia, *Viscosity and density measurements of aqueous amines at high pressures: MDEA-water and MEA-water mixtures for CO_2 capture,* J. Chem. Therm. **98**, 231 (2016).

[274] G. T. Rochelle, *Conventional amine scrubbing for CO_2 capture,* in *Absorption-Based Post-combustion Capture of Carbon Dioxide*, edited by P. H. Feron (Woodhead Publishing, 2016) pp. 35–67.

[275] M. N. Rodnikova, F. M. Samigullin, I. A. Solonina, and D. A. Sirotkin, *Molecular mobility and the structure of polar liquids,* J. Struct. Chem. **55**, 256 (2014).

[276] M. N. Rodnikova, Z. S. Idiyatullin, I. A. Solonina, D. A. Sirotkin, and A. B. Razumova, *Molecular self-diffusion coefficients in solutions of dimethylsulfoxide in monoethanolamine,* Russ. J. Phys. Chem. A **92**, 1486 (2018).

[277] B. P. Mandal, M. Kundu, and S. S. Bandyopadhyay, *Physical solubility and diffusivity of N_2O and CO_2 into aqueous solutions of (2-amino-2-methyl-1-propanol + monoethanolamine) and (N-methyldiethanolamine + monoethanolamine),* J. Chem. Eng. Data **50**, 352 (2005).

[278] T. C. Chan, H. T. Li, and K. Y. Li, *Effects of shapes of solute molecules on diffusion: A study of dependences on solute size, solvent, and temperature,* J. Phys. Chem. B **119**, 15718 (2015).

[279] R. J. Speedy and C. A. Angell, *Isothermal compressibility of supercooled water and evidence for a thermodynamic singularity at -45°C,* J. Chem. Phys. **65**, 851 (1976).

[280] W. Lu, H. Guo, I. M. Chou, R. C. Burruss, and L. Li, *Determination of diffusion coefficients of carbon dioxide in water between 268 and 473K in a high-pressure capillary optical cell with in situ Raman spectroscopic measurements,* Geochim. Cosmochim. Acta. **115**, 183 (2013).

[281] T. R. Carey, J. E. Hermes, and G. T. Rochelle, *A model of acid gas absorption/stripping using methyldiethanolamine with added acid,* Gas Sep. Purif. **5**, 95 (1991).

[282] Z. Qian, L.-B. Xu, Z.-H. Li, H. Li, and K. Guo, *Selective absorption of H_2S from a gas mixture with CO_2 by aqueous N-methyldiethanolamine in a rotating packed bed,* Ind. Eng. Chem. Res. **49**, 6196 (2010).

[283] X. Rozanska, A. Valtz, M. Riva, C. Coquelet, E. Wimmer, K. Gonzalez-Tovar, and F. de Meyer, *Selective H_2S absorption in aqueous tertiary alkanolamine solvents: Experimental measurements and quantitative kinetic model,* Ind. Eng. Chem. Res. **62**, 11480 (2023).

[284] M. E. Boot-Handford, J. C. Abanades, E. J. Anthony, M. J. Blunt, S. Brandani, N. M. Dowell, J. R. Fernández, M.-C. Ferrari, R. Gross, J. P. Hallett, R. S. Haszeldine, P. Heptonstall, A. Lyngfelt, Z. Makuch, E. Mangano, R. T. J. Porter, M. Pourkashanian, G. T. Rochelle, N. Shah, J. G. Yao, and P. S. Fennell, *Carbon capture and storage update,* Energy Environ. Sci. **7**, 130 (2014).

[285] P. Pal and F. Banat, *Comparison of thermal degradation between fresh and industrial aqueous methyldiethanolamine with continuous injection of H_2S/CO_2 in high pressure reactor,* J. Nat. Gas. Sci. Eng. **29**, 479 (2016).

[286] U. Shoukat, E. Baumeister, D. D. Pinto, and H. K. Knuutila, *Thermal stability and corrosion of tertiary amines in aqueous amine and amine-glycol-water solutions for combined acid gas and water removal,* J. Nat. Gas. Sci. Eng. **62**, 26 (2019).

[287] G. F. Versteeg and W. P. M. van Swaaij, *On the kinetics between CO_2 and alkanolamines both in aqueous and non-aqueous solutions—I. Primary and secondary amines,* Chem. Eng. Sci. **43**, 573 (1988).

[288] G. F. Versteeg and W. P. M. van Swaaij, *On the kinetics between CO_2 and alkanolamines both in aqueous and non-aqueous solutions-II. Tertiary amines,* Chem. Eng. Sci. **43**, 587 (1988).

[289] R. Littel, B. Filmer, G. Versteeg, and W. V. Swaaij, *Modelling of simultaneous absorption of H_2S and CO_2 in alkanolamine solutions: The influence of parallel and consecutive reversible reactions and the coupled diffusion of ionic species,* Chem. Eng. Sci. **46**, 2303 (1991).

[290] M. A. Pacheco and G. T. Rochelle, *Rate-based modeling of reactive absorption of CO_2 and H_2S into aqueous methyldiethanolamine,* Ind. Eng. Chem. Res. **37**, 4107 (1998).

[291] M. E. Adams, T. L. Marshall, and R. L. Rowley, *Diffusion coefficients significant in modeling the absorption rate of carbon dioxide into aqueous blends of N-methyldiethanolamine and diethanolamine and of hydrogen sulfide into aqueous N-methyldiethanolamine,* J. Chem. Eng. Data **43**, 605 (1998).

[292] Y. Yu, T. Zhang, G. Liu, Z. Zhang, and G. Wang, *Identifying the multi-ion effects on the phase flow, mass and heat transfer in amine absorption of CO_2,* Int. J. Heat Mass Transf. **114**, 501 (2017).

[293] Delft High Performance Computing Centre (DHPC), *DelftBlue Supercomputer (Phase 1),* https://www.tudelft.nl/dhpc/ark:/44463/DelftBluePhase1 (2022).

[294] M. S. Shah, M. Tsapatsis, and J. I. Siepmann, *Development of the transferable potentials for phase equilibria model for hydrogen sulfide,* J. Phys. Chem. B **119**, 7041 (2015).

[295] W. D. Cornell, P. Cieplak, C. I. Bayly, I. R. Gould, K. M. Merz, D. M. Ferguson, D. C. Spellmeyer, T. Fox, J. W. Caldwell, and P. A. Kollman, *A second generation force field for the simulation of proteins, nucleic acids, and organic molecules,* J. Am. Chem. Soc. **117**, 5179 (1995).

[296] G. A. Orozco, V. Lachet, C. Nieto-Draghi, and A. D. MacKie, *A transferable force field for primary, secondary, and tertiary alkanolamines,* J. Chem. Theory Comput. **9**, 2097 (2013).

[297] J. P. Foster and F. Weinhold, *Natural hybrid orbitals,* J. Am. Chem. Soc. **102**, 7211 (1980).

[298] A. E. Reed, L. A. Curtiss, and F. Weinhold, *Intermolecular interactions from a natural bond orbital, donor-acceptor viewpoint,* Chem. Rev. **88**, 899 (1988).

[299] B. L. Bhargava and S. Balasubramanian, *Refined potential model for atomistic simulations of ionic liquid [bmim][PF_6],* J. Chem. Phys. **127**, 114510 (2007).

[300] T. G. A. Youngs and C. Hardacre, *Application of static charge transfer within an ionic-liquid force field and its effect on structure and dynamics,* ChemPhysChem **9**, 1548 (2008).

[301] H. M. Polat, F. de Meyer, C. Houriez, C. Coquelet, O. A. Moultos, and T. J. H. Vlugt, *Transport properties of mixtures of acid gases with aqueous monoethanolamine solutions: A Molecular Dynamics study,* Fluid Phase Equilib. **564**, 113587 (2023).

[302] M. Jorge, M. C. Barrera, A. W. Milne, C. Ringrose, and D. J. Cole, *What is the optimal dipole moment for nonpolarizable models of liquids?* J. Chem. Theory Comput. **19**, 1790 (2023).

[303] M. Jorge, J. R. Gomes, and M. C. Barrera, *The dipole moment of alcohols in the liquid phase and in solution,* J. Mol. Liq. **356**, 119033 (2022).

[304] H. S. Salehi, A. T. Celebi, T. J. H. Vlugt, and O. A. Moultos, *Thermodynamic, transport, and structural properties of hydrophobic deep eutectic solvents composed of tetraalkylammonium chloride and decanoic acid,* J. Chem. Phys. **154**, 144502 (2021).

[305] A. L. Benavides, M. A. Portillo, V. C. Chamorro, J. R. Espinosa, J. L. F. Abascal, and C. Vega, *A potential model for sodium chloride solutions based on the TIP4P/2005 water model,* J. Chem. Phys. **147**, 104501 (2017).

[306] A. Z. Panagiotopoulos, *Simulations of activities, solubilities, transport properties, and nucleation rates for aqueous electrolyte solutions,* J. Chem. Phys. **153**, 010903 (2020).

[307] T. Janzen and J. Vrabec, *Diffusion coefficients of a highly nonideal ternary liquid mixture: Cyclohexane–toluene–methanol,* Ind. Eng. Chem. Res. **57**, 16508 (2018).

[308] D. Dubbeldam, D. C. Ford, D. E. Ellis, and R. Q. Snurr, *A new perspective on the order-n algorithm for computing correlation functions,* Mol. Sim. **35**, 1084 (2009).

[309] O. A. Moultos, Y. Zhang, I. N. Tsimpanogiannis, I. G. Economou, and E. J. Maginn, *System-size corrections for self-diffusion coefficients calculated from molecular dynamics simulations: The case of CO_2, n-alkanes, and poly(ethylene glycol) dimethyl ethers,* J. Chem. Phys. **145**, 074109 (2016).

[310] H. A. Al-Ghawas, D. P. Hagewiesche, G. Ruiz-Ibanez, and O. C. Sandall, *Physicochemical properties important for carbon dioxide absorption in aqueous methyldiethanolamine,* J. Chem. Eng. Data **34**, 385 (1989).

[311] N. Haimour and O. C. Sandall, *Molecular diffusivity of hydrogen sulfide in water,* J. Chem. Eng. Data **29**, 20 (1984).

[312] S. Blazquez, M. M. Conde, and C. Vega, *Scaled charges for ions: An improvement but not the final word for modeling electrolytes in water,* J. Chem. Phys. **158**, 054505 (2023).

[313] E. D. Snijder, M. J. te Riele, G. F. Versteeg, and W. P. van Swaaij, *Diffusion coefficients of several aqueous alkanolamine solutions,* J. Chem. Eng. Data **38**, 475 (1993).

[314] H. Sun, *Compass: An ab initio force-field optimized for condensed-phase applications – overview with details on alkane and benzene compounds,* J. Phys. Chem. B **102**, 7338 (1998).

[315] X. Song, Y. Zhang, C. Wu, X. Sheng, and H. Zhao, *Exploration of H_2S capture by alkanolamines,* Struct. Chem. **30**, 2419 (2019).

[316] Monu, B. K. Oram, and B. Bandyopadhyay, *Bridging H_2O and H_2S homomeric clusters via H_2O-H_2S mixed clusters: Impact of the changing ratio of H_2O and H_2S moieties,* Comput. Theor. Chem. **1213**, 113740 (2022).

[317] R. H. Weiland, J. C. Dingman, and D. B. Cronin, *Heat capacity of aqueous monoethanolamine, diethanolamine, N-methyldiethanolamine, and N-ethyldiethanolamine-based blends with carbon dioxide,* J. Chem. Eng. Data **42**, 1004 (1997).

[318] M. Shokouhi and R. Ahmadi, *Measuring the density and viscosity of H_2S-loaded aqueous methyldiethanolamine solution,* J. Chem. Therm. **102**, 228 (2016).

[319] E. B. Rinker, A. T. Colussi, N. L. McKnight, and O. C. Sandall, *Effect of hydrogen sulfide loading on the density and viscosity of aqueous solutions of methyldiethanolamine,* J. Chem. Eng. Data **45**, 254 (2000).

[320] D. D. D. Pinto, B. Johnsen, M. Awais, H. F. Svendsen, and H. K. Knuutila, *Viscosity measurements and modeling of loaded and unloaded aqueous solutions of MDEA, DMEA, DEEA and MAPA,* Chem. Eng. Sci. **171**, 340 (2017).

[321] M. E. Tuckerman, D. Marx, and M. Parrinello, *The nature and transport mechanism of hydrated hydroxide ions in aqueous solution,* Nature **417**, 925 (2002).

[322] D. Riccardi, P. König, X. Prat-Resina, H. Yu, M. Elstner, T. Frauenheim, and Q. Cui, *"Proton holes" in long-range proton transfer reactions in solution and enzymes: A theoretical analysis,* J. Am. Chem. Soc. **128**, 16302 (2006).

[323] T. Miyake and M. Rolandi, *Grotthuss mechanisms: from proton transport in proton wires to bioprotonic devices,* J. Phys. Condens. Matt. **28**, 023001 (2016).

[324] T. Helgaker, T. A. Ruden, P. Jørgensen, J. Olsen, and W. Klopper, *A priori calculation of molecular properties to chemical accuracy,* J. Phys. Org. Chem. **17**, 913 (2004).

[325] J. Klimeš, D. R. Bowler, and A. Michaelides, *Chemical accuracy for the van der waals density functional,* J. Phys. Condens. Matt. **22**, 022201 (2010).

[326] S. Dasgupta, E. Lambros, J. P. Perdew, and F. Paesani, *Elevating density functional theory to chemical accuracy for water simulations through a density-corrected many-body formalism,* Nat. Commun. **12**, 6359 (2021).

[327] H. Fu, Y. Zhou, X. Jing, X. Shao, and W. Cai, *Meta-analysis reveals that absolute binding free-energy calculations approach chemical accuracy,* J. Med. Chem. **65**, 12970 (2022).

[328] A. Z. Panagiotopoulos and S. Yue, *Dynamics of aqueous electrolyte solutions: Challenges for simulations,* J. Phys. Chem. B **127**, 430 (2023).

[329] T. C. Beutler, A. E. Mark, R. C. van Schaik, P. R. Gerber, and W. F. van Gunsteren, *Avoiding singularities and numerical instabilities in free energy calculations based on molecular simulations,* Chem. Phys. Lett. **222**, 529 (1994).

[330] L. N. Naden, T. T. Pham, and M. R. Shirts, *Linear basis function approach to efficient alchemical free energy calculations. 1. Removal of uncharged atomic sites,* J. Chem. Theory Comput. **10**, 1128 (2014).

[331] T. J. H. Vlugt, E. García-Pérez, D. Dubbeldam, S. Ban, and S. Calero, *Computing the heat of adsorption using molecular simulations: The effect of strong coulombic interactions,* J. Chem. Theory Comput. **4**, 1107 (2008).

[332] B. A. Wells and A. L. Chaffee, *Ewald summation for molecular simulations,* J. Chem. Theory Comput. **11**, 3684 (2015).

[333] D. Zahn, B. Schilling, and S. M. Kast, *Enhancement of the Wolf damped coulomb potential: Static, dynamic, and dielectric properties of liquid water from molecular simulation,* J. Phys. Chem. B **106**, 10725 (2002).

[334] P. Demontis, S. Spanu, and G. B. Suffritti, *Application of the Wolf method for the evaluation of Coulombic interactions to complex condensed matter systems: Aluminosilicates and water,* J. Chem. Phys. **114**, 7980 (2001).

[335] J. D. Madura and B. Pettitt, *Effects of truncating long-range interactions in aqueous ionic solution simulations,* Chem. Phys. Lett. **150**, 105 (1988).

[336] P. J. Steinbach and B. R. Brooks, *New spherical-cutoff methods for long-range forces in macromolecular simulation,* J. Comput. Chem. **15**, 667 (1994).

[337] P. Mark and L. Nilsson, *Structure and dynamics of liquid water with different long-range interaction truncation and temperature control methods in molecular dynamics simulations,* J. Comput. Chem. **23**, 1211 (2002).

[338] M. Tuckerman, B. J. Berne, and G. J. Martyna, *Reversible multiple time scale molecular dynamics,* J. Chem. Phys. **97**, 1990 (1992).

[339] S. K. Gray, D. W. Noid, and B. G. Sumpter, *Symplectic integrators for large scale molecular dynamics simulations: A comparison of several explicit methods,* J. Chem. Phys. **101**, 4062 (1994).

[340] W. Smith, C. Yong, and P. Rodger, *DL_POLY: Application to molecular simulation,* Mol. Sim. **28**, 385 (2002).

[341] W. H. Press, S. A. Teukolsky, W. T. Vetterling, and B. P. Flannery, *Numerical Recipes: The Art of Scientific Computing*, 3rd ed. (Cambridge University Press, New York, NY, USA, 2007).

[342] H. Kamberaj, R. Low, and M. Neal, *Time reversible and symplectic integrators for molecular dynamics simulations of rigid molecules,* J. Chem. Phys. **122**, 224114 (2005).

[343] J. P. Perdew, M. Ernzerhof, A. Zupan, and K. Burke, *Why density-gradient corrections improve atomization energies and barrier heights,* Adv. Quantum Chem. **33**, 1 (1998).

[344] W. R. Smith and R. W. Missen, *The effect of isomerization on chemical equilibrium,* Can. J. Chem. Eng. **52**, 280 (1974).

[345] K. A. Peterson, D. Feller, and D. A. Dixon, *Chemical accuracy in ab initio thermochemistry and spectroscopy: current strategies and future challenges,* Theor. Chem. Acc. **131**, 1 (2012).

[346] R. M. Enick and S. M. Klara, *CO_2 solubility in water and brine under reservoir conditions,* Chem. Eng. Commun. **90**, 23 (1990).

[347] E. C. W. Clarke and D. N. Glew, *Aqueous nonelectrolyte solutions. part viii. deuterium and hydrogen sulfides solubilities in deuterium oxide and water,* Can. J. Chem. **49**, 691 (1971).

[348] H. M. Polat, C. van der Geest, F. de Meyer, C. Houriez, T. J. H. Vlugt, and O. A. Moultos, *Densities, viscosities, and diffusivities of loaded and unloaded aqueous CO_2/H_2S/MDEA mixtures: A Molecular Dynamics simulation study,* Fluid Phase Equilib. **575**, 113913 (2023).

[349] L. S. Dodda, J. Z. Vilseck, J. Tirado-Rives, and W. L. Jorgensen, *1.14*CM1A-LBCC: Localized bond-charge corrected CM1A charges for condensed-phase simulations,* J. Phys. Chem. B **121**, 3864 (2017).

Summary

Molecular simulations predict the thermodynamic and transport properties by computing the interactions between the molecules in a system. These simulations offer practical alternatives to address challenges arising from experimental limitations in measuring Vapor-Liquid Equilibria (VLE) of acid gases at very low partial pressures and the diffusivities in reactive solutions. In this thesis, we investigated how force field-based molecular simulations can be used to compute reaction equilibria and transport properties, relevant for absorption-based CO_2 and H_2S removal. We introduced novel features to the Brick-CFCMC code (Chapter 2) and developed a versatile chemical reaction equilibria solver, called CASpy, to compute the concentration of species in any reactive liquid-phase absorption system, including CO_2 and H_2S absorption in aqueous alkanolamine solutions (Chapter 3). We also investigated transport properties of CO_2 and H_2S in aqueous solutions of two commonly used alkanolamines, MEA (Chapter 4) and MDEA (Chapter 5). In Chapter 2, we focused on the calculation of the excess chemical potential (μ^{ex}) by implementing thermodynamic integration with efficient bookkeeping, and the efficiency of MC simulations by implementing hybrid MD/MC trial moves. Thermodynamic integration eliminated the need for sampling the full λ-space in a single MC simulation and enabled the computation of μ^{ex} for ionic and/or polar species. The accuracy and reliability of our approach was demonstrated for the computation of the excess chemical potential of NaCl $\mu^{\text{ex}}_{\text{NaCl}}$ in water at infinite dilution, showing agreement with simulations and experimental data from literature. We also implemented hybrid MD/MC translation and rotation trial moves, demonstrating increased efficiency of MC simulations even when these trial moves consist of 0.1% of the trial moves. Chapter 3 revealed crucial insights into gas absorption and computing reaction equilibria using free energy and quantum chemistry calculations using CASpy. CASpy consistently delivered correct numerical solutions at chemical equilibria, as shown by the CO_2 isotherms computed from very low (10^{-7} kPa) to high (10^4 kPa) pressures in aqueous MDEA solutions. The computed single-component CO_2 isotherms and speciations in CO_2-loaded aqueous MDEA solutions showed excellent agreement with experimental data from literature. However, we faced challenges in achieving agreement between the computed binary adsorption isotherms of CO_2 and H_2S in aqueous MDEA solutions and experimental results from literature, indicating that refitting of the reaction equilibrium constants is needed for H_2S/CO_2/MDEA/water systems. The sensitivity of CO_2 absorption isotherms in aqueous MDEA solutions to the reaction equilibrium constants emphasizes the limitations of computing reaction equilibria using free energy and quantum chemistry calculations. A sensitivity analysis using different force fields (OPLS-AA force field and GAFF) and point charge scaling factors showed the critical role of accurate point charges in molecular simulations in computing accurate reaction equilibria as the computed values of μ^{ex}_i (and, consequently, the computed reaction equilibrium constants) are very

sensitive to point charges of the molecules. The effect of temperature and MEA concentration on the transport properties of acid gases in aqueous MEA solutions is investigated in Chapter 4. We computed the densities of pure MEA and 30 wt.% MEA/water solutions for a wide range of temperatures and scaling factors for MEA point charges (χ^q_{MEA}). Our results showed that a point charge scaling factor of $\chi^q_{\mathrm{MEA}} = 0.80$ played a crucial role in achieving agreement between the computed densities and experimental data from literature. To validate this scaling factor, we computed the viscosities and (finite-size corrected) self-diffusivities of pure MEA and 30 wt.% MEA/water solutions for a wide range of temperatures, showing excellent agreement between the computed transport properties and experimental ones from literature. The self-diffusivities of infinitely diluted CO_2 and H_2S in aqueous MEA solutions highlighted the significant dependence of acid gas diffusivities on temperature and, especially, MEA concentration in the solution. We also revealed an intriguing observation: despite the higher molecular weight of CO_2 (44.01 g mol^{-1}) compared to H_2S (34.1 g mol^{-1}), CO_2 diffuses faster than H_2S in aqueous MEA solutions. This is because (1) H_2S has the capability to form hydrogen bonds with the surrounding molecules (water and MEA) which can impede its diffusion, and (2) the linear shape of CO_2 allows for less hindrance in diffusion compared to the spherical H_2S. Chapter 5 focuses on the transport properties of acid gases in unloaded and, for the first time in literature, loaded aqueous MDEA solutions. Comparison between the computed densities and viscosities and experimental data from literature showed that a scaling factor for the point charges of MDEA $\chi^q_{\mathrm{MDEA}} = 0.90$ is needed. The computed self-diffusivities of CO_2 and H_2S in aqueous MDEA solutions revealed a significant dependence on the MDEA concentration in the solution, as both CO_2 and H_2S diffuse ca. 3.5 times faster in 10 wt.% MDEA/solutions compared to 50 wt.% MDEA/water solutions. Using the computed radial distribution functions, we showed that H_2S has stronger interactions with the surrounding molecules, resulting in a slower diffusion compared to CO_2 in these solutions. Our results emphasized the need for different point charge scaling factors for the reaction products of CO_2 ($\chi^q_{\mathrm{products}} = 0.90$) and H_2S ($\chi^q_{\mathrm{products}} = 0.75$) in acid gas-loaded aqueous MDEA solutions. We showed a significant decrease in the self-diffusivities of free CO_2, HCO_3^{-}, and MDEAH$^+$ in CO_2-loaded solutions, suggesting a slowdown in CO_2 absorption, with increasing CO_2 loading. This was not the case for H_2S absorption since the self-diffusivities of free H_2S, SH$^-$, and MDEAH$^+$ in H_2S-loaded aqueous MDEA solutions did not exhibit significant changes with increasing H_2S loading.

Samenvatting

Moleculaire simulaties voorspellen de thermodynamische en transporteigenschappen van bulkmaterialen door de interacties tussen de moleculen in een systeem te modelleren. Deze simulaties bieden een praktisch alternatief om uitdagingen te lijf te gaan die voortkomen uit experimentele beperkingen bij het meten van vloeistof-damp evenwichten (VLE) van CO_2 en H_2S bij zeer lage partiële drukken en de diffusie coëfficiënten in reactieve oplossingen. In dit proefschrift hebben we onderzocht hoe op krachtvelden gebaseerde moleculaire simulaties kunnen worden gebruikt om reactie evenwichten en transporteigenschappen te berekenen die relevant zijn voor op absorptie gebaseerde CO_2- en H_2S-verwijdering. We hebben nieuwe functionaliteiten geïntroduceerd in de Brick-CFCMC software (Hoofdstuk 2) en een veelzijdige solver voor chemische reactie evenwichten ontwikkeld, genaamd CASpy, om de concentratie van componenten in elk reactief vloeistoffase-absorptiesysteem te berekenen, inclusief CO_2 en H_2S-absorptie in waterige alkanolamine oplossingen (Hoofdstuk 3). We hebben ook de transporteigenschappen van CO_2 en H_2S onderzocht in waterige oplossingen van twee veelgebruikte alkanolamines, MEA (Hoofdstuk 4) en MDEA (Hoofdstuk 5). Brick-CFCMC is een state-of-the-art open-source Monte Carlo (MC) simulatie code voor de berekening van fase- en reactie evenwichten in verschillende ensembles met behulp van klassieke krachtvelden. In Hoofdstuk 2 presenteren we verbeteringen in de open-source Brick-CFCMC-simulatiecode door nieuwe functionaliteit te introduceren voor de berekening van fase- en reactie evenwichten, namelijk thermodynamische integratie en hybride MD/MC-trial moves. We concentreren ons op de berekening van de zogenaamde excess chemische potentiaal (μ^{ex}) met thermodynamische integratie met efficiënte boekhouding van de verschillende interacties. Thermodynamische integratie elimineert de noodzaak om de volledige λ-ruimte te sampelen in een enkele MC simulatie en dit maakt de berekening van μ^{ex} voor ionische en/of polaire componenten mogelijk. De nauwkeurigheid en betrouwbaarheid van onze aanpak werd gedemonstreerd voor de berekening van de excess chemische potentiaal van NaCl $\mu^{\text{ex}}_{\text{NaCl}}$ in water bij oneindige verdunning. Onze berekeningen komen overeen met simulaties en experimentele gegevens uit de literatuur. We hebben ook hybride MD/MC-translatie- en rotatie trial moves geïmplementeerd voor een verhoogde efficiëntie van de MC simulaties, zelfs als deze trial moves slechts 0.1% van alle trial moves uitmaken. Hoofdstuk 3 onthult cruciale inzichten in gasabsorptie voor het berekenen van reactie-evenwichten met behulp van vrije energie- en kwantumchemische berekeningen met behulp van CASpy. CASpy levert consistent correcte numerieke oplossingen van chemische reactie evenwichten, zoals blijkt uit de CO_2-isothermen berekend van zeer lage (10^{-7} kPa) tot hoge (10^4 kPa) drukken in waterige MDEA-oplossingen. De berekende zuivere-component CO_2 isothermen en zogenaamde speciation van CO_2-beladen waterige MDEA-oplossingen lijn in goede overeenstemming met experimentele gegevens uit de literatuur. We

werden echter geconfronteerd met uitdagingen bij het bereiken van overeenstem-
ming tussen de berekende binaire adsorptie-isothermen van CO_2 en H_2S in wa-
terige MDEA-oplossingen en experimentele resultaten uit de literatuur, wat erop
wijst dat het aanpassen van de reactie evenwichtsconstanten nodig is voor het
$H_2S/CO_2/MDEA/water$ systeem. De gevoeligheid van CO_2-absorptie-isothermen in
waterige MDEA-oplossingen voor de reactie-evenwichtsconstanten benadrukt de
beperkingen voor het berekenen van reactie-evenwichten met behulp van vrije
energie- en kwantumchemische berekeningen. Een gevoeligheidsanalyse met be-
hulp van verschillende krachtvelden (OPLS-AA en GAFF) en schaalfactoren voor
atomaire ladingen toont de cruciale rol aan van nauwkeurige atomaire ladingen
in moleculaire simulaties bij het berekenen van reactie evenwichten, aangezien de
berekende waarden van μ_i^{ex} (en bijgevolg de berekende reactie evenwichtsconstan-
ten) zeer gevoelig zij voor de ladingen van de atomen in het systeem. Het effect van
temperatuur en MEA-concentratie op de transporteigenschappen van zure gassen
(CO_2 en H_2S) in waterige MEA-oplossingen wordt onderzocht in Hoofdstuk 4. We
berekenen de dichtheden van zuivere MEA en 30 massa% MEA/water-oplossingen
voor verschillende temperaturen en schaalfactoren voor de ladingen van de atomen
in MEA (χ_{MEA}^q). Onze resultaten toonden aan dat een schaalfactor voor atomaire
ladingen van $\chi_{\text{MEA}}^q = 0,80$ een cruciale rol speelt bij het bereiken van overeenstem-
ming tussen de berekende dichtheden en experimentele gegevens uit de literatuur.
Om deze schaalfactor te valideren, berekenen we de viscositeit en zelf-diffusie co-
ëfficiënten (die laatste gecorrigeerd voor de eindige systeem grootte) van zuivere
MEA- en 30 massa% MEA/water-oplossingen voor een breed temperatuurbereik,
wat een uitstekende overeenkomst aantoont tussen de berekende transporteigen-
schappen en experimentele waardes uit de literatuur. De zelf-diffusie coëfficiën-
ten van oneindig verdund CO_2 en H_2S in waterige MEA-oplossingen benadrukken
de grote afhankelijkheid van de temperatuur en vooral de MEA-concentratie in de
oplossing. We onthulden ook een intrigerende observatie: ondanks het hogere
moleculgewicht van CO_2 ($44,01\ \text{g mol}^{-1}$) vergeleken met H_2S ($34,1\ \text{g mol}^{-1}$), dif-
fundeert CO_2 sneller dan H_2S in waterige MEA-oplossingen. Dit komt omdat (1)
H_2S de mogelijkheid heeft om waterstofbruggen te vormen met de omringende
moleculen (water en MEA) die de diffusie ervan kunnen belemmeren, en (2) de
lineaire vorm van CO_2 resulteert in minder hinder bij diffusie vergeleken met het
meer bolvormige H_2S. Hoofdstuk 5 richt zich op de transporteigenschappen van
zure gassen in onbeladen en (voor het eerst in de literatuur) met CO_2 en H_2S
beladen waterige MDEA-oplossingen. Een vergelijking tussen de berekende dicht-
heden en viscositeiten en experimentele gegevens uit de literatuur tonen aan dat
een schaalfactor voor de atomaire ladingen van MDEA $\chi_{\text{MDEA}}^q = 0,90$ nodig is. De
berekende zelfdiffusie coefficienten van CO_2 en H_2S in waterige MDEA-oplossingen
laten een significante afhankelijkheid van de MDEA-concentratie in de oplossing
zien, aangezien zowel CO_2 als H_2S ca. 3,5 keer sneller diffunderen in 10 massa%
MDEA oplossingen vergeleken met 50 massa% MDEA oplossingen. Met behulp van
de berekende radiale verdelingsfuncties hebben we aangetoond dat H_2S sterkere
interacties heeft met de omringende moleculen, wat resulteert in een langzamere
diffusie vergeleken met CO_2. Onze resultaten benadrukken de behoefte aan ver-

schillende schaalfactoren voor atomaire ladingen voor de reactieproducten van CO_2 met amines ($\chi^q_{\text{producten}} = 0,90$) en H_2S ($\chi^q_{\text{producten}} = 0,75$) in met zuur gas beladen waterige MDEA-oplossingen. We laten een significante afname zien in de zelfdiffusie van vrij CO_2, HCO_3^- en $MDEAH^+$ in CO_2 beladen oplossingen, wat duidt op een vertraging van de CO_2 absorptie bij een toenemende CO_2 belading. Dit is niet het geval voor H_2S-absorptie, aangezien de zelfdiffusie van vrij H_2S, SH^- en $MDEAH^+$ in met H_2S beladen waterige MDEA-oplossingen geen significante veranderingen vertonen bij toenemende H_2S belading.

Curriculum Vitæ

Hüsamettin Mert Polat

13-05-1994   Born in Turhal, Türkiye.

Education

2012–2017   BSc. in Metallurgical and Materials Engineering
Istanbul Technical University, İstanbul, Türkiye

2017–2019   MSc. in Materials Science and Engineering
Koç University, İstanbul, Türkiye,

2020–2024   PhD in Process & Energy
Delft University of Technology, Delft, The Netherlands
Thesis: Molecular Simulations of Acid Gas Absorption by Liquid Solvents
Promotor: Prof. dr. ir. T. J. H. Vlugt
Promotor: Dr. O. A. Moultos

List of Publications

Publications included in this thesis:

1. **H. M. Polat**, C. van der Geest, F. de Meyer, C. Houriez, T. J. H. Vlugt, and O. A. Moultos, *Densities, viscosities, and diffusivities of loaded and unloaded aqueous CO_2/H_2S/MDEA mixtures: A molecular dynamics simulation study*, Fluid Phase Equilib., **575**, 113913 (2023)

2. **H. M. Polat**, F. de Meyer, C. Houriez, O. A. Moultos, and T. J. H. Vlugt, *Solving Chemical Absorption Equilibria using Free Energy and Quantum Chemistry Calculations: Methodology, Limitations, and New Open-Source Software*, J. Chem. Theory Comput., **19**, 2616 (2023)

3. **H. M. Polat**, F. de Meyer, C. Houriez, C. Coquelet, O. A. Moultos and T. J. H. Vlugt, *Transport properties of mixtures of acid gases with aqueous monoethanolamine solutions: A molecular dynamics study*, Fluid Phase Equilib., **564**, 113587 (2023)

4. **H. M. Polat**, H. S. Salehi, R. Hens, D. O. Wasik, A. Rahbari, F. de Meyer, C. Houriez, C. Coquelet, S. Calero, D. Dubbeldam, O. A. Moultos, and T. J. H. Vlugt, *New Features of the Open Source Monte Carlo Software Brick-CFCMC: Thermodynamic Integration and Hybrid Trial Moves*, J. Chem. Inf. Model., **61**, 3752 (2021)

Publications not included in this thesis:

1. **H. M. Polat**, F. M. Coelho, T. J. H. Vlugt, L. F. M. Franco, I. N. Tsipanogiannis, and O. A. Moultos, *Diffusivity of CO_2 in H_2O: A Review of Experimental Studies and Molecular Simulations in the Bulk and in Confinement*, J. Chem. Eng. Data., 2024, *in press*, DOI: 10.1021/acs.jced.3c00778

2. **H. M. Polat**, S. Lasala, F. de Meyer, C. Houriez, O. A. Moultos, and T. J. H. Vlugt, *Scaling Towards the Critical Point in the Combined Reaction/Gibbs Ensemble*, Fluid Phase Equilib., **582**, 114084 (2024)

3. S. Lasala, K. Samukov, **H. M. Polat**, V. Lachet, O. Herbinet, R. Privat, J-N. Jaubert, O. A. Moultos, K. de Ras, and T. J. H. Vlugt, *Application of Thermodynamics at Different Scales to Describe the Behaviour of Fast Reacting Binary Mixtures in Vapour-Liquid Equilibrium*, Chem. Eng. J., **483**, 148961 (2024)

4. D. O. Wasik, **H.M. Polat**, M. Ramdin, O. A. Moultos, S. Calero, and T. J. H. Vlugt, *Solubility of CO_2 in Aqueous Formic Acid Solutions and the Effect of NaCl Addition: A Molecular Simulation Study*, J. Phys. Chem. C, **126**, 19424 (2022)

5. H. S. Salehi, **H.M. Polat**, F. de Meyer, C. Houriez, C. Coquelet, T. J. H. Vlugt, and O. A. Moultos, *Vapor Pressures and Vapor Phase Compositions of Choline Chloride Urea and Choline Chloride Ethylene Glycol Deep Eutectic Solvents from Molecular Simulation*, J. Chem. Phys., **155**, 114504 (2021)

6. S. Kavak, Ö. Durak, H. Kulak, **H. M. Polat**, S. Keskin, and A. Uzun, *Enhanced Water Purification Performance of Ionic Liquid Impregnated Metal–Organic Framework: Dye Removal by [BMIM][PF$_6$]/MIL-53(Al) Composite*, Front. Chem., **8**, 622567 (2021)

7. M. Zeeshan, H. Kulak, S. Kavak, **H. M. Polat**, Ö. Durak, S. Keskin, and A. Uzun, *Influence of anion size and electronic structure on the gas separation performance of ionic liquid/ZIF-8 composites*, Microporous Mesoporous Mater., **306**, 110446 (2020)

8. Ö. Durak, H. Kulak, S. Kavak, **H. M. Polat**, S. Keskin, and A. Uzun, *Towards complete elucidation of structural factors controlling thermal stability of IL/MOF composites: effects of ligand functionalization on MOFs*, J. Phys. Condens. Matt., **32**, 484001 (2020)

9. **H. M. Polat**, S. Kavak, H. Kulak, A. Uzun, and S. Keskin, *CO$_2$ separation from flue gas mixture using [BMIM][BF$_4$]/MOF composites: linking high-throughput computational screening with experiments*, Chem. Eng. J., **394**, 124916 (2020)

10. S. Kavak, H. Kulak, **H. M. Polat**, S. Keskin, and A. Uzun, *Fast and Selective Adsorption of Methylene Blue from Water Using [BMIM][PF$_6$]-Incorporated UiO-66 and NH$_2$-UiO-66*, Cryst. Growth Des., **20**, 3590 (2020)

11. S. Kavak, **H. M. Polat**, H. Kulak, S. Keskin, and A. Uzun, *MIL–53(Al) as a Versatile Platform for Ionic-Liquid/MOF Composites to Enhance CO$_2$ Selectivity over CH$_4$ and N$_2$*, Chem. Asian J., **14**, 3655 (2019)

12. **H. M. Polat**, M. Zeeshan, A. Uzun, and S. Keskin, *Unlocking CO$_2$ separation performance of ionic liquid/CuBTC composites: Combining experiments with molecular simulations*, Chem. Eng. J., **373**, 1179 (2019)

13. H. Kulak, **H. M. Polat**, S. Kavak, S. Keskin, and A. Uzun, *Improving CO$_2$ Separation Performance of MIL-53(Al) by Incorporating 1-n-Butyl-3-Methylimidazolium Methyl Sulfate*, Energy Technol., **7**, 1900157 (2019)

Acknowledgements